UNIVERSITAT POLITÈCNICA DE VALÈNCIA

Departamento de Máquinas y Motores Térmicos

DOCTORAL THESIS

Development of an installation to emulate altitude, ambient temperature, and ambient humidity on thermal engines. Application to the study of the impact over E6 engine performance

Presented by: D. ROBERTO TABET ALEIXANDRE

Supervised by: DR. D. JOSÉ RAMÓN SERRANO CRUZ

Co-supervised by: DR. D. JAVIER GÓMEZ GIL

in fulfillment of the requisites for the degree of
Doctor of Philosophy

Valencia, May 2022

Doctoral Thesis

“Development of an installation to emulate altitude, ambient temperature, and ambient humidity on thermal engines. Application to the study of the impact over E6 engine performance”

Presented by: D. ROBERTO TABET ALEIXANDRE

Supervised by: DR. D. JOSÉ RAMÓN SERRANO CRUZ

Co-supervised by: DR. D. JAVIER GÓMEZ GIL

THESIS EXAMINERS

Dr. D. AARON W. COSTALL

Dr. D. OCTAVIO ARMAS

Dr. D. RICHARD DAVID BURKE

DEFENSE COMMITTEE

Chairman: DR. D. HECTOR CLIMENT PUCHADES

Secretary: DR. D. Mª REYES GARCÍA CONTRERAS

Member: DR. D. RICHARD DAVID BURKE

Valencia, May 2022

Abstract

Increasingly restrictive regulations on pollutant emissions for motor vehicles imposed by the European Union have forced original equipment manufacturers (OEMs) to provide research centers with tools and facilities that can accurately and repeatedly reproduce different atmospheric conditions during the early stages of engine development. Nowadays, the European legislation includes real driving emissions (RDE) tests at different atmospheric conditions, with altitudes up to 1300 meters above sea level and temperatures reaching -7 ºC. This has been done typically using altimetric and climatic chambers, which allow the reproduction of the atmospheric conditions in the whole test cell. More recently, connecting to the engine altitude simulators coupled with air handling units (AHU).

In this Ph.D. Thesis, the improvement of the altitude simulator commercialized by the company HORIBA called MEDAS, carried out by inductive and deductive procedures, is presented to extend the installation's performance range, improve the combustion air pressure control accuracy, and reduce the installation global energy consumption. Furthermore, during this phase, the development of a 1D model of the altitude simulator is carried out, with which it is possible to obtain accurate results about the performance of the installation for different boundary conditions such as the engine operation point, the room pressure, or the cooling water temperature.

Following, two new pieces of equipment have been developed: MEDAS Temperature Module (MTM) and MEDAS Humidity Module (MHM), improving the control strategies and some key components (i.e., the bubbles water-column) to increase the accuracy of the combustion air temperature and humidity control. Together with the MEDAS, these two create a complete atmosphere simulator, which allows the independent control of the three psychrometric variables of the engine combustion air: pressure, temperature, and humidity.

Lastly, the atmosphere simulator developed is used to study the effect that the three psychometric variables of the ambient air have on the performance and the pollutant emissions of a Euro 6 turbocharged diesel engine, proving the significant effect that the ambient humidity has on the diesel engines pollutant emissions and the necessity of considering this parameter in the calibration strategies. Some results could be the reduction in power that the engine suffers when operating in altitude conditions, the changes that the ambient temperature causes at the turbocharger operative point, or the decrease in NOx emissions that happen when the ambient humidity increases.

Keywords: Atmosphere simulator, atmospheric conditions, diesel engine, 1D modeling, psychrometry

Resumen

Las normativas cada vez más restrictivas sobre las emisiones contaminantes de los vehículos de motor impuestas por la Unión Europea han obligado a los fabricantes de equipos originales (OEM) a proporcionar a los centros de investigación herramientas e instalaciones que pueden reproducir de forma precisa y repetida diferentes condiciones atmosféricas durante las primeras etapas del desarrollo del motor. En la actualidad la legislación europea incluye pruebas de emisiones reales en conducción (RDE) en diferentes condiciones atmosféricas, con altitudes de hasta 1300 metros sobre el nivel del mar y temperaturas que alcanzan los -7 ºC. Esto se ha hecho típicamente utilizando cámaras climáticas y altimétricas que permiten la reproducción de las condiciones atmosféricas en toda la celda de prueba, y más recientemente conectando a motor simuladores de altitud acoplados con unidades de tratamiento de aire (AHU).

En esta Tesis Doctoral, se presenta la mejora del simulador de altitud comercializado por la empresa HORIBA denominado MEDAS, utilizando procedimientos tanto inductivos como deductivos, con el objetivo de ampliar el rango de prestaciones de la instalación, así como mejorar la precisión del control de la presión del aire comburente y reducir el consumo energético global. Además, durante esta fase, se lleva a cabo el desarrollo de un modelo 1D del simulador de altitud, con el que es posible obtener resultados precisos sobre el desempeño de la instalación para diferentes condiciones de contorno, como puede ser el punto operativo del motor, la presión de la sala o la temperatura del agua de refrigeración.

A continuación, se han desarrollado dos nuevos equipos: el Módulo de Temperatura del MEDAS (MTM) y el Módulo de Humedad del MEDAS (MHM); mejorando las estrategias de control y algunos componentes clave (por ejemplo, la columna de agua de burbujas) para controlar con precisión la temperatura y la humedad del aire de combustión. Estos dos junto con el MEDAS crean un simulador de atmósfera completo, que permite el control independiente de las tres variables psicrométricas del aire de combustión del motor: presión, temperatura y humedad.

Por último, el simulador de atmósfera desarrollado se utiliza para estudiar el efecto que las tres variables psicométricas del aire ambiente tienen sobre el rendimiento y las emisiones contaminantes de un motor Diesel Euro 6 turboalimentado, demostrando el gran efecto que tiene la humedad ambiental sobre las emisiones contaminantes de los motores Diesel y la necesidad de considerar este parámetro en las estrategias de calibración. Algunos resultados obtenidos podrían ser la reducción de potencia que el motor sufre al operar en condiciones de altitud, los cambios que la temperatura ambiente causa en el

punto de operación del turbo grupo o como las emisiones de NOx se reducen cuando la humedad ambiente aumenta.

Resum

Les normatives cada vegada més restrictives sobre les emissions contaminants dels vehicles de motor imposades per la Unió Europea han obligat als fabricants d'equips originals (OEM) a proporcionar als centres d'investigació eines i instal·lacions que poden reproduir de manera precisa i repetida diferents condicions atmosfèriques durant les primeres etapes del desenvolupament del motor. En l'actualitat la legislació europea inclou proves d'emissions reals en conducció (RDE) en diferents condicions atmosfèriques, amb altituds de fins a 1300 metres sobre el nivell de la mar i temperatures que aconsegueixen els -7 °C. Això s'ha fet típicament utilitzant cambres climàtiques i altimètriques que permeten la reproducció de les condicions atmosfèriques en tota la cel·la de prova, i més recentment connectant a motor simuladors d'altitud acoblats amb unitats de tractament d'aire (AHU).

En aquesta Tesi Doctoral, es presenta la millora del simulador d'altitud comercialitzat per l'empresa HORIBA denominat MEDAS, utilitzant procediments tant inductius com deductius, amb l'objectiu d'ampliar el rang de prestacions de la instal·lació així com millorar la precisió del control de pressió de l'aire de combustió i reduir el consum energètic global. A més, durant aquesta fase, es du a terme el desenvolupament d'un model 1D del simulador d'altitud, amb el qual és possible obtindre resultats precisos sobre l'acompliment de la instal·lació per a diferents condicions de contorn, com pot ser el punt d'operació del motor, l'altitud d'instal·lació o la temperatura de l'aigua de refrigeració.

A continuació, s'han desenvolupat dos nous equips: el Mòdul de Temperatura del MEDAS (MTM) i el Mòdul d'Humitat del MEDAS (MHM); millorant les estratègies de control i alguns components clau (per exemple, la columna d'aigua de bambolles) per a controlar amb precisió la temperatura i la humitat de l'aire de combustió. Aquests dos juntament amb el MEDAS creen un simulador d'atmosfera complet, que permet el control independent de les tres variables psicromètriques de l'aire de combustió del motor: pressió, temperatura i humitat.

Finalment, el simulador d'atmosfera desenvolupat s'utilitza per a estudiar l'efecte que les tres variables psicomètriques de l'aire ambient tenen sobre el rendiment i les emissions contaminants d'un motor Dièsel Euro 6 *turboalimentado, demostrant el gran efecte que té la humitat ambiental sobre les emissions contaminants dels motors Dièsel i la necessitat de considerar aquest paràmetre en les estratègies de calibratge. Alguns resultats obtinguts podrien ser la reducció de potència que el motor pateix en operar en condicions d'altitud, els canvis que la temperatura ambient causa en el punt d'operació del turbo grup o com les emissions de NOx es redueixen quan la humitat ambiente augmenta.

List of publications

Roberto Tabet Aleixandre is co-author of the publications detailed in this section, with the supervision of other members of the I.U. CMT-Motores Térmicos (CMT), specially by Prof. José Ramón Serrano Cruz, and the thesis co-director (Dr. Javier Gómez Gil), from the company HORIBA GmbH.

The publications depicted in this section result from the research activities performed during the candidate's doctorate. The respondent carried out several experimental activities, which were analyzed and processed to back up the studies and assumptions pretended. The analysis and discussion of results and procedures were done in collaboration with the thesis director (Prof. José Ramón Serrano Cruz), the thesis co-director (Dr. Javier Gómez Gil), and the co-authors of each publication.

In each study, the contribution made by each author is specified in the "contributions description section" included in the different studies. Any requirement to guarantee the fulfillment of the Ph.D. works, such as materials, software licenses, and test benches, were provided by the UPV and CMT.

The works cited in this section have been improved, ordered, linked, completed, and further discussed in the present thesis manuscript.

For readiness and to avoid a reiterative structure at the beginning of each chapter, the publications mentioned above have not been cited every time. As part of the discussions, figures and results have been taken from these publications. However, they have been appropriately referred to in the document itself.

This section compensates and justifies that the basis of the innovative component has already been presented in the publications specified in this section, therefore constituting the thesis document.

Following the CMT signing order protocol, the CMT members sign the publication according to seniority. Therefore, the Ph.D. candidate becomes the last signer of the CMT members in every study/publication.

[1] A. Broatch, V. Bermúdez, J. R. Serrano, R. Tabet, J. Gómez, and S. Bender, "Analysis of passenger car turbocharged diesel engines performance when tested at altitude and of the altitude simulator device used," *Journal of Engineering for Gas Turbines and Power*, vol. 141, no. 8, Aug. 2019, doi: 10.1115/1.4043395.

[2] J. R. Serrano, P. Piqueras, A. Abbad, R. Tabet, S. Bender, and J. Gómez, "Impact on reduction of pollutant emissions from passenger cars when replacing

euro 4 with euro 6d diesel engines considering the altitude influence," *Energies*, vol. 12, no. 7, 2019, doi: 10.3390/en12071278.

[3] J. R. Serrano, A. Gil, P. Quintero, R. Tabet, and J. Gómez, "Design of a bubble reactor for altitude simulators used to humidify a combustion air stream by means of CFD multi-phase models," *Applied Sciences (Switzerland)*, vol. 11, no. 1, pp. 1–15, Jan. 2021, doi: 10.3390/app11010295.

[4] J. R. Serrano, J. Martín, P. Piqueras, R. Tabet, and J. Gómez, "Effect of natural and forced air charge humidity on medium-duty engines performance at high altitude and hot air conditions," *Energy*. Submitted for publication

Acknowledgments

Many thanks to Prof. José Ramón Serrano for his help and guidance during my doctorate and for his infinite patience and dedication. I could not have completed this Thesis. Also, thank you to Javier Gómez, who helped me start in the research world. Without him, I wouldn't have enjoyed my internship in Germany as I did.

A very special thank you to the technician team of the CMT, especially to Miguel Ortiz and Ali Abbad. They were fundamental for completing the experimental part of the Thesis and made the long hours in the laboratory much more enjoyable.

Also, thank you to the doctorate candidates' group with which I have shared the office these past years: Lukas, Vishnu, Alex, David, Barbara, and Vitor; this part of my training would have been very different without them.

And, lastly, an excellent thank you to my family, my parents Roberto and Mercedes, my brother Jorge and my girlfriend Mar for their support and motivation, without which I wouldn't have reached so far.

Valencia, May 2022

Contents

List of Figures

List of Tables

List of Equations

List of symbols

Latin characters

A	Area	m^2
C	Constant	-
Cd	Discharge coefficient	-
Cp	Specific heat capacity at constant pressure	J/(kg·K)
D	Diameter	m
D	Diameter	m
F	Friction factor	-
G	Volumetric flow rate	m^3/h
H	Heat transfer coefficient	$W/(m^2 \cdot K)$
K	Fitting coefficient	-
Kv	Flow coefficient	m^3/h
L	Length	m
$\dot{m}$	Mass flow rate	kg/h
N	Compressor speed	rpm
P	Compressor power	W
P	Pressure	bar
R	Specific gas constant	J/(kg·K)
SG	Specific gravity	-
T	Temperature	K
t	Time	S
U	Heat transfer rate	$W/(m^2 \cdot K)$
V	Volume	m^3
V	Flow velocity	m/s
w	Specific humidity	g_{water}/kg_{air}
Y	Mass fraction	-
z	Water-column height	m

Greek characters

ρ	Density	kg/m^3
μ	Dynamic viscosity	Pa·s
η	Efficiency	%
γ	Polytropic process exponent	-
Δ	Increment	-
Π	Pressure ratio	-
υ	Specific volume	m^3/kg

Sub- and Superscripts

2	Compressor outlet
3	Turbine inlet
*	Reduced value
air	Dry air
C	Compressor
cool	Cooler
corr	Corrected value
cyl	Cylinder
EI	Engine Intake
g	Gas
i	Interior boundary
id	Ideal value
in	Inlet section
max	Maximum value
min	Minimum value
norm	Normalized value
o	Exterior boundary
out	Outlet section
SP	Setpoint

ref	Reference value
T	Turbine
w	Water vapour
ws	Saturated water vapour

Acronyms

0D	Zero Dimensional
1D	One Dimensional
2D	Two Dimensional
3D	Three Dimensional
ACT	Apparent Combustion Time
AHU	Air Handling Unit
aTDC	After Top Dead Center
BMEP	Brake Mean Effective Pressure
BSFC	Brake Specific Fuel Consumption
CA	Crank Angle
CAD	Computer-Aided Design
CFD	Computational Fluid Dynamics
CI	Compression-Ignition
CO	Carbon Monoxide
CR	Compression Ratio
DPF	Diesel Particle Filter
DOC	Diesel Oxidation Catalyst
ECU	Engine Control Unit
EGR	Exhaust Gases Recirculation
FGT	Fixed Geometry Turbine
FP	Full Performance
HD	Heavy Duty
HE	Heat Exchanger

HP-EGR	High-Pressure EGR
HSDI	High-Speed Direct Injection
ICE	Internal Combustion Engine
ISO	International Organization for Standardization
LP-EGR	Low-Pressure EGR
LPC	Logic Programable Controller
MD	Medium Duty
MEDAS	Multifunctional Efficient And Dynamic Altitude Simulator
MHM	MEDAS Humidity Module
MTM	MEDAS Temperature Module
NACA	National Advisory Committee For Aeronautics
NEDC	New European Driving Cycle
NOx	Nitrogen Oxides
NTU	Number Of Transfer Units
OEM	Original Equipment Manufacturer
PID	Proportional Integral Derivative
PR	Pressure Ratio
RDE	Real Driving Emissions
RH	Relative Humidity
RoHR	Rate of Heat Release
S-RANS	Steady Reynolds-Averaged Navier-Stokes
SCR	Selective Catalytic Reduction
SI	Spark Ignition
ST	Standard
THC	Total Unburned Hydrocarbons
UNEP	United Nations Environment Programme
UPV	Universitat Politècnica de València
URANS	Unsteady Reynolds-Averaged Navier-Stokes
VEMOD	Virtual Engine Model

VGT	Variable Geometry Turbine
VGTv	Variable Geometry Turbine Valve
WCAC	Water Cooling Air Charge
WG	Waste-Gate
WLTC	Worldwide harmonized Light-duty Test Cycle

Chapter 1
Introduction

1.1. Background

The invention of the reciprocating internal combustion engine (ICE), first by Nicolaus Otto in 1876, developed the first spark ignition (SI) engine, and later in 1892, Rudolf Diesel introduced the compression ignition (CI) engine, revolutionized the transportation of both people and goods. These two engines displaced the previous steam ones becoming the new leading power source for ground and marine transport. This was possible due to the new engines' much higher power density than the former external combustion steam engines.

As the reciprocating ICE allowed more affordable and versatile ground transport, the number of vehicles circulating worldwide increased exponentially, reaching the billions. This caused a significant increase in the air pollution in prominent population nuclei, which forced the governments to introduce limits to the pollutant emissions of these engines. Advance the engines technologies to fulfill the increasingly restricting emissions legislation has been a great challenge for the automotive industry. The original equipment manufacturers (OEMs) have been fighting to accomplish this. In the case of Europe, this started with the first pollutant emissions regulation, the Euro 1, that came into force in 1992 [1].

The pollutant emission standards for automotive engines have been evolving and adopting more restricting limits and considering more aspects related to the pollutant's generations in an ICE. In the case of compression ignition (CI) engines, the Euro 2 [2] was the first great challenge, in which the emissions of carbon monoxide (CO) and unburned hydrocarbons (HC) were regulated, forcing the OEMs to install oxidation catalyzers in the exhaust lines of the engines to control the emissions of CO and HC.

Afterward, with the implementation of the Euro 3 and 4 [3], the restriction on the emissions of nitrogen oxides (NOx) and particulates forced the development of exhaust gases recirculation (EGR) and the inclusion of a diesel particulate filter (DPF) included at the end of the exhaust line. Also, new injection strategies and technologies were introduced, such as the common rail, which improved the engine performance while keeping or even reducing the pollutant emissions due to better control of injection and combustion processes. Lastly, with the Euro 5 and 6 [4], the EGR system was improved, mixing high and low-pressure EGR circuits and cooling the recirculated gases [5]. Also, new components were installed in the exhaust line to help with the NOx control, like the selective catalytic reduction (SCR) or the DeNOx, which traps the excess of NOx [6], [7].

The technology associated with the control and management of the pollutant emissions of the engine, more commonly called aftertreatment, has been increasing in complexity, adapting to the increasingly restrictive regulations, but this was not the end. When the Euro 6d regulation [8] came into force, it

included a new fundamental aspect in the homologation of new automotive engines: the atmospheric conditions in which the homologation tests are carried out, i.e., altitude and ambient temperature.

Thus, the development of laboratory installations that allow the engine manufacturers to study the effect of these two atmospheric conditions on the engine and calibrate it accordingly was a necessity.

1.2. Motivation

The geography of the European continent is varied and encompasses a wide range of climatic conditions, like the extreme cold found in the Nordic countries or the hot temperatures of the Mediterranean ones. Also, the results of a study carried out by the UNEP-World Conservation Monitoring Centre [9] showed that Europe is a mountainous continent, with 20% of its surface above 1000 meters over sea level, and in which its population frequently performs trips on-road at an altitude higher than 1000 meters above sea level.

This study collected the demographic characteristics of the European population according to the geographical level of each region [9], from which these two meaningful conclusions were extracted. In the first place, in Figure 1. 1A can be seen how the altitude distribution of the European surface, in which 20% is higher than 1000 meters above sea level and reaching 2000 meters on some roads in the Alps and Pyrenees.

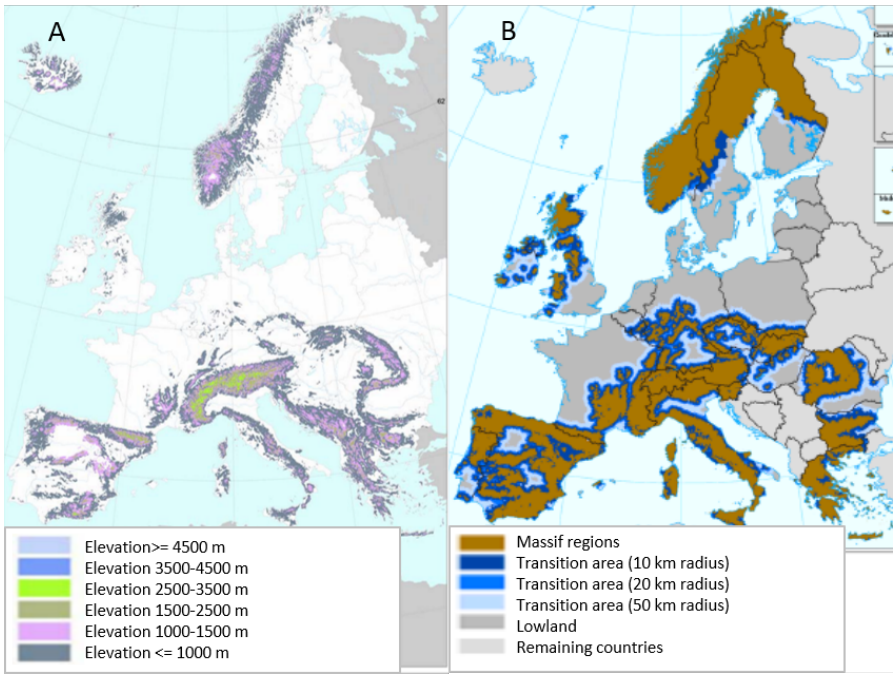

Figure 1. 1. Mountains of Europe: (A) Massif; (B) Massif transition areas, which involve surrounding circulation. Elaborated from reference [9]

Secondly, this report shows that 19.1% of the European population resides above 1000 m altitude. This represents almost 100 million people living in altitude conditions. The authors of reference [9] concluded that (sic) “on average, almost 20% of the total population of the study area live in mountain ranges (excluding enclaves); another 25% live within 10 km of massifs (low altitude areas near mountains); another 5% within 20 km; and a further 10% within 50 km. Thus, about 60% of the overall population in the study area lives in or close to massifs". This suggests that 60% of the population have frequent trips around massif areas, as shown in Figure 1. 1B.

A simple study about the largest population centers at altitudes in Europe is shown in Figure 1. 2. Figure 1. 2 illustrates with a clear trend how the population of the cities decreases as the altitude increases. The exception is Madrid (Spain), which is one of the largest cities in Europe but is located close to 700 m over sea level. This location emphasizes the interest in the impact of traffic in altitude conditions significantly. The data have been divided into sea-level cities, i.e., at an altitude lower than 500 m, and high-altitude cities, i.e., above 500 m. Looking at the shadowed areas, it can be observed that 65% of the studied population is located below 500 m, even considering a smaller sample of cities near sea level (4 towns) than that used for cities in height (13 cities).

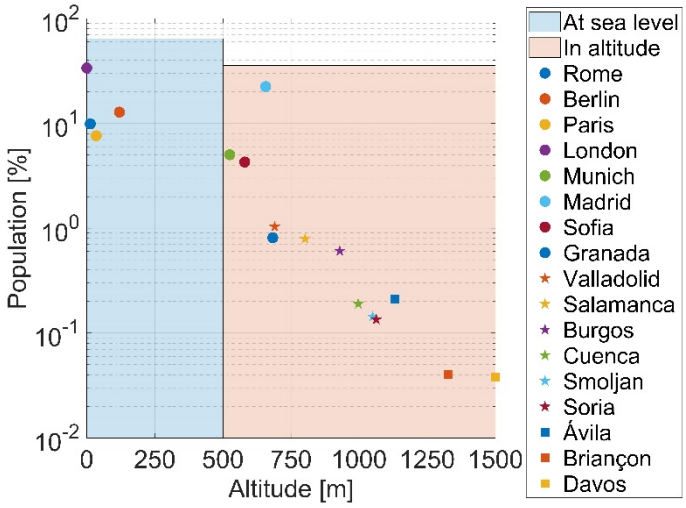

Figure 1. 2. Population distribution in European cities as a function of the altitude

Considering the population distribution presented by these different approaches, it can be concluded that altitude traffic represents a significant portion of the global European traffic. This conclusion supports the need to quantify and analyze the behavior, performance, and pollutant emissions of automotive engines when working at altitude. Therefore, the automotive engine's homologation tests increased the need to include the extended atmospheric conditions (1300 meters above sea level and -7ºC in the case of Euro 6d regulation [8]).

However, different atmospheric conditions during the homologation introduce the need to test the engines at altitudes and low temperatures during the early development phase. To carry out this kind of extensive testing, the laboratories must have installations that allow reproducing of different altitude and temperature conditions at the engine intake and exhaust accurately since the on-road testing is too expensive and not repetitive enough in the early phases of the engine development.

The classic installation used to substitute the on-road tests has been the altimetric and climatic chamber, which tests the engines or vehicles inside a room where the atmospheric conditions are reproduced. However, the altimetric chambers have limitations that reduce the number of tests performed. These limitations consist of the impossibility of carrying out variable altitude tests due to the massive volume of the chamber that must be conditioned or the health risk for vehicle drivers that appear when the room changes the pressure during a vehicle test in a chassis dyno [10]. Therefore, the development of altitude simulators has opened a cheaper and safer but equally accurate way than using

altimetric and climatic chambers to reproduce different ambient conditions in an engine's intake.

Moreover, the introduction of the altitude simulators allowed the reproduction of a complete round robin test in the laboratory, consisting of a dynamic operation of the engine speed and load with a dynamic change of the atmospheric condition on the engine intake and exhaust. This capability is the key to calibrating the engine correctly before starting the phase of on-road testing. Since detecting and fixing any issue in this phase is much more complex and expensive.

This Ph.D. Thesis is based on the previous development of an altitude simulator from the HORIBA company, called MEDAS (Multifunctional Efficient and Dynamic Altitude Simulator), which conditions the pressure and temperature of an engine intake and exhaust to emulate the stress that the engine would withstand when driving a vehicle in altitude conditions.

The MEDAS employs turbomachinery and control valves to accurately condition the engine's fresh air and tailpipe pressure following the scheme shown in Figure 1. 3. The air enters the MEDAS through an air filter (1 of Figure 1. 3) to remove all the particles that could cause damage to the MEDAS components. Then the air can be expanded in two ways: isothermally in a control valve (2) or cooling down in a variable geometry turbine (4) (VGT). Valve (2) controls the pressure of the engine intake and exhaust, while valve (3), located upstream of the VGT (4), controls the temperature at the engine intake. Since the air is cooled down in VGT (4), condensates can appear; therefore, a cyclonic separator (5) is included downstream to remove the water droplets.

Afterward, the engine sucks the necessary fresh air through (6), and the rest mixes with the engine's exhaust gases (8), flowing through the bypass duct (7). Then the mix is cooled down in the exhaust cooler (9) to protect downstream components from the high temperatures of the exhaust gases. Another cyclonic separator (10) is located downstream of the cooler (9) to remove the condensates generated in the cooling of the exhaust gases. Lastly, the cooled-down gas passes through a mechanical compressor (11), which forces the flow out of the MEDAS to the test cell extraction system (12). The compressor (11) controls the amount of mass flow that the MEDAS is conditioning to fit the engine demands of fresh air. Isolated from the primary air circuit, the compressor (13) dissipates the power generated by the turbine cooling to the ambient.

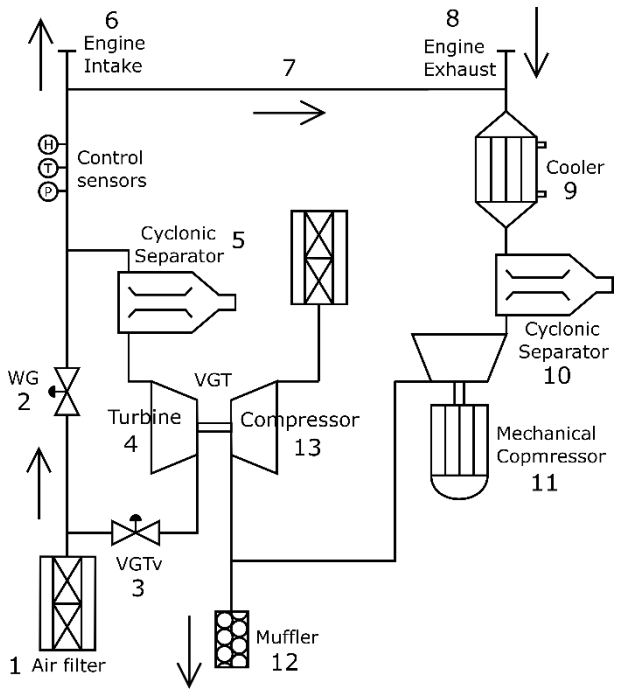

Figure 1. 3. Initial MEDAS layout

However, by improving several hardware and software points in the MEDAS, the performance could increase, and the energy consumption of the installation decrease. One of the points that could be improved is the limited control of the engine intake temperature, which control range could be increased even with its heavy dependence on the simulated altitude. Another is the significant pressure drop of the exhaust line (6 to 11 of Figure 1. 3), which increases up to 100 mbar due to the inefficient pipe sizing, significantly reducing the mass flow performance of the MEDAS. Finally, the energy absorbed by the turbine (4) and transmitted to the compressor (12) is being dissipated to the ambient, when it could be used to reduce the energy consumption of the mechanical compressor (11).

1.3. Objectives

The main objectives of the present Ph.D. Thesis are divided into three areas: the improvement in performance and control stability of the altitude simulator developed at U.P.V. research institute CMT - Motores Térmicos and commercialized by HORIBA, with the name of MEDAS (Multifunctional Efficient and Dynamic Altitude Simulator); the development of an atmosphere simulator able to reproduce dynamic pressure, temperature, and humidity profiles following the actual conditions measured during a road test; and the

study of the effect of the ambient conditions (mainly humidity) on a turbocharged diesel engine.

- The first objective is to improve the control strategies of the MEDAS developed in reference [11] to increase the accuracy of the control in both dynamic operations while performing altitude profiles and in steady-state operations while simulating a plateau.
- The second objective is to improve the hardware of the MEDAS to increase performance while reducing energy consumption. Also, to increase the monitoring of different components and supplies to increase the durability and safe operation of the installation.
- The third objective is to develop a 1D model software of the altitude simulator MEDAS, able to accurately predict the different components' behavior while in steady-state operation.
- The fourth objective is to develop the control strategies for the enhancement of temperature and humidity modules of the altitude simulator, presented in the patent from U.P.V and HORIBA [12], that will allow accurate and stable control of the atmospheric variables: pressure, temperature, and humidity; found on an automotive road in two cases: in steady atmosphere conditions (emulating a plateau) and in dynamic atmosphere conditions (reproducing actual driving ambient conditions).
- The fifth objective is to use the atmosphere simulator developed to carry out an extensive testing campaign on different turbocharged diesel engines to study the effect of the fresh air pressure, temperature, and humidity on engine performance and pollutant emissions. Prove that accurate data can be obtained with the system developed without modifying the engine layout.

1.4. Methodology

The present thesis follows a work methodology to accomplish the proposed objectives split into several tasks, which now will be detailed grouped in chapters.

Chapter 1 is dedicated to defining the problem that this research is trying to solve and the objectives to be fulfilled to carry out the present Ph.D. Thesis.

In Chapter 2, a bibliographic review is presented, encompassing the main knowledge topics that would be the basis of the present research, i.e., different technologies that allow the testing of an engine in different altitudes, previous studies testing ICE while varying the ambient conditions, and an introduction of the software used for the 1D modeling carried out.

In Chapter 3, the improvement of the altitude simulator MEDAS is presented through inductive and deductive procedures. In this chapter, advances in

hardware and software of the altitude simulator are introduced to increase the performance and durability of the installation while reducing energy consumption. Additionally, this chapter proposes the procedure to design new altitude simulators of a different range. Indeed, two new MEDAS models for medium and heavy-duty engines have been developed.

Chapter 4 shows the development of the control strategies for the two additional modules of MEDAS: MTM and MHM (MEDAS Temperature Module and MEDAS Humidity Module, respectively). Both together extend the temperature control range and allow humidity control. These two extension modules convert the altitude simulator into a complete atmosphere simulator since the MTM and MHM allow the independent control of the temperature and humidity at the engine's intake. Thus, the MEDAS, MTM, and MHM assembly can reproduce any pressure, temperature, and moisture found on an automotive road, but with a limitation of -15ºC as the lowest temperature available.

In Chapter 5, the atmosphere simulator developed is used to study the effect of the pressure, temperature, and mainly humidity on the performance and pollutant emission of three different turbocharged diesel engines.

Lastly, in Chapter 6, a set of conclusions obtained through the development of this thesis will be presented.

1.5. Bibliography

[1] European Council, "COUNCIL DIRECTIVE of 26 June 1991 amending Directive 70/220/EEC on the approximation of the laws of the Member States relating to measures to be taken against air pollution by emissions from motor vehicles," no. L 242/1. Official Journal of the European Communities, Jun. 26, 1991.

[2] European Parliament and Council, "DIRECTIVE 94/12/CE FROM EUROPEAN PARLIAMENT AND COUNCIL of 23 March 1994 relating to measures to be taken against air pollution by emissions from motor vehicles and by which the Directive 70/220/CEE is modified," no. L 100/42. Official Journal of European Communities, Mar. 23, 1994.

[3] European Parliament and Council, "DIRECTIVE 98/69/CE FROM EUROPEAN PARLIAMENT AND COUNCIL of 13 October 1998 relating to measures to be taken against air pollution by emissions from motor vehicles and by which the Directive 70/220/CEE is modified," no. L 350/1. Official Journal of the European Union, Oct. 13, 1998.

[4] European Parliament and Council, "REGULATION (CE) No715/2007 OF THE EUROPEAN PARLIAMENT AND OF THE COUNCIL of 20

June 2007 on the type of homologation of motor vehicles regarding emissions from passenger cars and light commercial vehicles (Euro 5 and Euro 6) and on access to information related to the repair and maintenance of vehicles," no. L 171/1. Official Journal of the European Union, Jun. 29, 2007.

[5] S. Reifarth, "EGR-Systems for Diesel Engines," Licentiate Thesis, Royal Institute of Technology, Stockholm, 2010.

[6] R. van Helen, R. Verbeek, F. Willenms, and R. van der Welle, "Optimization of Urea SCR DeNOx Systems for HD Diesel Engines," *SAE Technical Paper*, 2004-01-0154.

[7] M. F. Hsieh and J. Wang, "Development and experimental studies of a control-oriented SCR model for a two-catalyst urea-SCR system," *Control Engineering Practice*, vol. 19, no. 4, pp. 409–422, Feb. 2011, doi: 10.1016/j.conengprac.2011.01.004.

[8] European Commission Regulation, "COMMISSION REGULATION (EU) 2017/1347 of 13 July 2017 correcting Directive 2007/46/EC of the European Parliament and of the Council on type-approval of motor vehicles with respect to emissions from light passenger and commercial vehicles (Euro 5 and Euro 6) and on access to vehicle repair and maintenance information, amending Directive 2007/46/EC of the European Parliament and of the Council," no. L 192/1. Official Journal of the European Union, Jul. 13, 2017.

[9] "The delineation of European mountain areas," 2000. Accessed: Apr. 01, 2019. [Online]. Available: https://ec.europa.eu/regional_policy/sources/docgener/studies/pdf/montagne/ mount4.pdf

[10] W. D. Toff *et al.*, "Effect of Hypobaric Hypoxia, Simulating Conditions During Long-Haul Air Travel, on Coagulation, Fibrinolysis, Platelet Function, and Endothelial Activation," *Journal of the American Medical Association*, vol. 295, no. 19, pp. 2251–2261, 2006, doi: 10.1001/jama.295.19.2251.

[11] J. Gómez, "Development of an altitude simulator and analysis of the performance and emissions of turbocharged Diesel engines at different altitudes," Ph.D. Thesis, Universitat Politècnica de València, Spain, 2018. doi: 10.4995/Thesis/10251/101284.

[12] J. M. Desantes *et al.*, "Device, method and use for conditioning intake air for testing internal combustion engines," Patent WO 2019/114935 A1, 2019

Chapter 2
Literature Review

2.1. Atmosphere simulation

The control of the atmospheric conditions: pressure, temperature, and humidity, that an ICE must face while in operation is an essential aspect of the development of this component. Such control is included in the great majority of the land transport, of either people or goods. These boundary conditions, in which the engine must operate, significantly affect the engine performance and pollutant emissions, making it mandatory to consider them during the development phase to fulfill the homologation requirements defined by the governments.

2.1.1. Testing facilities

There are several means to control the atmospheric conditions. It can be achieved by relocating the testing resources to a location where the desired atmospheric conditions occur naturally, like the on-road tests or the portable rolling benches. Also, an entire room in which the engine or vehicle is installed can be conditioned to the required pressure, temperature, and humidity, like with the altimetric and climatic chambers. Lastly, the flow inside the engine piping can be conditioned to the atmospheric conditions demanded, as happens with the air handling units (AHU) or the altitude simulators.

2.1.1.1 On-road tests

Starting with the on-road tests, these are used during the late phase of the engine development to check the calibrations and strategies. For example, the pollutant emissions and the supercharging management are carried out typically through the EGR valves and the turbocharger with a variable geometry turbine (VGT) or a waste-gate, respectively. However, these kinds of testing are too expensive since they involve relocating all the needed equipment and personnel to carry out the work for an extended time.

During on-road tests, the atmospheric conditions are subject to the weather [1], which provides low repeatability to the tests. Therefore, when considering all the disadvantages mentioned, the on-road tests have been typically used during the final phases of the development as a last measure of the engine performance and validation or slight fine-tune of the control strategies, instead of during the development cycle of an ICE.

2.1.1.2 Portable rolling benches

The portable rolling benches are a solution between a test bench and an on-road test. With this option, it is possible to mount a vehicle test cell inside a truck like the one used by Wang et al. [2], which will drive to the location where the desired atmospheric conditions can be found and then test the vehicle that is being developed.

However, this test is much more expensive since more equipment should be transported to the measurement area. Additionally, the low repeatability of the atmospheric conditions and their dependence on the weather is maintained.

2.1.1.3 Altimetric and climatic chambers

Due to the significant disadvantages of the on-road tests and the portable rolling benches, altimetric and climatic chambers [3] have been the comprehensive solution for calibrating ICEs at different atmospheric conditions. These facilities control the pressure, temperature, and humidity independently inside the test cell, reproducing the same conditions that an engine or vehicle would withstand when driving on roads. However, climatic and altimetric chambers involve several new drawbacks that must be considered even while having less impact in an ICE development project than the previous solutions.

In the first place, the test cell operators, being technicians that must do maintenance on the installation or the drivers in the vehicle test cells, are subjected to the atmospheric conditions reproduced inside the chamber, which can put at risk their health. For example, the human body cannot withstand repeated and fast pressure changes [4]–[8], leading to hypoxia or problems with blood coagulation between other afflictions, limiting the testing hours in these kinds of installations.

Additionally, these installations are expensive and involve colossal investment and extensive infrastructure and construction planning, making this type of chamber very exceptional in the engine development centers [9]. For example, Mahle Powertrain recently built an altimetric chamber with an overall investment of £8m in the Northampton site [10].

Lastly, it is only possible to reproduce stable atmospheric conditions with the altimetric and climatic chambers. It is impossible to replicate the conditions during an on-road test since the control of the atmospheric conditions involves the conditioning of the whole test cell. This means that the control has huge inertias due to the large volume of air to be conditioned and makes it impossible to reproduce the evolution of neither the pressure, temperature, or humidity withstood during road tests.

2.1.1.4 Atmosphere simulators

Finally, a more recently developed option to solve the problem of controlling the atmospheric conditions that an ICE must withstand while in operation involves the conditioning of the pressure, temperature, and humidity only inside the engine piping while keeping the rest of the test cell at room conditions. This equipment is known as an atmosphere simulator, commonly consisting of an altitude simulator [11]–[14] in charge of controlling the pressure, an air handling unit (AHU) [15], [16] for conditioning the temperature, and a vapor generator to control the humidity.

There are different solutions for this kind of installation, as shown by the various suppliers present in the market. However, most of them share the same advantages as the other solutions for controlling atmospheric conditions. In the first place, they require a much cheaper investment than the altimetric and climatic chambers since they do not require any infrastructure or civil work built especially for their use, and the size of the installation is much smaller. Also, their use demands are cheaper than the other options since they do not involve any personnel or equipment relocation. Furthermore, the power supply needed is significantly reduced due to the need to condition less air volume for a given test.

Moreover, when controlling the atmosphere that the engine or vehicle is facing with them, the health risk for the test cell operator and the time limit for its use are removed since the test cell is kept at the same pressure conditions (the air conditioning is carried out only inside the engine piping). Lastly, the small air volume conditioned is the great advantage of this method since the installation is only conditioning the air that the engine is consuming. It allows the reproduction of a variable atmosphere, which can be found while climbing up/down a mountain (pressure and temperature change), or when it starts/stops raining (temperature and humidity change). For example, the maximum pressure and temperature variation in a high-speed high-step road is 0.25 mbar/s and 0.014 ºC/s. This allows reproducing on-road tests inside the test cells along the entire engine development cycle, which improves the quality of the early engine development phases and considerably reduces the cost of the whole project.

This partial conditioning of the ambient has one clear disadvantage: the need to reinforce the soft parts of the engine, such as compressor inlet and outlet connections, to avoid collapse due to the differential pressure that the soft pipe must withstand. Additionally, the air intake through the crankshaft sealings increases when some engines are tested with an altitude simulator due to the geometry of the sealings and the higher differences between the ambient and the sump pressure. Therefore, in some cases (depending on the engine), it is necessary to increase the blow-by section to avoid pressurizing the sump and consuming extra oil. Nevertheless, this testing method's advantages over the other options make it a worthy choice for the early development of the engine.

One example of the atmosphere simulators present in the market could be the one presented by Testa et al. [13], an altitude simulator that changes the pressure through two root compressors, one located upstream of the engine connected to the air filter and another downstream connected to the exhaust pipe, to reproduce altitude conditions. To generate a vacuum, the upstream volumetric compressor throttles the installation acting as a valve, while the downstream compressor oversees moving the flow. On the other hand, they exchange their functions to generate overpressure, the downstream compressor controls the backpressure to

the engine, and the upstream one controls the mass flow. Additionally, an AHU and a vapor generator are connected upstream to the altitude simulator coupled to the engine intake to control temperature and humidity.

Each atmosphere simulator available on the market presents different solutions for the problem of controlling the atmospheric variables at the engine intake and exhaust. A prototype of the atmosphere simulator consisting of the MEDAS, MTM, and MHM [17] and commercialized by HORIBA was already built when the Ph.D. started. However, only the MEDAS initial design has been studied and improved, as shown in reference [18]. Also, only the standalone MEDAS has been used to study the effect of the atmospheric conditions on an automotive turbocharged diesel engine. Therefore, during the current Ph.D. Thesis will focus on improving and developing the atmosphere simulator and its use to study how the ambient conditions affect a Diesel engine's performance and emissions.

It should be noted that the altitude simulator MEDAS has already been used to analyze the performance and emissions of a diesel engine in dynamic operation while performing a new European driving cycle (NEDC) at different altitudes, which conclusions have been reported at [19].

2.1.2. MEDAS validation

As mentioned previously, the first generation of MEDAS was already developed when the current Ph.D. Thesis started, and several studies concerning the altitude effect on a Diesel engine were carried out with it [18]–[22]. Furthermore, to validate the use of the MEDAS to obtain accurate results of an engine operating in altitude conditions, a back-to-back comparison against an altimetric chamber was carried out [23]. A summary of the results of the MEDAS validation is presented below.

The experiment designed to validate the MEDAS system is shown in Figure 2. 1 and consists of a turbocharged diesel engine coupled to a Foucault current brake, both located inside a hypobaric and climatic chamber while the MEDAS was placed outside. Several steady-state engine points were tested at two different altitudes and using two different systems to achieve the altitude conditions in total 16 engine points for each combination of altitudes (1300 m or 2300 m) and altitude emulation equipment (hypobaric chamber or MEDAS).

When the engine is connected to the MEDAS, the hypobaric chamber stops, and the MEDAS generates the vacuum for the engine (valves 1 and 2 open, and 3 and 4 closed). That means the environment around the engine is at sea level conditions, while the intake and exhaust line are at the desired vacuum. In this case, the Engine Control Unit (ECU) pressure sensor had to be either connected to a vacuum or modified its value at ECU to activate the altitude calibration due to being at room pressure when simulating altitude with MEDAS. The same tests were done with the engine disconnected from MEDAS and simulating the

altitude within the hypobaric chamber (valves 1 and 2 closed and 3 and 4 open). In this second case, the internal and external sides of the engine are withstanding the vacuum.

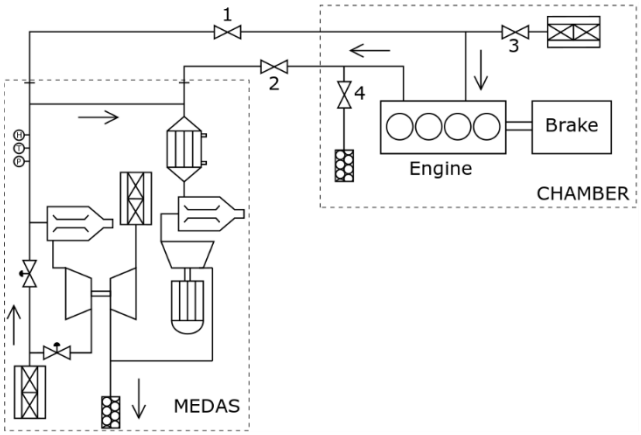

Figure 2. 1. Test cell layout for the comparison between MEDAS and altimetric chamber

In Figure 2. 2, obtained from reference [23], at 1300 meters over sea level, the results for the compressor operating point are equal between altitude simulation systems; but when going to 2300 meters and at high speed and load, slight differences in the measurements with both methods are shown. Therefore, before further analysis, a dispersion study was done using some engine operating points, in which each point was measured five times with every altitude simulation equipment.

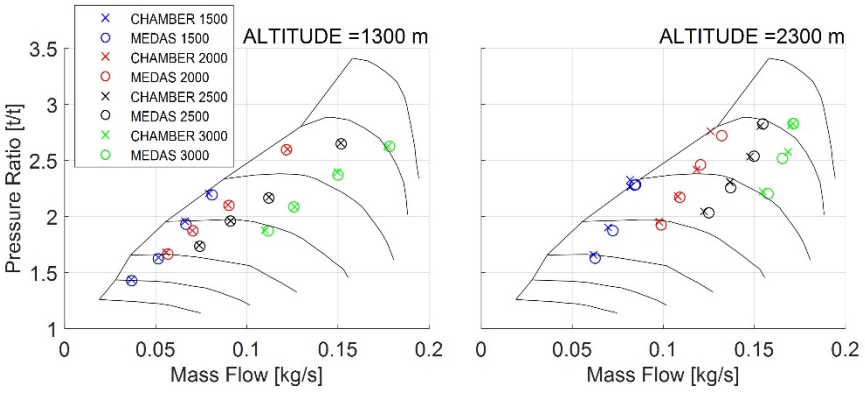

Figure 2. 2. Engine operative points at turbo compressor map and different altitudes. Referenced from [23]

Some of the results obtained after comparing engine variables between both altitude simulation technologies are shown in Figure 2. 3. The differences between both are not significant: being within the measured dispersion with each

altitude emulation device [23]. Also, the dispersion for some variables is higher with the MEDAS and for others with the hypobaric chamber. It should be noted that the effect of the altitude and the engine speed on the measurement dispersion is more apparent in pressure and temperature than in emissions due to the high inherent dispersion of the emission measurement systems that sometimes even damps the effect of instabilities in the test bench.

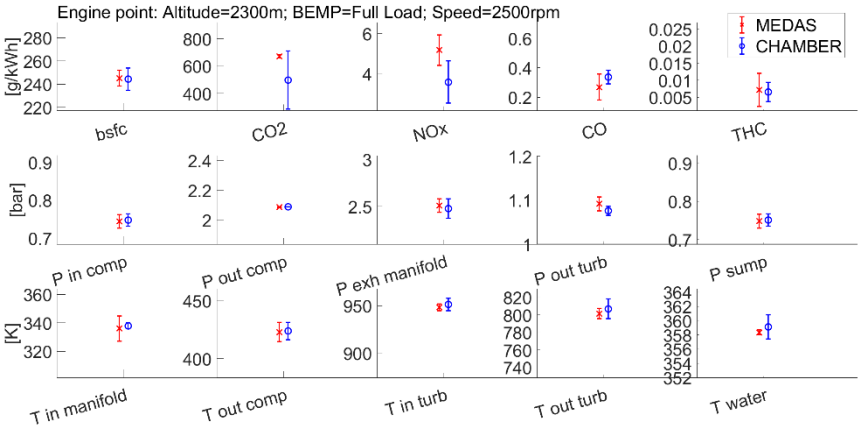

Figure 2. 3. Engine variables measurement dispersion at 2300 m, 2500 rpm, and full load. Referenced from [23]

The conclusion obtained after the analysis of the dispersion study was that the differences found in the engine's behavior for the three chosen points are caused mainly by instabilities in the engine's performance and dispersion in the measurement devices used in the engine bench. Therefore, there is no significant modification in the engine behavior at these control points when utilizing a MEDAS for conditioning intake and exhaust pressure than when operating the engine in the complete conditioned environment produced by a hypobaric chamber.

The similar behavior of some key engine variables is shown with the data arranged in a matrix of torque vs. speed graphs, differentiating by altitude and emulation technology for each engine operating point tested.

The case of the turbine inlet pressure is shown in Figure 2. 4 [23], where it can be seen how the islands of low pressure, which appear when testing with the hypobaric chamber, are reproduced when testing with the MEDAS. Moreover, the maximum and minimum values for both pressure and temperature at the turbine inlet are the same and in the same area of the engine map with any simulating equipment used.

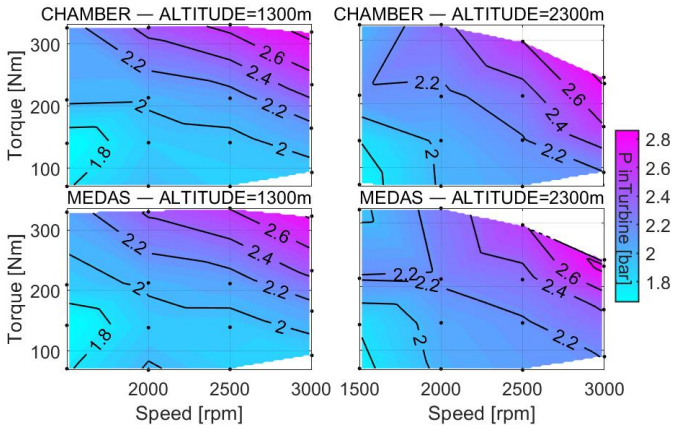

Figure 2. 4. Turbine inlet pressure. Referenced from [23]

Following with another crucial variable, the engine map of brake specific fuel consumption (BSFC) also has a very similar topography when testing with the MEDAS or with the hypobaric chamber, being the differences between both, mainly due to test bench instabilities in the measurement, as concluded in the previous section.

Concerning the pollutant emissions: NOx and THC shows how the topography of the engine map obtained when testing in a complete altitude environment inside the hypobaric chamber is, once again, well-reproduced when just connecting intake and exhaust to the MEDAS, with the high and low emission areas located in the same places in both cases.

In conclusion, no significant difference has been measured between testing the engine in a complete altitude environment and testing it connected to MEDAS, nor in engine performance or emissions, validating its use to obtain accurate results about the engine behavior in altitude.

2.1.3. Airstream moisturizing technologies

There are several options to increase the moisture of an airstream currently available in the market. Ranging from water atomizers, vapor generators, or bubbling water columns through which the airstream passes.

Atomizing water allows the amount of water injected into the air to be controlled accurately. Still, it needs piping length to let enough time for the water droplets to break up and dissolve into the airstream [24].

Following the vapor generators, the amount of water injected can be controlled accurately utilizing the amount injected in the air stream [25]. Currently is one of the most used solutions to control the humidity of the combustion air for an ICE and is used by manufacturers of engine testing equipment, such as AVL in

its product ConsysAir. However, the maximum amount of vapor generated is limited due to the high electrical power requirements of the vapor generation. In addition, they don't withstand overpressure or vacuum, so they must be used in room pressure conditions. The room-pressure condition limits the specific humidity absorbed by the air stream before condensation. This limits the possibility of generating high relative humidity values at altitude, as it happens in several places on Earth, which cannot be simulated with this technique. This limitation will be discussed along with the thesis manuscript, and an innovative solution will be proposed and tested in this thesis.

Lastly, the bubbling water column moistens the air up to 100% RH. Therefore, the humidity control must be carried out by external valves, which let the airstream pass through the water to achieve the desired humidity. This solution allows a vast range of combustion air humidity control without boiling water or extra piping. Since it can work at pressure and heat the air to the same temperature as the water, however, the footprint and height of this equipment must be fitted to the maximum amount of air that must pass through it, to control the maximum air velocity [26] and avoid an excessive increase in the water level that could lead to overflowing.

The water and vapor injection solutions are widespread and available in the current market of equipment designed for engine testing, with well-known advantages and disadvantages for each answer. However, the existing technologies for the bubbling water column are focused on large-scale installations, such as industrial chemistry plants, with a high working mass flow rate of over 1 kg/s [24], [27], or small facilities such as dedicated laboratories with mass flow rates below 0.01 kg/s [28]. These water-column solutions are quite like fluidized bed technologies, widely used in the chemical industry, with the procedure of design focused on the interaction between the particles and the fluid [29]. Instead, the application of a bubbling water column should be focused on the increase in the height of the emulsion, which is the main factor that leads to the reactor overflowing, which is not studied in detail [30].

2.2. Effect of the atmospheric conditions on diesel engine

2.2.1. Altitude

The main effect that the change in altitude has considering the boundary conditions of the engine is that the air density of the combustion air decreases when increasing the altitude [31]. This has a significant impact on the engine performance and pollutant emissions due to the appearance of some phenomena that lead to changes in the combustion process and the engine behavior.

One of the phenomena that appear when increasing the altitude is the generation of smaller fuel drop sizes for the injected fuel [32]. This lowers the coalescence of the spray [33], as the fuel evaporates and mixes with the air better inside the

combustion chamber. However, the lower air density inside the combustion chamber decreases the spray angle, thus increasing the fuel spray penetration [34].

Additionally, the backpressure generated by the variable geometry turbine increases to keep the boosting since there is a higher need for compression rate to achieve the boosting than at sea level. The increase in back pressure can lead to backflows in the exhaust valves, increasing the internal EGR (exhaust gases recirculation) rate as well as the pumping losses of the engine, which reduces the performance and increases the pollutant emissions [35].

2.2.1.1 Performance

The effect of the altitude on the engine performance can be observed through critical parameters in a turbocharged diesel engine, such as the EGR strategy, the pressure and temperature of the turbine inlet, or the brake-specific fuel consumption (BSFC).

One commonly used strategy when the engine operates in altitude conditions is to close the EGR gradually with the altitude until it is fully close. In references [19], [36] is shown how the low-pressure EGR closes partially when the altitude is increased up to around 1000 meters above sea level but is fully closed when increasing the altitude above 2000 meters. This has been reduced due to the NOx emissions limit while in altitude operation imposed by the newer regulations [32]. However, reducing the LP-EGR rate still protects critical engine components like the turbocharger.

Moreover, when operating in altitude conditions, a turbocharged diesel engine suffers a reduction in the maximum torque that can provide [22], which is intentionally caused by the ECU to protect some components of the engine, avoiding overcoming operative limits like the turbo compressor maximum speed, the surge limit, or the turbine gas inlet temperature.

The reduction or even removal of the EGR and the increase of the fuel-to-air ratio due to a decrease in combustion air mass flow [37]–[39] makes it easier to reach the limits mentioned above of the turbocharger. It is the leading cause of the performance reduction of a turbocharged diesel engine in altitude.

The turbine inlet pressure (p3) decreases with the altitude when the open-loop control of the VGT is active [40]. However, when an acceleration happens and the closed-loop is active, p_3 increases to reach the compression ratio target in the intake [19].

In the case of the turbine inlet temperature (T_3), the reduction of EGR and the increase in the fuel-to-air ratio that happens when increasing the altitude causes a progressive rise in T_3 [40], [41], which makes it easier to reach the turbine temperature limit and is one of the reasons for limiting the engine maximum torque in altitude.

Another crucial variable is the BSFC, which is significantly affected when increasing the altitude. There is an increase in the BSFC in the low load areas of the engine, while in the high load areas, the difference when increasing the altitude is insignificant [22], [42]. This happens due to the inlet manifold pressure's significant dependence on combustion air mass flow at low load [39]. This decreases the air in the cylinder when increasing the altitude and forces to increase the fuel injected to keep the brake mean effective pressure (BMEP). Contrarily, at high load, the increase of altitude has a more negligible effect on the BSFC since the amount of combustion air and fuel-injected increases and dampens the impact of reducing inlet manifold pressure.

2.2.1.2 Pollutant Emissions

The pollutant emissions of a diesel engine are also heavily affected by the altitude since the decrease in the air density inside the combustion chamber, and the closing of the EGR valve causes an increase in the fuel-to-air ratio and a reduction of inert gases that modify the combustion conditions and thus the generation of pollutants.

In the first place, the NOx emissions suffer an increase in production when increasing the altitude due to the mainstream strategy of closing the EGR when a diesel engine operates at altitude to protect the turbocharger [19]. This has a serious effect at low loads. The generation of NOx is greatly increased when increasing altitude due to the action of EGR, which is partially open at altitudes around 1000 meters but ends up completely closed when increasing the altitude further. Contrarily, the difference decreases with the altitude at high loads since the EGR is fully closed in all the cases. [35], [43]–[45].

Also, reference [36] shows that when increasing the altitude, the NOx produced by the engine increases at low altitude (below 2400 meters above sea level) [43], while at higher altitudes, it decreases. This is caused by the EGR closing that happens when increasing the altitude until it is entirely closed, which compensates for the effect of the decrease in air density and causes an increase in NOx emission. Afterward, the lack of O_2 available during the combustion caused by the altitude reduces the NOx emission despite the higher combustion temperature [38].

But nowadays, RDE legislation, pollutant emission control is mandatory even at altitude conditions [32]. Therefore, the air management systems calibration, such as the turbocharger and the EGR valves, must be revised, and no clear rules are defined yet. The necessity of pollutant emissions management in altitude operation forces a redesign of these systems calibration to achieve the increasingly restricting limits imposed by the governments.

Following this trend, Bermudez et al. [46] have found that in altitude conditions, a lower boosting pressure allows the control of the NOx emissions using low-pressure EGR (LP-EGR). The lower boosting requirements cause a reduction in

the pumping losses and reduce the risk of reaching turbocharger limits, allowing the use of LP-EGR even in altitude conditions. This happens without significantly influencing the rest of the pollutant emissions or the fuel consumption due to the increase of the after-treatment system efficiency in these operative conditions. Therefore, in altitude conditions, an engine air management strategy focused on reducing pollutant emissions instead of the power output (closing EGR and trying to keep the boosting pressure) makes it possible to achieve the emissions limits defined by the legislation.

Concerning the THC, the reduced density of the air inside the combustion chamber increases the fuel jet penetration and the jet-to-wall-impingement [47], which ends up in a higher amount of unburned fuel that goes out of the cylinder [19], [21]. This happens despite the higher combustion temperature caused by the EGR closing. Also, the increase in THC is amplified during engine accelerations in which exhaust gas back-flows are generated at the exhaust valves due to the backpressure increase caused by the aggressive closing of the VGT to keep the boost pressure [2], [48].

The CO follows a similar trend as the THC, increasing the emission with the altitude [36]. The decrease in air density in the combustion chamber reduces the fuel spray angle, reducing the air diffusion in the fuel jet, worsening the combustion [49], [50]. This added to the increased jet-to-wall impingement [47] and the increase of the fuel-to-air ratio to keep the power provided by the engine [39], [42], causing an increase in the CO when increasing the altitude at which the engine is operating.

Similarly, the soot emissions are increased with altitude [39]. The increase in the fuel-to-air ratio, the reduction of air diffusion on the fuel jet, and the jet-to-wall impingement inside the combustion chamber [47], [49], [50] increase the amount of incomplete combustion, which is the main reason for the increase of the exhaust soot emissions [39], [42].

2.2.2. Temperature

The ambient temperature has a significant effect on the engine’s performance, mainly affecting the combustion process's temperature and the engine's heat transfer, which reduces the engine efficiency and increases pollutant emissions.

2.2.2.1 Engine performance

The higher density of the combustion air due to the lower ambient temperature leads to an improvement of the engine’s volumetric efficiency, which measures the effectiveness of the air intake system [51]. However, when the ambient temperature lowers, the heat transfer during the combustion and to the ambient in the exhaust manifold increases, which decreases the engine's efficiency [52] due to lower temperatures during the combustion phase and at the turbine inlet.

Additionally, the low ambient temperature is also a conditioning parameter for the use of EGR. The low combustion air temperature added to the lower O_2 available due to the EGR lead to instabilities in the combustion process during the engine warm-up, significantly increasing the emissions of pollutants like CO, THC, and soot; and even causing misfiring in some cylinders [53]–[55]. The disabling of the EGR is a common strategy used by OEMs to avoid instabilities in the combustion [52] due to the low ambient temperatures, only activating it when the engine coolant water reaches a predefined temperature threshold [55]. Additionally, it should be noted that, as shown in reference [52], even when the engine counts with the two EGR systems: low-pressure EGR (LP-EGR) and high-pressure EGR (HP-EGR), in cold conditions, only the HP-EGR is activated to control the NOx.

However, like with the altitude, the extended ambient conditions included in the RDE tests force using the EGR system in cold conditions to achieve the pollutant emissions limits. This makes the study of the effect of the ambient temperature a must for the OEMs, which translates into having facilities and equipment to do it with high accuracy and low cost, to fulfill the current pollutant emission limits.

2.2.2.2 Engine out pollutant emissions

Some engine-out pollutant emissions are increased due to the decrease in combustion temperature, which leads to incomplete combustions.

The NOx emissions in cold conditions (below 0ºC) are increased due to the closing of the EGR to avoid combustion instabilities [56], which causes an increase in the maximum combustion temperature since the close of the EGR has a heavier impact than the ambient temperature on this parameter. Moreover, as the effect of the HP-EGR is lower than the LP-EGR in the NOx control [57]–[60], even when the EGR is activated in cold ambient temperature conditions, the production of NOx is higher than in hot conditions.

Following this, Bermudez et al. [46] found that in a Euro 6d-Temp diesel engine, it is possible to control the NOx emissions employing LP-EGR if the boost pressure is lowered instead of keeping it as high as possible to increase the power output of the engine. This has been achieved with the ambient temperature below 0ºC and without a significant increase in the rest of pollutant emissions or fuel consumption. Therefore, nowadays, it is possible to calibrate the air management systems of the engine focused on pollutant emissions reduction even in cold ambient conditions to achieve the pollutant emissions limits required by the legislation.

In the case of the THC, during the cold start of the engine, the THC engine-out emissions are increased dramatically due to the low temperature, which leads to incomplete combustions [61] and a higher quantity of unburned fuel attached to the cylinder walls [62].

It should be noted that the engine-out NOx and THC behave contrarily during the engine's warm-up. On the one hand, the engine-out NOx emissions increase during engine warm-ups since the combustion temperature and the engine coolant temperature increase with time [63]. On the other hand, the engine-out THC emissions decrease since the problems associated with low-temperature combustion, like incomplete combustions and excessive wall impingement, are reduced during the warm-up.

Lastly, the CO emissions show a decrease for the hot ambient case due to the lower rate of EGR [55], [60]. The CO and THC emissions share similar trends following the combustion quality. However, the different trends found in reference [52] suggest that the CO is more sensitive to the O_2 concentration, while the THC is more affected by the combustion temperature.

2.2.3. Humidity

In the case of ambient humidity, its effect on the combustion process or over a thermal engine has not been studied in much detail. The studies carried out focus on the injection of water in the intake manifold or creating an emulsion of water with the fuel injected, which shows the significant impact that the increase of water content has on the combustion efficiency and thus on the performance of the engine. This has been demonstrated with different kinds of thermal engines, such as gas turbines [64], diesel internal combustion engines [65]–[71], and petrol engines [66], [72]–[74]; obtaining the same result trend about the effect of the combustion air humidity on the performance and pollutant emissions of a thermal engine.

2.2.3.1 Engine performance

Focusing on the results shown for the diesel engine study, the ambient temperature has been emulated through the injection of atomized water in the engine's intake manifold. The effect of water content in the combustion air impacts the combustion process, which delays the start of the combustion and reduces the maximum heat released during the main combustion phase. This ends up in the reduction of the engine efficiency [65], which forces an increase in the amount of fuel injected to maintain the power output of the engine [68].

Additionally, the increase in water content reduces the density of the combustion air, which reduces the mass flow for a given engine operating point. Additionally, the addition of water to the dry air causes a reduction of O_2 due to substituting it with water. This leads to a remarkable decrease in the available O_2 for the combustion process, further increasing the fuel-to-air ratio, significantly affecting pollutant emissions.

2.2.3.2 Pollutant emissions

Concerning the pollutant emissions, the combustion air humidity affects mainly NOx generation, which is significantly reduced due to the lower amount of available O_2 during the main phase of the combustion, despite the higher combustion maximum temperature [65]. This provides a new way to control the NOx emissions in a diesel engine, with the same potential of NOx control as more common strategies like the EGR.

Furthermore, reference [70] shows how the soot emissions when controlling the NOx with water are much lower than those with EGR, obtaining a better NOx-soot trade-off with the water injection strategy [69]. The cause for the improvement in this trade-off is presented as the delay of the main combustion and the increase in the fuel-injected when using the water injection than the EGR, which leaves a higher amount of unburned fuel for the post-injection combustion phase that helps to oxidize the soot generated during the main combustion.

In the case of CO, the increase of the fuel-to-air ratio due to the efficiency reduction leads to a richer combustion process with lower mixing of O_2 in the fuel jet [71], which causes an increase in this pollutant emission with the combustion air humidity.

Lastly, the THC emissions are also increased. The combustion delay and extra fuel injected to increase the amount of unburned fuel present during the post-injection phase, leaving the cylinder before being completely burned.

2.3. 1D modeling

The tool VEMOD (Virtual Engine Model) developed by the Institute CMT-Motores Térmicos of the Universitat Politècnica de València has been used for the 1D modeling that will be presented in the current Ph.D. Thesis. This tool, based on wave-action models that carry out the thermo-and-fluid dynamics calculations of the gas, provides the capabilities of modeling all aspects of an internal combustion engine employing 1D and 0D elements [75].

Additionally, different sub-models are included to consider the various phenomena inside the engine, such as the combustion process calculated using the Apparent Combustion Time (ACT) 1D model, which predicts the rate of heat release the NOx formation. Also, experimental correlations are included to indicate the rest of the main pollutants (CO, THC, and Soot), which, coupled with the after-treatment (Oxidation catalyst and particulate filter) sub-models, allow for calculating the tailpipe pollutant emissions of the engine.

Lastly, the sub-models developed for the turbocharger [76], [77] and the ECU [78], [79] provide the capability of considering the turbocharger performance and the vehicle and driver gear change and throttling characteristics to obtain a complete engine simulation.

Several studies involving the different aspects of this modeling tool have been carried out to validate its use and obtain valuable conclusions concerning the behavior of the various technologies installed in an internal combustion engine. One of them was focused on the increase in efficiency of the after-treatment [80], which compares the effect of different opening and closing timing for the intake and exhaust valves in terms of exhaust temperature, fuel consumption, a warm-up of the after-treatment, and light-off time of the oxidation catalyst, and the final effect of these parameters on the global pollutant emissions of the engine.

During this piece of research, Serrano et al. [80] found that with the proper valve timing, the increase in exhaust temperature decreases the CO and THC emissions since the warm-up process of the oxidation catalyst is reduced. However, it also implies an increase in fuel consumption that could be as high as 20% during the low-speed phases of the worldwide harmonized light-duty test cycle (WLTC), which forces a trade-off between both parameters.

Another kind of study carried out with VEMOD is the effect of insulating the exhaust line (exhaust ports, manifold, and turbine housing and volute) on the engine and after-treatment warm-up and the exhaust temperature during transients [81], which provided exciting results depicting that the efficiency of the diesel oxidation catalyst (DOC) increases when the exhaust elements are insulated, reducing the number of pollutant emissions to the ambient up to a 40% in the case of CO and THC emissions. The warm-up time for the DOC is significantly reduced in this case. However, this increases the time needed for the engine warm-up since a more significant part of the thermal energy is going out of the engine with the exhaust gases instead of the coolant circuit.

2.4. Bibliography

[1] V. Betageri and R. Mahesh, “Effects of the Real Driving Conditions on the NOx Emission of a Medium Duty Diesel Commercial Vehicle,” in *SAE Technical Papers*, Jan. 2017, 2017-26-0124. doi: 10.4271/2017-26-0124.

[2] X. Wang, Y. Ge, L. Yu, and X. Feng, “Effects of altitude on the thermal efficiency of a heavy-duty diesel engine,” *Energy*, vol. 59, pp. 543–548, Sep. 2013, doi: 10.1016/j.energy.2013.06.050.

[3] J. H. Roberts, W. R. Beyerly, M. W. Mason, J. R. Glazier, and R. H. Wiley, “PW4084 engine testing in altitude & sea level test facilities,” *SAE Technical Papers*, 1994, 942140. doi: 10.4271/942140.

[4] W. D. Toff *et al.*, “Effect of Hypobaric Hypoxia, Simulating Conditions During Long-Haul Air Travel, on Coagulation, Fibrinolysis, Platelet Function, and Endothelial Activation,” *Journal of the American Medical*

Association, vol. 295, no. 19, pp. 2251–2261, 2006, doi: 10.1001/jama.295.19.2251.

[5] C. J. Bartholomew *et al.*, "The effect of moderate levels of simulated altitude on sustained cognitive performance," *International Journal of Aviation Psychology*, vol. 9, no. 4, pp. 351–359, 1999, doi: 10.1207/s15327108ijap0904_3.

[6] G. Osculati *et al.*, "Effects of hypobaric hypoxia exposure at high altitude on left ventricular twist in healthy subjects: Data from HIGHCARE study on Mount Everest," *European Heart Journal Cardiovascular Imaging*, vol. 17, no. 6, pp. 635–643, Jun. 2016, doi: 10.1093/ehjci/jev166.

[7] J. J. Cottrell, "Altitude exposures during aircraft flight. Flying higher," *Chest*, vol. 93, no. 1, pp. 81–84, 1988, doi: 10.1378/chest.93.1.81.

[8] B. Bendz, M. Rostrup, K. Sevre, T. 0 Andersen, and P. M. Sandset, "Association between acutehypobaric hypoxia and activation ofcoagulation in human beings," *The Lancet*, vol. 356, 2000, doi: 10.1016/S0140-6736(00)03165-2.

[9] D. G. Gardner, V. A. Zaccardi, P. A. Jalbert, and M. D. Bryant, "Reducing the Cost of Aircraft Engine Emission Measurements," *Proc. Int. Instrum. Symp.*, vol. 49, pp. 57–66, 2003.

[10] Mahle Powertrain, "MAHLE Powertrain takes delivery of altitude and climatic equipment for new RDE test facility," *Mahle Powertrain press release*. 2017. Accessed: Mar. 21, 2022. [Online]. Available: https://www.mahle-powertrain.com/en/news-and-press/press-releases/-mahle-powertrain-takes-delivery-of-altitude-and-climatic-equipment-for-new-rde-test-facility-58305

[11] H. Erlach and J. Simperl, "Method for supplying an internal combustion engine with conditioned combustion gas, device for carrying out said method, method for determining the quantities of pollutants in the exhaust gases of an internal combustion engine, and device for carrying out said method," Patent US 7302834 B2, 2007

[12] J. C. Smith, P. J. Maloney, and M. Osterhout, "Altitude simulator for dynamometer testing," Patent US 6561014 B1, 2003

[13] D. Testa, "Apparatus and method for altimetric conditioning of internal combustion engines," Patent EP 2295950 B1, 2013

[14] J. M. Desantes, J. Galindo, F. Payri, P. Piqueras, and J. R. Serrano, "Device for conditioning the atmosphere in tests of alternative internal combustion engines, method and use of said device," Patent WO 2016/116642 A1, 2016

[15] R. L. Brugler, "Air handling unit," Patent 270483, 1952

[16] L. Leckelt, R. Vetsch, and B. Boudreau, "U-shaped air treatment arrangement in an air handling unit," Patent WO 2018/035217 A1, 2018

[17] J. M. Desantes, J. Benajes, J. R. Serrano, V. Bermúdez, P. Piqueras, and J. Gómez, "Device, method and use for conditioning intake air for testing internal combustion engines," Patent WO 2019/114935 A1, 2019

[18] J. Gómez, "Development of an altitude simulator and analysis of the performance and emissions of turbocharged Diesel engines at different altitudes," Ph.D. Thesis, Universitat Politècnica de València, Spain, 2018. doi: 10.4995/Thesis/10251/101284.

[19] V. Bermúdez, J. R. Serrano, P. Piqueras, J. Gómez, and S. Bender, "Analysis of the role of altitude on diesel engine performance and emissions using an atmosphere simulator," *International Journal of Engine Research*, vol. 18, no. 1–2, pp. 105–117, Feb. 2017, doi: 10.1177/1468087416679569.

[20] J. Galindo, J. R. Serrano, P. Piqueras, and J. Gómez, "Description and Performance Analysis of a Flow Test Rig to Simulate Altitude Pressure Variation for Internal Combustion Engines Testing," *SAE International Journal of Engines*, vol. 7, no. 4, pp. 1686–1696, Oct. 2014, doi: 10.4271/2014-01-2582.

[21] V. Bermúdez, J. R. Serrano, P. Piqueras, J. Gómez, and S. Bender, "Using an altitude simulation machine to analyze performance and emissions of a turbocharged Diesel engine operating on plateaus at high altitude," *THIESEL Conference*, 2016.

[22] A. Broatch, J. R. Serrano, A. Abbad, R. Tabet, S. Bender, and J. Gómez, "Emissions and performance correlations of a turbocharged diesel engine when operating on plateaus at high altitude inside an altitude chamber or connected to an altitude simulator," *EAEC Conference*, 2017.

[23] A. Broatch, V. Bermúdez, J. Ramón Serrano, R. Tabet-Aleixandre, J. Gómez, and S. Bender, "Analysis of passenger car turbocharged diesel engines performance when tested at altitude and of the altitude simulator device used," *ASME ICEF Conference*, 2018, ICEF2018-9549.

[24] S. Chen, C. Liu, Z. Wu, and Q. Yu, "Effects of co-current airflow on water atomization in a curved diffuser," *Energy Exploration and Exploitation*, vol. 39, no. 2, pp. 657–668, Mar. 2021, doi: 10.1177/0144598720905699.

[25] Armstrong International Inc., "Conditioned steam humidifiers," 2020. Accessed: Jan. 19, 2022. [Online]. Available: https://haarla.fi/wp-

content/uploads/2021/06/Conditioned-Steam-Humidifiers-598-20171101.pdf

[26] M. R. Rampure, A. A. Kulkarni, and V. v. Ranade, "Hydrodynamics of bubble column reactors at high gas velocity: Experiments and computational fluid dynamics CFD simulations," in *Industrial and Engineering Chemistry Research*, Dec. 2007, vol. 46, no. 25, pp. 8431–8447. doi: 10.1021/ie070079h.

[27] H. An, P. Cui, L. Fang, W. Wang, D. Zhao, and W. Yuan, "Study on the Performance of Heat and Mass Transfer of Cross Flow Dehumidifier in an Industrial Plant," in *Procedia Engineering*, 2017, vol. 205, pp. 1515–1522. doi: 10.1016/j.proeng.2017.10.381.

[28] D. Chen and H. Peng, "A thermodynamic model of membrane humidifiers for PEM fuel cell humidification control," *Journal of Dynamic Systems, Measurement and Control, Transactions of the ASME*, vol. 127, no. 3, pp. 424–432, Sep. 2005, doi: 10.1115/1.1978910.

[29] M. Rüdisüli, T. J. Schildhauer, S. M. A. Biollaz, and J. R. van Ommen, "Scale-up of bubbling fluidized bed reactors - A review," *Powder Technology*, vol. 217. pp. 21–38, Feb. 2012. doi: 10.1016/j.powtec.2011.10.004.

[30] C. E. Agu, L. A. Tokheim, M. Eikeland, and B. M. E. Moldestad, "Improved models for predicting bubble velocity, bubble frequency and bed expansion in a bubbling fluidized bed," *Chemical Engineering Research and Design*, vol. 141, pp. 361–371, Jan. 2019, doi: 10.1016/j.cherd.2018.11.002.

[31] "Vehicles in use Europe 2017," 2017. Accessed: Apr. 01, 2019. [Online]. Available: https://www.acea.be/statistics/article/Report-Vehicles-in-Use

[32] European Commission Regulation, "COMMISSION REGULATION (EU) 2017/1347 of 13 July 2017 correcting Directive 2007/46/EC of the European Parliament and of the Council on type-approval of motor vehicles with respect to emissions from light passenger and commercial vehicles (Euro 5 and Euro 6) and on access to vehicle repair and maintenance information, amending Directive 2007/46/EC of the European Parliament and of the Council," no. L 192/1. Official Journal of the European Union, Jul. 13, 2017.

[33] A. Ramos, J. Muñoz, F. Andrés, and O. Armas, "NOx emissions from diesel light duty vehicle tested under NEDC and real-word driving conditions," *Transportation Research Part D: Transport and Environment*, vol. 63, pp. 37–48, Aug. 2018, doi: 10.1016/j.trd.2018.04.018.

[34] A. Ramos, "Emisiones contaminantes diésel en condiciones transitorias de motores y vehículos empleando combustibles alternativos," Ph.D, Thesis, Universidad De Castilla-La Mancha, Spain, 2016.

[35] D. M. Human, T. L. Ullman, and T. M. Baines, "Simulation of High Altitude Effects on Heavy-Duty Diesel Emissions," *SAE International*, 1990, 900883.

[36] X. Wang *et al.*, "On-vehicle emission measurement of a light-duty diesel van at various speeds at high altitude," *Atmospheric Environment*, vol. 81, pp. 263–269, Dec. 2013, doi: 10.1016/j.atmosenv.2013.09.015.

[37] M. Yang, Y. Gu, K. Deng, Z. Yang, and Y. Zhang, "Analysis on altitude adaptability of turbocharging systems for a heavy-duty diesel engine," *Applied Thermal Engineering*, vol. 128, pp. 1196–1207, 2018, doi: 10.1016/j.applthermaleng.2017.09.065.

[38] Z. Liu and J. Liu, "Effect of Altitude on the Performance and Combustion Characteristics of Direct Injection Compression Ignition Engines," *International Journal of Engine Research*, 2021, Accessed: Dec. 27, 2021. [Online]. Available: http://mc.manuscriptcentral.com

[39] M. Ghazikhani, M. Ebrahim Feyz, O. Mahian, and A. Sabazadeh, "Effects of altitude on the soot emission and fuel consumption of a light-duty diesel engine," *Transport*, vol. 28, no. 2, pp. 130–139, Jun. 2013, doi: 10.3846/16484142.2013.798743.

[40] M. Szedlmayer and C. B. M. Kweon, "Effect of Altitude Conditions on Combustion and Performance of a Multi-Cylinder Turbocharged Direct-Injection Diesel Engine," in *SAE Technical Papers*, Apr. 2016, 2016-01-0742. doi: 10.4271/2016-01-0742.

[41] M. Lapuerta, O. Armas, J. R. Agudelo, and A. F. Agudelo, "Estudio del efecto de la altitud sobre el proceso de combustión de motores diesel. Study of altitude effect on diesel engine combustion process."

[42] L. Yu *et al.*, "Experimental investigation of the impact of biodiesel on the combustion and emission characteristics of a heavy duty diesel engine at various altitudes," *Fuel*, vol. 115, pp. 220–226, 2014, doi: 10.1016/j.fuel.2013.06.056.

[43] C. He *et al.*, "Emission characteristics of a heavy-duty diesel engine at simulated high altitudes," *Science of the Total Environment*, vol. 409, no. 17, pp. 3138–3143, Aug. 2011, doi: 10.1016/j.scitotenv.2011.01.029.

[44] M. Lapuerta, O. Armas, J. R. Agudelo, and C. A. Sánchez, "Study of the Altitude Effect on Internal Combustion Engine Operation. Part 1:

Performance," *Información Tecnológica*, vol. 17, no. 5, pp. 21–30, Nov. 2006, doi: 10.4067/S0718-07642006000500005.

[45] C. A. Chaffin and T. L. Ullman, "Effects of Increased Altitude onHeavy-Duty Diesel Engine Emissions," in *SAE Technical*, 1994, no. 412, pp. 776–5760. doi: 10.4271/940669.

[46] V. Bermúdez, J. R. Serrano, P. Piqueras, and B. Diesel, "Fuel consumption and aftertreatment thermal management synergy in compression ignition engines at variable altitude and ambient temperature," *International Journal of Engine Research*, 2021, vol. 1, no. 13, doi: 10.1177/14680874211035015.

[47] Y. Zama, W. Ochiai, T. Furuhata, and M. Arai, "Experimental study on spray angle and velocity distribution of diesel spray under high ambient pressure conditions," *Atomization and Sprays*, vol. 21, no. 12, pp. 989–1007, 2011.

[48] J. W. Dennis, "Turbocharged Diesel Engine Performance at Altitude," *SAE Transactions*, vol. 80, no. 4, pp. 2670–2689, Sep. 1971, Accessed: Dec. 28, 2021. [Online]. Available: https://www.jstor.org/stable/44650353

[49] H. Hiroyasu, M. Arai, and M. Tabata, "Empirical Equations for the Sauter Mean Diameter of a Diesel Spray," *SAE Transactions*, vol. 98, pp. 868–77, Jan. 1989, Accessed: Dec. 27, 2021. [Online]. Available: http://www.jstor.org/stable/44580992.

[50] K. D. Kihm, D. P. Terracina, Payne S. E., and J. A. Caton, "Synchronised droplet size measurements for coal-water slurry sprays generated from a high-pressure diesel injection system," 1993. Accessed: Dec. 27, 2021. [Online]. Available: http://minsfet.utk.edu/publications/1994_Synchronized%20Droplet%20Size.pdf

[51] G. de Nicolao, R. Scattolini, and C. Siviero, "Modelling the volumetric efficiency of IC engines: parametric, non-parametric and neural techniques," *Control Engine Practice*, vol. 4, no. 10, pp. 1405–1415, 1996, doi: 10.1016/0967-0661(96)00150-5.

[52] A. Moratal, "Experimental analysis of thermal management influence on performance and emissions in diesel engines at low ambient temperature," Ph.D. Thesis, Universitat Politècnica de València, 2018.

[53] H. Peng, Y. Cui, L. Shi, and K. Deng, "Effects of exhaust gas recirculation (EGR) on combustion and emissions during cold start of direct injection (DI) diesel engine," *Energy*, vol. 33, no. 3, pp. 471–479, 2008, doi: 10.1016/j.energy.2007.10.014.

[54] A. S. Ramadhas and H. Xu, “Influence of Coolant Temperature on Cold Start Performance of Diesel Passenger Car in Cold Environment,” in *SAE Technical Papers*, Feb. 2016, 2016-28-0142. doi: 10.4271/2016-28-0142.

[55] B. Nitu, I. Singh, L. Zhong, K. Badreshany, N. A. Henein, and W. Bryzik, “Effect of EGR on Autoignition, Combustion, Regulated Emissions and Aldehydes in DI Diesel Engines.,” *SAE Transactions*, vol. 111, pp. 2028–2042, 2002, Accessed: Dec. 28, 2021. [Online]. Available: http://www.jstor.org/stable/44743219

[56] J. Ko, D. Jin, W. Jang, C. L. Myung, S. Kwon, and S. Park, “Comparative investigation of NOx emission characteristics from a Euro 6-compliant diesel passenger car over the NEDC and WLTC at various ambient temperatures,” *Applied Energy*, vol. 187, pp. 652–662, Feb. 2017, doi: 10.1016/j.apenergy.2016.11.105.

[57] A. Maiboom, X. Tauzia, S. Rahman Shah, and J.-F. Hétet, “Experimental Study of an LP EGR System on an Automotive Diesel Engine, compared to HP EGR with respect to PM and NOx Emissions and Specific Fuel Consumption,” *Source: SAE International Journal of Engines*, vol. 2, no. 2, pp. 597–610, 2010, doi: 10.2307/26275447.

[58] Y. Park and C. Bae, “Experimental study on the effects of high/low pressure EGR proportion in a passenger car diesel engine,” *Applied Energy*, vol. 133, pp. 308–316, Nov. 2014, doi: 10.1016/j.apenergy.2014.08.003.

[59] D. Heuwetter, W. Glewen, C. Meyer, D. Foster, M. Andrie, and R. Krieger, “Effects of low pressure EGR on transient air system performance and emissions for low temperature diesel combustion,” *SAE International*, 2011, 2011-24-0062. doi: 10.4271/2011-24-0062.

[60] V. Bermúdez, J. M. Lujan, B. Pla, and W. G. Linares, “Effects of low pressure exhaust gas recirculation on regulated and unregulated gaseous emissions during NEDC in a light-duty diesel engine,” *Energy*, vol. 36, no. 9, pp. 5655–5665, 2011, doi: 10.1016/j.energy.2011.06.061.

[61] M. Weilenmann, P. Soltic, C. Saxer, A. M. Forss, and N. Heeb, “Regulated and nonregulated diesel and gasoline cold start emissions at different temperatures,” in *Atmospheric Environment*, 2005, vol. 39, no. 13, pp. 2433–2441. doi: 10.1016/j.atmosenv.2004.03.081.

[62] J. Kashdan, S. Mendez, and G. Bruneaux, “An investigation of unburnned hydrocarbon emissions in wall guided, low temperature diesel combustion,” *Oil and Gas Science and Technology*, vol. 63, no. 4, pp. 433–459, 2008, doi: 10.2516/ogst:2008018.

[63] Y. Zeldóvich, “Oxidation of Nitrogen in Combustion and Explosions,” *Acta Pysichochimica*, vol. 21, pp. 557–628, 1946, doi: 10.1515/9781400862979.404.

[64] J. Bird and W. Grabe, “Humidity effects on gas turbine performance,” *ASME 1991 International Gas Turbine and Aeroengine Congress and Exposition*, vol. 2, 1991, doi: 10.1115/91-GT-329.

[65] X. Tauzia, A. Maiboom, and S. R. Shah, “Experimental study of inlet manifold water injection on combustion and emissions of an automotive direct injection Diesel engine,” *Energy*, vol. 35, no. 9, pp. 3628–3639, 2010, doi: 10.1016/j.energy.2010.05.007.

[66] A. A. Iyer, “Experimental study on the effect of water injection in an internal combustion engine,” *IOSR Journal of Mechanical and Civil Engineering*, vol. 17, no. 10, pp. 58–64, Mar. 2017, doi: 10.9790/1684-17010055864.

[67] B. Kegl and S. Pehan, “Reduction of diesel engine emissions by water injection,” in *SAE Transactions Section 3: JOURNAL OF ENGINES*, 2001, vol. 110, pp. 2040–2047. [Online]. Available: https://about.jstor.org/terms

[68] M. Kettner, S. Dechent, M. Hofmann, E. Huber, H. Arruga, and R. Mamat, “Investigating the influence of water injection on the emissions of a diesel engine,” *Journal of Mechanical Engineering and Sciences*, vol. 10, no. 1, pp. 1863–1881, Jun. 2016, doi: 10.15282/jmes.10.1.2016.11.0179.

[69] D. T. Hountalas, G. C. Mavropoulos, T. C. Zannis, and S. D. Mamalis, “Use of water emulsion and intake water injection as NOx reduction techniques for heavy duty Diesel engines,” *SAE Technical Paper*, 2006, 2006-01-1414, doi: 10.4271/2006-01-1414.

[70] X. Ma, F. Zhang, K. Han, Z. Zhu, and Y. Liu, “Effects of intake manifold water injection on combustion and emissions of diesel engine,” *Energy Procedia*, vol. 61, pp. 777–781, 2014, doi: 10.1016/j.egypro.2014.11.963.

[71] K. A. Subramanian, “A comparison of water-diesel emulsion and timed injection of water into the intake manifold of a diesel engine for simultaneous control of NO and smoke emissions,” *Energy Conversion and Management*, vol. 52, no. 2, pp. 849–857, Feb. 2011, doi: 10.1016/j.enconman.2010.08.010.

[72] A. Li, Z. Zheng, and Y. Song, “A simulation study of water injection position and pressure on the knock, combustion, and emissions of a direct injection gasoline engine,” *ACS Omega*, vol. 6, no. 28, pp. 18033–18053, Jul. 2021, doi: 10.1021/acsomega.1c01792.

[73] Y. Karagöz, L. Yüksek, T. Sandalci, and A. S. Dalkiliç, "An experimental investigation on the performance characteristics of a hydroxygen enriched gasoline engine with water injection," *International Journal of Hydrogen Energy*, vol. 40, no. 1, pp. 692–702, Jan. 2015, doi: 10.1016/j.ijhydene.2014.11.013.

[74] S. Sm and Srinivas M, "Improvement of fuel efficiency in a petrol engine by using water injection," *Int J Chem Sci*, vol. 15, no. 2, p. 123, 2017, [Online]. Available: www.tsijournals.com

[75] J. Martin, F. Arnau, P. Piqueras, and A. Auñon, "Development of an Integrated Virtual Engine Model to Simulate New Standard Testing Cycles," in *SAE Technical Papers*, 2018, 2018-01-1413. doi: 10.4271/2018-01-1413.

[76] J. R. Serrano, R. Navarro, L. M. García-Cuevas, and L. B. Inhestern, "Turbocharger turbine rotor tip leakage loss and mass flow model valid up to extreme off-design conditions with high blade to jet speed ratio," *Energy*, vol. 147, pp. 1299–1310, Mar. 2018, doi: 10.1016/j.energy.2018.01.083.

[77] J. R. Serrano, F. J. Arnau, L. M. García-Cuevas, and V. Samala, "A robust adiabatic model for a quasi-steady prediction of far-off non-measured performance in vaneless twin-entry or dual-volute radial turbines," *Applied Sciences (Switzerland)*, vol. 10, no. 6, Mar. 2020, doi: 10.3390/app10061955.

[78] B. Pla, J. de la Morena, P. Bares, and I. Jiménez, "Cycle-to-cycle combustion variability modelling in spark ignited engines for control purposes," *International Journal of Engine Research*, vol. 21, no. 8, pp. 1398–1411, Oct. 2020, doi: 10.1177/1468087419885754.

[79] J. M. Luján, C. Guardiola, B. Pla, and P. Bares, "Estimation of trapped mass by in-cylinder pressure resonance in HCCI engines," *Mechanical Systems and Signal Processing*, vol. 66–67, pp. 862–874, 2016, doi: 10.1016/j.ymssp.2015.05.016.

[80] J. R. Serrano, F. J. Arnau, J. Martín, and Á. Auñón, "Development of a variable valve actuation control to improve diesel oxidation catalyst efficiency and emissions in a light duty diesel engine," *Energies*, vol. 13, no. 17, Sep. 2020, doi: 10.3390/en13174561.

[81] F. J. Arnau, J. Martín, P. Piqueras, and Á. Auñón, "Effect of the exhaust thermal insulation on the engine efficiency and the exhaust temperature under transient conditions," *International Journal of Engine Research*, vol. 22, no. 9, pp. 2869–2883, Sep. 2021, doi: 10.1177/1468087420961206.

Chapter 3
Altitude Simulator: MEDAS

3.1. Introduction

The altitude simulator HORIBA MEDAS is an installation that allows the control of the pressure and partially the temperature of the intake air of an ICE. This is carried out mainly by the action of controlled valves, a VGT turbocharger, and a mechanical centrifugal compressor.

Figure 3. 1 shows the MEDAS state of development [1] before this work, in which t<the air path starts in the air filter (1), through which the airflow enters the installation. Afterward, the flow has two options: an isothermal expansion in a controlled valve (2) or a cooled expansion in the turbine (4). The pressure is controlled at the engine intake with valve (2). In addition, before the turbine, a controlled valve (3) is included to control the temperature of the engine intake air by increasing or reducing the flow rate through the turbine. After cooling down in (4), the water content of the air can condense or even create ice if the temperature is low enough. Therefore, a cyclonic separator (5) is installed downstream of the turbine to remove the condensates. Then the two streams are remixed and arrive at the engine intake connection (6), from which the engine takes the amount needed, and the rest flows through the bypass duct (7). The bypassed flow mixes with the exhaust flow from the engine exhaust connection (8). The bypass duct (7) is one of the critical components of the MEDAS since it assures that the engine intake and exhaust are operating at the same pressure as would happen in real driving conditions. Also, (7) is the component that decouples the engine operating point and the MEDAS operating point, allowing the MEDAS to work in steady-state conditions with the engine performing dynamic cycles or vice versa.

Once the bypass flow and the engine exhaust flow are remixed, the air passes through an exhaust cooler (9), which cools down the flow to protect the components downstream. Same as with the turbine, when the exhaust flow is cooled down, it can condense water. Hence, another cyclonic separator (10) is located downstream (9). Then, the airstream reaches the mechanical compressor (11), which is the one that generates the vacuum in the installation and manages the amount of airflow that moves through the MEDAS. Lastly, the exhaust stream is expelled to the test cell extraction system through a muffler (12).

Disconnected from the primary air circuit, a turbo compressor (13) dissipates the power generated in the turbine (4) with an almost fixed compression ratio.

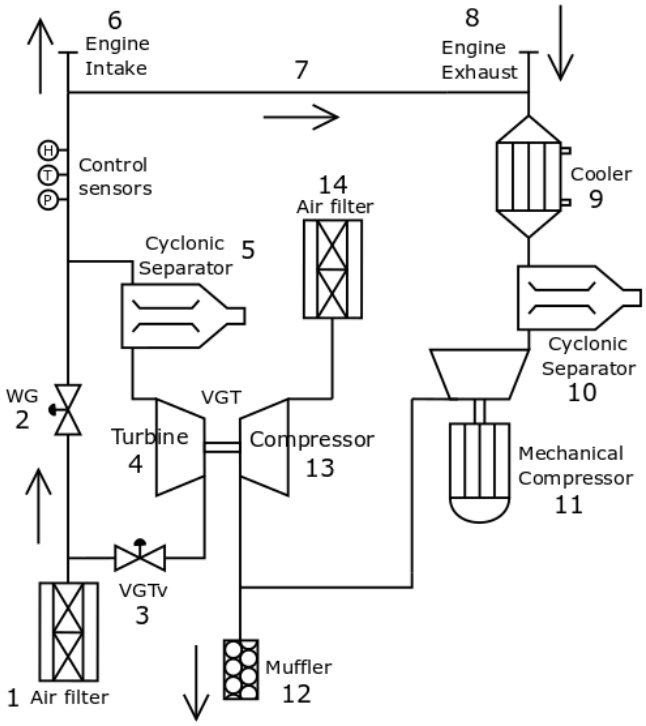

Figure 3. 1. MEDAS original layout [1]

3.2. MEDAS enhancements by inductive procedures

Building on the base MEDAS system developed in a previous thesis [1], various improvements have been implemented. These improvements have been designed through observation while testing the installation. The majority focused on increasing mass flow performance range and energy efficiency.

However, there have been enhancements motivated by industry needs, such as further improvements in the safety of the equipment concerning the supplies provided to the MEDAS, i.e., cooling water or pneumatic air supply. Or improve the thermal insulation to allow the MEDAS to work under freezing ambient conditions.

3.2.1. MEDAS improvement: 2nd Generation

The improvement of the MEDAS to achieve a 2nd generation installation includes both hardware and software enhancements. The main objectives are to increase the cooling capability and mass flow range at all reachable altitudes, reduce the installation's energy consumption for a given operating point, and improve the pressure and temperature control accuracy. The MEDAS mass flow

and cooling performance before the improvement presented in this Ph.D. Thesis is shown in Figure 3. 2.

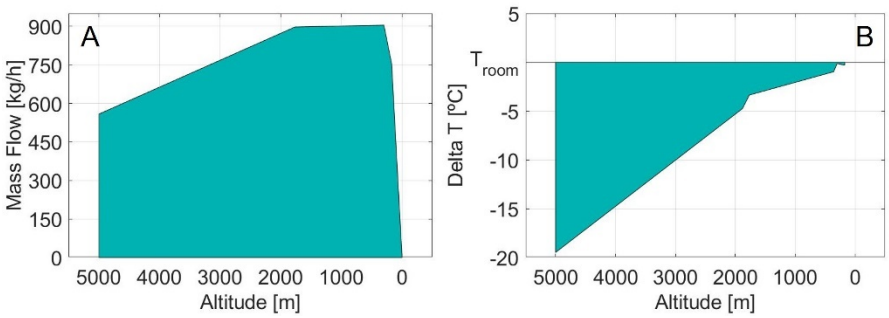

Figure 3. 2. Initial MEDAS performance range: (A) Mass flow; (B) Temperature

3.2.1.1 Hardware improvement

a) 2 stage compression

The mechanical compressor is the main component that limits the performance and the heaviest load in terms of electrical power consumption. Hence, the first idea to try and improve the MEDAS was to reduce the power demand for the mechanical compressor for a given operative point. The turbo compressor was used to achieve this, connecting it in series with the mechanical compressor to use the power extracted from the turbine. This would reduce the pressure ratio of the mechanical compressor when the turbine can extract enough power from expanding the air, thus reducing the electrical power consumption.

The MEDAS layout is modified to connect the two compressors in series and is presented in Figure 3. 3. It should be noted that there are operation points of the MEDAS in which the turbine cannot extract enough power from the air expansion. Therefore, the turbo compressor cannot be used to help the mechanical compressor. In these cases, the turbo compressor works as a rotative valve, introducing an extra back pressure to the installation, which, contrary to expected, increases the mechanical compressor's power consumption.

To avoid this problem, a one-way flow valve (check-valve) is installed in parallel with the turbo compressor (13 of Figure 3. 3), which would open when the power available for the turbo compressor is not enough. The application described opens when the pressure difference exceeds 15 mbar in the check-valve. Figure 3. 4 shows a 3D model of both configurations: in Figure 3. 4A, the previous solution in which the compressor dissipates the power generated in the turbine to the ambient; and in Figure 3. 4B, the solution with the turbo compressor in series with the mechanical compressor.

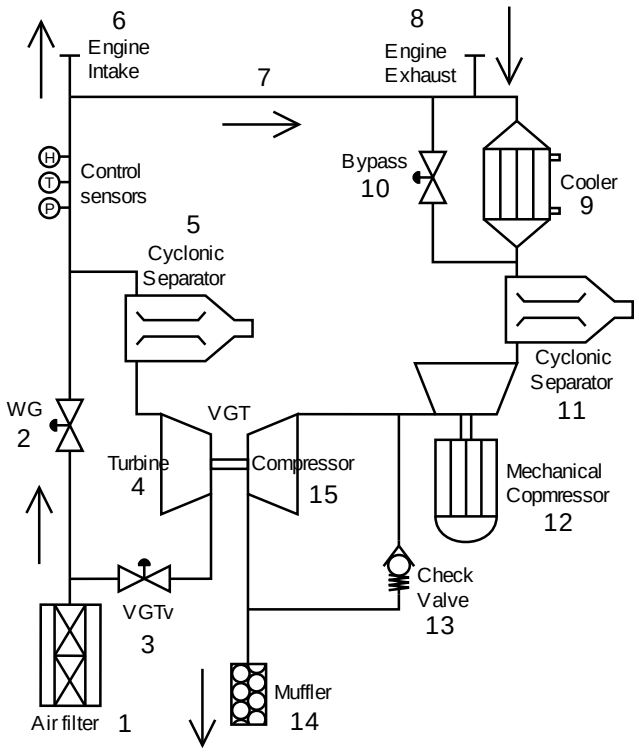

Figure 3. 3. MEDAS 2nd Generation layout

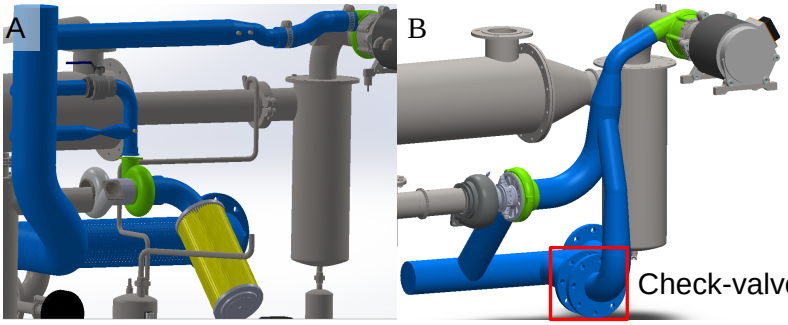

Figure 3. 4. Turbo compressor configuration: (A) Independent power dissipation; (B) Series connection to the mechanical compressor

The improvement obtained from this modification is shown in Figure 3. 5. The real mass flow passing through the installation (*y-axis*) is represented against the altitude simulated by the MEDAS (*x-axis*). The symbols represent the mechanical compressor speed defined as 50, 70, and 90% of the maximum speed, while the colors represent the different configurations for the MEDAS.

First, the compressors are connected in series (Figure 3. 4B) but with the MEDAS intake pressurized up to 2.5 bar to increase the expansion in the turbine (blue). Second, the compressors are connected in series (Figure 3. 4B) with the intake pressure at 1 bar (green). Third, the original configuration (Figure 3. 4A) with the mechanical compressor separated from the turbo compressor (red).

Suppose the focus is on green and red colors (the two compressors in series without boosting and the mechanical compressor alone). In that case, it can be seen how the new layout with the two compressors connected in series causes a decrease in performance for the three speeds when the mass flow increases. This shows that when the MEDAS is working aspirating from room pressure, the back pressure introduced by the new layout is more dominant than the help provided by the turbo compressor. However, suppose the blue color (two compressors in series with the turbine inlet boosted) is considered against the red case (original layout with the mechanical compressor alone). In that case, it can be seen how the performance increases significantly, with a higher increase in the lower mechanical compressor speed area.

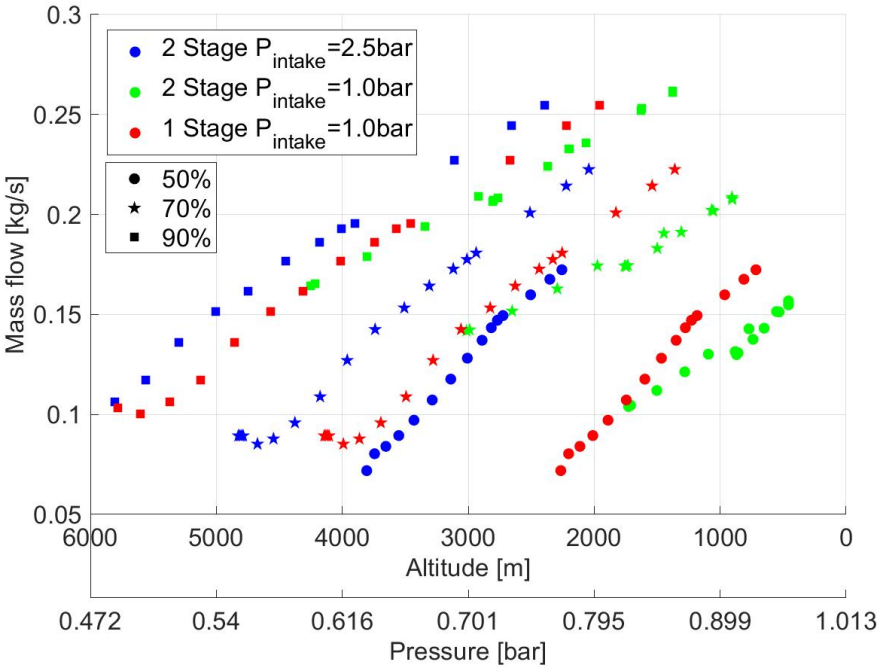

Figure 3. 5. 2 stage compression: Mass flow performance improvement

These results show that the expected improvement in performance and energy is not achieved if the MEDAS works as stand-alone equipment but has excellent potential when coupled with a boosting system. An example of this kind of

installation can be the MEDAS Temperature Module or MTM, an extension of the MEDAS developed while in this Ph.D., explained in Chapter 4.

Additionally, it has been observed that when there is too much back pressure in the test cell exhaust system, hot backflows appear through the air filter of the turbo compressor (point 14 of Figure 3. 1), which could damage the electronical components located inside the MEDAS box. Therefore, connecting the compressors in series provides an extra advantage as this problem is naturally solved since the air filter is removed to attach the inlet of the turbo compressor to the outlet of the mechanical compressor.

b) Exhaust line pressure loss

Optimizing the exhaust line (from 6 to 12 of Figure 3. 3) pressure drop is one of the most critical actions to improve the MEDAS performance and energy consumption. The reduction of the exhaust line pressure drop increases the pressure at the inlet of the mechanical compressor for a given pressure setpoint. This leads to a lower pressure ratio as the compressor outlet pressure is fixed by the ambient (Equation 3. 1). Lower corrected mass flow in the compressor (Equation 3. 2) reduces the compressor's power consumption for a given operative point of MEDAS.

$$\Pi_C = \frac{p_{C,out}}{p_{C,in}}$$

Equation 3. 1

$$\dot{m}_{corr} = \dot{m} \frac{\sqrt{T_{C,in}/T_{ref}}}{p_{C,in}/p_{ref}}$$

Equation 3. 2

The reduction of the pressure drop of the MEDAS exhaust line is focused on the outlet figure of the exhaust cooler (9 of Figure 3. 3), which is the main contributor to this part of the MEDAS. The geometry is changed from an aggressive reduction of diameter (Figure 3. 6A) to a more progressive cone-shaped reduction of diameter (Figure 3. 6B). The pressure drop decreased tremendously with this change, causing a significant increase in performance, as shown in Figure 3. 6C, which makes this modification worthy even with the rise of the MEDAS length that a progressive section reduction implies.

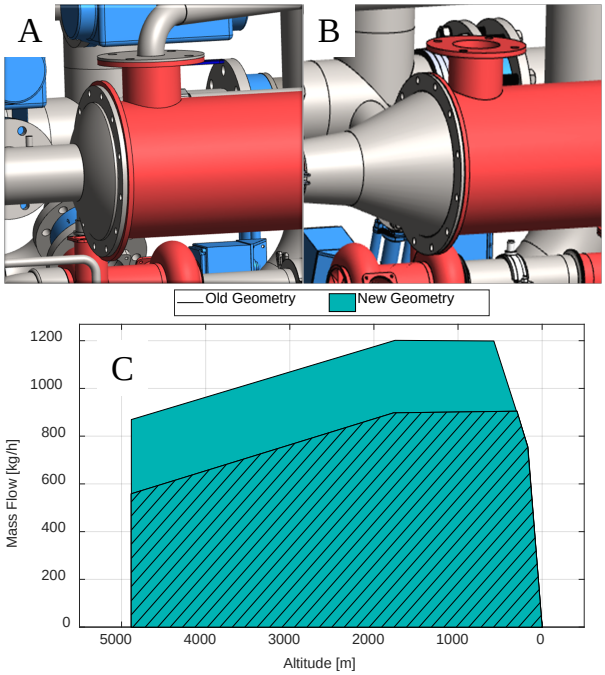

Figure 3. 6. Cooler outlet geometry: (A) Old geometry; (B) New geometry; (C) Performance improvement

c) Condensates extraction system

Another issue detected when using the MEDAS extensively with an engine coupled is that it is impossible to perform long testing sessions, especially when the cooling water in the exhaust gas cooler is below 25 ºC. The condensates generated in this case from the cooling of the exhaust gases accumulate, and it is necessary to stop the installation to drain them. To solve this problem and allow an uninterrupted performance of the MEDAS, an automatic condensates extraction system has been designed.

The extraction of condensates during the MEDAS operation poses a challenge since the inside of the piping is, in most cases, at a lower pressure than the ambient. Therefore, if any valve is opened with the MEDAS operating, an intake of air is produced, which can damage or even break the shaft of the mechanical compressor due to a sharp increase in the impeller load. Hence, a system that isolates the condensates deposit and pumps the condensates outside the machine is needed.

This can be carried out mainly in two ways: with a self-priming water pump (Figure 3. 7A) that must deal with any air bubble that could be present in the condensate line or pressurizing the condensates deposit to a higher pressure

(Figure 3. 7B) to pump out the condensates. Since the MEDAS has a pneumatic air circuit, the option of pressurizing the deposit was the most convenient to be implemented.

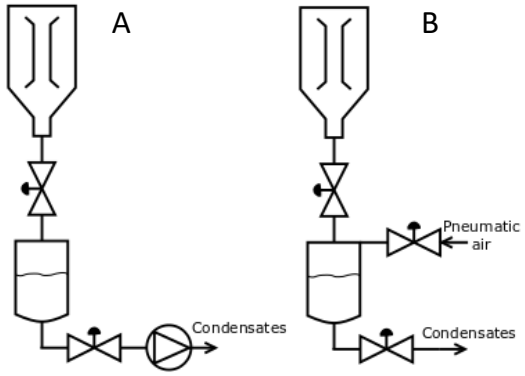

Figure 3. 7. Solutions for the condensates extraction from a vacuum system: (A) Self-priming water pump; (B) Pneumatic air injection

In Figure 3. 8 can be seen the first installation on a prototype of the selected system, but after testing, design improvements were identified. The system always extracted the condensates correctly when the pressure in the cyclonic separator (1 of Figure 3. 8) is closer (slightly lower) to the room pressure, but not when the pressure in the cyclone is much lower (MEDAS operating and generating vacuum).

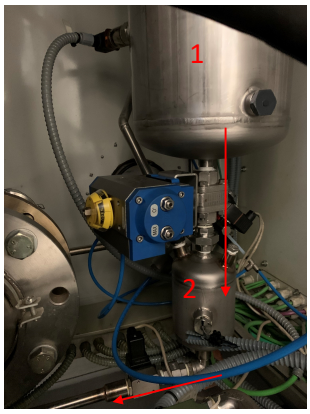

Figure 3. 8. First installation of the condensates extraction system

The cause was the creation of an air bubble inside the condensate deposit (2 of Figure 3. 8) that prevented the flow of the water into the deposit. To let the water flow to the deposit, it is necessary to allow the air inside to flow out. To achieve this, the available section of the pipe must be divided between the flowing liquid

and the air that must be evacuated. If this is not achieved, an air bubble is eventually formed in the deposit, and the water flow is stopped.

To solve this issue, there are two options: increase the size of the duct through which the water is flowing to allow the air to pass together with the water, or create a different path through which the air can flow freely and evacuate from the deposit. The first option was not viable due to the size restrictions of the components, as the total size of the MEDAS cannot be increased. Therefore, the second option was adopted.

In Figure 3. 9, the final solution is shown. The water collected in the cyclonic separator flows to the deposit through the valve (1), and the air is evacuated through the valve (2). Valve (3) is the one that opens or closes the compressed air flow to the deposit, and valve (4) opens the connection to the test cell drain system. There are two sensors included in the extraction system: one located in the deposit (5) that detects when the deposit is full to start the extraction sequence. And the other is located in the cyclone body (6) to detect a problem with the extraction system and stop the MEDAS before the water reaches the mechanical compressor.

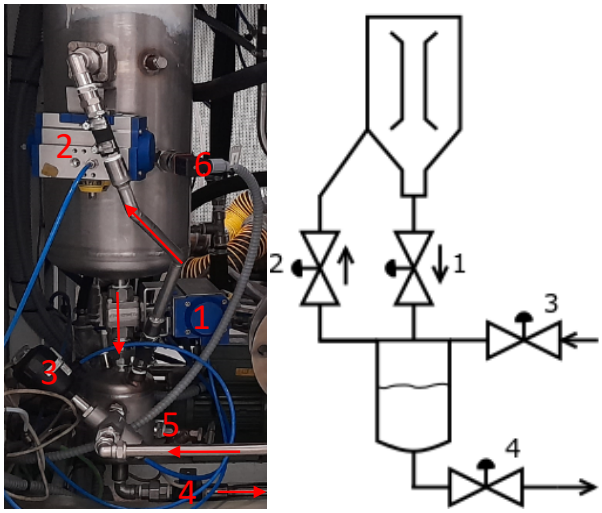

Figure 3. 9. MEDAS condensates extraction system

The extraction sequence followed by the hardware shown in Figure 3. 9 is quite simple and is carried out totally by electric contacts:

- First, valves (1) and (2) are open, while valves (3) and (4) are closed to allow the condensates to flow into the deposit.
- Then, when the level sensor (5) is activated, (1) and (2) close to isolate the primary air circuit from the deposit. Afterward, (3) and (4) open to allow the pneumatic air to pump the condensates to the drain circuit.

- Finally, when sensor (5) is deactivated, valves (3) and (4) close, and valves (1) and (2) open to start the process again and accumulate condensates in the deposit.
- Only, if there is a problem in the extraction system, i.e., a clog in any duct or filter or a malfunctioning valve, the water would be accumulated in the cyclone body, and the sensor (6) would activate, stopping the MEDAS to avoid damaging the mechanical compressor.

It should be noted that once the air evacuation circuit is installed, the MEDAS can extract all the condensates generated at any given working pressure inside the control range without further problems.

d) Exhaust Cooler bypass

To reduce the condensate generation rate and thus reduce the stress over the extraction system, a bypass is included for the exhaust gases cooler (9 of Figure 3. 3) to control the mechanical compressor inlet temperature constant at 50ºC, at which the condensation of ICE exhaust gases stops [2].

The bypass of the exhaust gases cooler allows controlling the temperature at the mechanical compressor inlet ($T_{C,in}$) during engine transients, which translates as a finer control of the mass flow through the installation. Without a bypass for the cooler, when the engine performs a transient to an operating point of higher or lower power, $T_{C,in}$ changes without control due to the evolution of the exhaust gas temperature.

This change in the temperature at the compressor inlet causes a difference in the compressor's power consumption (Equation 3. 3). Therefore, in a transient of $T_{C,in}$ the mass flow that passes through the installation is affected. Of course, this is true only if it is assumed that the compressor is working at a constant point in its map and the mechanical compressor inlet pressure ($p_{C,in}$) does not change due to the pressure control of the MEDAS. However, it is a valid hypothesis that these stationary conditions are met during the initial phase of an engine transient.

For example, suppose that $T_{C,in}$ suddenly changes from 30 ºC to 50 ºC, while the $p_{C,in}$ is kept constant at 0.85 barA, and the corrected mass flow is controlled to 0.4 kg/s. Then, the real mass flow through the installation will decrease from 0.33 to 0.32 kg/s, following Equation 3. 4, causing a perturbance on every control present in the MEDAS.

$$P_C = \frac{\dot{m} \cdot C_p \cdot T_{C,in} \cdot \left(\left({p_{C,out}}/{p_{C,in}} \right)^{{\gamma-1}/{\gamma}} - 1 \right)}{\eta_C}$$

Equation 3. 3

$$\dot{m}_{real} = \dot{m}_{corr} \frac{p_{C,in}/p_{ref}}{\sqrt{T_{C,in}/T_{ref}}}$$

Equation 3. 4

This sudden change in the mass flow introduces a perturbance in the system, which reduces the accuracy and stability of the pressure control itself. Therefore, if the evolution of $T_{C,in}$ can be dampened, the control of the installation can be improved during the engine transients. Nevertheless, the control of $T_{C,in}$ is flexible to allow extending the maximum mass flow of MEDAS at the expense of increasing the condensate production. When the mechanical compressor reaches maximum speed and the actual mass flow is below the target, the setpoint for $T_{C,in}$ is lowered to increase the mass flow. However, this causes an increase in the condensate production rate, increasing the stress that the extraction system must withstand. Also, it is possible to reach or even exceed the maximum condensate extraction rate of the system designed, causing an accumulation of water in the cyclone body.

Hence, $T_{C,in}$ is controlled to be at 50ºC except when the current mass flow is below the target, and the mechanical compressor speed reaches its maximum speed. Then, the target for $T_{C,in}$ is slowly reduced to increase the mass flow and try to get the demanded setpoint.

3.2.1.2 Control software improvement

a) Pressure control

The pressure control of MEDAS has been improved with two main objectives: to improve the control stability and accuracy and increase the cooling capability of the MEDAS. The solution adopted to achieve this is to use a single PID controller but extend it to two actuators, the WG valve and the VGT vanes (2 and 4 of Figure 3. 3, respectively), which work in series.

In this case, the VGT vanes are entirely open when the WG controls the pressure. Only when the WG is completely closed, and the pressure is above the setpoint do the VGT vanes start closing to reach the pressure target. In this way, the maximum airflow is passing through the turbine, and the cooling capabilities of the MEDAS are maximized since the mix at the engine intake has a higher percentage of cooling flow.

This control strategy allows a smother pressure control than the previous solution. The WG valve carried out the pressure control, and correlations operated the VGT vanes in an open-loop [1]. With the new pressure control, only one of the actuators (WG and VGT vanes) moves, which removes the chance of coupling between them and reduces the system's perturbances.

The accuracy during steady-state operation for both options is presented in Figure 3. 10, which shows the pressure control results for both controls proposed. Here the pressure measurement against time at six different setpoints is presented. The maximum error and the average error with respect to the pressure setpoint are included in each case. It can be seen how the pressure accuracy has improved in most of the altitudes tested with the new control, while it stays the same in the rest.

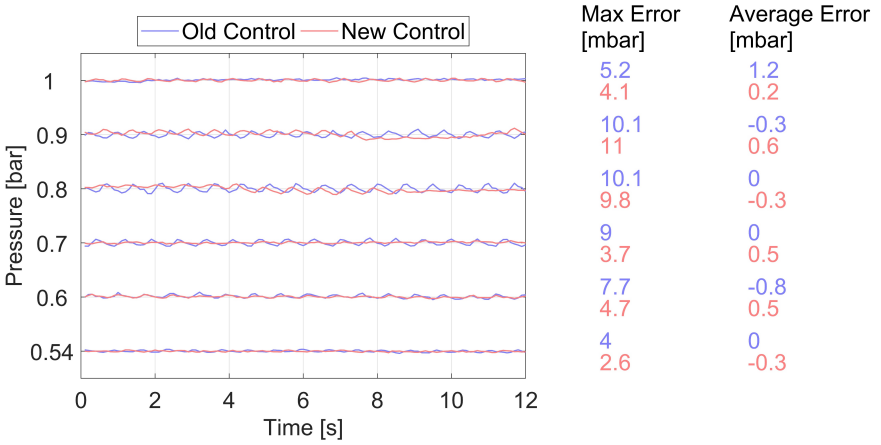

Figure 3. 10. New pressure control stability improvement

The objective of increasing the cooling capabilities of the MEDAS has also been reached with the new control. Figure 3. 11 shows the temperature reached at the engine intake connection (6 of Figure 3. 3) while operating in a steady-state at different altitudes. During these tests, a boosting system was connected upstream of the MEDAS, providing 2.3 bar of boosting pressure, and the temperature and mass flow setpoints were fixed at -15 ºC and 0.21 kg/s, respectively.

Suppose the focus is on the area where the temperature setpoint is not reached, between 0 meters and 3000 meters above sea level. It can be seen how with the new control, the temperature reached is lower than with the original, even reaching the setpoint up to 2000 meters. It should be noted that the results shown in the current section are obtained employing a laboratory prototype unit available at CMT-UPV labs, which has a lower cooling and mass flow performance than the brand new commercial units of MEDAS.

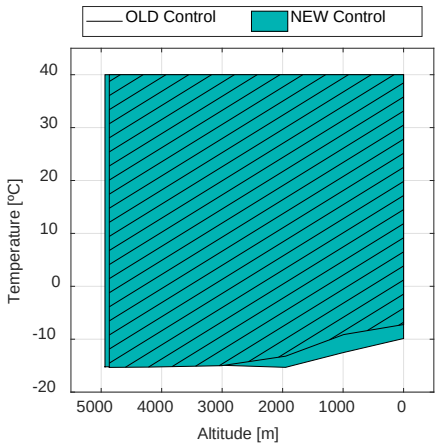

Figure 3. 11. Cooling performance improvement: Temperature setpoint -15 ºC; Mass flow setpoint 0.21 kg/s

b) Pressure step demand protection ramp

Changing operative points of MEDAS is one of the riskiest situations since the mass flow and pressure in the installation changes. This can be very sudden if the control software does not adequately protect the MEDAS from pressure setpoint changes in giant steps. This can lead to the failure of some components, mainly the mechanical compressor and the turbocharger shaft, due to the sudden load increments that the aggressive change in airflow can generate. Therefore, two protection strategies were designed to assure the safety of the components and force a milder behavior of the installation during the point-to-point step changes.

Firstly, the so-called 'nearest-point' strategy consists of an open-loop control that brings the MEDAS actuators to the proximity of the final controlling position following an experimentally defined map. This strategy was designed in previous works and can be found in Section 4.6.2 of the reference [1]. Here, the process of calculating the demanded point from the map and the parameters used to build the map from identifying the actuators involved are explained. However, the 'nearest-point' strategy is only active in some cases, mainly when there is no boosting system upstream of the MEDAS or the 'Dynamic' operation is OFF.

In some operation conditions of MEDAS, the 'nearest-point' strategy cannot be used due to the low accuracy caused by the contour conditions (boosting system connected upstream) or because it is not helpful for the set of user demands ('Dynamic' conditions ON). For example, suppose the user is performing a real driving altitude profile. In that case, it is not helpful to bring the actuators to the position calculated from the map since the variation of the setpoint is small and

only with the action of the PID's the control is more accurate. Moreover, the 'nearest- point' strategy uses the pressure ratio in the WG control valve (Figure 3. 3) to calculate the point in the map, referenced to a room pressure between 1.013 and 0.795 mbar (0 meters and 2000 meters above sea level, respectively). Therefore, when a boosting system is connected upstream of the MEDAS, this reference is distorted by the increased pressure at the MEDAS inlet, which significantly reduces the accuracy of the open-loop control defined.

The new protection strategy, named 'step-demand-protection-ramp,' was designed to be active in cases where the 'nearest-point' strategy could not be activated, with the logic for using one or the other shown in Table 3. 1. The 'step-demand-protection-ramp' imposes a maximum slope for the pressure setpoint variation. This assures a milder change of operative points and prevents the step-loading of the compressor wheel from happening due to sudden changes in pressure and mass flow in the installation.

Figure 3. 12A shows the pressure change at the engine intake connection due to a step demand in the pressure setpoint without the ramp protection. Contrarily, in Figure 3. 12B, the same kind of setpoint change but with the 'step demand protection ramp' activated. These figures, Figure 3. 12A and B, have a vast difference in the time scale on the *x-axis* and cannot be compared directly. This shows the pressure peak in detail in Figure 3. 12A and how the protection developed can remove it in Figure 3. 12B.

It should be noted that the imposed ramp during the 'step-demand-protection-ramp' (1 mbar/s) corresponds to a more aggressive altitude variation than any road present on Earth. Suppose the steepest part of a cycling race, 'Tour de France,' with a maximum slope of 8%, is considered an extreme high-speed mountain road. Then, the pressure variation that a vehicle driving at 100 km/h faces is 0.22 mbar/s, proving that the MEDAS can emulate any test carried out with a commercial vehicle on-road with the new protection implemented.

Table 3. 1. Truth table for the step demand protection ramp

Upstream boosting case	Dynamic button case	Activate protection ramp
Connected	ON	ON
Connected	OFF	ON
Disconnected	ON	ON
Disconnected	OFF	OFF

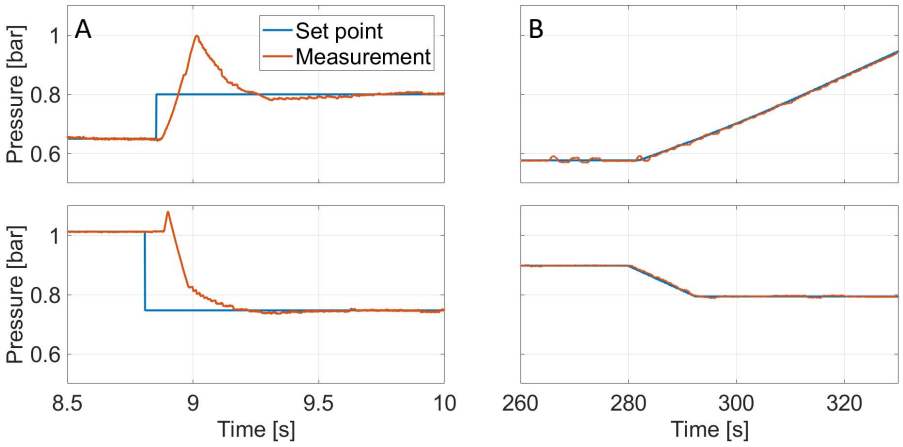

Figure 3. 12. Pressure behavior against a setpoint step: (A) Without protection ramp; (B) With protection ramp

c) Mechanical compressor map improvement

The mechanical compressor is the core of the installation. It is the component in charge of generating the vacuum, moving, and measuring the mass flow circulating through the MEDAS. Using the compressor as a flow meter provides a significant advantage over a hot plate mass flow sensor. It is unnecessary to install a considerable piping length before and after the sensor to develop the flow and assure a precise measurement. Therefore, an accurate and detailed compressor map is essential for the correct mass calculation (and correct operation) of the MEDAS.

In a first attempt, the map used for measuring the mass flow was provided by the Rotrex (the mechanical compressor) manufacturer, shown in Figure 3. 13. Still, it was identified that it was not accurate enough, so a test campaign to characterize the compressor and measure the map was designed.

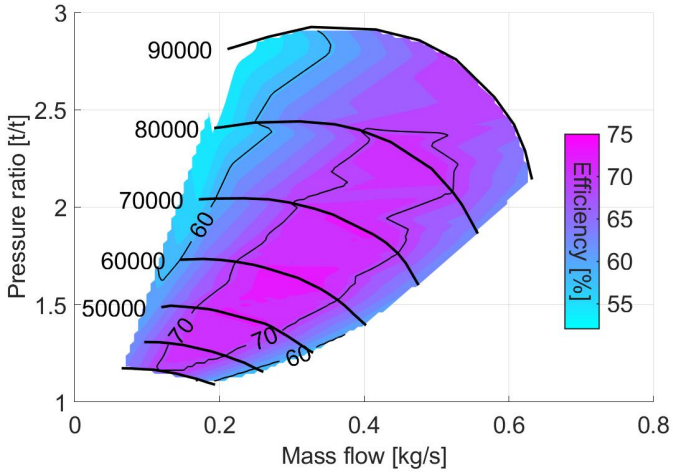

Figure 3. 13. Mechanical compressor map provided by the manufacturer

The MEDAS is essentially a flow test rig so that the compressor performance can be measured without any extra work or changes in the layout. Concerning the experimental campaign defined, the compressor performance is measured every 10% of the maximum speed in steady-state operation. Then, the WG valve was used for every speed to move the compressor operation point from choke to surge, measuring ten times every iso-speed. The results of the testing campaign are shown in Figure 3. 14, which, compared to the manufacturer-provided data (Figure 3. 13), is different in both topography of the iso-speed lines and maximum pressure ratio and mass flow values.

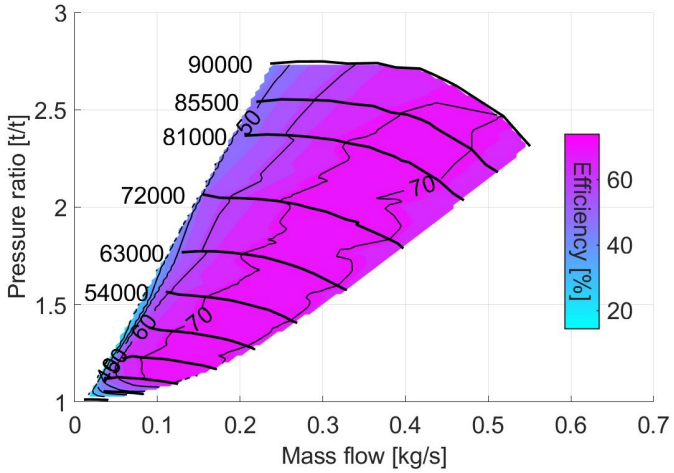

Figure 3. 14. Mechanical compressor first experimental map

However, as the MEDAS used for the compressor characterization tests is the first prototype ever built, the complete choke area of the compressor map could not be measured. This is caused by the high pressure losses present in this equipment due to the not optimized pipe distribution and size. The main consequence of not measuring the choke is that the iso-speed lines that the MEDAS will use to estimate the mass flow in the choke area will be completely vertical. This means that the mass flow will be identified as constant for a given iso-speed in all the choke area and equal to the highest mass flow measured.

One of the main points that should be considered is that the mechanical compressor used in the MEDAS is not working in the operating conditions in which a typical compressor is designed, pushing against a pressurized volume. Instead, it generates a vacuum at its inlet, making the compressor work with a low to medium compression ratio and high corrected mass flow, following Equation 3. 1 and Equation 3. 2. This means that the compressor works mainly in or near the choke zone, so this part of the map is essential for this application.

Therefore, as it was not possible to measure the compressor previously in this area due to the pressure losses present in the installation, the map characterization was used as a base for a compressor map extrapolation algorithm, included in the 1D virtual engine modeling software VEMOD, to predict the choke area of this compressor. In Figure 3. 15, the result of the extrapolation is presented along the experimental map obtained previously (Figure 3. 14), which show a very optimistic estimation of the topology of the iso-speed lines with a slight slope in the choke area. Meaning that if the results of VEMOD are trusted, the MEDAS can reach a higher maximum mass flow and reduce the energy consumption since the compressor speed needed is lower to achieve the setpoint demanded.

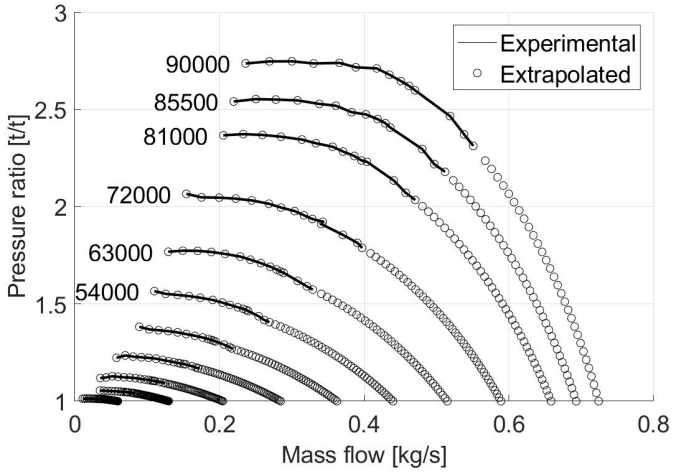

Figure 3. 15. Choke area extrapolation

Thus, another testing feature is designed to obtain an accurate compressor map focused on the choke flow to check if the VEMOD prediction is correct. To fully measure choke points (compression ratio close to 1), it was necessary to disconnect some piping of the MEDAS prototype (Figure 3. 16A) to reduce the pressure losses before and after the compressor. The results obtained confirm that the estimation done by the extrapolation software was accurate. The complete experimental map and the choke prediction obtained through VEMOD are shown in Figure 3. 16B, which can be used as a validating result of the use of VEMOD to get accurate compressor maps from a few points of experimental data.

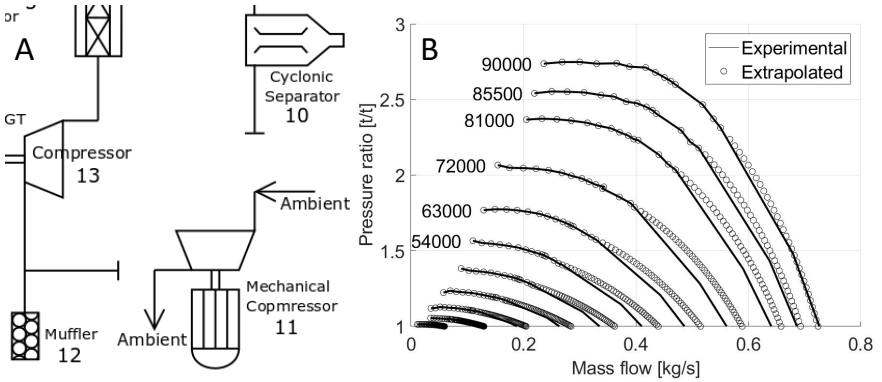

Figure 3. 16. Validation of VEMOD prediction: (A) MEDAS layout modification; (B) Prediction vs. Experimental measurement

In conclusion, the improvement of the compressor map provided a much closer measured mass flow value to the actual mass flow passing through the MEDAS, which allowed to increase the maximum mass flow that the MEDAS can provide to the engine and reduce the energy consumption for a given operative point of the installation.

It should be noted that the air mass flow is not increasing, as the compressor at a given speed and compression ratio provides the same mass flow. Instead, the improved compressor map reduces the required compressor speed (e-charger) since the MEDAS identifies a higher mass flow. Therefore, it reduces the initially required e-charger speed since the measured mass flow is better fitted to the real one without the previously detected excess.

d) Minimum mass flow control

Another efficient way to reduce the energy consumption of the MEDAS is to adjust the amount of conditioned air to the demand of the engine connected. The amount of conditioned air for testing a 1.5 liters engine should not be the same as a 3 liters engine, as the intake air required is much lower. This is addressed by implementing a new minimum mass flow for the MEDAS.

Previously, the minimum mass flow that could be demanded was fixed at 0.235 kg/s, defined for a safe operation at a maximum altitude of 5000 meters above sea level (avoiding surge in the mechanical compressor -similar to an e-charger-). The mass flow operative range of MEDAS depends heavily on the performance map of the mechanical compressor since this is the element that generates the vacuum and moves the air through the installation. Figure 3. 17 shows how the minimum mass flow limit of 0.235 kg/s reduces the operative map of the compressor in terms of corrected mass flow and thus of the MEDAS. This implies that when a small light-duty engine (around 0.08 kg/s of maximum fresh air consumption) is connected to the MEDAS, most of the mass flow conditioned is bypassed, wasting the energy used to achieve the setpoints demanded.

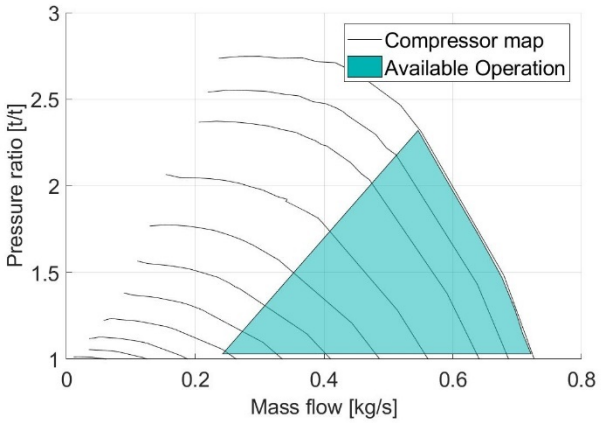

Figure 3. 17. Mechanical compressor performance map with a fixed minimum mass flow

The solution proposed for this improvement is to define a variable minimum limit for the mass flow depending on the pressure ratio of the compressor to calculate the minimum mass flow with which the MEDAS can work at every instant. This minimum mass flow limit is necessary since it is impossible to use all the compressor map mainly for two reasons. Firstly, when the operative point of the compressor approaches too much surge limit, the flow is not stable, which is not acceptable for an actuator of the MEDAS. And secondly, near surge, the slope of the iso-speed lines tends to zero, which significantly reduces the resolution of the mass flow estimation through the pressure ratio and mechanical compressor speed.

Therefore, considering these two limitations for the minimum mass flow, the definition of the mass flow curve was carried out experimentally to maximize the compressor's available working area to its acceptable limits. The mechanical compressor is tested at several speeds while installed in the MEDAS, increasing the pressure ratio for a given speed until the non-stable area near surge is

reached. The results of the experimental campaign are shown in Figure 3. 18, in which the experimental curve of minimum mass flow (red curve) is plotted on the compressor map. The polynomial equation that fits the experimental points defines the minimum mass flow curve. However, it includes a safety margin to reach a minimum gradient in the speed lines, ensuring that the MEDAS will always work in stable flow conditions (blue curve). In Equation 3. 5, the polynomial equation used to calculate the minimum actual mass flow during MEDAS operation is shown, being CR the compression ratio of the mechanical compressor.

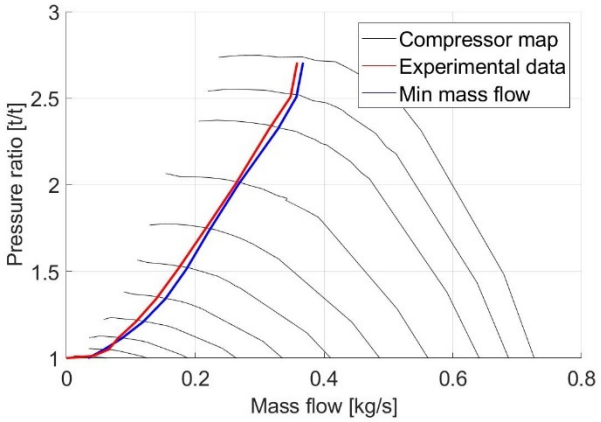

Figure 3. 18. MEDAS minimum mass flow characterization results

$$\dot{m}_{MEDAS} = \frac{-2.5411 \cdot CR^4 + 19.467 \cdot CR^3 - 54.941 \cdot CR^2 + 70.576 \cdot CR - 30.3}{\sqrt{T_{C,in}}/p_{C,in}}$$

Equation 3. 5

Then, with this improvement, the mass flow map of the MEDAS widens, as shown in Figure 3. 19, allowing to reduce the amount of conditionate air flow wasted when testing smaller engines and thus improving the energy consumption efficiency of the MEDAS up to an 18.5%.

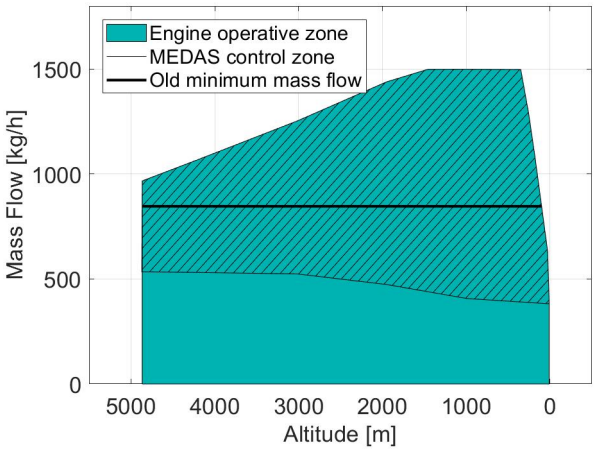

Figure 3. 19. MEDAS minimum mass flow performance improvement

3.2.2. Components safety strategies

Following, one crucial thing that was overlooked during the initial development of the MEDAS was to make sure that the supplies of the different components, i.e., oil for the turbocharger or cooling water, were enough and not lacking in any way while the installation was operating, or that the electric box was working at an adequate temperature. Therefore, new sensors and monitoring strategies are defined to ensure that all the components work in optimal conditions.

3.2.2.1 Turbocharger oil

In the case of the turbocharger oil, the safety sensor installed is an oil level sensor consisting of a floating contact located below visual access installed in the canister. Also, a pressure sensor was located at the oil pump outlet. The pressure sensor makes sure that there is enough oil flowing through the turbocharger (oil pressure must be above 1.3 barA) and that there is no leakage through the turbocharger sealing due to a too high oil pressure (oil pressure must be below 5.5 barA).

Additionally, to avoid oil leaks to the primary air circuit through the turbocharger sealings during operation, it is necessary to establish a constant blowby to the oil canister through the oil sealings of the turbocharger. This is achieved by reducing the pressure in the oil deposit below the pressure in the backplate of the compressor and turbine impellers. This reference pressure can be estimated as the average between compressor and turbine inlet and outlet [3]. Therefore, it can be assumed that if Equation 3. 6 and Equation 3. 7 are fulfilled, there will not be any leak of oil through the turbocharger sealings to the primary air circuit.

$$p_{oil,canister} < \frac{p_{C,in} + p_{C,out}}{2}$$

Equation 3. 6

$$p_{oil,canister} < \frac{p_{T,in} + p_{T,out}}{2}$$

Equation 3. 7

To achieve the necessary vacuum, the turbocharger oil canister should be connected to the pipe section with the lowest pressure in the MEDAS system, located at the mechanical compressor inlet (between 11 and 12 of Figure 3. 3). However, as this connection can drag oil mist or droplets, the connection is moved before the cyclonic separator (between 9 and 11 of Figure 3. 3) to remove the oil droplets and as much oil mist as possible from the air to avoid damaging the compressor blades and dirtying the exhaust system of the test cell.

Moreover, when a boosting unit is connected upstream of the MEDAS, an extra element is installed to help the vacuum generation in the turbocharger oil canister. This element is a venturi vacuum pump, which generates a vacuum in the canister using the pressurized air present at the MEDAS inlet. It creates a high-speed airstream and drags air from the canister due to the lower local pressure generated, thus generating a vacuum in the oil canister [4].

A schematic of both systems, along with the rest of the MEDAS 2nd Generation components explained previously, is shown in Figure 3. 20.

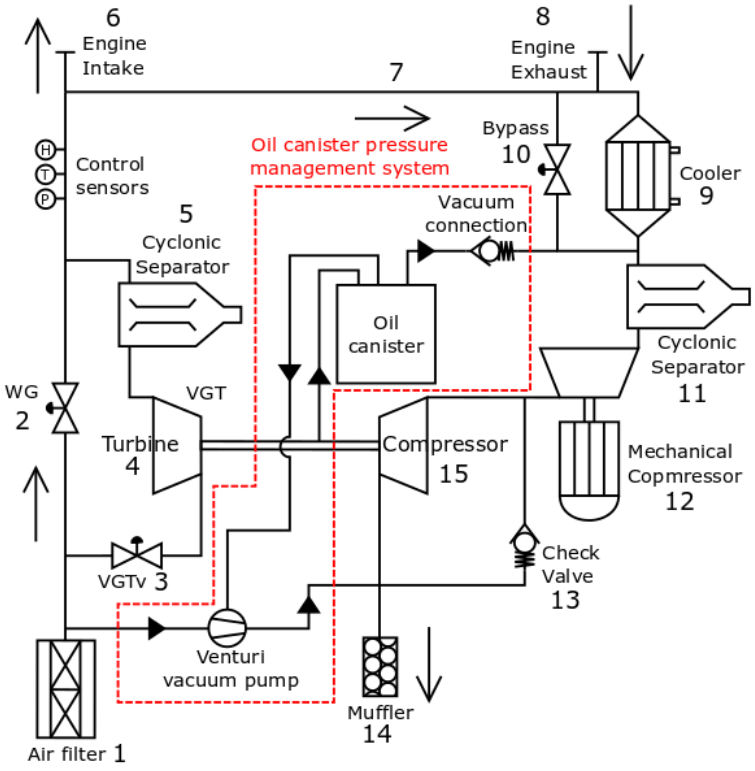

Figure 3. 20. MEDAS 2nd Generation layout, including the pressure management of the turbocharger oil canister

3.2.2.2 Pneumatic air and cooling water

The pneumatic air supply monitoring is carried out by a pressure switch calibrated at 5 barA, which sends a signal when there is not enough pneumatic air supply to actuate the controlled valves of the system (2, 3, and 10 of Figure 3. 3). Concerning the cooling water, the water flow is monitored through a mass flow meter in the intake line of the cooling system of MEDAS, which sends a signal when the cooling water flow drops too much. The minimum accepted mass flow for the cooling water depends on the MEDAS model (Table 3. 2) since it depends on the size and number of components.

Table 3. 2. Cooling water volumetric flow specifications

MEDAS model	Cooling water required [m^3/h]
5009, 5012 and 5015	5
5031 (MD or Medium Duty)	10
5050 (HD or Heavy Duty)	15

3.2.2.3 Electric box temperature

The electric box requires that the temperature inside is controlled to keep it between the specified working temperature range of the electrical components to avoid damage. Also, when the ambient temperature increases, the efficiency of the power electronics is reduced, which can be prevented with this control. Hence, a simple PID control of this temperature has been implemented utilizing a thermocouple which measures the air temperature near the hottest point of the electrical panel and the actuation of several fans. This control actuates increasing or decreasing the electric box ventilation depending on the need to control the temperature around 35ºC.

3.2.2.4 Mechanical compressor oil health

Lastly, the oil of the mechanical compressor must be monitored closely since its degradation can lead to damage and early failures of the mechanical components such as the gearbox or the compressor impeller. An oil health sensor has been installed in the original oil circuit (Figure 3. 21).

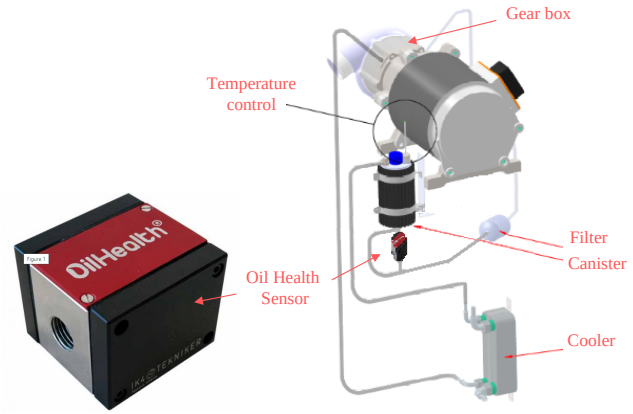

Figure 3. 21. Mechanical compressor oil circuit

This sensor uses optical techniques [5] to measure the opacity of the oil, which after defining the reference of unused oil opacity and the maximum oil opacity admissible, provides a continuous measurement of the percentage of the oil degradation. These two parameters were defined considering several samples of the mechanical compressor oil obtained from different mechanical compressors working with different gases, i.e., unfiltered exhaust gases, filtered exhaust gases, and clean air.

The details of the samples used for the sensor calibration are represented in Figure 3. 22. The *y-axis* is a percentage scale of the oil degradation following the default calibration of the oil health sensor, and the *x-axis* is the working hours of the oil samples. It can be seen how the slope of degradation increases

with the particle content of the compressor working gas. This is expected as the increase in particulate matter in the working gas increases the oil contamination rate. The mechanical compressor forces blowby from the impeller to the oil circuit to avoid oil leaks.

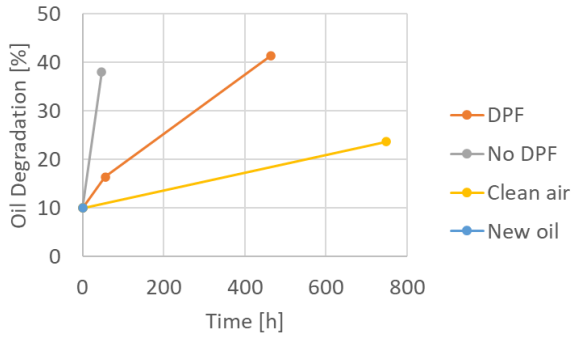

Figure 3. 22. Oil samples used for the calibration of the oil health sensor

The maximum opacity admissible adopted as 100% of oil degradation corresponds with the 'Clean air' series endpoint (yellow line of Figure 3. 22) since the unfiltered and filtered exhaust gases samples broke the compressor shaft. Therefore, a safety margin from these values is needed. Additionally, the value corresponding to new oil was defined as 22% of oil degradation, which allows the oil health sensor to be used as an oil level sensor. If the measurement of oil degradation is below 22%, then there is not enough oil in the circuit, and the sensor is measuring air.

The oil health sensor is installed in a prototype to test its response, accuracy, and measurement stability and fine-tune the oil degradation calibration. The installation of the sensor in the prototype is shown in Figure 3. 23A, following the scheme shown in Figure 3. 21, and with the oil flow marked with red arrows. Furthermore, several measurements have been performed, which results are presented in Figure 3. 23B, showing the evolution that the oil degradation follows a simple trend, almost linear. So, a simple correlation has been included in the MEDAS code to inform the user of the number of hours that the MEDAS can work before an oil change is needed. It should be noted that the perturbances shown in Figure 3. 23B are caused by the effect that the oil temperature has on the measurement accuracy of the sensor, which can make oscillate the degradation measurement +/- 5 %.

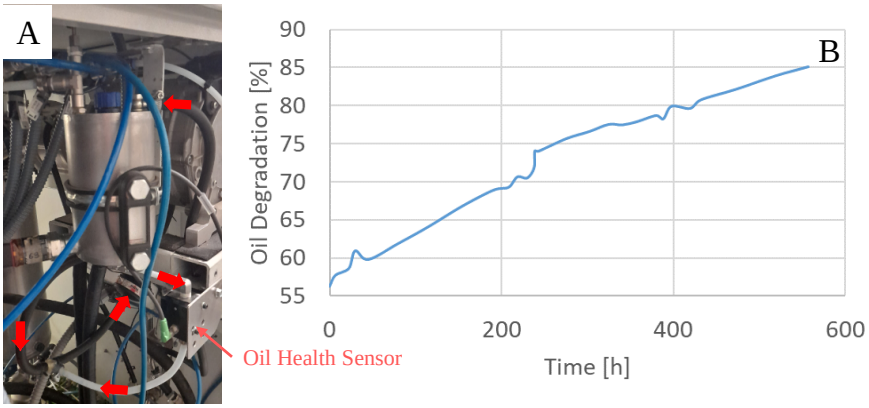

Figure 3. 23. Oil health sensor: (A) Prototype installation; (B) Experimental measurements

3.2.3. Freezing ambient enhancement

As the MEDAS has limited control of the temperature, it is possible to use it coupled with a climatic chamber. In this case, the climatic chamber sets the temperature demanded, and then the MEDAS takes air from the chamber to condition the pressure. This can be done with the MEDAS outside or inside the chamber. On the one hand, in the case of installing the MEDAS outside the chamber, there is no modification needed for the MEDAS. The only demerit is that the non-controllable altitude range or 'dead zone' of the pressure control [1] widens due to the increase in length of the engine-to-MEDAS connection and the intake pipes of the MEDAS, which are taking air from the chamber.

On the other hand, when the MEDAS is installed inside the chamber, all the components and supplies must withstand the extreme temperature present in this ambient. This is a considerable challenge for the installation, but especially for the electronics inside the electric box, the most critical components. These components have a minimum ambient temperature to avoid the formation of ice crystals in the interior that, after heating up again, melt and damage the internal circuits.

Therefore, the electric box temperature control defined in Section 3.2.2.3 must be expanded to heat the inside of the electric box if the MEDAS is installed inside the climatic chamber. This is achieved by employing electrical air heaters that work with the fans to keep the temperature at 35 ºC. Also, the electric box is insulated to minimize the heat losses to the ambient. The expanded control logic of the electric box temperature is presented in Table 3. 3, in which the activation of the four actuators is defined depending on the temperature inside the electric box.

Table 3. 3. Activation logic for the electric box temperature control actuators

	Fans (Group 1)	Fans (Group 2)	Heaters (Group 1)	Heaters (Group 2)
T_{SP} – 5ºC > Temperature	0	0	1	1
T_{SP} > Temperature > T_{SP} - 5 ºC	0	0	1	0
Temperature = T_{SP}	0	0	0	0
T_{SP} + 5 ºC > Temperature > T_{SP}	1	0	0	0
Temperature > T_{SP} + 5 ºC	1	1	0	0

Once the heating strategy of the electric is defined, a 3-day extended test is performed, in which the climatic chamber starts cooling from 30 ºC and is set to control -25 ºC with the MEDAS inside. In Figure 3. 24, the internal temperatures of the MEDAS during the test are shown. It can be seen how the electric box temperature control can keep the inside temperature (red line) above 0 ºC. The target of 35 ºC is not achieved in these conditions. Still, the temperature inside the electric box is always above 0 ºC, higher than the minimum working temperature specified for the electronic components (-25 ºC) [6].

Also, it can be seen how the rest of the temperatures recorded are below 0ºC and reach a minimum of -25 ºC, depending on the height of the measuring point with respect to the floor. The installation height of each temperature sensor has been represented qualitatively in a simple diagram in Figure 3. 24 with the base of the test cell as the reference.

It should be noted that the temperature peaks present for every signal are caused by the cyclic defrosting periods performed by the cooling system of the chamber and not caused by the MEDAS.

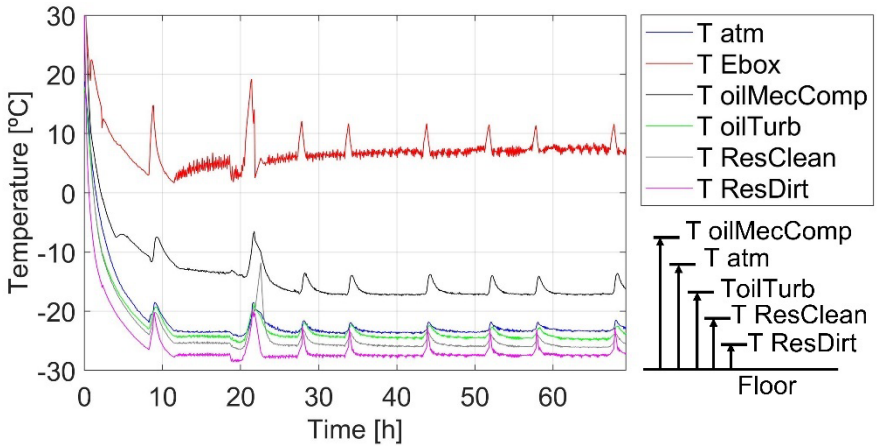

Figure 3. 24. MEDAS temperature evolution within a climatic chamber controlled at -25 ºC for three days

However, aside from controlling the electric box temperature (T Ebox), the MEDAS supplies also suffer from freezing temperatures. To avoid freezing the water inside the system, the cooling water must be mixed with the correct percentage of glycol depending on the minimum temperature expected inside the chamber. Also, the pneumatic air must be dried with an adsorption system to avoid freezing the little moisture that the pneumatic air has. In addition, the condensates extraction must be modified since the condensates (mainly water with some particulate matter) can freeze inside the installation. It is necessary to include electrical heaters around the condensate deposits to keep the water liquid and ready to extract or even re-evaporate it.

The oil circuits also suffer from the freezing temperature inside the climatic chamber. The low temperatures significantly increase the oil's viscosity, which causes overcurrent in the electric motors used to move the turbocharger oil pump and the mechanical compressor. Therefore, it is necessary for a progressive start-up of these two components to slowly heat the oil to a correct working temperature and avoid increasing the current consumption over the limit.

In the case of the turbocharger oil pump, it does not have speed control. Hence, it is impossible to perform a slow start-up to heat the oil. This forces the disabling of the MEDAS temperature control when the turbocharger oil temperature is too cold (below 0 ºC). The VGTv valve (3 of Figure 3. 3) is closed to avoid the turbocharger spinning without oil. In this case, the temperature at the engine intake must be entirely controlled by the climatic chamber.

Contrarily, the electric motor of the mechanical compressor has a frequency driver that allows the needed progressive start-up. Therefore, a heat-up strategy is designed for the mechanical compressor oil and presented in Figure 3. 25. The *y-axis* is the electric motor speed demanded, and the *x-axis* is the oil temperature. The different compressor speeds were defined experimentally, trying to speed the motor as much as possible in each temperature step to heat up the oil faster, but without overcoming the motor’s maximum torque that stresses the component and leads to an aggressive stop. Also, an example of the warm-up procedure is shown in Figure 3. 26, in which the MEDAS is started up after spending the night inside a climatic chamber set up at -20 ºC.

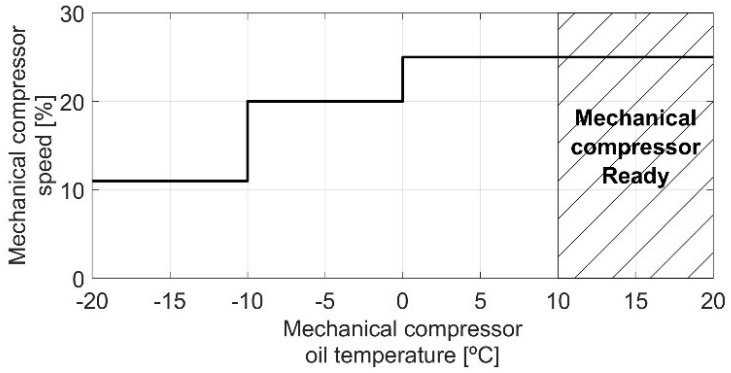

Figure 3. 25. Mechanical compressor warm-up process

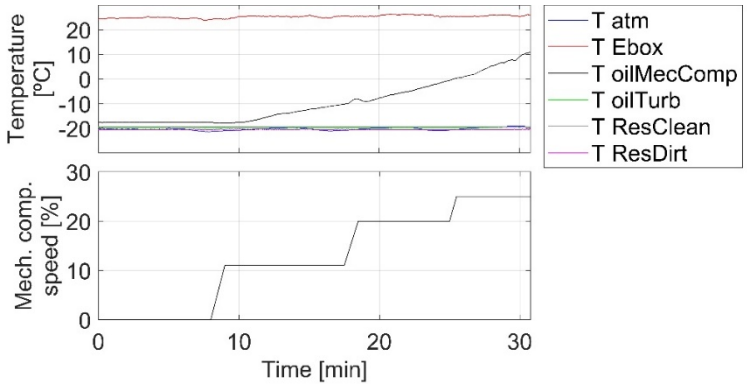

Figure 3. 26. Mechanical compressor warm-up test with ambient at -20 ºC

3.2.4. Parallel connection configuration

Another feature that can be improved is the maximum mass flow that can conditionate the MEDAS, which is the parameter that limits the engine size that can be connected to it. The increase in the maximum mass flow of MEDAS can be achieved in two ways: increasing the MEDAS size or increasing the number of MEDAS connected to the engine. The first consists of developing a new MEDAS of bigger size, but this option requires time and tremendous effort. It should be noted that this way of mass flow increase will be explored in the following sections of this chapter. The second option would be to connect two or more MEDAS in parallel, multiplying the maximum mass flow without too much effort.

The viability of this second option will be discussed in this section since connecting two MEDAS to the same engine can lead to unexpected problems, i.e., control instabilities or mass flow imbalance between MEDAS. The layout of the parallel connection of two MEDAS is depicted in Figure 3. 27. This figure

shows how two standard MEDAS, but with the bypass duct closed, are connected to an external bypass, from which the engine takes the needed intake air and returns the exhaust gases.

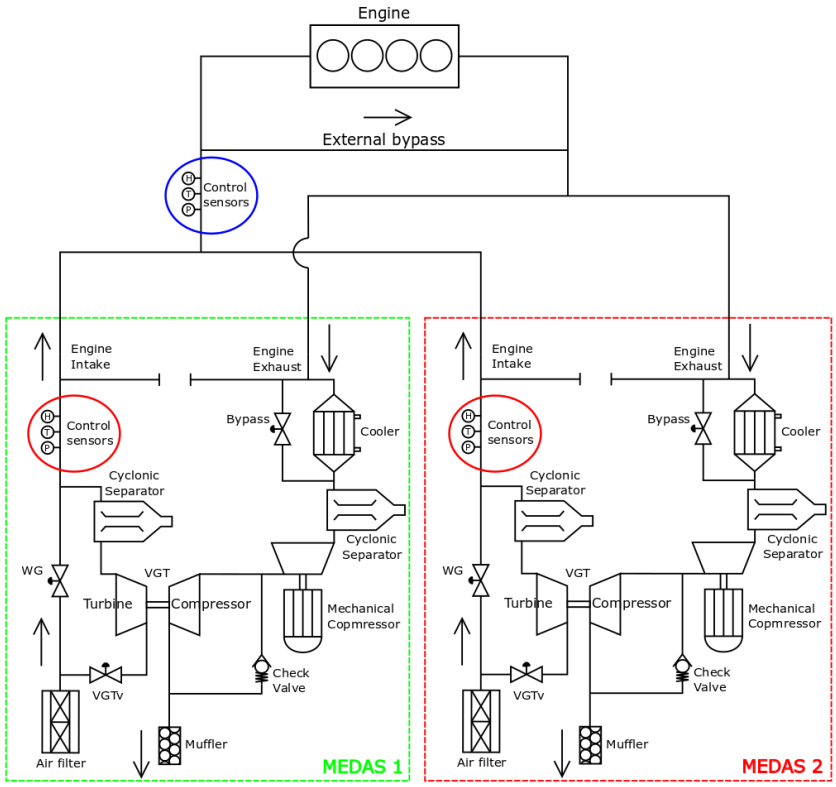

Figure 3. 27. Diagram of 2 MEDAS connected in parallel to an engine

Concerning the pressure and temperature control sensors, there are two options: they can be kept in the original location, each MEDAS controlling with their sensors without communicating between them (red circles), or they can be located at the new external bypass and be shared by both MEDAS (blue circle). These two cases have been tested, and the results are plotted in Figure 3. 28. Nevertheless, it is necessary to connect all the MEDAS to a setpoint manager to send the demanded setpoints and keep all the MEDAS controlling the same pressure, temperature, and mass flow in both cases. This manager can be programmed in the test bench control software or can be an external device without any difference between both options.

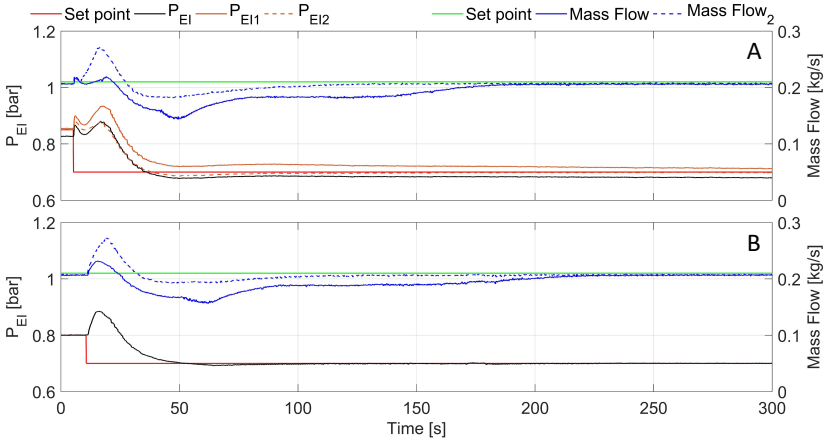

Figure 3. 28. Two MEDAS connected in parallel steady-state point stabilization: (A) Independent sensors; (B) Common sensors

If the focus is put on Figure 3. 28A, when each MEDAS works with its sensors, there are no instabilities in the control or other abnormal behavior in the MEDAS. Still, the pressure at the engine intake connection of the external bypass (black line) is lower than the setpoint (red line). This is caused by the increase in piping length from the control point to the engine intake, which introduces a pressure drop dependent on the mass flow demanded. Moreover, while the mass flow through the mechanical compressor (blue lines) in both MEDAS would be equal, the mass flow through the intake line of the MEDAS (mass flow through the air filter) will be different.

On the one hand, the exhaust line mass flow is imposed by the mechanical compressors controlling with the same setpoint. However, it will be achieved with different compressor speeds due to the engine exhaust-to-MEDAS connection differences. On the other hand, the differences between the MEDAS-to-external bypass connection of both MEDAS force differences in mass flow through the intake line for each one to achieve the same pressure in the engine intake connection of the external bypass.

Contrarily, when the control sensors are shared and located on the external bypass (Figure 3. 28B), the pressure at the engine intake connection is the one demanded by the user. In this case, the mass flow distribution is similarly affected by the asymmetries of the external bypass connection to both units of MEDAS. However, with the control sensors shared, the stabilization time of a steady-state point decreases without affecting the stabilization time for the mass flow.

Therefore, considering the advantages described in this section, the solution adopted is using common sensors between both MEDAS for the control since it has faster steady-state stabilization and higher accuracy in the pressure control.

At the same time, it does not introduce any disadvantage with respect to the independent control sensors.

Once the solution has been defined, both MEDAS are tested in steady-state and dynamic operation to obtain a performance map of two MEDAS connected in parallel and the capabilities of following pressure and temperature profile. In Figure 3. 29, the results of the performance tests for a stand-alone MEDAS (Figure 3. 29A) and two MEDAS working in parallel (Figure 3. 29B) are shown, respectively. When comparing both, the mass flow doubles in all the altitude range when connecting two MEDAS in parallel, with the added advantage of not increasing the size of the 'dead zone' of the installation, defined in reference [1].

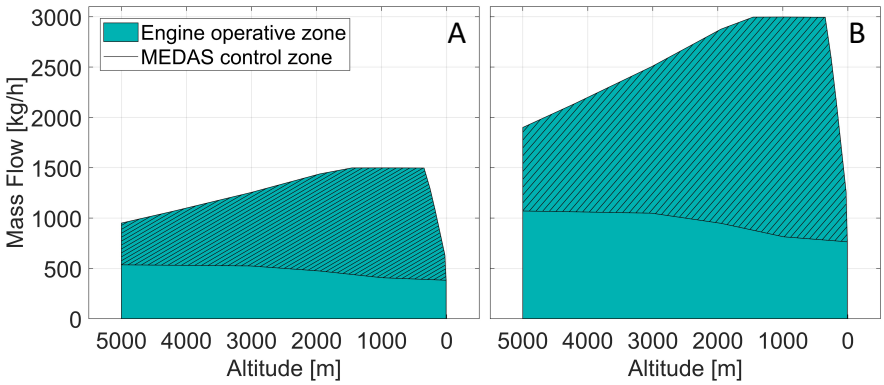

Figure 3. 29. MEDAS mass flow performance: (A) MEDAS stand-alone; (B) 2 MEDAS connected in parallel

Concerning the dynamic profile tests, Figure 3. 30 shows the result of one of the tests carried out. In this figure, the time is located on the *x-axis* with the altitude and temperature instantaneous measurement and setpoint in the top graphs. The percentual and absolute errors are represented in the bottom graphs. It can be seen how the altitude is kept between +/- 50 meters of the setpoint and the temperature between +/- 1 ºC of the setpoint, respectively 1% and 2% of the full control scale during the test. These results are well within the MEDAS specifications and entirely satisfactory, despite the aggressive profiles reproduced (Table 3. 4), which validates the dynamic capability of the MEDAS connected in parallel.

Table 3. 4. Equivalent road test reproduced with 2 MEDAS in parallel

Vehicle speed [km/h]	100
Road slope [%]	11.6

It should be noted that the testing and development of this option to increase mass flow for the MEDAS was tested with only two MEDAS connected in parallel. However, the result is valid and should work the same if more MEDAS are added to the net to increase the mass flow further.

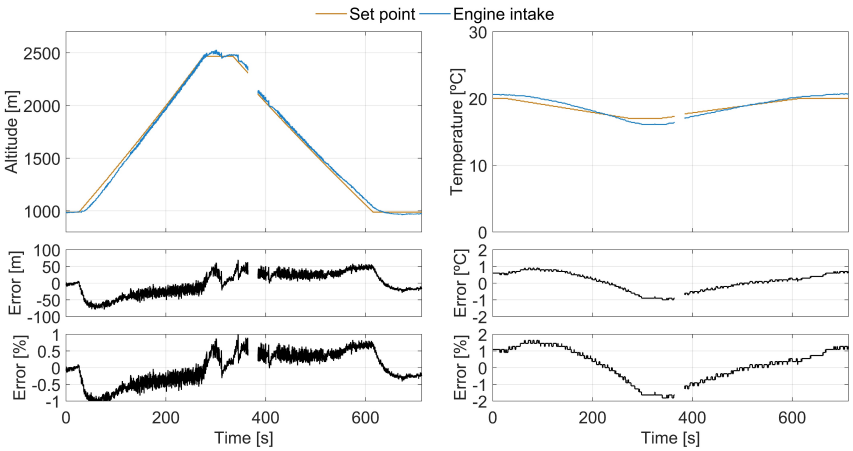

Figure 3. 30. Dynamic altitude and temperature profile performance for two MEDAS connected in parallel

3.3. MEDAS family development by deductive procedures

As discussed previously, one of the options to increase the mass flow conditioned by the MEDAS is to develop a new bigger size model, which is the objective of the current section. Following deductive procedures, the development of a new model of MEDAS designed for heavy-duty (MEDAS HD) and medium-duty (MEDAS MD) ICE will be explained. This section starts with the definition of a layout of the components and follows with the selection or design of those components. Then, programming a 1D model to study the viability of the previously designed layout and elements, and finally, the development of a functional prototype, validating the 1D model and obtaining the final performance of the equipment.

3.3.1. Layout design

The layout design is based on the one developed to improve the MEDAS to the 2nd generation (Figure 3. 3). Still, with one difference, instead of using the cooled air from the turbine to control the temperature at the engine intake connection, it is used to reduce the temperature of the dilution flow to help the exhaust coolers to cool down the exhaust gases coming from the engine. This modification reduces the power demand in the exhaust coolers but removes the MEDAS temperature control that must be done by connecting a temperature conditioning unit upstream. However, this configuration introduces the

advantage of increasing the exhaust cooling power installed in the MEDAS without increasing its size.

The two new MEDAS models to develop, the MEDAS MD and HD, share the same layout. Both need a power increase in the exhaust coolers to cool down the exhaust gases and keep the temperature at the mechanical compressor inlet. In Figure 3. 31A, the layout for the MEDAS HD is shown, being the highlighted area the only difference from the MEDAS MD. It is the number of mechanical compressors needed in parallel to achieve the maximum mass flow target defined for each one. Additionally, in Figure 3. 31B, an axonometric view of the 3D model of the MEDAS HD is shown, with the elements depicted in Figure 3. 31A identified.

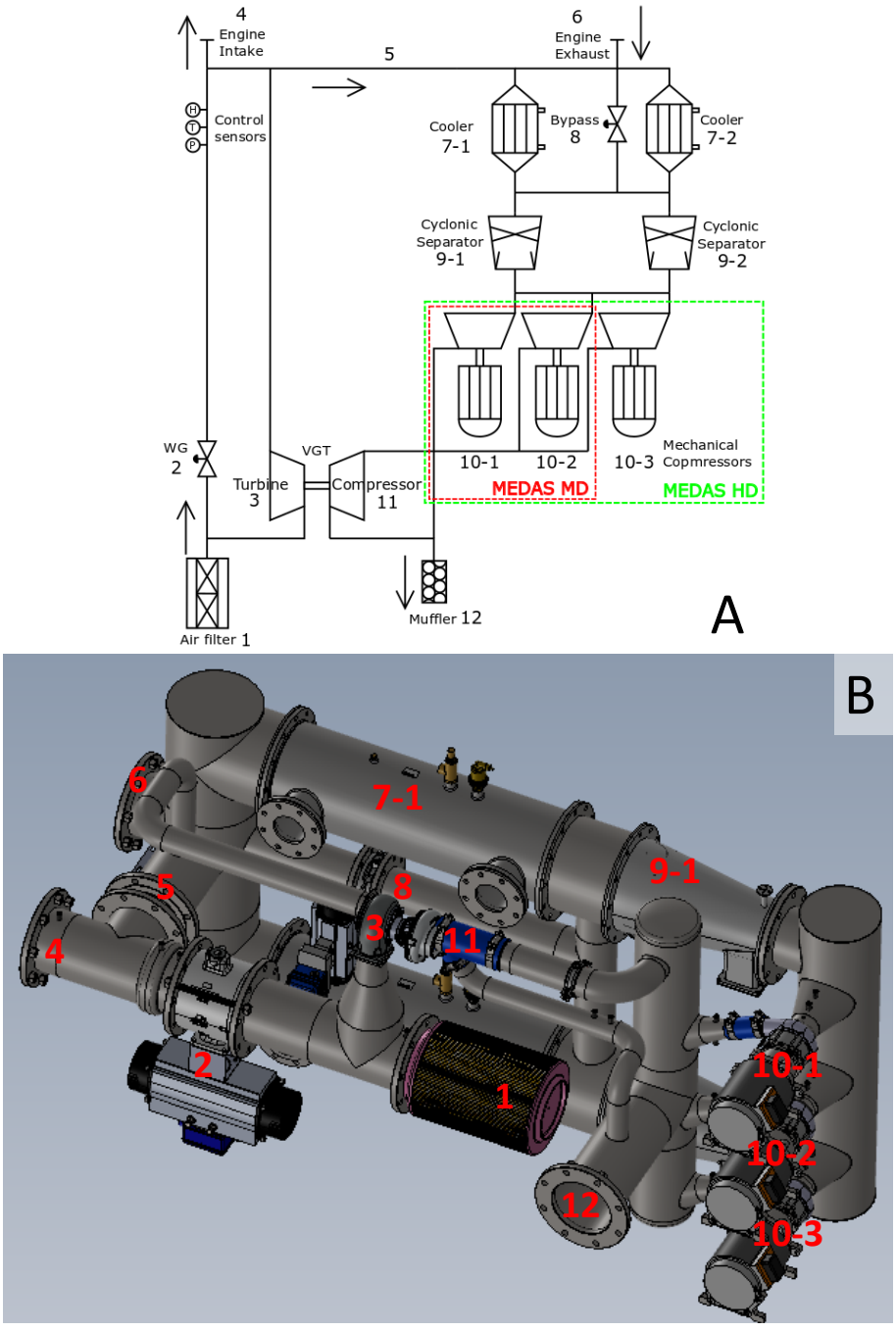

Figure 3. 31. MEDAS HD and MD layout: (A) Layout outline; (B) Axonometric view of the 3D model

In these two MEDAS, the air enters through the air filter (1) and then has two options, to go through the WG valve (2) or go through the variable geometry turbine (VGT) (3) to be cooled down. These two components, (2) and (3), control the pressure at the engine intake connection (4) working simultaneously. The simultaneous work of both controllers allows a more accurate pressure control since the WG valve (2) works as a rougher control, and the VGT vanes (3) acts as the refined control.

Then, in (4), the engine takes as much air as it needs, and the rest goes to the dilution pipe (5), which assures that the intake and exhaust of the engine work at the same pressure as would happen in a road test. It is in the middle of this dilution pipe (5) where the air that passes through (3) is injected, lowering the temperature of the dilution flow, which then mixes with the exhaust gases that come from the engine exhaust connection (6).

Afterward, the dilution and exhaust gases mix and pass through the exhaust coolers (7-1 and 7-2), which cool down the airflow to avoid damaging the mechanical compressors. The circuit is divided into two parallel branches to keep both aspects: the compactness of the MEDAS and the increased cooling power needed when expanding the mass flow control range. Parallel to the coolers, a butterfly valve (8) controls the amount of air that bypasses the coolers to keep 50 ºC at the inlet of the mechanical compressors. This reduces the number of condensates generated when cooling exhaust gases. The condensates are then separated in the cyclonic separators (9-1 and 9-2) to avoid damaging the compressors with the water droplets.

Once the water droplets are removed, the air goes to mechanical compressors (10-1, 10-2, and 10-3) connected in parallel to achieve the maximum mass flow demanded. These compressors are actuated simultaneously and control the mass flow passing through the MEDAS. Lastly, most of the flow goes directly to the MEDAS exhaust (12), while a small part goes through the turbo compressor (11) to dissipate the power generated in the turbine and then to (12).

3.3.2. Component selection

Depending on the maximum mass flow required for the installation, the size or number of components for a given task can vary. Therefore, a selection of the element which best fits the demands is required.

3.3.2.1 WG valve

The WG valve is the leading pressure controller and is where most of the conditioned mass flow must pass. The specifications for this valve are very demanding since it is one of the most important components found in MEDAS:

- Low pressure drop when completely open. This is the main factor in the size of the area called the ‘dead zone’ of the pressure control in the

MEDAS map. A maximum pressure below the ambient pressure over which the MEDAS cannot operate due to the pressure losses inside the ducts and in this valve [1].

- High resolution for the actuator movement. One of the main contributors to the inaccuracies of the pressure control is the resolution of the WG valve actuator, meaning how small the actuator's minimum movement is. Since it moves between discreet actuator positions, there are occasions in which it cannot achieve the demanded pressure. It keeps oscillating around the setpoint due to the minimum movement of the valve being bigger than needed.
  An example of this problem can be seen in Figure 3. 32, in which the set point of the pressure is represented together with the measured pressure in the top graph, and the actuation of the WG valve demanded by the control is shown in the lower chart. If the focus is put around second 100, it is shown how the pressure is above the setpoint before second 100 while the valve is closing. There is no change in the pressure despite the valve movement until second 100, in which the pressure decreases too much and ends up below the setpoint. This same phenomenon is repeated several times along the timeframe shown.
  This shows clearly how the minimum movement of this valve has a more significant effect than needed to adjust the pressure, which leads to thinking that if the valve could perform more minor actions, the control would be better. However, even with this identified limitation, the pressure control can maintain the error with the setpoint in the expected range (+/- 10 mbar) during the test shown in Figure 3. 32.

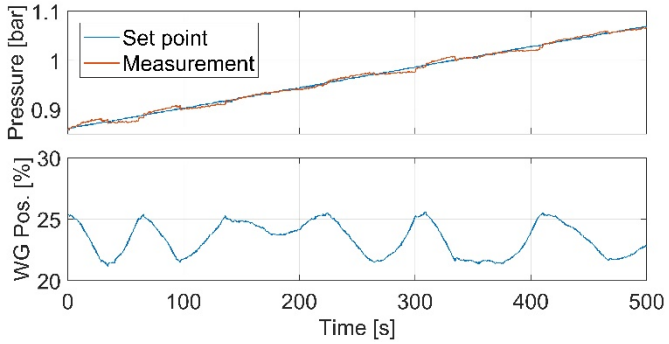

Figure 3. 32. Movement resolution deficiency in the WG valve actuator

- High yield valve with a wide range of mass flow. As the mass flow is defined as a range and not as a maximum, the valve must accurately control the pressure in the range of mass flow defined.

Considering all these required aspects, the type of valve selected is a ball sector pneumatically controlled valve instead of the sliding gate valve used in smaller

models of MEDAS. This kind of valve allows a much wider section when fully open, like the butterfly valves, but has a better movement accuracy and resolution and better control of the pressure at low mass flow.

Following, the valve size for the two new MEDAS are selected considering the percentage of opening needed to achieve the maximum pressure drop demanded, i.e., 473 mbar when simulating maximum altitude (5000 meters above sea level or 0.54 barA) assuming the installation of the equipment at sea level (1.013 barA); and minimizing the pressure drop at maximum flow. In Figure 3. 33, this study is presented, in which two sizes of valves are shown for each new model of MEDAS. In the case of the MEDAS HD, the two sizes proposed are presented in Figure 3. 33A and B, and in Figure 3. 33C and D are the ones offered for the MEDAS MD. In these figures, the *x-axis* represents the pressure drop in the valve on a logarithmic scale, and the *y-axis* the mass flow through it. The different colored lines represent the opening percentage of the valve and the colored area the performance range of the MEDAS.

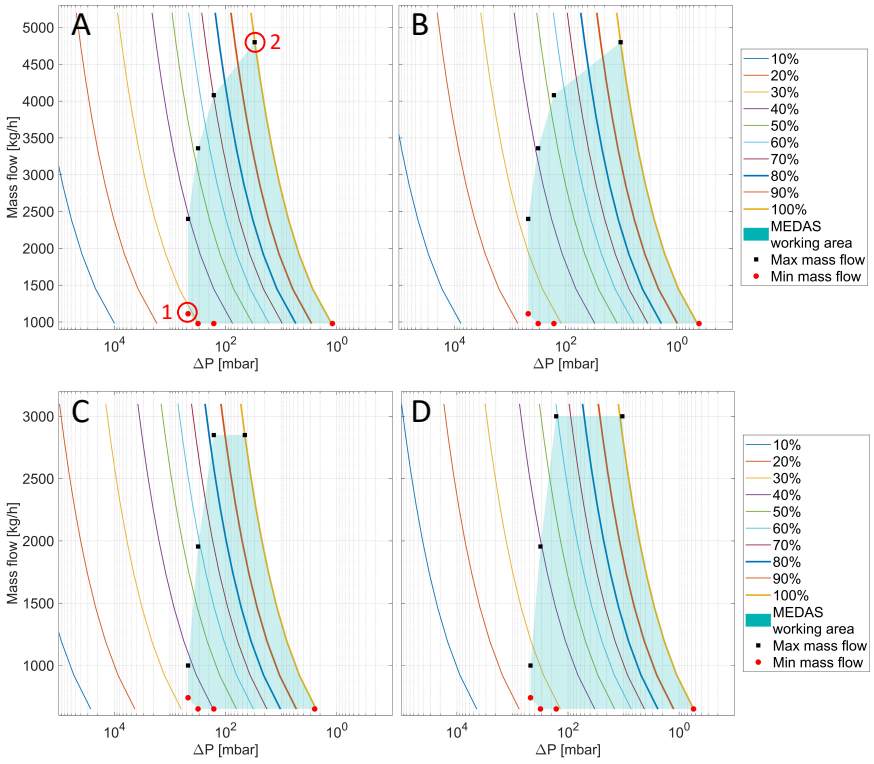

Figure 3. 33. WG valve size selection: (A) DN150 MEDAS HD; (B) DN200 MEDAS HD; (C) DN100 MEDAS MD; (D) DN150 MEDAS MD

Focusing on the MEDAS HD case, it can be seen how the smaller valve (Figure 3. 33A) has a narrower working range since the maximum altitude specified (point 1 of Figure 3. 33A) is achieved with an opening of 30% or higher. Also, the pressure drop at maximum mass flow (2 of Figure 3. 33A) is much higher than with the bigger valve (Figure 3. 33B), reaching 30 mbar instead of 9 mbar. The same happens in the case of the MEDAS MD shown in Figure 3. 33C and D, in which the smaller valve has a similarly reduced working range and a higher pressure drop at maximum mass flow. It should be noted that smaller and bigger valves are not presented for any option but were considered. However, they were discarded due to the increased pressure drop or MEDAS size that the increased piping diameter causes. Finally, considering the characteristics of the different sizes for the application presented, the selected valve size for both models is compiled in Table 3. 5.

Table 3. 5. WG valve size

MEDAS model	WG size
MD (Medium Duty)	DN150
HD (Heavy Duty)	DN200

3.3.2.2 Turbocharger

In the case of the turbocharger installed, as the objective has changed from a cooling element to a pressure control valve in parallel with the WG valve, it is not necessary to increase the effective section of this branch. Since the need to mix cold flow with the hot flow to achieve a given temperature is removed, there is no need to increase the turbocharger size or install more units in parallel. Therefore, the same turbocharger unit as the previous MEDAS has been used for these two new models. It is a component fully validated from which every important aspect is known, i.e., requirements for the oil circuit, expected performance, and durability.

3.3.2.3 Exhaust coolers bypass valve

The main priority for the exhaust cooler bypass valve is a low pressure drop when fully open and the capability to withstand high temperatures. It must be able to bypass engine exhaust gases at as high as 550 ºC from the two shell and tubes exhaust coolers with an expected maximum pressure drop of 30 mbar. Moreover, in this case, the accuracy of the actuator is not as important as with the WG valve. Therefore, the solution selected is a butterfly valve, which is more economical than the sector ball valve. To choose the valve size, the intake conditions must be considered. In this section of the MEDAS, the pressure and temperature can vary significantly depending on the user's demands and the engine operating point.

The study has been carried out for the MEDAS HD conditions at three different cooler inlet temperatures and pressures: 150, 350, and 550 ºC, and 1, 0.7, and

0.55 barA, while spanning a wide movement range of the valve from 100% to 10%. Also, to define the mass flow expected to pass through the bypass in each case, a simple energy balance in the mix of the bypass flow with the cooling flow was done following Equation 3. 8. For this calculation some hypotheses are considered: $T_{C,in} = 50\,°C$, $T_{out,cool}$ is the same as the cooling water temperature (7 ºC), and $\dot{m}_{MEDAS}$ varies along the mass flow range of the MEDAS HD, from 500 to 5200 kg/h.

$$\dot{m}_{Bypass} = \dot{m}_{MEDAS} \cdot \frac{T_{C,in} - T_{out,cool}}{T_{in,cool} - T_{out,cool}}$$

Equation 3. 8

It should be noted that for the MEDAS MD, the same component as in the MEDAS HD will be used, as the differences in the exhaust line between both are minimal, and thus the results obtained for the HD can be assumed correct for the MD.

In Figure 3. 34, the result of the pressure drop for two valve sizes is shown. In these graphs, the *x-axis* represents the mass flow through the bypass, and the *y-axis* is the pressure drop in the valve described on a logarithmic scale. The colors and symbols represent the different inlet temperatures and pressures, respectively. Moreover, the minimum pressure drop expected in the coolers for the three inlet pressures and an inlet temperature of 150 ºC has been included as three colored horizontal lines. This figure shows that the smaller valve (Figure 3. 34A) reaches pressure drops higher than the ones expected in the exhaust coolers, which does not assure the existence of enough bypass when the engine connected to the MEDAS is operating at points of low load.

On the contrary, the pressure drop calculated for the bigger valve (Figure 3. 34B) is lower than the minimum expected for the exhaust coolers in all the inlet pressures analyzed. Therefore, installing the DN125 butterfly valve is the solution chosen for this application.

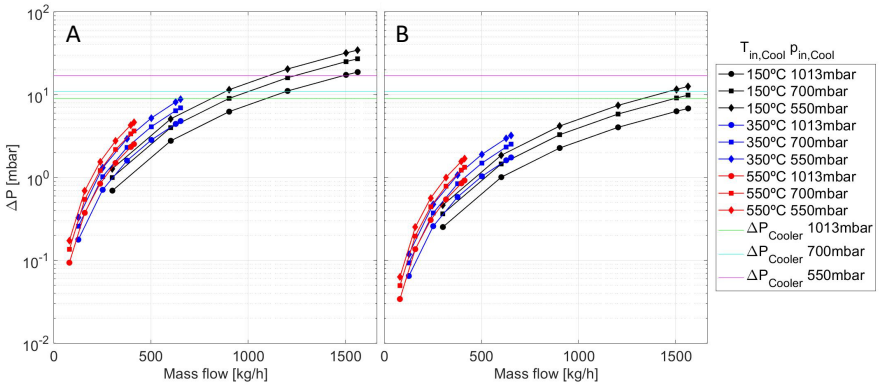

Figure 3. 34. Exhaust cooler bypass valve selection: (A) DN100; (B) DN125

3.3.2.4 Mechanical compressor

For the mechanical compressor, the solutions proposed were two. On the one hand, use the compressor already used in previous models, known as Compressor 1, but install several units in parallel. On the other hand, design a new compressor, named Compressor 2, that can provide the mass flow required with a single unit.

Firstly, the viability of installing several units of the already known mechanical compressor is studied, mainly to understand how many units connected in parallel are necessary to achieve the maximum mass flow required. Also, it is investigated how much dilution flow could be possible depending on the number of units used. The dilution flow is measured as a percentage of MEDAS mass flow. It is defined as a minimum value to assure that there is always enough through the dilution pipe (5 of Figure 3. 31) to avoid the recirculation of exhaust gases to the engine intake. But also, it is used to lighten the cooling power load of the exhaust coolers, which is the main objective of increasing it.

Starting with the MEDAS HD case, Figure 3. 35 shows the compressor map of Compressor 1. The markers correspond with the operation point of a single compressor working at maximum mass flow and different altitudes. The two marker colors (blue and red) define the dilution flow for each case: 20% and 30% of dilution, respectively. Also, the two graphs, Figure 3. 35A and B, show the installation of 2 and 3 compressors in parallel, respectively.

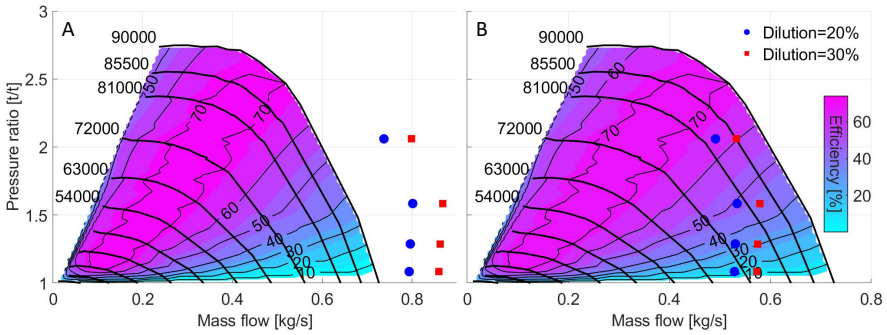

Figure 3. 35. Theoretical operative point of the MEDAS HD mechanical compressor: (A) 2 compressors in parallel; (B) 3 compressors in parallel

It can be seen how the operative points in Figure 3. 35A are way outside the compressor map, making them impossible to achieve, while all the points depicted in Figure 3. 35B are inside the compressor map. Therefore, if Compressor 1 is used, the minimum number of units needed would be three connected in parallel.

Concerning the dilution flow, all the operative points can be reached using three compressors in parallel (Figure 3. 35B) for both cases, 20% and 30%. Also, it should be noted that this parameter should be as high as possible since the higher the dilution, the lower the power demand on the exhaust coolers. So, the dilution flow should be fixed at 30% if this option is selected.

In the case of designing a new compressor, the manufacturer was confident that it could reach the mass flow target with fewer units in parallel than when using Compressor 1. Still, the process would expend a lot of resources and would have delayed the MEDAS HD development project significantly, with the Compressor 2 units being more expensive than Compressor 1. Moreover, following the estimations of performance supplied by the manufacturer, it was necessary to install two units in parallel to achieve the mass flow target. This tipped the balance in favor of continuing using Compressor 1.

For the MEDAS MD, the proposed solution is directed to continue using Compressor 1 but installing only two units, as the mass flow target for this equipment is much lower. Figure 3. 36 shows the performance map of Compressor 1, with the marker being the operative points of a single compressor working with the maximum mass flow at different altitudes. Also, the dilution flow of 20% and 30% are represented by the marker colors blue and red, respectively. It can be seen how both options are achievable when installing two units in parallel, so the dilution flow should also be fixed at 30% of the MEDAS total flow.

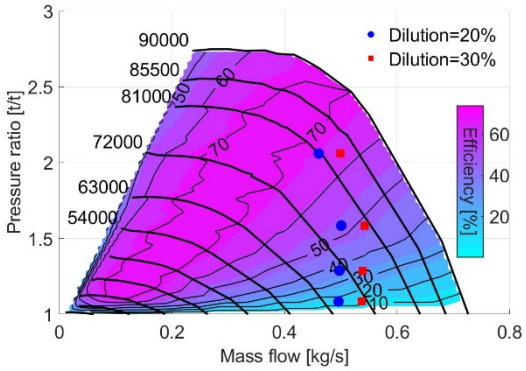

Figure 3. 36. Theoretical operative point of the MEDAS MD mechanical compressor: 2 compressors in parallel

3.3.3. Special components design

Some of the components included in the MEDAS could not be bought from suppliers due to being too customized for the application, so the design of these elements, i.e., the exhaust coolers or the cyclonic separators, must be done and then manufactured.

3.3.3.1 Exhaust coolers

The exhaust coolers are components that can be bought from suppliers, but as the target is a compact element with the maximum possible efficiency, its design is a necessity. The type of cooler selected is shell and tubes, with the air passing through the tubes to facilitate the cleaning of the deposited soot. The design of this component is carried out following a step-by-step methodology:

- First, an estimation of the possible results is obtained using a 0D theoretical model.
- Then, a 3D model is built and calculated with CFD code.
- The CFD results are used to adjust the 0D model, to obtain fast and accurate information.
- A prototype is built following the conclusions obtained with the adjusted 0D model calculations.
- Lastly, an experimental campaign is carried out to validate the design and adjust the 0D model.

a) Preliminary 0D model

The available information to develop a 0D model and an initial solution for the exhaust cooler consisted of the complete geometry of a smaller exhaust cooler, data from several estimated operative points for the solution proposed by the manufacturer, and the boundary conditions for the nominal operating conditions

of the cooler to be designed. The boundary conditions are compiled in Table 3. 6.

Table 3. 6. Boundary conditions for the exhaust cooler design

Maximum length	1.028 m
Maximum shell diameter	324 mm
Gas mass flow rate	3100 kg/h
Inlet gas temperature	450 ºC
Outlet gas temperature	50 ºC
Cooling water volumetric flow	15 m3/h
Inlet water temperature	10 ºC

The equations proposed for the heat transfer correlations of this model are presented in Equation 3. 9, Equation 3. 10, and Equation 3. 11. Being $K_1, K_2\ and\ K_3$ fitting parameters and $d_o\ and\ d_i$ the external and internal diameter of the cooler tubes, respectively. Also, h_i is the heat transfer coefficient to the gas side inside the cooler tubes, and h_o the heat transfer coefficient to the coolant side outside the cooler tubes.

$$\frac{\mathbf{1}}{\boldsymbol{U_o}} = \frac{\boldsymbol{K_1}}{\boldsymbol{h_0}} + \boldsymbol{K_2} + \boldsymbol{K_3}\frac{\mathbf{1}}{\boldsymbol{h_i}}\frac{\boldsymbol{d_o}}{\boldsymbol{d_i}}$$

Equation 3. 9

$$\boldsymbol{h_i}\begin{cases} \boldsymbol{Re < 2100 \rightarrow Nu = 1.86\left(Re\dfrac{Pr \cdot d_i}{L}\right)^{0.33}\left(\dfrac{\mu}{\mu_w}\right)^{0.14}} \\ \boldsymbol{2100 \leq Re \leq 10000 \rightarrow Nu = 0.116Re\left(\dfrac{Re^{0.66} - 125}{Re}\right)Pr^{0.33}\left(\dfrac{\mu}{\mu_w}\right)^{0.14}} \\ \boldsymbol{Re > 10000 \rightarrow Nu = 0.023Re^{0.8}Pr^{0.33}} \end{cases}$$

Equation 3. 10

$$\boldsymbol{h_0 \rightarrow Nu = 1.04Re^{0.4}Pr^{0.36}\left(\frac{Pr}{Pr_w}\right)^{0.25}}$$

Equation 3. 11

$K_1, K_2\ and\ K_3$ parameters of Equation 3. 9 are fitted with the operative points provided by the manufacturer, which have been assumed as valid experimental data for this first step. Figure 3. 37 shows the validation of the model developed against the data provided. In this figure, the results for the heat transfer parameter (U) are shown, which presents a good fitting of the 0D model, with the manufacturer data on the *x-axis* and the model result on the *y-axis*.

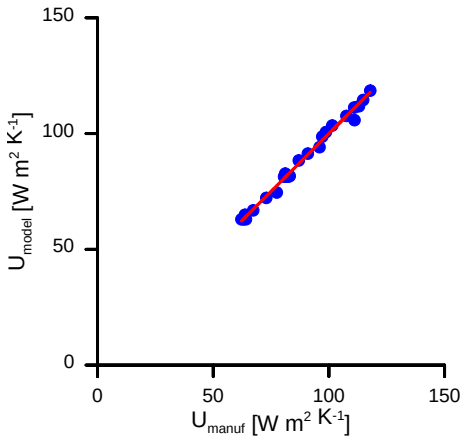

Figure 3. 37.Heat transfer coefficient fitting

Then, several parametric studies depending on the number of heat exchangers installed in parallel are carried out (Figure 3. 38) to define a preliminary size and number of exhaust coolers. Firstly, a study about the cooler length needed to achieve 50 ºC at the outlet is carried out. The results are shown in Figure 3. 38A, with the number of heat exchangers on the *x-axis* against the length of the heat exchanger on the *y-axis*. It can be seen how, when increasing the number of heat exchangers from one to two, the size decreases since the heat transfer area is increased. But when rising to three heat exchangers, the length does not decrease, even increases when further increasing the number of coolers. This is caused by the reduction in the turbulence due to the lower flow velocity inside the heat exchangers ducts. This is caused by the decrease in mass flow through each cooler when increasing the number of coolers, which has a more significant effect than the surface increase.

Following, the outlet temperature is studied while fixing the heat exchanger length to 1.028 m (the size of the solution proposed by the exhaust cooler manufacturer). The result is presented in Figure 3. 38B, which offers a similar trend when increasing the number of coolers like the one explained in the previous heat exchanger length study.

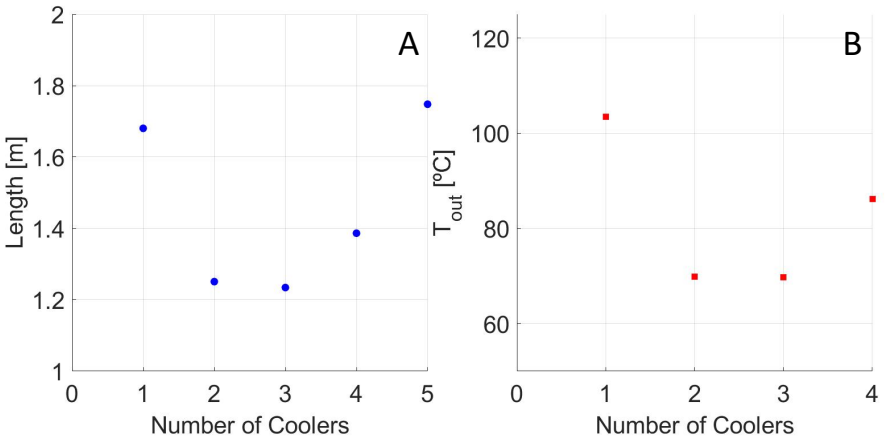

Figure 3. 38. Parametric study: (A) Necessary exhaust cooler length to achieve 50 ºC at the outlet; (B) Outlet temperature when fixing the exhaust cooler length to 1.028 m

Nevertheless, it should be noted that with the model fitted and validated with the manufacturer-provided data, the specifications for this heat exchanger are not achieved.

Additionally, a pressure drop analysis has been done for both studied cases: imposing the length to 1.028 m and estimating the outlet temperature, and imposing the outlet temperature at 50 ºC and estimating the cooler length. The pressure drop has been obtained following Equation 3. 12 with the results obtained presented in Figure 3. 39A and B. Being f the friction factor obtained through Equation 3. 13, L the length of the tube, d_i the internal diameter of the tubes, G the volumetric flow of the gas, and ρ_g the density of the gas. In both cases, the pressure drop decreases with the number of heat exchangers.

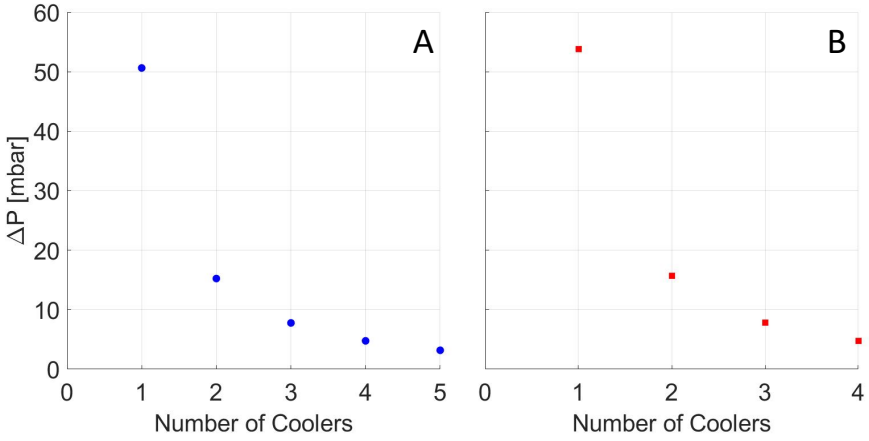

Figure 3. 39. Parametric study: (A) Pressure drop when imposing outlet temperature and estimating length; (B) Pressure drop when imposing length and estimating outlet temperature

$$\Delta p = 4f \cdot L \frac{G^2}{2d_i \cdot \rho_g}$$

Equation 3. 12

$$f \begin{cases} Re < 2100 \rightarrow f = \dfrac{16}{Re} \\ Re \geq 2100 \rightarrow f = 1.2\left(0.0014 + 0.0125 Re^{-0.32}\right) \end{cases}$$

Equation 3. 13

Lastly, a study on the effect of the cooling water inlet temperature and volumetric flow on the estimated length and outlet temperature is carried out. The results are plotted in Figure 3. 40, in which can be seen how the necessary length to achieve 50 ºC at the cooler outlet is reduced proportionally with the cooling water inlet temperature (Figure 3. 40A), with a similar effect on the outlet temperature (Figure 3. 40B). Still, there is no significant effect of increasing the volumetric water flow.

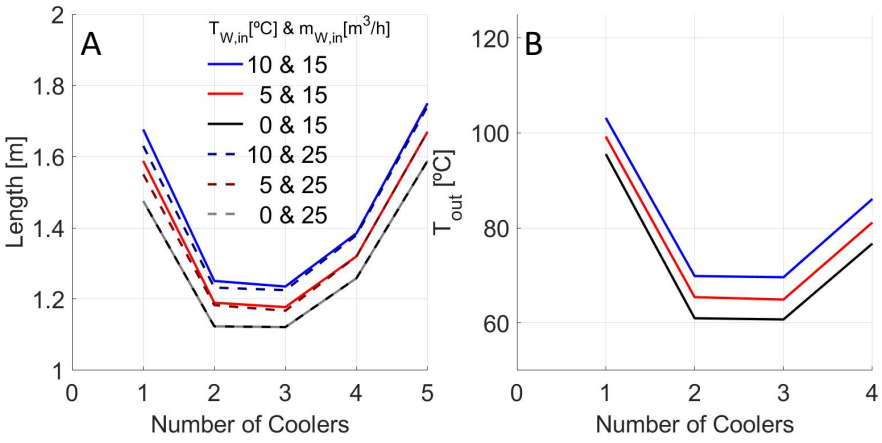

Figure 3. 40. Parametric study: (A) Effect on the exhaust cooler length of the inlet temperature and volumetric flow of the cooling water; (B) Effect on the exhaust cooler outlet temperature of the inlet temperature of the cooling water

Therefore, considering all the results obtained from the parametric studies performed, it can be concluded that the best configuration in term of heat transfer and pressure drop would be installing three parallel heat exchangers. However, considering the size limitation of the MEDAS and the results obtained for two coolers, the adopted preliminary solution is two heat exchangers installed in parallel, with similar performance as three and much smaller sizes.

b) 0D and CFD model

Following, a CFD model is built considering the geometry characteristics provided by the manufacturer and the analysis of previous heat exchanger units, which results would then be used to adjust the 0D model developed previously. The features of the CFD code used are listed below:

- The solver used is StarCCM+ 15.02.007 Steady S-RANS.
- The turbulence model applied is a realizable SST k-Omega model.
- And the heat transfer model is a conjugate heat transfer through gas tube walls.

For the computational domain, the mesh topology is composed of polyhedral cells of a standard size of 3 mm, with a minimum cell size of 65 μm, and distributed in a 3D domain. Additionally, the parametric studies with the CFD model are performed by imposing the boundary conditions compiled in Table 3. 7.

Table 3. 7. Boundary conditions for the exhaust cooler CFD calculations

Inlet gas temperature	450 ºC
Inlet water temperature	10 ºC
Gas mass flow rate	550, 1050, and 1500 kg/h (minimum, medium, and maximum mass flow of MEDAS)
Cooling water volumetric flow	from 2.5 to 15 m3/h with a 2.5 m3/h steps

On the one hand, the heat transfer coefficient in the gas side (h_i, inside the cooler tubes) is modified to fit the results obtained from the CFD study since the previous hypothesis included in the 0D model provides results that do not match the ones obtained through the CFD calculations. The h_i is calculated considering more subdivisions for the Reynolds number than initially proposed in Equation 3. 10. Also, the base correlations used to calculate this parameter are modified and adapted from the initial Bell-Delawere method [7] to a more complex correlation to achieve higher accuracy in the model predictions. The correlations used for the internal heat transfer coefficient are presented in Equation 3. 14. Being L the length of the heat exchanger, f the friction factor in the tube side defined in Batti-Shah correlation and obtained from Equation 3. 15, the C is a constant calculated using Equation 3. 16, and d_i the internal diameter of the tubes.

$$h_i \begin{cases} Re \leq 2100 \rightarrow Nu = 3.66 + \dfrac{0.688\, Re \dfrac{Pr \cdot d_i}{L}}{1 + 0.4\left(Re \dfrac{Pr \cdot d_i}{L}\right)^{\frac{2}{3}}} \\ 2100 < Re \leq 4000 \rightarrow Nu = 0.023 Re^{0.8} Pr^{\frac{1}{3}} \left(\dfrac{\mu}{\mu_w}\right)^{0.14} \\ 4000 < Re \leq 8000 \rightarrow Nu = \dfrac{\left(\dfrac{f}{2}\right) Re\, Pr}{C + 12.7 \cdot \left(\dfrac{f}{2}\right)^{1/2} (Pr^{2/3} - 1)} \left(\dfrac{\mu}{\mu_w}\right)^{0.25} \\ Re > 8000 \rightarrow Nu = 0.023 Re^{0.8} Pr^{\frac{1}{3}} \left(\dfrac{\mu}{\mu_w}\right)^{0.14} \end{cases}$$

Equation 3. 14

$$f = A + B \cdot Re^{-1/m}$$

$$\begin{cases} Re < 2100 \rightarrow f = \dfrac{16}{Re} \\ 2100 \leq Re \leq 4000 \rightarrow A = 0.0054,\ B = 2.3 \cdot 10^{-8},\ m = -2/3 \\ 4000 < Re \leq 10^7 \rightarrow A = 0.00128,\ B = 0.1143 \cdot 10^{-8},\ m = 3.2154 \end{cases}$$

Equation 3. 15

$$C = 1.07 + \frac{900}{Re} - \frac{0.63}{1 + 10Pr}$$

Equation 3. 16

On the other hand, the heat transfer coefficient for the water side (h_o, outside the cooler tubes) correlations are also modified to fit the data obtained with the CFD code. This is calculated following Equation 3. 17 instead of Equation 3. 11. Equation 3. 17 considers five different types of flow that can appear inside the shell of a tube and shell cooler. Each of these characterized flows is represented graphically in Figure 3. 41, where the stream distribution in the water side considered in this model is shown. These five coefficients that characterize the type of flow present in the shell are adjusted to fit the h_o correlation to the CFD results.

To simplify the modeling and reduce the calculation costs of the 0D model, all the flow inside the exhaust cooler shell is assumed as turbulent $J_r = 1$. Neither the leakage in the baffles (A and E streams) nor the bypass flow (C and F streams) has been included, hence $J_l \; and \; J_b = 1$ respectively. Following, the two coefficients $J_c \; and \; J_s$ related to the geometrical baffle distribution and its effect on the flow in the cooler shell are assumed as 0.924 and 0.95, which are in the typical range for these parameters [0.65 – 1.15] and [0.85 – 1.1], respectively. Finally, h_{id} corresponds with the ideal convection coefficient for cross-flow defined by the Zukauskas correlation [8].

$$h_o = J_c \cdot J_l \cdot J_b \cdot J_r \cdot J_s \cdot h_{id}$$

Equation 3. 17

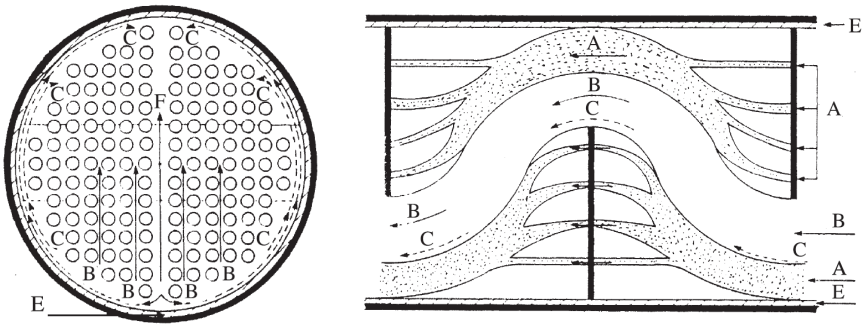

Figure 3. 41. Flow distribution diagram through a shell tubes cooler shell [7]

Lastly, modifications are also needed for the pressure drop model on the gas side since the results obtained through the CFD and with the 0D model do not match. Therefore, the pressure drop correlation shown in Equation 3. 12 is modified, including more complexity to the correlation to increase the accuracy of the pressure drop prediction. The pressure drop correlation for the gas side

obtained is presented in Equation 3. 18. Being L the length of the tubes, ρ_{in} the inlet density, d_i the internal tube diameter, and $A_{o,t}$ the total area of the tubes. For this correlation, it is assumed that there is no change in the gas density along the tube and the friction coefficient follows the Batti-Shah correlation (Equation 3. 15).

$$\Delta \boldsymbol{p} = \left(\frac{\boldsymbol{4f \cdot L}}{\boldsymbol{2\rho_{in} \cdot d_i \cdot A_{o,t}^2}} + \boldsymbol{K_{adj}} \right) \dot{\boldsymbol{m}}^{\boldsymbol{2}}$$

Equation 3. 18

After the adjustment of the 0D model discussed, a parametric study with three different gas mass flows: 550, 1050, and 1500 kg/h; are calculated with the CFD and 0D model to validate the results obtained with the new correlations proposed. Figure 3. 42 shows the results of these calculations for variables such as gas outlet temperature, coolant outlet temperature, heat transferred, and pressure drop on the gas side. It can be observed how the results obtained with the 0D model and CFD model are very similar, validating the use of the 0D for more definitive design conclusions.

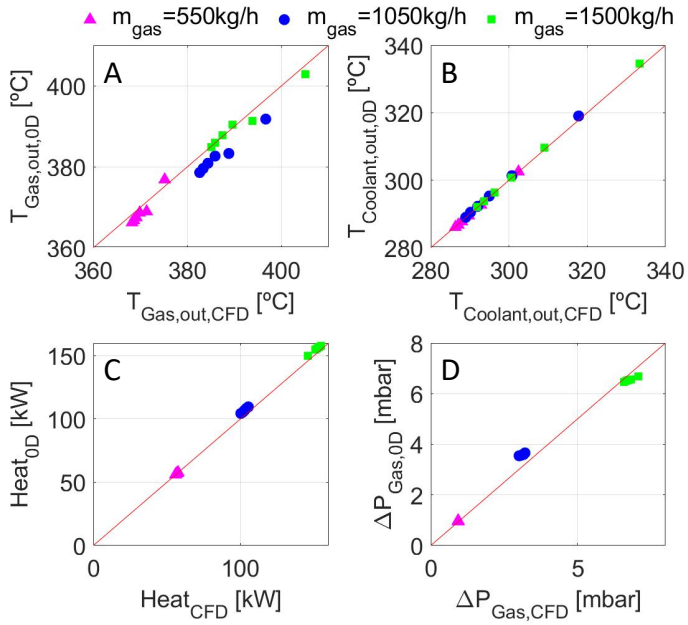

Figure 3. 42. Comparison between results obtained employing CFD code and 0D model: (A) Gas outlet temperature; (B) Coolant outlet temperature; (C) Heat transferred; (D) Gas side pressure drop

Then, to improve the cooler's efficiency, a study of the distribution of the heat transfer resistance in this system should be carried out to identify the best way

to achieve this objective. The distribution obtained is shown in Figure 3. 43A, in which it can be seen that most of the resistance is focused on the gas side (represented by pink markers and located inside the ducts). Also, in Figure 3. 43B is shown the mean temperatures of the gas, tube wall, and coolant, in which can be seen how the wall temperature is almost the same as the water temperature (green markers compared to blue markers). Therefore, to improve the cooling power of the exhaust cooler, it is not helpful to modify the shell and the water coolant path since the walls cannot be colder than the coolant temperature. The effort should be put on the gas side: actuating over the ducts' size, number, and distribution to improve the heat transfer from the gas to the tube walls.

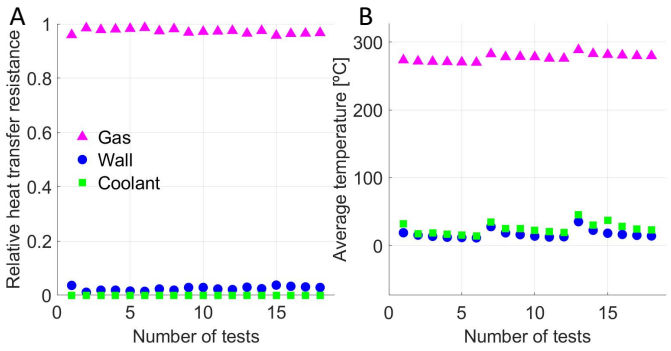

Figure 3. 43. Exhaust cooler heat transfer analysis: (A) Relative heat transfer resistance; (B) Average temperature in the cooler tubes

Once the 0D model is adjusted correctly and the parameters on which the design should focus are identified, a parametric study modifying the geometrical characteristics of the gas tubes is carried out. A single gas operative point has been considered for the study, with 1550 kg/h of mass flow, 450 ºC of inlet temperature, and 0.95 barA of inlet pressure. Some results are presented in Figure 3. 44, in which can be seen different variables such as the outlet gas temperature and the pressure drop in the gas side depending on the tube length and tube internal diameter (Figure 3. 44A and C); and depending on the shell and the inner tube diameter (Figure 3. 44B and D).

These figures show clearly that the threefold objective proposed: compactness of the component, outlet gas temperature of 50 ºC, and low pressure drop, cannot be achieved with the maximum performance (mass flow and exhaust gas temperature) defined for the MEDAS. For example, suppose the target of compactness is imposed, and thus the maximum length and shell diameter are limited. In that case, the internal tube diameter must be smaller to achieve the target of 50 ºC at the cooler outlet. But suppose the tube diameter is reduced to reach the temperature target. In that case, the pressure drop in the cooler and the

number of tubes increase sharply, reducing the MEDAS mass flow performance and increasing the manufacturing difficulty and price.

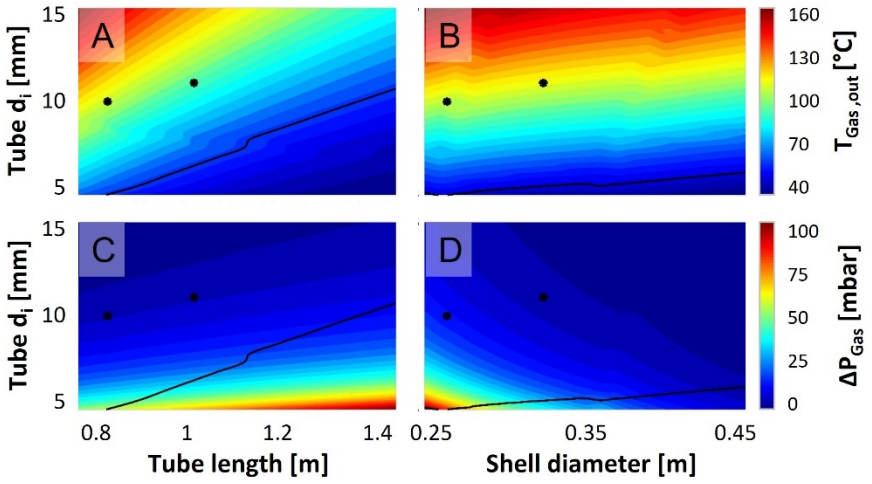

Figure 3. 44. Parametrical analysis of the gas side geometry: (A) Outlet gas temperature depending on the tube internal diameter and tube length; (B) Outlet gas temperature depending on the tube internal diameter and shell diameter; (C) Pressure drop depending on the tube diameter and tube length; (D) Pressure drop depending on the tube diameter and shell diameter

Therefore, it was needed to compromise on the trade-off between compactness and performance. So, it was decided to adopt the most extensive geometry available without exceeding the size limits imposed and reaching a compromise between ease of manufacture and good performance in the case of tube number and diameter. These two designs, one for the MEDAS HD and the other for the MEDAS MD, are marked in Figure 3. 44 with black dots, while the black line is the objective of 50 ºC at the outlet of the cooler:

- MEDAS HD
  - Length: 1.028 m.
  - Shell diameter: 0.324 m.
  - Tube internal diameter: 11 mm.
- MEDAS MD
  - Length: 0.826 m.
  - Shell diameter: 0.324 m.
  - Tube internal diameter: 10 mm.

Furthermore, it should be noted that in this particular application, the pressure drop of these components has more weight than the outlet temperature during the proposal of the final solution since if the user needs higher cooling capabilities, it is possible to install an extra exhaust cooler before the engine

exhaust connection to MEDAS. In this way, the temperature of the gas at the MEDAS exhaust coolers inlet is decreased, which could open the possibility, if the exhaust cooler efficiency is maintained, to achieve the target of 50 ºC at the mechanical compressor inlet in any MEDAS operative point, with minimum pressure drop in the cooling system.

c) Experimental campaign

To finally validate the designed geometry obtained through the 0D model, and hence the model itself, an experimental campaign is carried out with a prototype of the exhaust heat exchanger. In Figure 3. 45, the test rig used for the experimental measurements can be seen. The tests are performed considering the operation conditions compiled in Table 3. 8.

Table 3. 8. Experimental campaign for the validation of the exhaust cooler

Inlet gas temperature	120 ºC	190 ºC
Gas mass flow rate	from 100 to 1100 kg/h with a step of 100 kg/h and a maximum flow of 1150 kg/h	from 100 to 600 kg/h with a step of 100 kg/h and a maximum flow of 690 kg/h

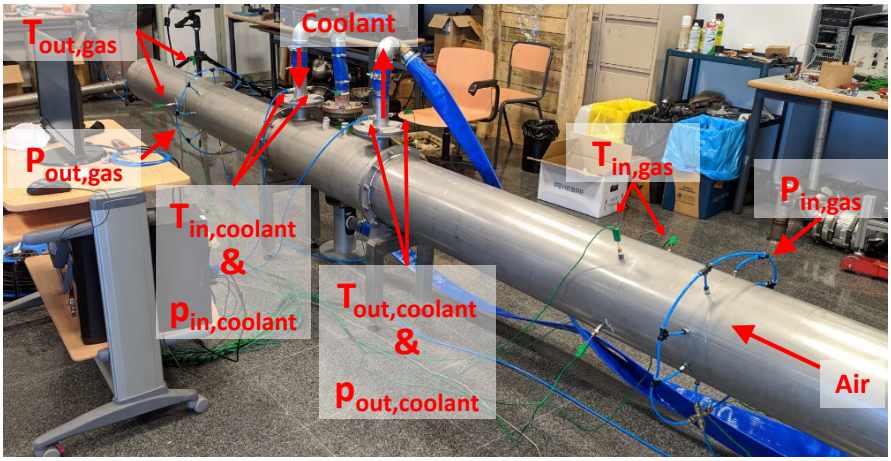

Figure 3. 45. Experimental facility for the exhaust cooler model validation

Figure 3. 46 compares the results from the experimental measurements with the results obtained with the 0D model. In Figure 3. 46A, B, and C, the gas outlet temperature, coolant water outlet temperature, and pressure drop on the gas side are presented with the experimental measurement on the *x-axis* and the modeled result on the *y-axis*. The blue markers correspond to the tests carried out with a temperature of 120 ºC and the black ones with a temperature of 190 ºC. Also, in

Figure 3. 46D, the pressure drop in the gas side is plotted on the *y-axis* against the gas mass flow on the *x-axis*, with the blue and black markers corresponding to model data and the pink and green ones corresponding to the experimental data. In all these graphs, the results show a good model prediction accuracy referenced to the experimentally measured values, which validates the previously obtained geometrical results.

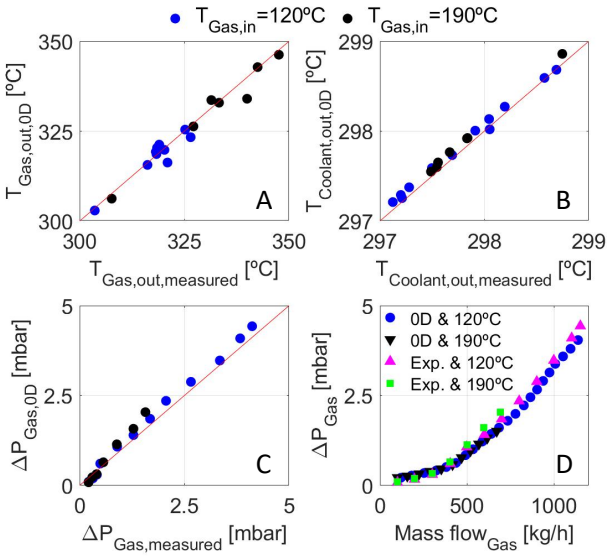

Figure 3. 46. Experimental validation of 0D model: (A) Gas outlet temperature; (B) Coolant outlet temperature; (C) Pressure drop on the gas side; (D) Pressure drop against the mass flow on the gas side

3.3.3.2 Cyclonic separator

One of the most significant contributors to the total pressure drop in the MEDAS exhaust line is the tangential cyclonic separator, found in reference [1], since the needed velocities inside to separate the droplets, with the addition of the 90º change of direction on the tangential separators introduce a lot of turbulence in this component. Therefore, to reduce the MEDAS exhaust line pressure drop and reach the mass flow target of the new models, it is necessary to redesign this component. The proposed solution uses an axial cyclonic separator instead of a tangential separator, which provided excellent filtering efficiency and pressure drop results in previous projects such as reference [9]. The main advantage of this kind of cyclonic separator is that it does not need to change the flow direction, which dramatically reduces the turbulence of the air and thus the pressure losses while maintaining the filtering efficiency. These two types of cyclonic separators are shown in Figure 3. 47, with the tangential separator presented in Figure 3. 47A and the axial one in Figure 3. 47B.

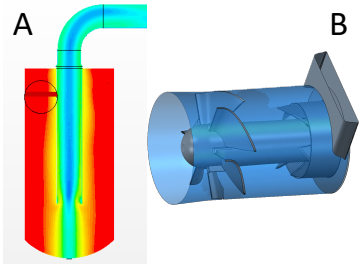

Figure 3. 47. Type of cyclonic separators: (A) Tangential; (B) Axial, image obtained from reference [10]

This component's development is carried out through CFD calculations to achieve a good trade-off between a low pressure drop and a high enough filtering efficiency to protect downstream turbomachinery. The characteristics of the CFD code used are listed below:

- The solver used is StarCCM+ 14.04.11 Steady S-RANS.
- The CAD models are obtained with Apace Claim 2020.
- The turbulence model applied is a realizable k-Epsilon Two-Layer model.
- And the distribution of the particles adopted is a Langrangian multiphase distribution.

Concerning the computational domain, the mesh topology is composed by polyhedral cells of a standard size of 4 mm, with a minimum cell size of 1 mm, and distributed in a 3D domain.

In this case, the geometry of the cyclone is restricted by the maximum permissible MEDAS length and the diameter of the inlet and outlet piping previously defined, which impose limits on the geometrical characteristics of the cyclone:

- Inner inlet diameter: 314 mm.
- Inner outlet diameter: 180 mm.
- Maximum length: 500 mm.

Additionally, to study the particle filtering efficiency of the cyclonic separator, the system is fed with ISO 12103-1, A4 coarse test dust [10], which distribution is shown in Figure 3. 48. On the *x-axis*, the particle size is shown, with the volumetric fraction presented in a bar graph on the left *y-axis* and the cumulative distribution of the particles shown on the right *y-axis*.

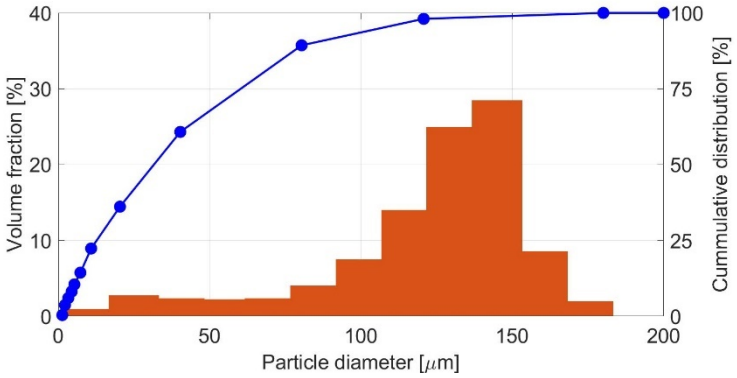

Figure 3. 48. Particle distribution proposed to evaluate the filtering efficiency

Then, considering all the characteristics and restrictions listed, a preliminary design for the cyclonic separator is proposed, shown in Figure 3. 49. The design consists of a NACA profile with blades attached (1), which provide the swirl that separates the droplets from the airflow. A diffuser (2) traps the separated droplets in the cyclone periphery and lets the clean airflow through the center. A particle trap in the drainpipe (3) to avoid the return of the suspended droplets to the central airstream due to local turbulence. And lastly, a drain channel (4) to collect the water that can be accumulated when the MEDAS stops or to help the drainpipe if there is a water stream during operation due to excessive condensate flow.

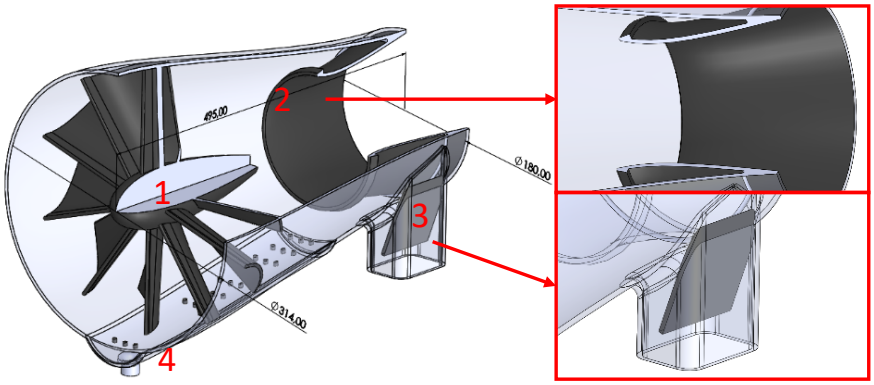

Figure 3. 49. Preliminary design for the axial cyclonic separator

The performance of the cyclonic separator is calculated for three nominal operative points presented in Table 3. 9: three mass flow levels with the inlet pressure and temperature conditions corresponding to the maximum performance while simulating sea level for all of them.

Table 3. 9. Cyclonic separator design points

	Design point 1	Design point 2	Design point 3
Mass flow [kg/s]	0.706	0.353	0.177
Inlet pressure [bar]	0.956	0.956	0.956
Inlet temperature [ºC]	86	86	86

The results obtained in particle filtering efficiency and pressure drop for the preliminary design in the operative points defined are shown in Figure 3. 50. In Figure 3. 50A can be seen the collection efficiency against the particle size injected for three mass flows: 100%, 50%, and 25% of MEDAS maximum mass flow (Design points 1, 2, and 3 of Table 3. 9, respectively). Additionally, Figure 3. 50B shows the global collection efficiency and the pressure drop against the mass flow tested.

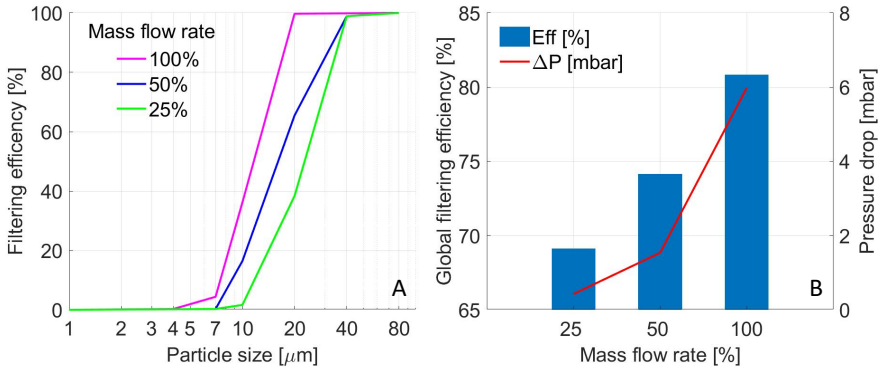

Figure 3. 50. Filtering and pressure drop results for the preliminary geometry of the axial cyclonic separator: (A) Filtering efficiency distributed by particle size; (B) Global filtering efficiency and pressure drop

It can be seen how, despite the low global collection efficiency shown in Figure 3. 50B for low mass flow rate, all the particles bigger than 40 μm are filtered, as shown in Figure 3. 50A. This means that the mechanical compressor located downstream of the cyclone is protected, and the cyclone collects all the harmful water droplets since water droplets smaller than 45 μm can be considered mist [11] and cannot damage a centrifugal compressor [12]. Furthermore, the obtained pressure drop is much lower than expected, reaching 6 mbar at maximum mass flow, instead of 67 mbar obtained for the best design of the tangential cyclone shown in reference [1].

In Figure 3. 51 are presented the velocities inside the cyclone when the maximum mass flow is passing through, in which the maximum velocity is kept at 86 m/s with an outlet swirl of 38º. One concern of the water collecting pipe

design is the existence of airflow through the drain circuit, which could drag the water again to the central airstream. Therefore, the air particles' movement through the drain system is included in the calculations (blue lines encased in the red square in Figure 3. 51). Here is shown how air particles (maximum mass flow = 0.5 g/s) enter the drain circuit through the drain channel located at the beginning of the cyclone and reach the main drainpipe but are trapped there and do not return to the central airstream.

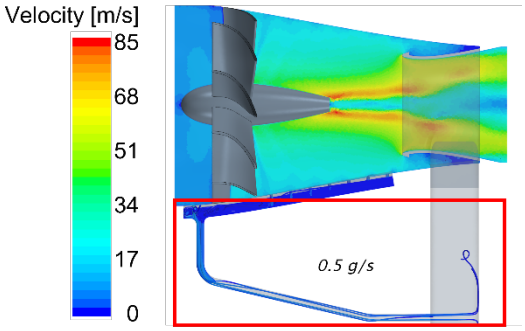

Figure 3. 51. Flow velocity in the axial cyclonic separator

Following, to further improve the pressure drop, it was proposed to install an anti-swirl at the outlet of the cyclone. In theory, if the air at the outlet of the cyclone is not spinning, the velocity is lower, and thus the pressure losses are reduced. The solution proposed is shown in Figure 3. 52, in which can be seen the new diffusor with blades installed to counteract the swirl highlighted in a red square.

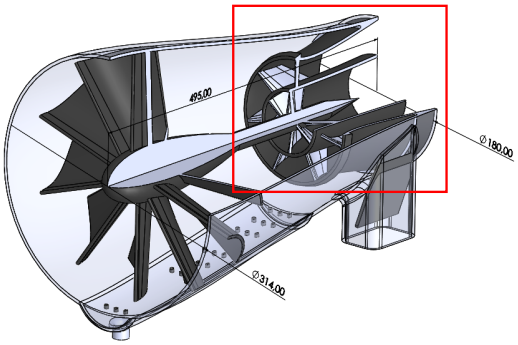

Figure 3. 52. Anti-swirl diffuser

However, in Figure 3. 53A and B can be seen that while the particle collecting efficiency does not change, the pressure drop increases when the anti-swirl diffusor is used. This is caused by the reduction in the effective section of the diffuser that increases the velocity more than it is reduced by removing the swirl,

the maximum velocity being 96 m/s in this case. The velocity inside the cyclone is shown in Figure 3. 53C. Therefore, removing the rotation from the outlet stream is discarded as it is counterproductive to the pressure drop, and the initial solution is maintained.

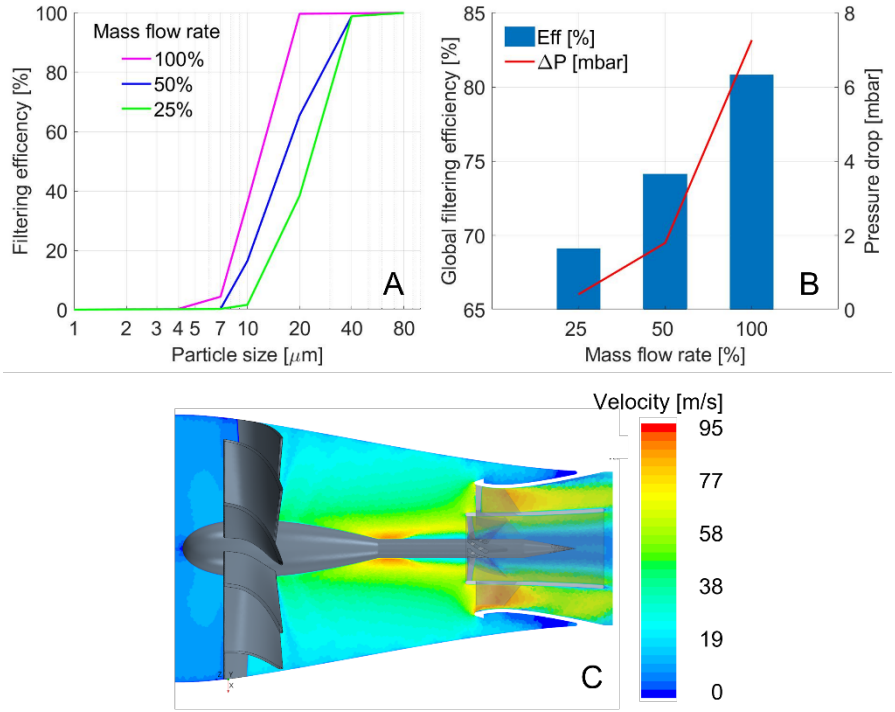

Figure 3. 53. Anti-swirl geometry results

The following issue for this component is the manufacture since the proposed design has highly complex shapes, i.e., the diameter reduction, which is not linear but follows a spline, or the diffuser, a convergent-divergent pipe. These pats cannot be manufactured from standard steel piping, and thus it is necessary to use a 3D printer. The printer was used for the prototypes, but the size of the component increased too much the manufacturing price, which forced to split the cyclone into two parts for the printing and then glue them together.

This solution failed when the prototypes were tested since the union of the two parts was not strong enough to withstand the vacuum conditions imposed by the MEDAS operation coupled with the highly turbulent flow located inside the cyclone. Therefore, a new solution for the manufacture of the cyclone is necessary.

The solution proposed is to print the complex shape of the NACA profile and the blades, while the rest is simplified and manufactured from steel piping. Then,

encasing the printed geometry inside the steel structure to avoid withstanding the mechanical stress with the weaker material (Figure 3. 54).

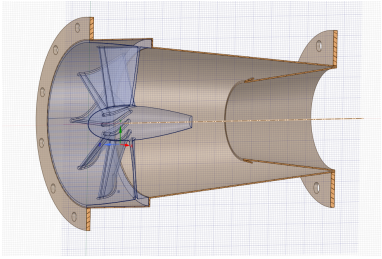

Figure 3. 54. Manufacture solution proposed for the axial cyclonic separator

However, the simplification of the cyclone shapes introduces an increase in the pressure drop due to the higher turbulence generated inside with respect to the smoother contours designed. This happens mainly in the diffuser area, whose shape significantly affects the lift-off of the airstream, increasing the pressure losses. In Figure 3. 55, the velocities for two proposed solutions can be seen, both with the diameter reduction done by a straight cone but with differences in the complexity of the diffuser shape. Figure 3. 55A has a convergent-divergent diffuser, while Figure 3. 55B has a straight cone diffuser. It can be seen how the simpler straight cone diffuser (Figure 3. 55B) reaches higher velocities due to the effective section reduction caused by the lift-off of the airflow from the diffuser walls and the more extensive area of low speed in the diffuser outlet, both marked by red lines in Figure 3. 55B.

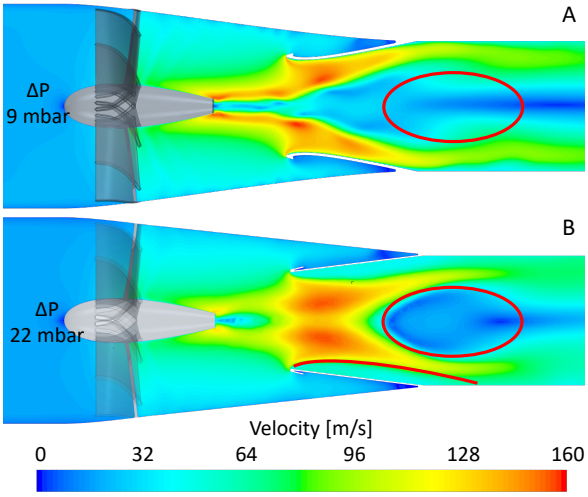

Figure 3. 55. Flow velocity in the axial cyclonic separator: (A) Convergent-divergent diffuser; (B) Cone diffuser

Therefore, an optimization process of the simplified cyclone is carried out to bring as close as possible the pressure drop in the cyclone to the original of 6 mbar (Figure 3. 50). The two parameters proposed to study are the end of the NACA profile and the diffuser's shape since these two are the cyclone areas with higher flow velocity considering the previously obtained results (Figure 3. 51).

Starting with the NACA profile shape, the results for different proposed solutions are shown in Figure 3. 56, in which is shown how the best solution is the original truncated profile (Figure 3. 56A), which avoids the sharp increase of air velocity at the end of the NACA profile shown for the rest of the proposed solutions.

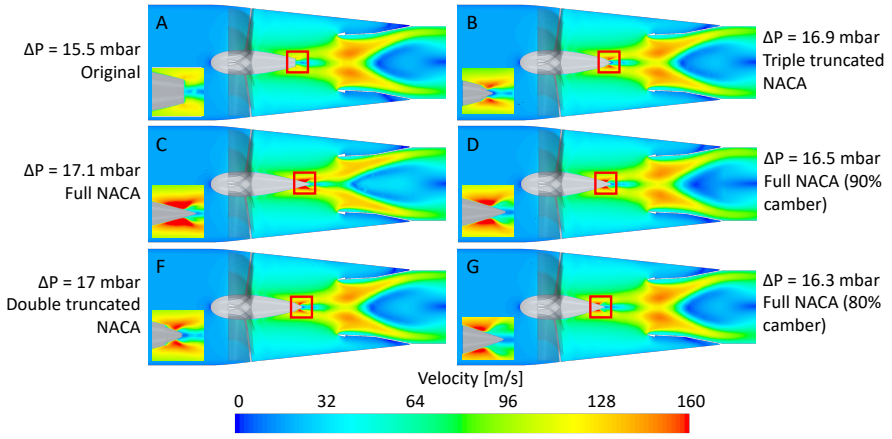

Figure 3. 56. NACA profile optimization results: (A) Original geometry (Truncated NACA); (B) Triple truncated NACA; (C) Full NACA; (D) Full NACA (90% camber); (F) Double truncated NACA; (G) Full NACA (80% camber)

Concerning the diffuser shape, the solutions proposed are shown in Figure 3. 57. It can be seen how when the diffuser's form gets more complex, emulating the original shape, the pressure drop decreases. It should be noted that the rounding of the inlet section of the diffuser has a significant impact on how the flow enters the diffuser and thus on the pressure drop. If the focus is put on Figure 3. 56G and F, the effective section of the diffuser increases when the entry is rounded with respect to the most complex triple cone diffuser. Lower flow lift-off leads to lower velocity and explains the lower pressure drop obtained.

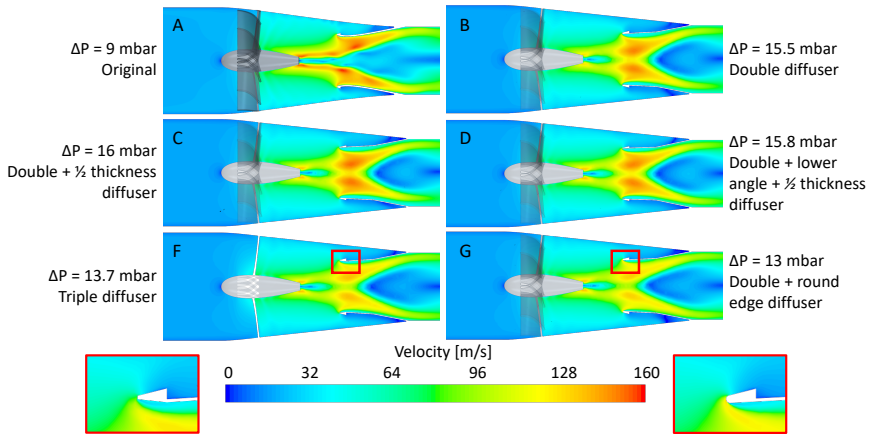

Figure 3. 57. Diffuser optimization results: (A) Original geometry (convergent-divergent pipe); (B) Double cone diffuser; (C) Double cone + ½ thickness of the diffuser walls; (D) Double cone + lower cone angle + ½ thickness of the diffuser walls; (F) Triple cone diffuser; (G) Double cone + round edges at the diffuser inlet

Therefore, considering the results for both parametrical studies, the final solution proposed for the axial cyclonic separator consists of a truncated NACA profile with a double diffuser with rounded entry.

Lastly, to check the particle filtering efficiency of the final solution, three new operative points are defined and compiled in Table 3. 10 to analyze the filtering efficiency in the broader operative range of MEDAS. These points are tested with the ISO particle distribution previously explained (Figure 3. 48). The results obtained are shown in Figure 3. 58, which shows how the filtering efficiency for particles above 40 μm is maintained in all cases, ensuring that all the water particles that could damage the mechanical compressor impeller are removed.

Table 3. 10. Operative point for the validation of the axial cyclonic separator solution

	Operative point 1	**Operative point 2**	**Operative point 3**
Mass flow [kg/s]	0.86	0.54	0.48
Inlet pressure [bar]	0.85	0.55	0.70
Inlet temperature [ºC]	58.08	51.05	50.91

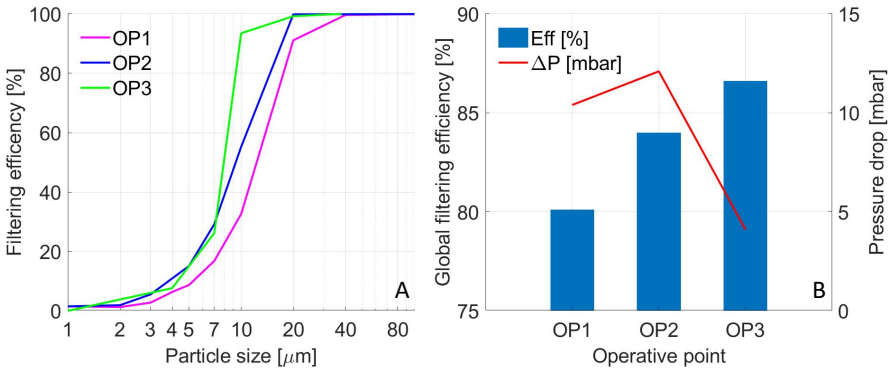

Figure 3. 58. Result of the axial cyclonic separator solution: (A) Filtering efficiency by particle size; (B) Global filtering efficiency and pressure drop

Thus, considering the results obtained from the CFD calculations for both pressure drop and filtering efficiency, the solution adopted is a 3D printed truncated NACA profile (Figure 3. 56A) and blades encased in a steel structure to withstand the mechanical stress, and with a rounded entry and double cone diffuser (Figure 3. 57G), emulating the original convergent-divergent duct.

3.3.3.3 Piping geometry optimization

One of the key elements to minimize the pressure drop of the MEDAS while keeping the layout compact is the piping distribution and the connection geometry between elements. Hence, to decrease the pressure drop in the MEDAS piping and improve the mass flow performance, a study of the pressure drop of the layout is carried out using CFD calculations. The layout shown in Figure 3. 31 is divided into five main geometries, which will be the object of the current study. The geometries are shown in Figure 3. 59, with the elements that define the boundaries identified according to the numbers used in Figure 3. 31 to facilitate the identification of each geometry in the global layout.

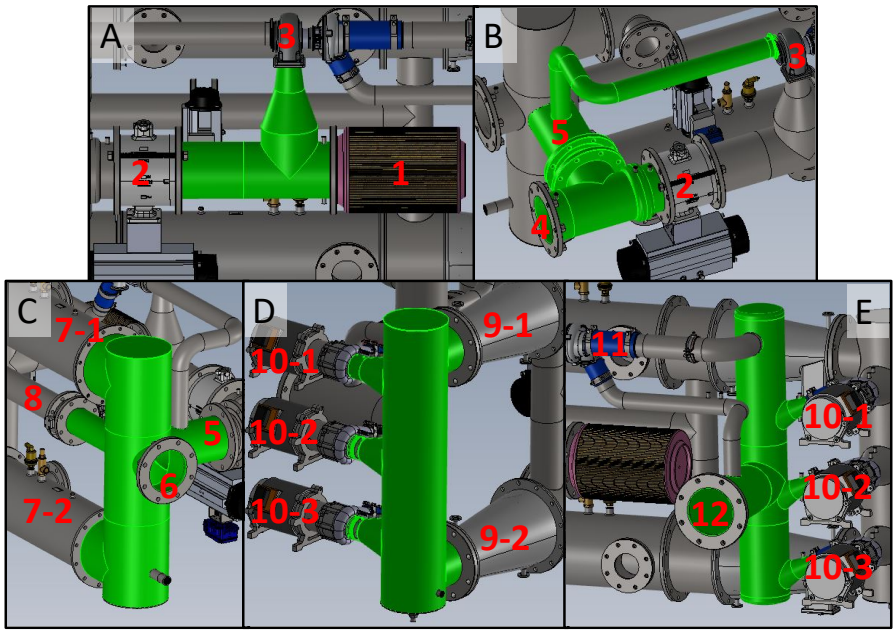

Figure 3. 59. MEDAS piping geometries for the pressure drop study: (A) MEDAS intake; (B) Engine intake connection and dilution pipe; (C) Engine exhaust connection and exhaust coolers inlet; (D) Mechanical compressors inlet; (E) Mechanical compressors outlet & MEDAS exhaust. Component identification according to Figure 3. 31

Several flow paths have been defined to evaluate the pressure drop in each figure, considering the number of inlets and outlets that a particular geometry has and the different combinations through which the air can flow. As an example, in the geometry MEDAS intake (Figure 3. 59A), the flow inlet is the air filter section (1), and the flow outlets are the WG (2) and VGT (3) sections. In this case, there would be two flow paths, one starting in the air filter and ending in the WG, and the other beginning in the air filter and ending in the VGT. The segmentation of the piping allows a direct translation of the CFD results to a pressure drop correlation in the 1D model, explained in Section 3.3.4.3.

The pressure drop of the defined geometries has been calculated in several operative points with a CFD code. The highest pressure drop at the most unfavorable conditions (mass flow, pressure, and temperature) is compiled in Table 3. 11, which allows identifying the most significant part of the system to focus there the optimization process. In this case, two studied geometries could be improved, i.e., the inlet and outlet geometry of the mechanical compressors (Figure 3. 59D and E). These two have a maximum pressure drop consistently

higher than the rest and could be optimized to increase the performance of the MEDAS.

Table 3. 11. CFD maximum pressure drop calculation result by flow path

MEDAS intake	**Δp [mbar]**
Air filter 1 – WG inlet 2	2.06
Air filter 1 – VGT inlet 3	8.29
Engine intake and dilution pipe	**Δp [mbar]**
WG outlet 2 – Engine intake connection 4	0.47
WG outlet 2 – Dilution pipe 5	7.16
VGT outlet 3 – Dilution pipe 5	7.86
Exhaust coolers inlet	**Δp [mbar]**
Engine exhaust connection 6 – Cooler 7-1 inlet	11.02
Engine exhaust connection 6 – Cooler 7-2 inlet	10.72
Dilution pipe 5 – Cooler 7-1 inlet	4.08
Dilution pipe 5 – Cooler 7-2 inlet	3.79
Mechanical compressors inlet	**Δp [mbar]**
Cyclone 9-1 outlet – Mechanical compressor 10-1 inlet	24.64
Cyclone 9-1 outlet – Mechanical compressor 10-2 inlet	16.73
Cyclone 9-2 outlet – Mechanical compressor 10-2 inlet	11.31
Cyclone 9-2 outlet – Mechanical compressor 10-3 inlet	13.47
MEDAS exhaust	**Δp [mbar]**
Mechanical compressor 10-1 outlet – MEDAS exhaust 12	354.51
Mechanical compressor 10-2 outlet – MEDAS exhaust 12	359.16
Mechanical compressor 10-3 outlet – MEDAS exhaust 12	331.99

Concerning the compressor inlet geometry, the leading cause of the high pressure drop is the turbulence generated by sudden section change of the ducts at the manifold located between the cyclones and the compressors. Also, the double direction change of the air, first from the cyclone outlet to the collecting manifold and then to the compressor inlet pipe (Figure 3. 59D). Hence, as the cyclonic separator outlet cannot be modified, a parametric study of the cone angle in the compressor inlet duct and the distance between the inlet compressor pipes has been carried out. The objective is to smoothen the flow path in this geometry without introducing high complexity geometries that could lead to a more expensive and challenging manufacturing process.

The cone angle tested were 25º, 20º, and 0º for a distance between cones of 350 mm, and the distance between cones tested were 300 and 350 mm for a cone angle of 25º. The results are compiled in Table 3. 12, showing almost no difference between the results for 25º and 20º, but the pressure drop increases significantly if the angle is 0º. Moreover, when the distance between the cones is reduced, the pressure drop of the top and bottom pipes increases significantly.

Table 3. 12. Results of the parametric study for the mechanical compressors inlet geometry

Cone angle [º]	**Δp Compressor 10-1 inlet [mbar]**	**Δp Compressor 10-2 inlet [mbar]**	**Δp Compressor 10-3 inlet [mbar]**
0	14.20	17.35	14.40
20	4.93	8.49	5.40
25	5.08	8.66	5.40
Distance between pipes [mm]	**Δp Compressor 10-1 inlet [mbar]**	**Δp Compressor 10-2 inlet [mbar]**	**Δp Compressor 10-3 inlet [mbar]**
300	8	8.05	9.24
350	5.08	8.66	5.40

In the case of the cone angle, the result shown in Table 3. 12 is caused mainly by the progressive section change when the angles are 25º and 20º, which reduces the turbulence and lift-off of the airstream at the mouth of the compressor inlet pipe and thus the pressure drop compared to the abrupt section change of 0º case.

For the case of the distance between pipes, as the reference is in the middle section of the manifold (Compressor 10-2 location), when the distance between the inlet pipes is reduced, the top and bottom pipes move nearer to the central line. This increases the distance of the Compressor 10-1 and 10-3 inlet pipes from the cyclone outlet pipes. This forces a more considerable change in the air direction, increasing pressure losses. Therefore, if the distance between

compressor inlet pipes increases, the top and bottom compressor's flow path straightens and reduces the pressure drop.

To clarify the phenomenon caused by the distance between inlet pipes, Figure 3. 60 shows a simple 2D diagram of the mechanical compressor inlet geometry, including the main flow path (red line) for the top compressor. Figure 3. 60A shows the case in which the distance between the inlet pipes is 350 mm, and Figure 3. 60B presents the case in which the distance between the inlet compressor pipes is 300 mm. In this figure, the distances have been exaggerated to show better the differences between both cases.

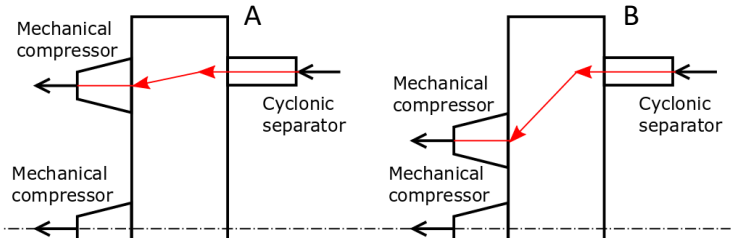

Figure 3. 60. Flow diagram through the inlet compressor geometry

Therefore, considering the previous explained results, the solution adopted for the compressor inlet geometry consists of cones of 25º (one for each mechanical compressor), due to more accessible parts supply (standard) than 20º, separated 350 mm from each other.

Following, in the case of the MEDAS exhaust geometry, the high Δp shown in Table 3. 11 is caused by the massive velocity of the flow in the mechanical compressors outlet pipe, as can be seen in Figure 3. 61, in which the flow velocity in this point of the MEDAS can reach up to 281 m/s.

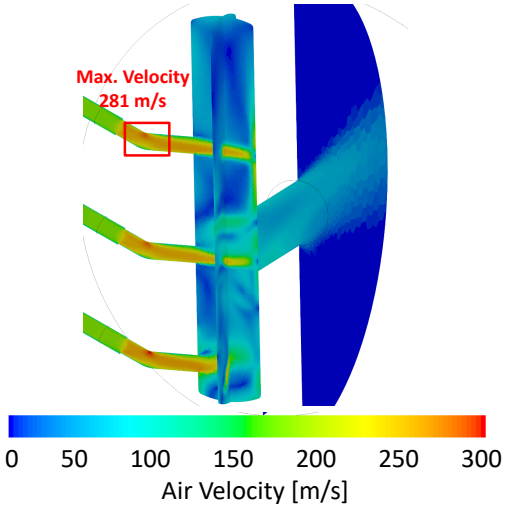

Figure 3. 61. Air velocity at the mechanical compressor outlet

Some of the several proposed solutions to reduce the pressure drop in this geometry are presented in Figure 3. 62. All these proposed solutions have in common the target of reducing the air velocity through a diffuser, gradually increasing the duct's section to reduce the velocity, and avoiding the airstream lift-off from the walls as much as possible. In DESIGN 1, the section increase proposed employs straight semi cones in the mechanical compressor outlet pipes, which is the easiest to manufacture. Following, DESIGN 2 presents a more complex solution of an optimized double cone that allows a more gradual section increase. Lastly, DESIGN 3 proposes the most complex geometry, including a diffuser in the manifold and the double cones. The results for the pressure drop of the proposed solutions are included in Table 3. 13.

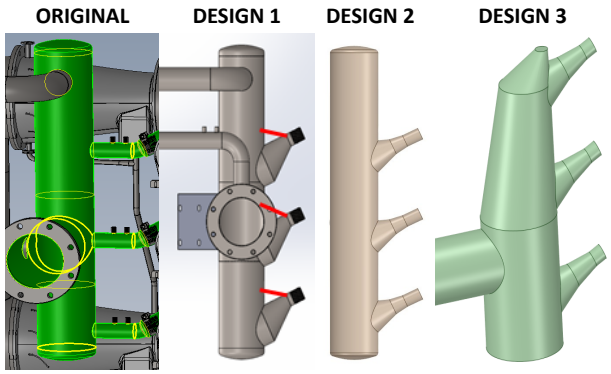

Figure 3. 62. Solutions proposed for the mechanical compressors' outlet geometry

Table 3. 13. Calculated pressure drops for the proposed solutions of the mechanical compressors' outlet geometry

Solution	Δp Compressor 1 outlet [mbar]	Δp Compressor 2 outlet [mbar]	Δp Compressor 3 outlet [mbar]
ORIGINAL	301.0	309.9	293.6
DESIGN 1	253.1	279.1	296.2
DESIGN 2	132.0	131.0	133.0
DESIGN 3	128.0	147.0	149.0

Considering the results shown in Table 3. 13 and the ease of manufacture, the solution adopted for this geometry is the DESIGN 2 (Figure 3. 62), which offers the best pressure drop improvement and is not too complex for standard manufacturing. Despite its complexity, it should be noted that DESIGN 3 does not introduce a clear improvement in the pressure drops of the geometry with respect to DESIGN 2. This leads to thinking that to improve this geometry further, the focus should not be on the manifold but more on the individual outlet pipes of each mechanical compressor, allowing the flow to develop more in a long line before discharging to the manifold, which is difficult for space constraints.

3.3.4. 1D model development

The next step is to develop a model of the new MEDAS with the available information on the selected components, validate their use, and obtain a preliminary result of the installation performance and the possible control strategies that would fit the equipment. Firstly, the definition of the control strategies of the installation will be carried out. Then, the modeling of the individual components present in the MEDAS will be explained, with the methodology to introduce the pressure drop correlations afterward. Lastly, the expected performance of the MEDAS will be obtained from the complete 1D model developed.

3.3.4.1 Control strategies

To define the control strategies, it is necessary to know which variables will be controlled and the available actuators. In the case of the MEDAS HD and MD, the controlled variables will be the pressure at the engine inlet connection, the temperature at the mechanical compressors' inlet, and the mass flow that the mechanical compressors are moving. While the available actuators are the WG valve, the VGT vanes, the exhaust cooler bypass valve, and the speed of the mechanical compressors.

a) Mass flow control

Two options were proposed for the mass flow control. The first one is actuating all the mechanical compressors simultaneously to the same speed to achieve the setpoint demanded. This option benefits a more straightforward control since it comprises a simple PID structure but several identical outlets.

The second proposed solution is to implement a complex PID with the mechanical compressors starting progressively depending on the setpoint demanded. When the setpoint can be reached with only one compressor, the rest remain stopped. This allows widening the mass flow range with respect to the first solution. The minimum mas flow is defined by only one compressor instead of several added together and increases the installation energy efficiency.

While the progressive start-up seems the better option, this control option implies a more complex control strategy and includes extra components. When one of the mechanical compressors is spinning, trying to generate the mass flow and pressure ratio, the rest are stopped. These are essentially open holes that communicate the mechanical compressors' vacuum zone upstream with the ambient pressure downstream. Therefore, to use the progressive start-up strategy, it is necessary to install one-way valves at the mechanical compressors' outlet to avoid the return of the flow through the stopped compressors.

Considering these two constraints, which would increase the end price of the MEDAS without a significant advantage, it is decided to use the more straightforward option of controlling several mechanical compressors simultaneously. Additionally, keeping all the mechanical compressors always working at a similar operative point avoids stressing excessively a single unit, sharing the air load between all units instead of focusing most of the work on the first-to-start compressor.

b) Pressure control

The proposed solution for the pressure control is to use the WG valve in parallel with the VGT vanes, which would be working as coarse and fine-tune actuators, respectively, both trying to achieve the pressure setpoint at the engine intake. Also, to increase the accuracy and stability of the pressure control when the pressure measurement is close to the setpoint (+/- 10 mbar), the WG would freeze in place to avoid perturbances caused by the low resolution of this actuator and to allow the VGT vanes to adjust the setpoint accurately.

c) Mechanical compressor inlet temperature control

Lastly, the exhaust cooler bypass valve controls the mechanical compressor inlet temperature, which, using a variable gain PID, dampens the changes in the exhaust temperature caused by the engine's operative point and keeps the mechanical compressor inlet temperature around 50 ºC.

The setpoint of 50 ºC is selected by hygrometry criteria since this is the temperature around which the combustion engine exhaust gases stop

condensation [2]. The PID parameters change when the error with respect to the setpoint exceeds +/- 5ºC, in which the actuation speeds up to react accordingly to the engine transients and sudden point change.

Moreover, this control has an additional variant to support the mass flow control. When the mechanical compressor speed reaches maximum speed and the mass flow is below the desired value, the setpoint of the mechanical compressor inlet temperature is lowered to increase the provided mass flow by the mechanical compressors. This allows to improve the maximum mass flow performance of the MEDAS, but with the detriment of stressing the condensates extraction system more due to the higher condensates production rate. The performance increase is caused by the reduction of power consumption of the compressor and the rise in gas density at the compressor inlet. Both phenomena happen when the inlet temperature decreases, as shown in Equation 3. 3, which increases the mass flow for a given supplied power and imposed pressure ratio.

3.3.4.2 Components modeling

The modeling of the components is based on translating the information obtained from manufacturers and experimental measurements into the templates included in the 1D modeling software VEMOD. There are five main elements in the model developed: control valves, turbocharger, mechanical compressors, exhaust heat exchangers, and cyclonic separators.

a) Control valves

In the case of the controlled valves included in the MEDAS: WG valve and exhaust cooler bypass valve, the manufacturers have provided the discharge flow coefficient (K_v) characterization depending on the valve opening, which is presented in Figure 3. 63 with the WG valve on the left and the Bypass valve on the right.

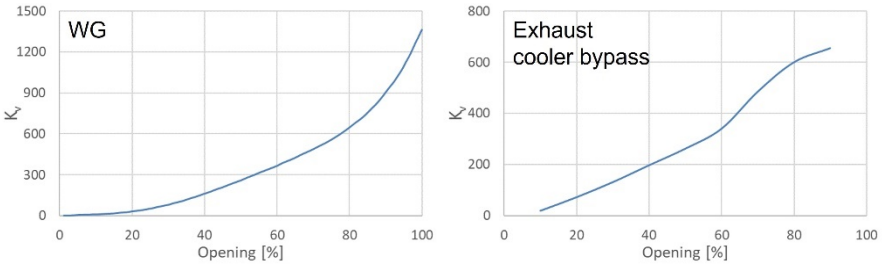

Figure 3. 63. Valve characterization from manufacturer: (Left) WG; (Right) Exhaust cooler bypass valve

Then, to translate the discharge flow coefficient (K_v) to a valve discharge coefficient (C_d), the Equation 3. 19 is used, in which ρ [kg/m^3] is the gas density,

D [m] is the cross-section diameter of the inlet pipe and $SG = 0.001$ is the specific gravity of the fluid with which the valve is working.

$$C_d = \frac{K_v}{\pi \frac{D^2}{4}} \sqrt{\frac{2 \cdot SG}{\rho}} \cdot \frac{1}{3600\sqrt{10^5}}$$

Equation 3. 19

Lastly, the obtained C_d for each valve opening is introduced in VEMOD for a given nominal cross-section of the valve.

b) Mechanical compressor

The mechanical compressors are modeled in VEMOD using the turbocharger element but ignoring the turbine part due to imposing the turbocharger speed. This approximation was necessary since the element corresponding to an electrically driven compressor was not available when this model was developed. However, the selected setup provides the same result as would be achieved with a dedicated element for this component, only missing the estimation of the electrical power used, which must be calculated during the data post-processing.

To model the geometry of the mechanical compressor, one unit was disassembled to measure the characteristic magnitudes of the compressor demanded by VEMOD, which are compiled in Table 3. 14 and shown in a diagram in Figure 3. 64. The compressor map used for these models is the improved compressor map introduced in Section 3.2.1.2c).

Table 3. 14. Mechanical compressor geometric parameters

Mechanical compressor	
Wheel diameter (D_W)	100 mm
External diameter (D_E)	161 mm
External length (L_E)	60 mm

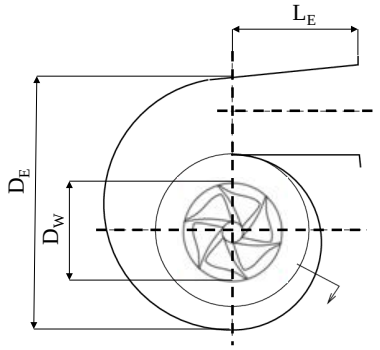

Figure 3. 64. Mechanical compressor geometry diagram

c) Turbocharger

In the turbocharger case, it is included with its dedicated element in the VEMOD code. The turbocharger has also been disassembled to measure the characteristic magnitudes of both turbine and compressor demanded by VEMOD to achieve a model as accurate as possible of the turbocharger geometries, which are shown in Figure 3. 65 and compiled in Table 3. 15. Also, in Figure 3. 65, the particular VGT actuator mechanism of the turbocharger selected has been included.

Table 3. 15. Turbocharger geometric parameters

Compressor	
Wheel diameter (D_W)	100 mm
External diameter (D_E)	161 mm
External length (L_E)	60 mm
Turbine	
External diameter (D_E)	250 mm
External length (L_E)	113 mm
Inlet diameter (D_i)	67 mm
Wheel diameter (D_W)	76 mm
Wheel outlet diameter (D_{wo})	66 mm
Nut diameter (D_{Nut})	22.6 mm
Blade height (H_B)	20.8 mm
Volume ($V_{Turbine}$)	2076 cm^3
Beta angle	0.9424 º

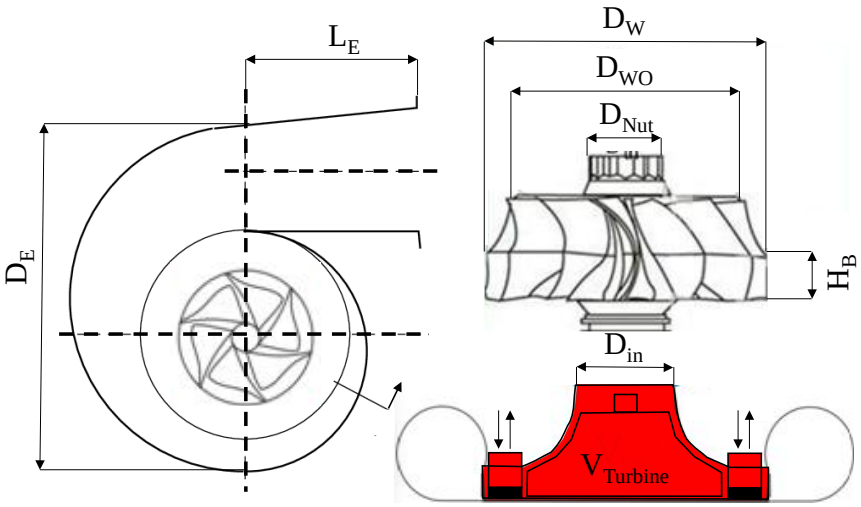

Figure 3. 65. Turbocharger geometry diagram

The turbocharger turbine and compressor performance maps were obtained through an experimental campaign before the current Ph.D. Thesis, which can

be found in reference [1], and its results are compiled in Figure 3. 66. The compressor map is directly introduced in the model as done in the case of the mechanical compressors. However, when introducing the VGT map, an extrapolation error was detected.

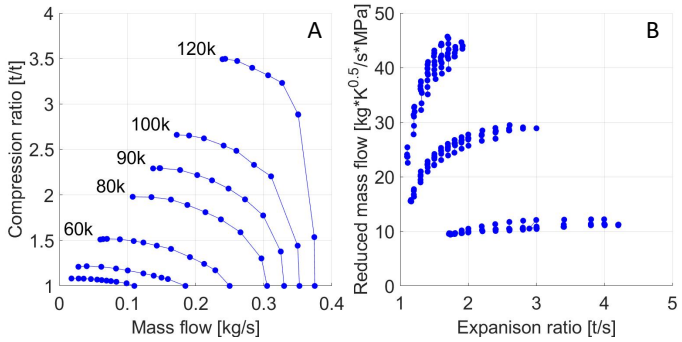

Figure 3. 66. Turbocharger performance maps: (A) Compressor; (B) Variable geometry turbine

The error in the extrapolation code is assumed to be caused by the not-so-common actuator of the VGT used in MEDAS, which moves up and down the backplate of the turbine stator. This affects the stator cannels' height instead of rotating the stator blades. Due to this mechanism of the VGT, the map extrapolation code of VEMOD, designed for rotating blades, cannot extrapolate a complete turbine map from the experimental data of different VGT positions. To be precise, it is impossible without some re-design of the model coefficients already defined (a-priori) as the initial values for non-linear fitting algorithms. Therefore, a methodology is proposed to achieve the correct extrapolation of variable geometry turbine maps with this kind of actuation mechanism.

The process defined is presented in a flow diagram in Figure 3. 67. Here, graphs depicting the results of fitting the experimental data with the direct extrapolated map and following the proposed methodology are included. As the first step, in Figure 3. 67A, the direct extrapolation of the VGT map from the experimental data is shown, which provided an average error value for the reduced mass flow of 12.4 %; too high to be accepted as a valid model.

Then, the proposed following step is to simplify the experimental data of the VGT to the same number of fixed geometry turbines (FGT) as VGT positions measured and obtain an individual extrapolation result for each one. These extrapolations are presented in Figure 3. 67B and provide a more accurate result since the maximum average error found for the reduced mass flow is 4.7 %. Finally, Figure 3. 67C shows the complete map extrapolation result, obtained with the FGT (red lines) individual extrapolation used as experimental data to generate a comprehensive map of the VGT (blue lines). Also, the experimental data (blue dots) has been included in this figure. There are no apparent

differences between both models presented, and the average error for the complete VGT map is close to the FGT case (6.3 %). This can validate the use of the methodology proposed to obtain a more accurate model of a VGT.

Additionally, Figure 3. 67D presents the final extrapolated map for the VGT with the direct extrapolation result and the experimental data to show qualitatively how the result obtained through the proposed methodology is better fitted to the experimental data.

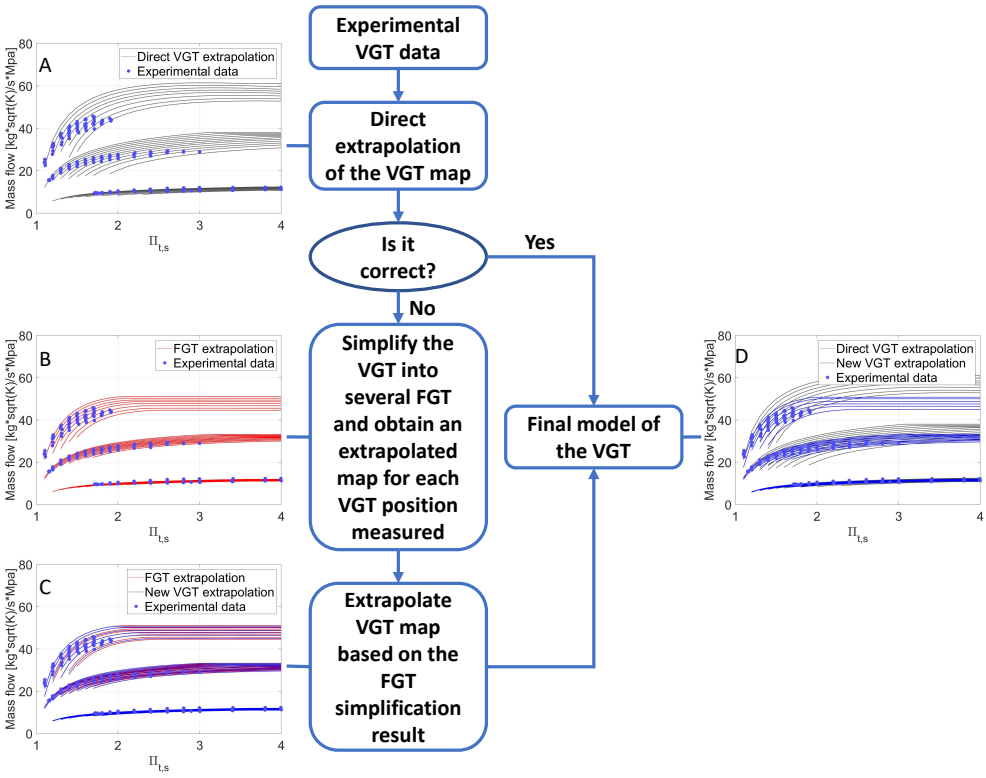

Figure 3. 67. Flow diagram of the proposed methodology proposed with VEMOD code for obtaining a model of a VGT with a backplate displacement actuator: Mass flow map case

The methodology proposed is also applicable when the focus is on the efficiency map instead of the mass flow map of the turbine. Figure 3. 68 presents the flow diagram with the efficiency results of a single blade position (50 %) of the studied turbine. In the first place, in Figure 3. 68A, the direct extrapolation carried out by the extrapolation software included in VEMOD is shown. However, similarly to the mass flow case, this extrapolation has an average error for the adiabatic efficiency of 13.6 %, which is too high for a valid model.

Then, the simplification of the VGT to three different FGTs is carried out following the process previously explained. The extrapolation result for the 50 % vanes position is shown in Figure 3. 68B, which provides a maximum average error for adiabatic efficiency of 5.5 %.

Lastly, in Figure 3. 68C, the previous FTG extrapolation (red lines) and the experimental data (blue dots) are plotted alongside the complete VGT efficiency map extrapolation (blue lines). Like in the mass flow case, there are no significant differences between both extrapolations presented in either map topology or average error. In the case of the complete efficiency map, the average error for the adiabatic efficiency is 6.9 %. This further validates using the proposed methodology for extrapolating VGTs with sliding backplate actuation using the software VEMOD.

Also, Figure 3. 68D presents the direct extrapolation of the VGT efficiency map and the final result obtained through the methodology proposed for the case of the 50 % vanes position. The significant differences between both extrapolations and how the experimental data (blue dots) fit better with the proposed methodology results can be seen qualitatively.

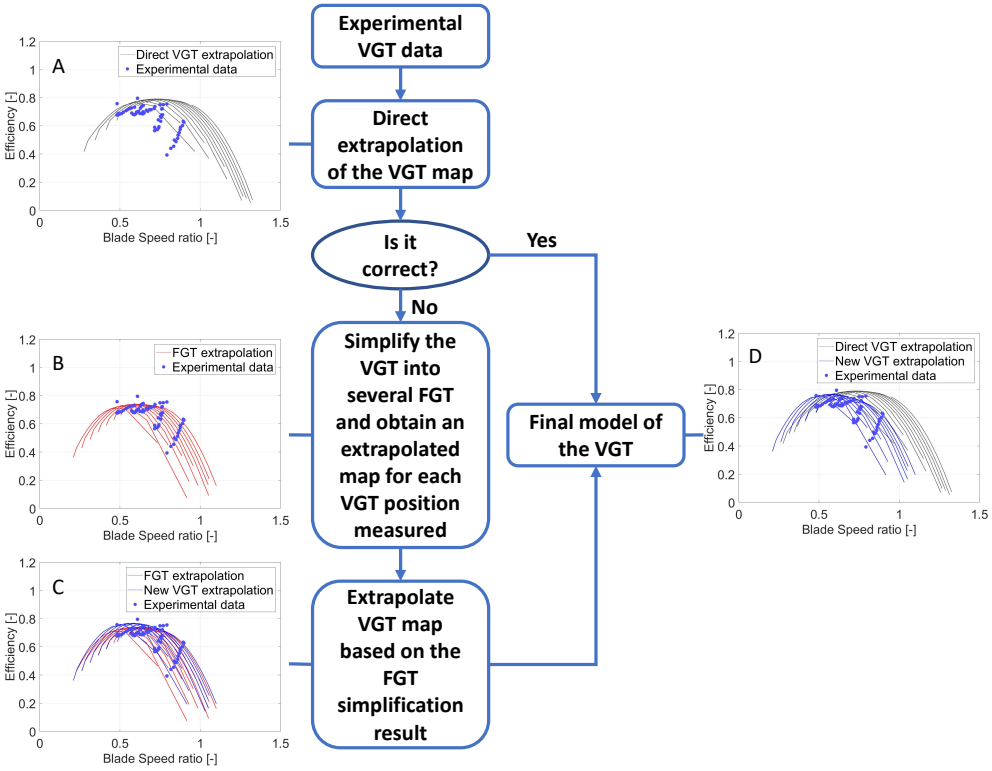

Figure 3. 68. Flow diagram of the proposed methodology proposed with VEMOD code for obtaining a model of a VGT with a backplate displacement actuator: Efficiency map case, 50% blade position

d) Exhaust heat exchanger

For the heat exchanger model, a table is included in the 0D heat exchanger element of VEMOD, characterizing the number of transfer units (NTU), the heat capacity ratio (Cr), and efficiency parameters for different flow conditions, which are obtained with the help of the 0D model previously developed in Section 3.2.1.1b). The flow conditions considered in the characterization table are included in Table 3. 16.

Table 3. 16. Flow conditions considered for the exhaust cooler characterization

Parameter	Range	Step division
Gas inlet pressure [bar]	0.55 – 1.05	0.1
Gas mass flow [kg/s]	0.1 – 1.1	0.2
Gas inlet temperature [ºC]	150 – 550	100
Water inlet temperature [ºC]	0 – 30	10
Water mass flow [kg/s]	1.4 – 4.2	1.4

e) Cyclonic separator

To translate the pressure drop of the cyclonic separator to a value of discharge coefficient (C_d) understandable by VEMOD, a simple model shown in Figure 3. 69 is built. The cyclone inlet pressure and temperature and the mass flow passing through the cyclone (1, 2, and 3 of Figure 3. 69) can be controlled. This will be done to fit the design operative points shown in Table 3. 10. The cyclonic separator is represented by a controlled valve (2 of Figure 3. 69), which changes its discharge coefficient to impose the pressure drop estimated by the CFD calculations for each design point selected.

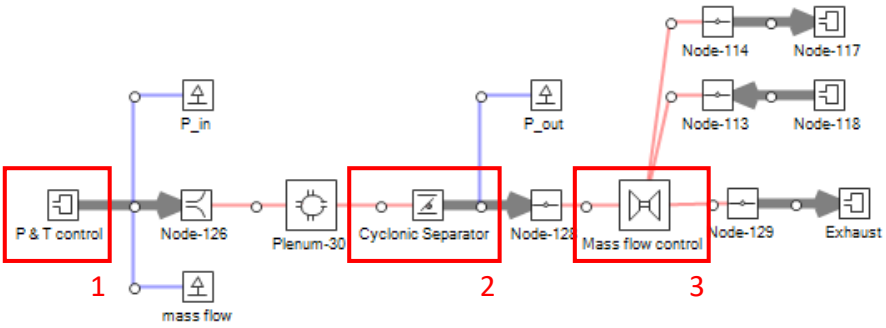

Figure 3. 69. VEMOD model for the characterization of the cyclonic separator discharge coefficient

Once the pressure drop is translated to a C_d value, a correlation for the C_d dependant on the Reynolds number at the cyclone inlet is developed. The Reynolds number and C_d obtained for the data set of the cyclonic separator are shown in Table 3. 17. It can be seen how the C_d does not change significantly between design points. It is reasonable to assume the C_d value as a constant and equal to the average of all the design points to reduce the complexity of the global MEDAS model.

Table 3. 17. Cyclonic separator discharge coefficient characterization result

Design point	Pressure drop [mbar]	Inlet Reynolds Number (Re_{in})	Discharge coefficient (C_d)
Point 1	9.3	$2.12 \cdot 10^5$	0.545
Point 2	2.5	$1.06 \cdot 10^5$	0.523
Point 3	0.6	$5.32 \cdot 10^4$	0.529

Then, as the correlation result is a constant value for the C_d, this element is introduced in the MEDAS VEMOD model as a Fixed Discharge Coefficient with a value of 0.532 and a reference diameter of 0.2 m.

3.3.4.3 Pressure drop correlations

The piping pressure drop obtained in Section 3.3.3.3 must be converted to correlations depending on the flow conditions: pressure, temperature, and mass flow. These will be included in the 1D model developed to estimate the pressure drop for a given operative point and thus obtain an accurate estimation of the performance of the MEDAS. To get the pressure drop correlations, a simple methodology has been proposed.

Firstly, the flow paths should be defined for each geometry studied. The flow paths for each geometry are described in Table 3. 11, for each of the geometries defined in Section 3.3.3.3 and presented in Figure 3. 59. It should be noted that in the mechanical compressor inlet geometry of the MEDAS HD, the flow path cyclonic separator 9-1 to mechanical compressor 10-2 has been selected over cyclonic separator 9-2 to mechanical compressor 10-2 due to the more significant impact of this path in the pressure drop shown in Table 3. 11.

Once the flow paths are defined for every geometry, the pressure drop estimated by CFD must be translated into a discharge coefficient to be used inside VEMOD. This is carried out following a similar methodology as in Section 3.3.3.2. The pressure drop estimated for a given flow path is focused on a single PID-controlled valve while imposing the inlet pressure, temperature, and mass flow conditions. However, a significant difference is included in this case. Instead of building an isolated VEMOD model to study each flow path, the study is carried out simultaneously for every flow path in a complete MEDAS model. The advantage of this global approach is that the individual C_d is obtained considering possible perturbances from the rest of the correlations. This allows for identifying couplings or instabilities between correlations during the earlier phases of the model development instead of during the late stages.

Once the pressure drop data is translated to C_d, the pressure drop correlations are defined as a linear equation (Equation 3. 20). Here, y is the discharge coefficient that would provide the desired pressure drop, x is the input parameter that groups the instantaneous flow conditions, and m and n are the coefficients of the equation.

$$\boldsymbol{y = m \cdot x + n}$$

Equation 3. 20

The definition of x, the parameter that compiles the flow conditions of the flow path and on which will depend the C_d that should be applied in each instance, is carried out following Equation 3. 21. This equation considers the flow conditions through the Reynold number at the flow path's inlet (Re_{in}) and outlet (Re_{out}). Additionally, the tunning coefficients β and α are used to fit the correlation to the data obtained from VEMOD.

$$x = {Re_{out}}^{\alpha} / {Re_{in}}^{\beta}$$

Equation 3. 21

Following, the β and α coefficients are adjusted to obtain the pressure drop correlations with the structure shown in Equation 3. 20. The polynomial order of the correlations could be increased if necessary to improve the fitting quality. An example of the pressure drop correlation is shown in Figure 3. 70, in which the case of the flow path from the air filter to the WG valve inlet is shown.

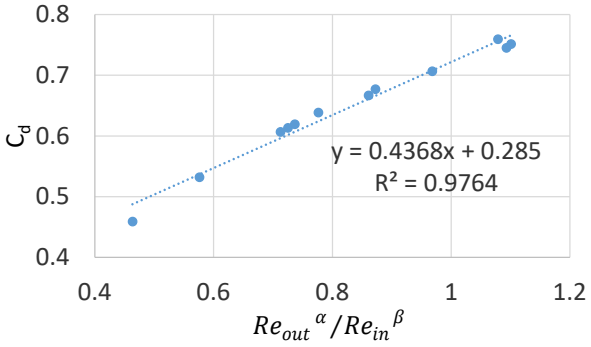

Figure 3. 70. Pressure drop correlation for the Air filter to WG inlet flow path

The results for all the flow paths studied are compiled in Table 3. 18, in which all the correlations are simple linear equations. It should be noted that even with the low fitting quality (R^2 between 0.5 and 0.3) shown in most cases, the linear equation is selected as the solution since the increase of polynomial order did not provide a significant quality increase.

Table 3. 18. Pressure drop correlations by flow path

MEDAS intake	**α**	**β**	**Δp Correlation**	**R^2**
Air filter 1 – WG inlet 2	1.31	1.3	$y = 0.4368x + 0.285$	0.98
Air filter 1 – VGT inlet 3	1.7	0.7	$y = 7 \cdot 10^{-6}x + 0.0046$	0.98
Engine intake and dilution pipe	**α**	**β**	**Δp Correlation**	**R^2**
WG outlet 2 – Engine intake connection 4	-	-	$y = 1$	-
WG outlet 2 – Dilution pipe 5	1.29	1	$y = 0.0188x + 0.3456$	0.30
Exhaust coolers inlet	**α**	**β**	**Δp Correlation**	**R^2**
Dilution pipe 5 – Cooler 7-1 inlet	0.6	0.6	$y = -6.6673x + 6.5995$	0.40
Dilution pipe 5 – Cooler 7-2 inlet	0.6	0.6	$y = -7.5839x + 7.4916$	0.52
Mechanical compressors inlet	**α**	**β**	**Δp Correlation**	**R^2**
Cyclone 9-1 outlet – Mechanical compressor 10-1 inlet	0.9	1	$y = 0.0683x - 0.0432$	0.32
Cyclone 9-1 outlet – Mechanical compressor 10-2 inlet	1	1	$y = 6.7292x - 6.9824$	0.41
Cyclone 9-2 outlet – Mechanical compressor 10-3 inlet	1.1	1	$y = 0.1211x - 0.2372$	0.50
MEDAS exhaust	**α**	**β**	**Δp Correlation**	**R^2**
Mechanical compressor 10-1 outlet – MEDAS exhaust 12	1.1	1	$y = 0.2046x + 0.0827$	0.37
Mechanical compressor 10-2 outlet – MEDAS exhaust 12	1.1	1	$y = 0.2134x + 0.0623$	0.41
Mechanical compressor 10-3 outlet – MEDAS exhaust 12	1.1	1	$y = 0.1801x + 0.2052$	0.34

Finally, to introduce the correlations in the model, the Reynolds number must be calculated for each boundary area of every geometry since VEMOD does not provide online access to this parameter. This is carried out following Equation 3. 22, being D the cross-section diameter in which the Reynolds number is being

calculated, $\dot{m}$ the gas mass flow passing through and v the dynamic viscosity of the air dependant on the temperature of the gas.

$$\boldsymbol{Re = \frac{4\dot{m}}{\pi D v}}$$

Equation 3. 22

Then, the independent variable of the correlation shown in Equation 3. 21 is built with the Reynolds number result. Lastly, the correlation input is used to enter a 2D table, in which the equation shown in Table 3. 18 is programmed and provides the C_d that should be imposed in the controlled valve. It should be noted that several limiters are included in the process to ensure that every value stays within the correct range. The program block done for this process is shown in Figure 3. 71, in which the steps explained are shown.

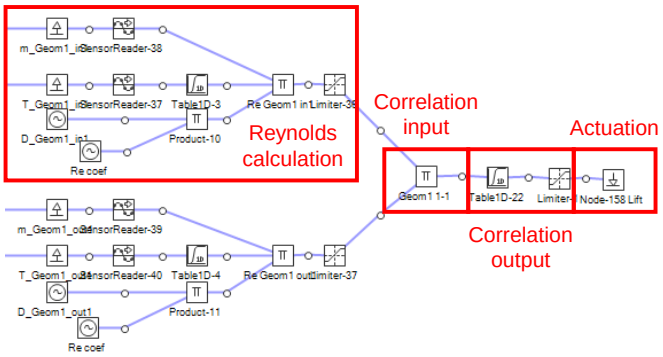

Figure 3. 71. Programming of the piping pressure drop correlation

Finally, it was necessary to remove some flow paths defined during the CFD study phase due to incompatibilities or model instabilities when including all the possible flow paths defined in Table 3. 18. An example of incompatibilities could be found in the exhaust coolers inlet geometry, with two possible flow entries for each flow outlet but two different pressure drop values. This causes an incompatibility when simplifying the pressure drop to a single element, as is the correlation's objective. Therefore, one of the flow inlets (exhaust gas inlet, 6 of Figure 3. 59C) has been removed since no flow may pass through this inlet, i.e., when there is no engine connected to the MEDAS or it is stopped. Also, one of the two possible flow paths for the mechanical compressor 10-2 inlet has been removed for the same reason.

For the model instabilities, it is necessary to remove all the pressure drop correlations for the flow path originating from the VGT outlet, which tends to close too much due to the low mass flow, causing convergence problems in the model.

3.3.4.4 Performance results

Considering all the aspects explained in Section 3.3.4, the preliminary performance results of the new MEDAS for Medium Duty and Heavy Duty engines are obtained from these models. Also, an overview of the MEDAS HD 1D model developed is shown in Figure 3. 72, in which the components layout is shown in Figure 3. 72A, with the control PIDs and the pressure drop correlations in Figure 3. 72B. If the highlighted green area is removed from Figure 3. 72, the 1D model becomes the one corresponding to the MEDAS MD.

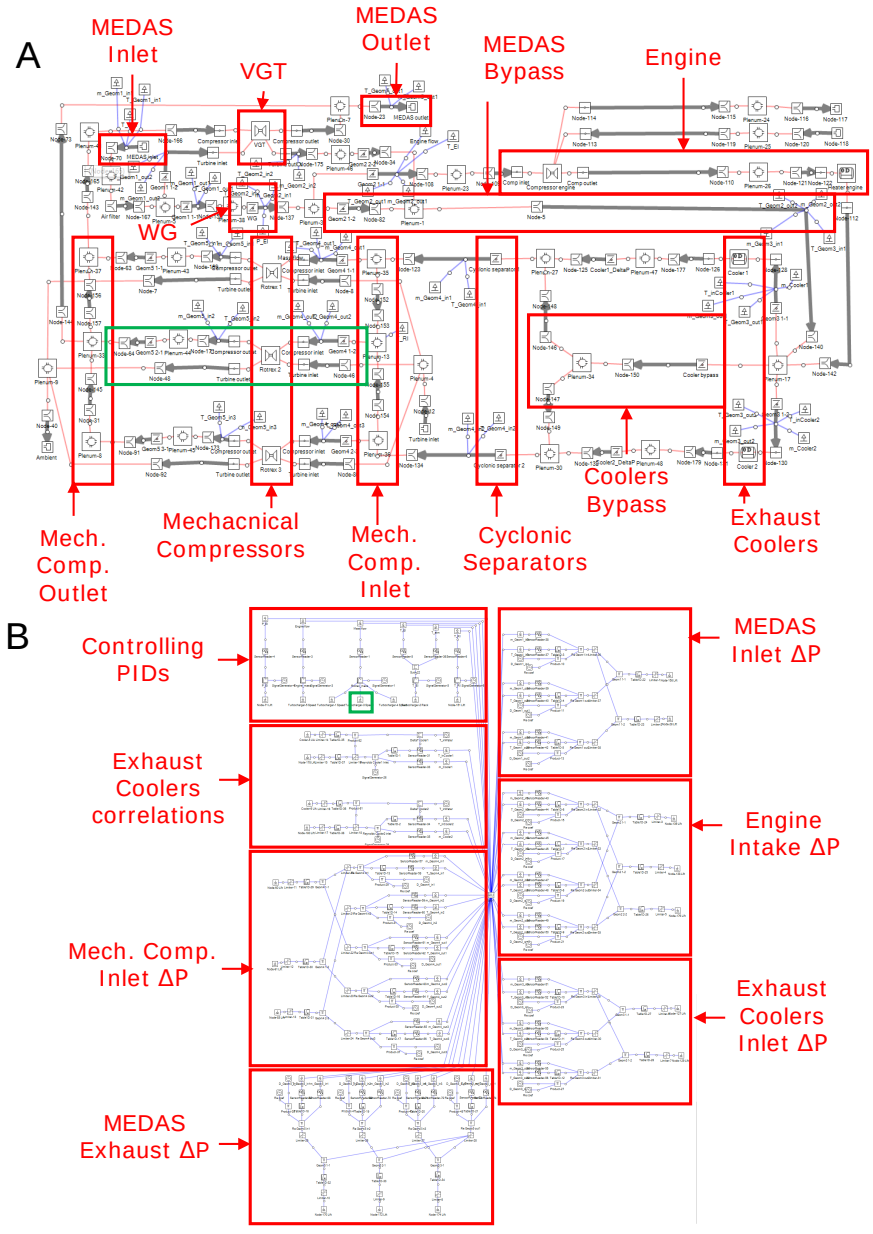

Figure 3. 72. MEDAS HD and MD 1D model developed with VEMOD: (A) Component layout; (B) PID control and pressure drop correlations

The performance obtained through the models corresponds to the steady-state altitude and mass flow range, theoretically available with the MEDAS HD and MD, shown in Figure 3. 73A and B, respectively. However, these models'

results must be validated through an experimental testing campaign and can only be used as an estimation at this point.

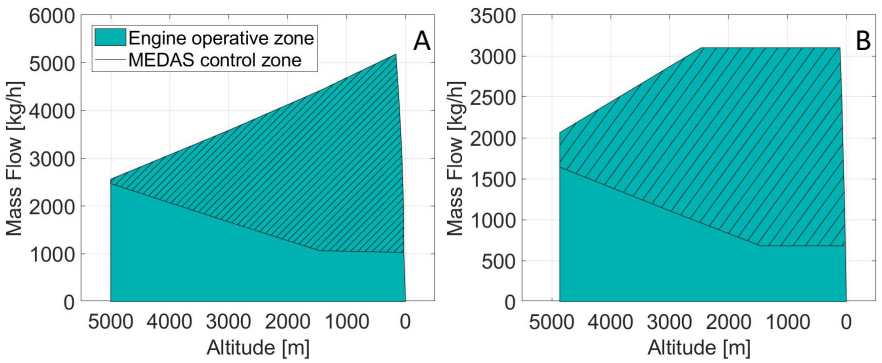

Figure 3. 73. 1D model estimation of the MEDAS mass flow performance map: (A) MEDAS Heavy Duty; (B) MEDAS Medium Duty

3.3.5. Prototype development

The development of a prototype is only carried out for the case of the MEDAS HD. Concerning the MEDAS MD, all the phases described in the previous section of the current Ph.D. Thesis were carried out, but just before starting the prototype phase, the project was stopped, leaving the development of the MEDAS MD on stand-by.

Therefore, the current section will be focused solely on results obtained with the MEDAS HD, which will consist of a study of its performance capabilities, in both steady-state operation and while reproducing realistic altitude profiles. Moreover, in the current section, the experimental adjustment process of the 1D model of the MEDAS HD and the steady-state testing used to validate its results will be included.

3.3.5.1 Performance

a) Steady-state

The steady-state operation is an essential part of the MEDAS since it emulates the behavior of an automobile running through a plateau or an aircraft traveling at a constant altitude. Additionally, it is what defines the performance capabilities of the MEDAS.

The pressure and mass flow range of the MEDAS HD has been characterized experimentally through an extensive testing campaign, encompassing engine intake pressures from 1.013 to 0.55 barA with steps of 0.05 bar and with several mass flow levels for each pressure, from minimum to maximum. The mass flow levels tested cannot be standardized since the maximum mass flow depends on the simulated pressure, decreasing when the pressure decreases.

Figure 3. 74 shows the experimental map obtained for the MEDAS HD. This figure presents the engine intake pressure on the *x-axis* and the real mass flow passing through the installation on the *y-axis*. Also, there is a color map representing a third study variable, which in the case of Figure 3. 74 is the standard deviation of the engine intake pressure. It can be seen how the maximum mass flow target of 1.44 kg/s (5200 kg/h) has been achieved up to 0.8 barA (2000 meters above sea level) and reaching 0.86 kg/s (3100 kg/h) at maximum vacuum (0.54 barA or 5000 meters above sea level). Moreover, the maximum standard deviation in the pressure control at the engine intake is 2 % of the pressure control full scale (470 mbar), which fulfills the accuracy specifications defined for the MEDAS HD (+/- 10 mbar).

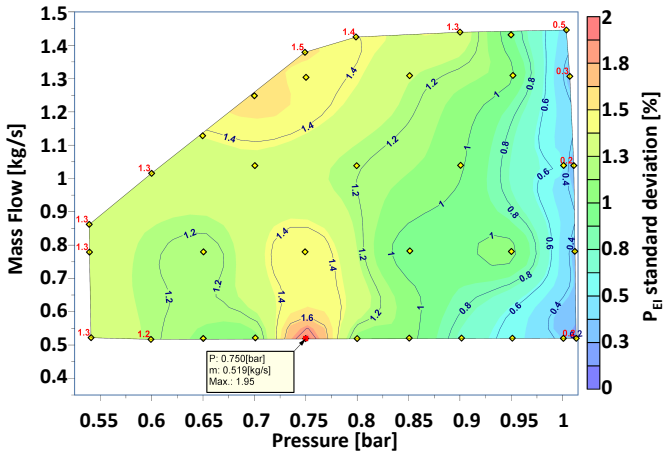

Figure 3. 74. MEDAS HD performance map: Standard deviation of the pressure at the engine intake

The WG valve and the turbocharger vanes, the two actuators selected for the pressure control of the MEDAS, are shown in Figure 3. 75A and B, respectively. If the focus is on Figure 3. 75A, it is shown how the WG closes progressively when decreasing the pressure. Additionally, it can be seen how the effect of the WG movement over the pressure increases when the absolute pressure value decreases.

For example, it is necessary to close 35 % of the WG to reduce the pressure from 1.013 barA to 0.95 barA at minimum flow, but it is only required to close it 5 % to decrease the pressure from 0.8 barA to 0.75 barA. Contrarily, when focusing on Figure 3. 75B, it is impossible to observe any trend either with the pressure at the engine intake connection or the mass flow.

The simultaneous use of the WG valve as a coarse actuator and the turbocharger vanes as a fine-tune actuator is the cause of the behavior of the two actuators. The VGT vanes work at random areas all along its span, depending on the

previous MEDAS operative point and the new point demanded. While the WG valve has a more linear evolution of its position with the pressure change, opening when the pressure increases and closing when it decreases.

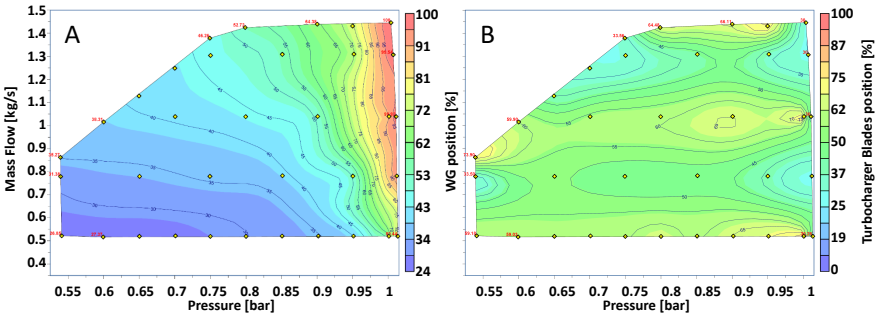

Figure 3. 75. MEDAS HD performance map: (A) WG valve position; (B) Turbocharger vanes position

Following, if the focus is put on the mechanical compressor operative point, Figure 3. 76 shows on the compressor map how the three mechanical compressors work in similar operative points, with the dispersion between the three increasing with the compressor speed.

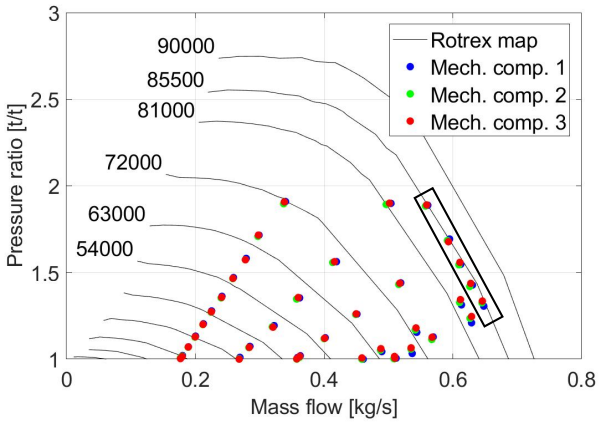

Figure 3. 76. MEDAS HD mechanical compressors points on the compressor map

Also, it can be seen how the operative point of the compressors at maximum speed (marked with a black box in Figure 3. 76) does not reach the map maximum speed line, even when demanding the maximum speed to the frequency driver, as shown in Figure 3. 77A. This is caused by the mechanical compressor inlet temperature, shown in Figure 3. 77B, which is higher than the reference temperature (15 ºC) used for the definition of the compressor map. This causes an increase in the compressor power demand (Equation 3. 3) and

reduces the corrected speed (Equation 3. 2). This reduces the maximum mass flow that can move the compressor and displaces the operative point to the left in the compressor map.

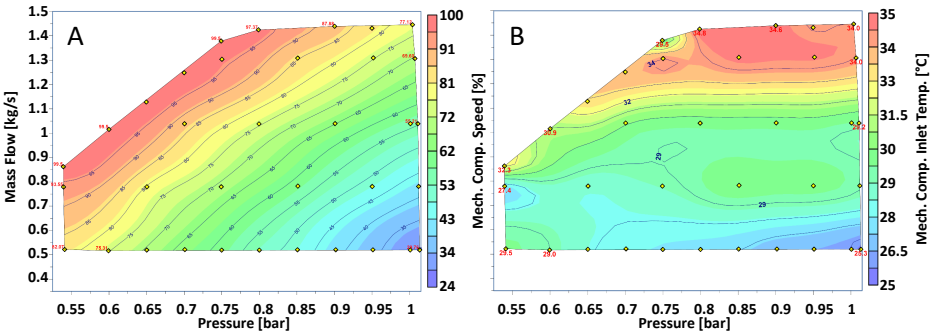

Figure 3. 77. MEDAS HD performance map: (A) Mechanical compressor speed; (B) Mechanical compressor inlet temperature

b) Dynamic

The test for dynamic performance is used mainly to evaluate the stability of the pressure control and the accuracy in following a changing pressure setpoint by the MEDAS. The MEDAS's dynamic capabilities allow the reproduction of real driving tests in the laboratory. Also, it is the leading difference from other vacuum generation technologies like the altimetric chamber.

In Figure 3. 78, two altitude profiles are presented, the first in Figure 3. 78A from 0.55 barA up to 0.91 barA (4865 meters above sea level to 890 meters) and the other in Figure 3. 78B going from 0.91 barA down to 0.55 barA (890 meters to 4865 meters). It should be noted that the pressure profile used to perform these tests corresponds to a vehicle driving through the Sierra Nevada mountain road at a vehicle speed of 100 km/h.

Sierra Nevada mountain road is a commonly used road in OEMs' on-road calibration for automotive engines. However, this road only reaches up to 2000 meters above sea level. Therefore, the original pressure profile has been repeated three times with an altitude offset to reach 4865 meters above sea level.

In Figure 3. 78A and B are two graphs. The upper one is the pressure profile being simulated on the *y-axis* against time on the *x-axis*, presenting the setpoint demanded in orange and the measured value in blue. And the lower graph, the error between measured value and setpoint is also shown against time. The error in the pressure control is kept between +/- 10 mbar in both cases for all the pressure range tested, which is lower than 2 % of the pressure range full scale of the MEDAS. These results obtained validate the stability of the pressure control and the capability of the MEDAS HD to follow a real driving altitude profile.

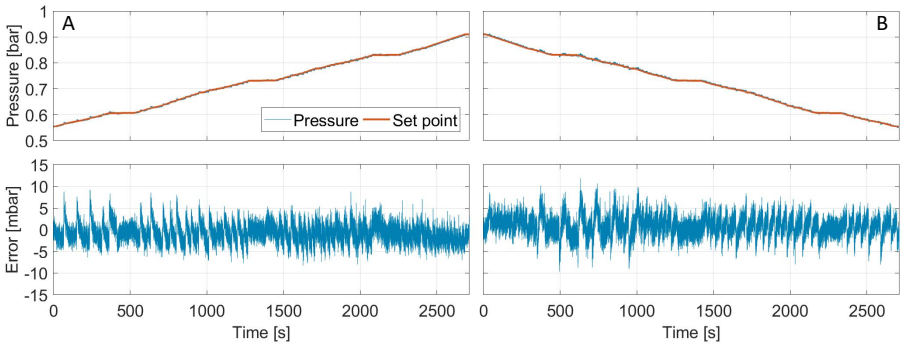

Figure 3. 78. MEDAS HD dynamic cycles: (A) Decreasing the altitude; (B) Increasing the altitude

3.3.5.2 1D model validation

To wrap up the development of the new MEDAS models, the steady-state testing results are used to validate the results obtained and improve the 1D model predictive accuracy. The dynamic results are not considered since the current 1D model programmed in VEMOD does not have dynamic capabilities.

When the mass flow calculated by the model is compared to the mass flow map obtained experimentally, both shown in Figure 3. 79, huge differences can be found. The biggest ones were in the maximum mass flow achievable at low altitudes and in the minimum flow (minimum of striped area) at which the MEDAS HD could operate at high altitudes.

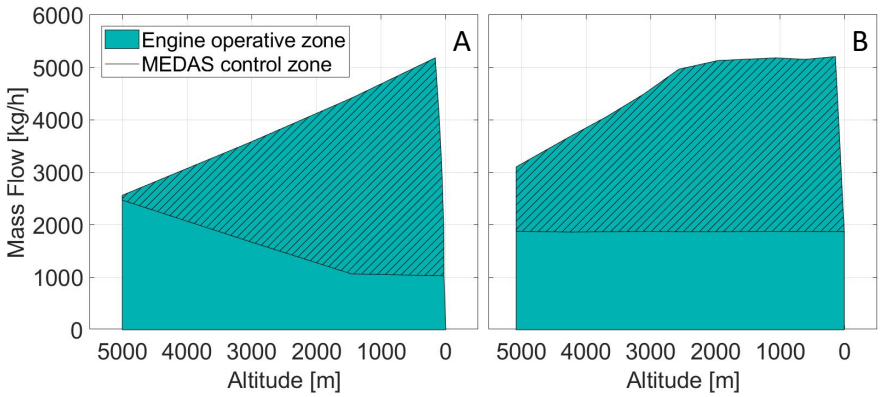

Figure 3. 79. MEDAS HD mass flow performance: (A) Initial performance estimation through 1D model; (B) Experimental performance map

These vast differences between the predicted and the actual mass flow performance are caused by an overestimation of the pressure drop in the exhaust line (from 5 to 10 in Figure 3. 31) by the pressure drop correlations included in the 1D model. In Figure 3. 80A is shown in a comparative graph, the

experimental results for the pressure drop in the exhaust line on the *x-axis* against the pressure drop predicted by the model on the *y-axis*. It is clear that the pressure drops in the model are overestimated and should be re-adjusted to fit the experimental data to achieve a more accurate prediction of the MEDAS performance with the 1D model. The cause found for the discrepancies in the exhaust line pressure drop is the suction effect of the compressor, which helps the flow pass through the inlet pipes and reduces the pressure losses, but was not considered during the CFD study.

Therefore, the correlations for the pressure drop in the mechanical compressor inlet geometry (D of Figure 3. 59) have been fitted to the experimental results obtained. This is carried out by applying a constant offset while maintaining the slope of the correlation equations obtained from CFD. This leads to the development shown in Figure 3. 80B, which shows how the prediction of the pressure drop is much better fitted to the experimental data. The new correlations obtained after the empirical fitting can be seen in Table 3. 19. The original and modified correlations are shown for each flow path defined for the mechanical compressor inlet geometry.

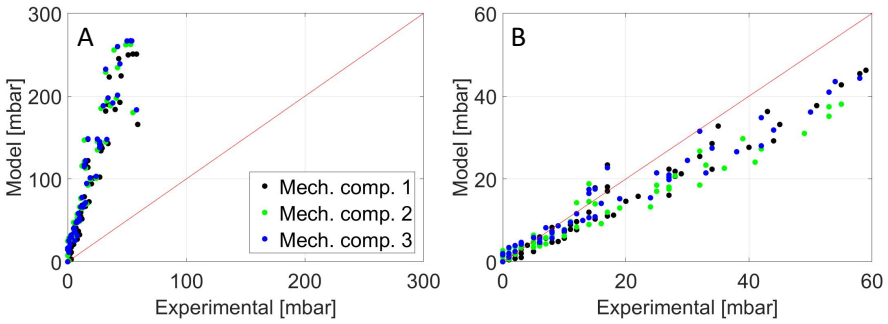

Figure 3. 80. Exhaust line pressure drop prediction from engine intake connection to mechanical compressors inlet: (A) Initial pressure drop correlations; (B) Adjusted pressure drop correlations to experimental data

Table 3. 19. Experimental fitting results of the pressure drop correlations for the mechanical compressor inlet geometry

Mechanical compressor inlet	Δp Correlation original	Δp Correlation modified
Cyclone 9-1 outlet – Mechanical compressor 10-1 inlet	$y = 0.0683x - 0.0432$	$y = 0.0683x$
Cyclone 9-1 outlet – Mechanical compressor 10-2 inlet	$y = 6.7292x - 6.9824$	$y = 6.7292x - 8.6087$
Cyclone 9-2 outlet – Mechanical compressor 10-3 inlet	$y = 0.1211x - 0.2372$	$y = 0.1211x - 0.2273$

Additionally, the pressure drop correlations obtained to calculate the mechanical compressor outlet geometry are also overestimating the backpressure that the compressors are facing, as shown in Figure 3. 81A. Here, the outlet compressor pressure is shown for the three compressors, with the *x-axis* being the experimental results and the *y-axis* the model calculated results.

Hence, the correlations for the three path flows (mechanical compressor outlet 10-1, 10-2, and 10-3 to MEDAS exhaust) must be fitted to the experimental results. There are two possible causes for the vast discrepancies between the CFD results and the experimental measurements in this geometry. On the one hand, the high flow complexity in this geometry, caused by the high flow velocity and swirl generated by the compressors, is not accurately considered by the CFD code used. On the other hand, the turbo compressor was not considered during the CFD study of the pressure drop due to assuming that the mass flow through it was negligible with respect to the total mass flow of the MEDAS. This caused an increase in the expected mass flow through the ducts and increased the predicted pressure drop.

In the case of this geometry, the correlations for the three flow paths defined must be disabled to achieve a correct fitting to the experimental data, which means forcing the C_d of the three flow paths to 1 (Table 3. 20). The effect of disabling the correlations for the MEDAS exhaust geometry is shown in Figure 3. 81B, where a clear improvement in the estimation of the pressure drop in the exhaust line is presented.

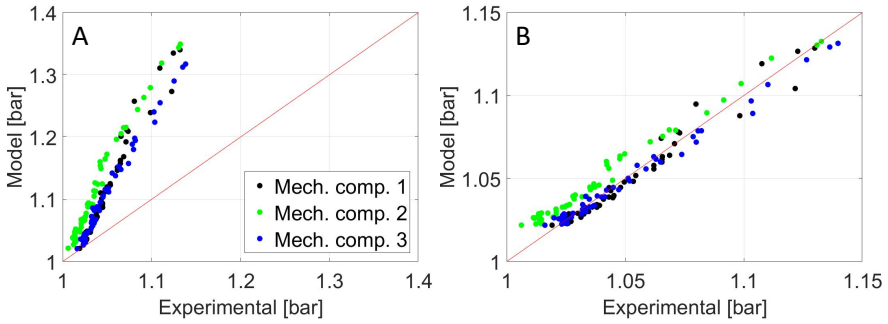

Figure 3. 81. Exhaust line pressure drop prediction from mechanical compressors outlet to MEDAS exhaust connection: (A) Initial pressure drop correlations; (B) Adjusted pressure drop correlations to experimental data

Table 3. 20. Experimental fitting results of the pressure drop correlations for the MEDAS exhaust geometry

MEDAS exhaust	Δp Correlation original	Δp Correlation modified
Mechanical compressor 10-1 outlet – MEDAS exhaust 12	$y = 0.2046x + 0.0827$	$y = 1$
Mechanical compressor 10-2 outlet – MEDAS exhaust 12	$y = 0.2134x + 0.0623$	$y = 1$
Mechanical compressor 10-3 outlet – MEDAS exhaust 12	$y = 0.1801x + 0.2052$	$y = 1$

Finally, after fitting the pressure drop correlations to the experimental measurements in the mechanical compressor inlet and MEDAS exhaust, it is possible to obtain accurate performance results with the 1D model for the MEDAS HD, as shown in Figure 3. 82. Fortunately, the experimental results were consistently more positive than the model predictions. Therefore, the design strategy has been proved to be on the security side, and it has shown clearly what aspects should be paid more attention to for different designs to be more accurate in the model-based first step.

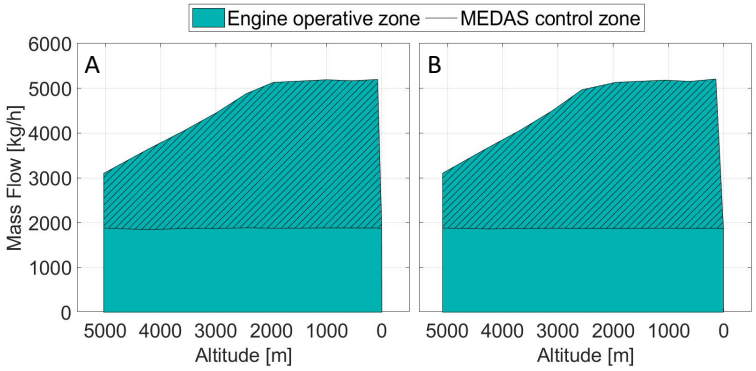

Figure 3. 82. MEDAS HD mass flow performance: (A) Performance estimation through 1D model; (B) Experimental performance map

3.4. Bibliography

[1] J. Gómez, "Development of an altitude simulator and analysis of the performance and emissions of turbocharged Diesel engines at different altitudes," Ph.D. Thesis, Universitat Politècnica de València, Spain, 2018. doi: 10.4995/Thesis/10251/101284.

[2] J. R. Serrano, P. Piqueras, E. Angiolini, C. Meano, and J. de La Morena, "On Cooler and Mixing Condensation Phenomena in the Long-Route Exhaust Gas Recirculation Line," in *SAE Technical Papers*, Sep. 2015, 2015-24-2521. doi: 10.4271/2015-24-2521.

[3] F. Payri, J. Galindo, H. Climent, and C. Guardiola, "Measurement of the oil consumption of an automotive turbocharger," *Experimental Techniques*, vol. 29, pp. 25–27, 2005, doi: 10.1111/j.1747-1567.2005.tb00236.x.

[4] A. Baylar and F. Ozkan, "Applications of venturi principle to water aeration systems," *Environmental Fluid Mechanics*, vol. 6, no. 4, pp. 341–357, Aug. 2006, doi: 10.1007/s10652-005-5664-9.

[5] E. Gorritxategi, "Online Wear Pattern Diagnostics in Rotating Machines Advanced Monitoring Technologies," Sep. 2018. Accessed: Dec. 22, 2021. [Online]. Available: https://www.mrotalk.eu/wp-content/uploads/2018/09/Atten2_Oil-sensors-for-industry.pdf

[6] Beckhoff Automation GmbH, "Beckhoff EL33xx-00x0," Jul. 2021. Accessed: Dec. 22, 2021. [Online]. Available: https://download.beckhoff.com/download/document/io/ethercat-terminals/el33xxen.pdf

[7] R. K. Shah, E. C. Subbarao, and R. A. Mashelkar, “Heat transfer equipment design.” Hemisphere Publishing Corp., 1988. doi: 10.1080/07373938908916636.

[8] A. Zukauskas and J. Ziugzda, “Heat transfer of a cylinder in crossflow.” 1985. Accessed: Dec. 22, 2021. [Online]. Available: https://ui.adsabs.harvard.edu/abs/1985wdch.book.....Z

[9] “Design of compressor air inlet protection for electrical ECS,” 2014. [Online]. Available: https://cordis.europa.eu/project/id/323414

[10] “ISO 12103-1 Arizona Test Dust Contaminants,” 2015. Accessed: Dec. 22, 2021. [Online]. Available: https://www.fiatec.com/upload/meine_bilder/dust-pdf/ISO_12103-1_Arizona_Test_Dust_A2_A4_2015.pdf

[11] S. Savic, G. Mitsis, C. Haertel, S. Khaidarov, and P. Pfeiffer, “Spray interaction and droplet coalescence in turbulent air-flow. an experimental study with application to gas turbine high fogging,” 2002. [Online]. Available: https://www.researchgate.net/publication/268056048

[12] J. R. Serrano, B. Tormos, K. L. Gargar, and F. Bouffaud, “Study of the effects on turbocharger performance generated by the presence of foreign objects at the compressor intake,” *Experimental Techniques*, vol. 37, no. 2, pp. 30–40, Mar. 2013, doi: 10.1111/j.1747-1567.2011.00795.x.

Chapter 4
Atmosphere Simulator: MEDAS + MTM + MHM

4.1. Introduction

One of the altitude simulator limitations developed during previous works [1] and improved in the current Ph.D. Thesis is that the MEDAS has a very narrow temperature control range and does not control the humidity of the combustion air provided to the engine. Therefore, to extend the control range of both temperature and humidity, two new equipment have been developed: the temperature extension module and the humidity extension module.

Together with MEDAS (A of Figure 4. 1), these two systems can control the three psychrometric variables of the atmosphere: pressure, temperature, and humidity. HORIBA has commercially called them: MTM (MEDAS Temperature Module) and MHM (MEDAS Humidity Module), shown in Figure 4. 1, identified by B and C, respectively.

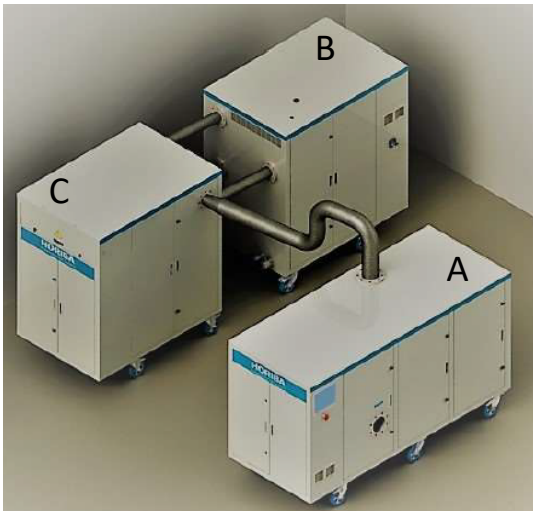

Figure 4. 1. Atmosphere simulator set: (A) MEDAS; (B) MTM; (C) MHM

These three pieces of equipment have been designed specifically for the experimental analysis of engines operation against variable atmospheric conditions, and they are conceived to be used at engines laboratories.

The development of the atmosphere simulator is focused on the design of the control strategies that govern the many actuators present in the MTM. The control will be designed based on PID-type controllers, who directly manage the variables to be controlled. In addition, the management of these variables is carried out with a cascade connection between actuators, which adds actuators to a specific control loop to handle a particular variable. It must be noted that this type of control has been chosen instead of other more precise ones, such as

predictive control by models or neural networks, due to the lack of memory of the PLC selected for the prototype.

The current section will be structured as follow. In the first place, the development of the control strategies of the MTM will be presented respecting the base installation layout found in the equipment patent [2]. Afterward, the design of the MHM main component, i.e., the bubble reactor, using computational fluid dynamics (CFD) calculations, will be presented together with the necessary modifications to the control strategies due to the addition of the MHM to the MEDAS + MTM set. Then, the atmosphere simulator's final combustion air conditioning performance is depicted in two operation modes: emulating a steady-state atmosphere and performing a dynamic atmosphere profile. Lastly, the atmosphere simulator developed is used to reproduce different road tests on an engine test cell installed at the laboratories of HORIBA MIRA in Nuneaton, England. In these tests, the pressure, temperature, and humidity are controlled by reproducing on the engine intake and exhaust the atmospheric conditions that the vehicle faced during the several RDE tests.

4.2. MTM development

The MTM is designed to extend the range of the temperature control of the MEDAS in two ways: controlling the MEDAS inlet temperature in hot or cold conditions and increasing the MEDAS inlet pressure to increase the cooling capabilities of the turbine through the increased expansion ratio. Moreover, as the MTM has installed a chiller, it can dry the air. This provides an additional but limited humidity control (just drying the ambient air) to the MEDAS + MTM set. The layout of this equipment was conceived by the Institute CMT-UPV previous to this Ph.D., and it was patented in 2019 [2]. The current section will be based on improving the accuracy of the control, the performance, and the energy efficiency of the whole assembly.

As the first step in this chapter, the layout described in the patent will be explained, introducing some modifications to the baseline patent from 2019 [2], which have been shown as necessary to improve the installation performance. Then, the control strategies developed for the different actuators and control targets will be described. Lastly, the steady-state and dynamic performance coupled with the MEDAS will be presented, and the improvement will be shown against the stand-alone MEDAS.

4.2.1. Layout

The layout of the MTM is designed to achieve all temperature and humidity combinations: hot and cold temperatures at the MTM outlet while keeping the possibility in each case of drying the air or not with the minimum number of components. The layout is shown in Figure 4. 2, in which the scheme of the MTM components coupled with the MEDAS is presented in Figure 4. 2A, with

an axonometric view of the MTM in Figure 4. 2B. In both figures, the elements have numbered identification to make it easier to follow the airflow path through the installation.

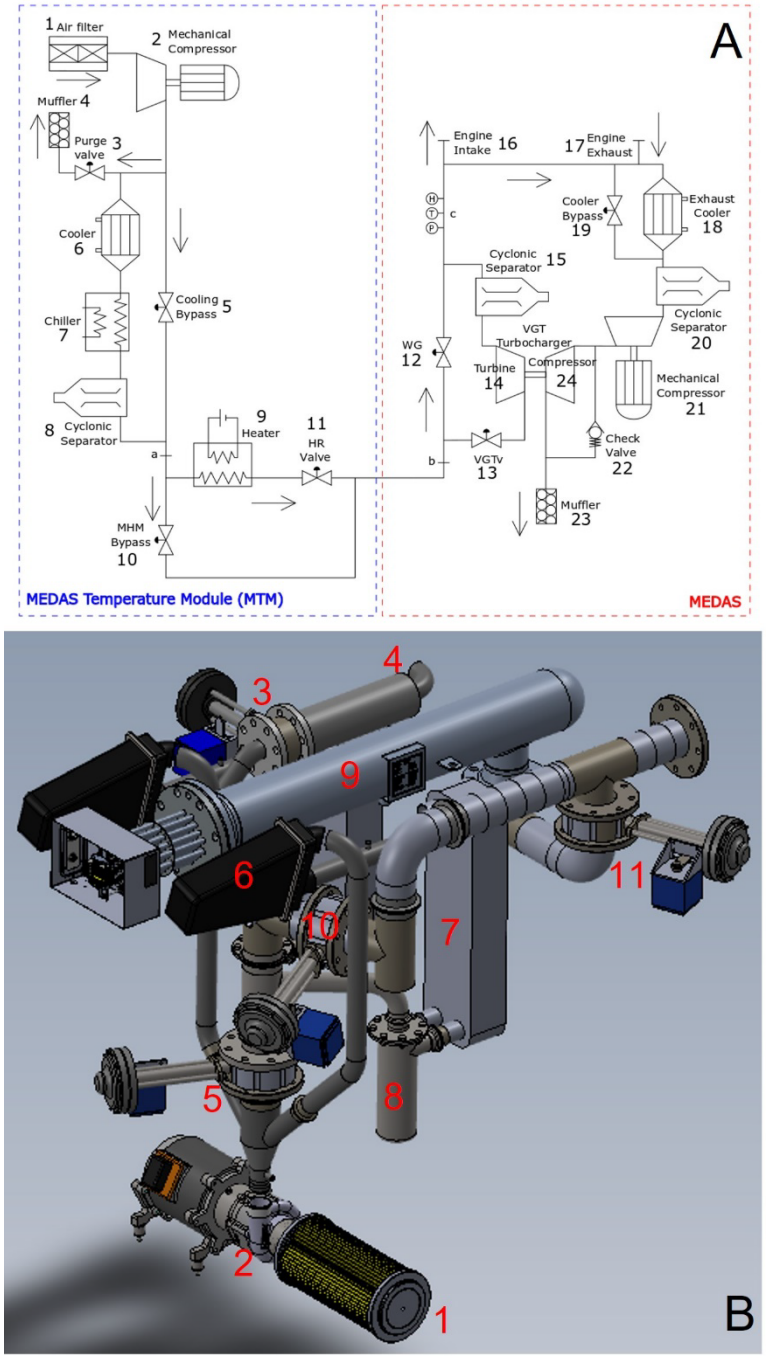

Figure 4. 2. MEDAS + MTM layout: (A) Elements scheme; (B) MTM 3D model axonometric view

The installation sucks air through the air filter (1 of Figure 4. 2A) and then goes to a mechanical compressor (2). Downstream is a purging valve (3) that prevents the mechanical compressor from entering the surge zone. It increases the mass flow rate through the compressor by opening the way to a discharge duct (4) with a muffler. The valve (3) controls the maximum pressure ratio with which the compressor can work at any given speed. Also, downstream of the mechanical compressor, the control valve (5) manages the temperature at point 'a' by mixing flow cooled down in the cooling branch with hot flow from the compressor (2) outlet. The cooling unit consists of a water-to-air cooler (6), which precools the air below 60ºC to protect the air-to-glycolic water chiller (7), which cools down the air to 5 ºC. After (7), the air plus water condensates generated during the cooling go to an inertial separator (8). The water droplets are separated from the air stream and extracted into the test cell drain system. It should be noted that the cooling circuit composed of heat exchangers (6 and 7) and a cyclonic separator (8) is divided into two symmetrical branches (Figure 4. 2B) to reduce the size of the components and increase the compactness of the MTM.

It was experimentally observed that when valve (5) was completely open, around 15% of the flow was still passing through the cooling branch, reducing the temperature at point 'a' when not needed. Therefore, for future evolutions, an additional valve should be included in the layout shown in the patent after the cyclonic separators (8), which should move in opposition to valve (5) to assure all the flow is bypassing the cooling system when hot conditions are necessary at point 'a'.

Once the air has been cooled and dried, the air could be reheated using an electric heater (9), if necessary, to achieve the temperature set point at far point 'c.' Also, the control valve (10) works in series with the electric heater. This helps avoid the thermal inertia of (9) when performing a point change from hot to cold conditions or vice versa. The control valve (11) is operated in opposition to (10) to make sure that all the flow is bypassing the heater (9) when the objective is to avoid its thermal inertia.

Once finished, the pre-treated air stream in the MTM enters MEDAS for the final adjustments in pressure and temperature. After entering MEDAS, the airflow can choose two paths: an isothermal expansion path or a cooling branch. In the isothermal course, the control valve (12) is located to manage the pressure at point 'c.' Contrarily, in the cooling path, control valve (13) is installed, which controls the temperature in point 'c' by regulating the amount of flow that passes through it. Following, only the quantity of combustion air needed by the engine flows through (16) towards the engine intake filter, while the remaining flow passes through the called 'bypass' or 'dilution' pipe. Downstream (16), the by-passed air mixes with the exhaust gases from the engine (17). Afterward, the mixture enters a water-to-air cooler (18) that cools it down to protect the

mechanical compressor (21) from overheating. The compressor (21) oversees controlling the mass flow rate through the installation, sucking the mix of air and exhaust gasses to keep them flowing out. Further explanations about the MEDAS conditioning process and operation are found in detail in Chapter 3 of the current Ph.D. Thesis, including the function and capabilities of all the components and control strategies.

4.2.2. Control strategies

The MTM objective is to conditionate the airstream temperature and dry it to get the pressure, temperature, and humidity conditions that the MEDAS needs to achieve the setpoints demanded by the user. The airstream will pass later through the MEDAS intake part for final conditioning. This is carried out by the share of information between both equipment (MEDAS and MTM), in which the MEDAS ask to increase or decrease the set points in the MTM (controlled in point 'a' and 'b' of Figure 4. 2A) while the MTM inform the MEDAS of its current state. This process can be summarized in two independent control blocks: one that controls the temperature and the other managing the pressure at the outlet of the MTM. It should be noted that the objective of these two control blocks is to help the MEDAS to achieve the setpoints demanded by the user while keeping the actuators involved far from saturation. If saturation is reached, the effect over the control variable would be lower, and thus there would be delays in the system's dynamic response.

Additionally, an extra control block is included to protect the mechanical compressor of the MTM against the surge. Since the MEDAS imposes the operative point of the compressor, the compressor may end up operating with high pressure ratio combined with low mass flow, which means working too close or even inside the surge area.

These three control blocks must be operated by the actuators available in the MTM, which are composed mainly of four types: control valves, a mechanical compressor, an electric heater, and heat exchangers. In the current section, the control strategies developed for the MTM will be discussed, and the function and target of the different actuators found in the MTM will be detailed for every control mode.

4.2.2.1 Pressure control

The pressure control of the MTM is directly managed by the demands of the MEDAS and actuates solely over the mechanical compressor speed. This control influences the three control variables: pressure, temperature, and humidity, which means that all the MEDAS set points can cause a change in the MTM compressor speed. For example, to further increase the engine intake pressure (point 'c') when the WG valve (12 of Figure 4. 2) is entirely open or to reduce the engine intake temperature when the VGTv (13 of Figure 4. 2) is also fully open, or to dry the air when the cooling bypass (5 of Figure 4. 2) is fully

closed. Therefore, a hierarchical sequence between the three controlled variables should be implemented to prioritize the main feature and avoid couplings with the rest.

The main variable that should be achieved is the pressure, which is the one that defines the altitude at which the engine is operating and the focus of most MEDAS users. The next in the hierarchy is the temperature, which the atmosphere simulator will try to achieve if it does not conflict with the pressure demands. And lastly comes, humidity, which will be achieved only if the other two variables: pressure and temperature, are inside the accepted accuracy range of their setpoints (also due to the influence of pressure and temperature in relative humidity).

Therefore, the pressure control of the MTM is achieved by controlling the mechanical compressor speed (2 of Figure 4. 2) considering the MEDAS demands but imposing the hierarchy sequence defined. This process will be explained below.

a) Base speed

The MTM mechanical compressor has a minimum speed equal to 70% of the compressor speed of the MEDAS, which is the base speed (pre-defined control state) from which the pressure control starts correcting the MTM compressor speed to achieve the MEDAS setpoints. This is done to obtain a reference speed when starting up the system and define a working point if the MEDAS does not have any demand on its inlet pressure.

b) Minimum pressure estimation

Considering the pressure, temperature, and humidity setpoints demanded, another minimum pressure is defined. To achieve it, two equations have been proposed. The first one will be determined by considering the cooling power in the MEDAS turbine (14 of Figure 4. 2), which will estimate the minimum pressure at the MEDAS inlet to achieve the pressure and temperature set points. And the second equation, by considering the drying capabilities of the cooling branch of the MTM (6, 7, and 8 of Figure 4. 2), estimates the minimum pressure necessary to achieve the humidity setpoint. Afterward, taking the maximum value from these two equations, the minimum theoretical pressure at the MEDAS inlet to fulfill the three demands is obtained.

Starting with the first equation, the initial step is to define a pressure ratio in the MEDAS inlet ($PR_{MEDAS,in}$, between point 'b' and 'c' of Figure 4. 2). This pressure ratio is presented in Equation 4. 1, dependent on the MEDAS inlet pressure ($p_{MEDAS,in}$, point 'b') and the target pressure ($p_{SP,}$ point 'c').

$$\boldsymbol{PR_{MEDAS,in}} = {}^{\boldsymbol{p_{SP}}}/_{\boldsymbol{p_{MEDAS,in}}}$$

Equation 4. 1

Afterward, experimental characterization of the cooling capability in the turbine line, dependent on the pressure ratio, is performed. The results are shown in Figure 4. 3 through blue markers, from which a correlation for the expected cooling in the turbine line can be obtained. The correlation is represented by a black line in Figure 4. 3 and presented in Equation 4. 2. $\Delta T_{Turbine}$ is the minimum temperature drop expected in the three elements of the turbine line: the VGT valve (13), the turbine itself (14) and the cyclonic separator (15), and $PR_{MEDAS,in}$ is the pressure ratio at the MEDAS inlet defined in Equation 4. 1. The turbine cooling correlation has been fitted to the minimum performance expected by the turbine line to always sub-estimate the cooling capabilities of the turbine line. When considering the lowest performance shown by the turbine line during the experiments, the compressor speed of the MTM will be higher, and the VGTv valve (13), which controls the temperature at point 'c,' is operating with a partial opening instead of saturating. This strategy improves the time response against perturbances or changes in the setpoints, although the energy consumption increases slightly (around 5%).

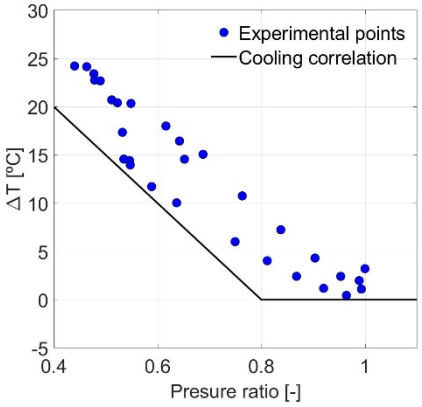

Figure 4. 3. Experimental characterization of the turbine cooling capabilities

$$\Delta T_{Turbine} = 40 - 50 * PR_{MEDAS,in}$$

Equation 4. 2

Also, the cooling that the MEDAS must perform to reach the temperature setpoint can be estimated following Equation 4. 3, in which the turbine cooling needed ($\Delta T_{Turbine} = \Delta T_{MEDAS}$) is known by the difference between the inlet temperature ($T_{MEDAS,in}$, point 'b'), which ideally should be 5ºC (temperature setpoint of the chiller, which is the colder point of the MTM), and the temperature setpoint demanded by the user (T_{SP}, point 'c').

$$\Delta T_{Turbine} = \Delta T_{MEDAS} = T_{MEDAS,in} - T_{SP}$$

Equation 4. 3

Then, combining Equation 4. 1, Equation 4. 2 and Equation 4. 3, the minimum pressure needed at the MEDAS inlet to achieve the pressure and temperature set point is obtained through Equation 4. 4.

$$p_{MEDAS,in} = \frac{p_{SP}}{\frac{40 - T_{MEDAS,in} + T_{SP}}{50}}$$

Equation 4. 4

The second equation considers the minimum pressure needed at the MEDAS inlet to achieve the humidity setpoint demanded by the user (w_{SP}). This is obtained by solving the psychrometric equation (Equation 4. 5) for the pressure, in which p_w is the water vapor pressure obtained through Equation 4. 6, p_{ws} is the saturated water vapor pressure obtained with Equation 4. 7, and $T_{Chiller,out}$ and $RH_{Chiller,out}$ are the temperature and relative humidity of the airstream at the outlet of the MTM cooling branch (point 'a' of Figure 4. 2), respectively.

$$w_{SP} = \frac{621.96 * p_w}{p_{MEDAS,in} - p_w}$$

Equation 4. 5

$$p_w = {RH_{Chiller,out} * p_{ws}}/{100}$$

Equation 4. 6

$$p_{ws} = 10^{2+2.6543-\frac{1435.264}{208.30199+T_{Chiller,out}}}$$

Equation 4. 7

Then, to achieve the final correlation shown in Equation 4. 8, it is assumed that $T_{Chiller,out}$ is 5 ºC, which is the temperature target of the MTM cooling branch (6, 7, and 8), and $RH_{Chiller,out}$ is 100% since there is condensation in the cooling branch.

$$p_{MEDAS,in} = 0.01 + \frac{5.2359}{w_{SP}}$$

Equation 4. 8

Therefore, the minimum pressure that the MEDAS requires at its inlet to achieve the three set points is defined by taking the maximum from both pressure equations, Equation 4. 4 and Equation 4. 8.

Then, pressure losses in the MTM are calculated by comparing two pressure sensors, one located at the MTM mechanical compressor outlet ($P_{C,out,sensor}$, downstream 2 of Figure 4. 2) and the other at the MEDAS inlet ($P_{MEDAS,in,sensor}$, point 'b'). Afterward, when the pressure losses in the MTM are considered, the

minimum needed pressure at the mechanical compressor outlet in the MTM (2 of Figure 4. 2) can be calculated (Equation 4. 9).

$$\boldsymbol{p_{C,out}} = \boldsymbol{p_{MEDAS,in}} + \left(\boldsymbol{p_{C,out,sensor}} - \boldsymbol{p_{MEDAS,in,sensor}}\right)$$

Equation 4. 9

Lastly, with a normalized mass flow map for the compressor, the minimum speed necessary to achieve the three set points of the MEDAS is obtained, dependant on the mass flow set point of the MEDAS and the pressure ratio needed on the mechanical compressor of the MTM.

In the first place, the pressure ratio in the MTM mechanical compressor ($\Pi_{C,MTM}$, 2 of Figure 4. 2) is defined following Equation 4. 10, in which $p_{C,out}$ is the compressor outlet pressure calculated from Equation 4. 9, and $p_{C,in,sensor}$, which is the measurement of the pressure sensor located at the compressor inlet.

$$\Pi_{\boldsymbol{C,MTM}} = {\boldsymbol{p_{C,out}}}/{\boldsymbol{p_{C,in,sensor}}}$$

Equation 4. 10

Following, the normalization of the compressor map is carried out with the methodology explained below. Firstly, the compressor map's corrected mass flow and pressure ratio are normalized to their maximum and minimum value. This is done following Equation 4. 11, in which α_{norm} is the normalized result, α is the variable to be normalized, α_{max} is the maximum value in the compressor map for the variable to be normalized, and α_{min} is the minimum value in the compressor map for the variable to be normalized.

$$\boldsymbol{\alpha_{norm}} = \frac{\boldsymbol{\alpha - \alpha_{min}}}{\boldsymbol{\alpha_{max} - \alpha_{min}}}$$

Equation 4. 11

The pressure ratio (Π_C) is obtained through Equation 4. 12 and the corrected mass flow ($\dot{m}_{corr}$) with Equation 4. 13. Being $\dot{m}$ the real mass flow that passes through the compressor, $p_{C,out}$ the compressor outlet pressure, $p_{C,in}$ the compressor inlet pressure, and $T_{C,in}$ the compressor inlet temperature.

$$\Pi_{\boldsymbol{C}} = {\boldsymbol{p_{C,out}}}/{\boldsymbol{p_{C,in}}}$$

Equation 4. 12

$$\boldsymbol{\dot{m}_{corr}} = \boldsymbol{\dot{m}} * \frac{\sqrt{{\boldsymbol{T_{C,in}}}/{\mathbf{288.15}}}}{{\boldsymbol{p_{C,in}}}/{\mathbf{1.013}}}$$

Equation 4. 13

Once these two parameters are normalized, the compressor map can be collapsed through a correlation parameter (X). Then, with this correlation, the compressor speed can be obtained for a given combination of pressure ratio and mass flow.

The proposed solution for X is presented in Equation 4. 14, in which α and β are the correlation coefficients that will be used to collapse the compressor map, while $\Pi_{C,norm}$ and $\dot{m}_{corr,norm}$ are the pressure ratio and the corrected mass flow of the compressor map normalized following Equation 4. 11, respectively.

$$X = \sqrt{\dot{m}_{corr,norm}{}^{\alpha} + \Pi_{C,norm}{}^{\beta}}$$

Equation 4. 14

In Figure 4. 4, the compressor map points are represented by blue dots. The *x-axis* represents the correlation parameter defined in Equation 4. 14, and the *y-axis* the corrected speed of the compressor. To achieve these results, the coefficients α and β have been selected as 3.5 and 2, respectively, for the mechanical compressor used in MTM (2 of Figure 4. 2). Also, the points used to build the correlation equation are marked with red dots, corresponding to the lower value of the parameter defined in Equation 4. 14 for each corrected speed.

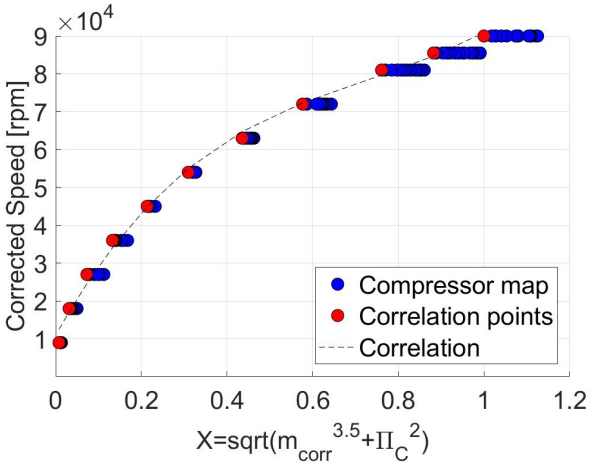

Figure 4. 4. Result of applying the correlation to the collapse of the mechanical compressor map

Finally, the correlation obtained by fitting the red dots to a polynomial is presented in Equation 4. 15. The theoretically minimum mechanical compressor speed of the MTM will be estimated for every set of setpoints defined by the user for the MEDAS. Being N the compressor speed, $T_{C,in}$ the compressor inlet temperature and X the result obtained from applying Equation 4. 14 to the setpoints demanded.

$$\boldsymbol{N = \left(103856X^3 - 226306X^2 + 202385X + 10963\right) * \sqrt{T_{Cin}/288.15}}$$

Equation 4. 15

A summary of the whole process is depicted in Figure 4. 5 through a flow diagram. The different equations used to obtain the MTM minimum mechanical compressor speed estimation are shown step by step. Here are shown two processes first, the generation of Equation 4. 15 by simplifying the compressor map. And then, the second calculates the minimum speed needed to achieve the set of user demands: pressure, temperature, and humidity.

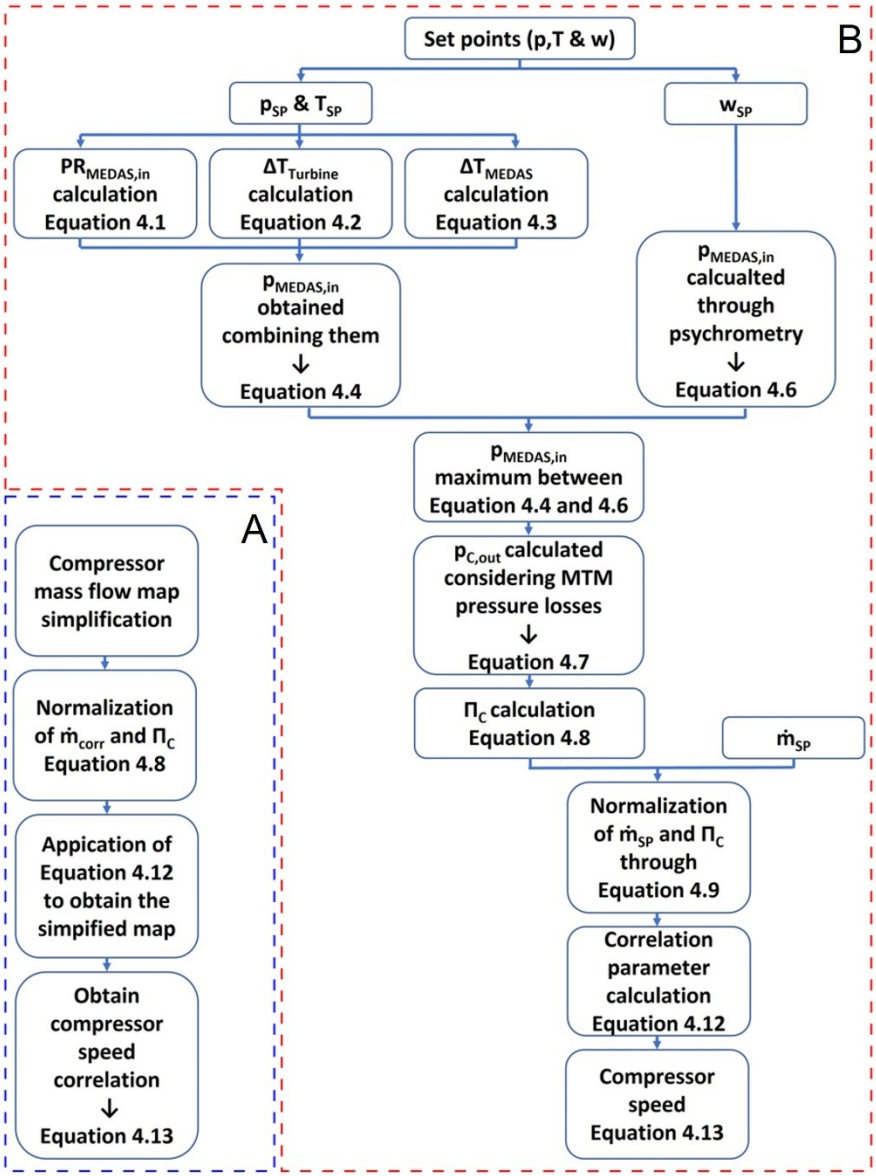

Figure 4. 5. Flow diagram of the MTM minimum mechanical compressor speed calculation process: (A) Correlation of the compressor map; (B) Calculation of the minimum speed for a set of user demands

c) MEDAS pressure control extension

Another way in which the MEDAS can demand a change in the MTM compressor speed is through its pressure proportional integral derivative (PID)

controller. When the MTM is connected to the MEDAS, the pressure PID, which actuates the WG valve (12) and the VGT vanes (14), is extended, adding the MTM mechanical compressor (2) as an extra actuator in series with the other two. Meaning that if the WG valve and the VGT vanes are saturated at a fully open position, and the pressure setpoint is not reached (lower pressure than demanded), the mechanical compressor of the MTM will increase its speed to achieve the pressure set point at point 'c' of Figure 4. 2. Moreover, suppose both actuators (WG valve and VGT vanes) are fully saturated, and the pressure setpoint is lower than the measurement. In that case, the mechanical compressor changes its speed but decreases it to achieve the pressure demanded.

The control sequence of the pressure control when the MTM is connected to the intake of MEDAS is shown in Figure 4. 6, in which can be seen how the three actuators: WG valve (12), VGT vanes (14), and MTM mechanical compressor (2); work in series. In this figure, the *y-axis* represents the actuation percentage (opening for the valves and speed for the compressor), and the *x-axis* represents the pressure demand. The higher the pressure demanded by the control, the more to the right in the graph is displaced the current operative point. The compressor speed appears twice in the scheme since it can increase when both valves are fully open (right side) or decrease when both valves are fully closed (left side).

In the case of the VGT vanes shown in Figure 4. 6, the actuation decreases when trying to increase the pressure due to the control signal configuration of this actuator. Contrarily to the WG valve, the VGT vanes are controlled by imposing a closing percentage. Therefore, to open the flow passage through the turbine, the actuation should decrease until it reaches 0% of closing, and vice versa to close it.

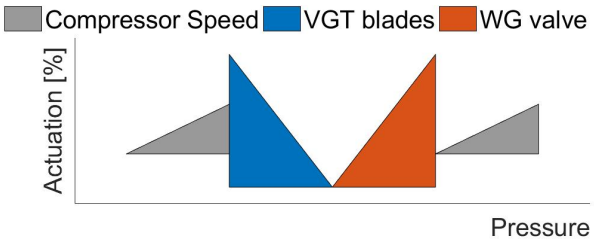

Figure 4. 6. Pressure PID actuation sequence

Additionally, when the MTM is connected, the actuation range of the pressure control actuators, such as the WG valve (12) and VGT vanes (14), should be limited to improve its dynamic response. This is needed due to the low response areas of the actuators that appear near the saturation of the actuation range (0% and 100% opening), in which the movement of the valves has a negligible effect on the pressure downstream introducing a delay. This small effect area of the actuation range appears until the excellent control area of their actuation range is reached. Therefore, these actuators are limited in their maximum and

minimum opening to try and avoid these non-responsive working areas. The solution adopted for the actuators of the pressure control installed in the MEDAS is compiled in Table 4. 1.

Table 4. 1. MEDAS pressure control actuators' actuation range

Actuator	Actuation range [%]
WG valve	10 - 80
VGT vanes	30 - 100

d) Temperature setpoint corrections

There is a correction to the MTM compressor pressure (and accordingly compressor speed) considering the temperature control of the MEDAS. When the MEDAS cannot reach a low-temperature setpoint due to lacking expansion ratio in the turbine to cool down the air, or the expansion is too high, and thus the minimum cooling in the turbine is too much, the mechanical compressor of the MTM (2 of Figure 4. 2) increases or reduces its speed accordingly.

These cases are defined by the position of the VGTv valve (13 of Figure 4. 2), which controls the flow through the turbine and the temperature in point 'c' of Figure 4. 2. When the VGTv is fully open, the cooling in the turbine (14) is not enough to reach the temperature setpoint, and MEDAS demands the MTM for an increase in pressure. However, this only happens when the cooling bypass valve (5) is closed, meaning that the cooling branch in the MTM (6, 7, and 8 of Figure 4. 2) is working at full power. Even when the MEDAS is demanding higher pressure, it is assumed to be a better solution if the setpoint is reached by reducing the MEDAS inlet temperature. It introduces fewer perturbances in the rest of the controls.

Contrarily, when the VGTv is fully close, and the temperature is below the setpoint, the cooling in the turbine is too high. Therefore, the MEDAS demands the MTM to reduce the pressure at its inlet. In this case, the cooling system of the MTM is not considered since reducing the compressor speed is always a good strategy. It reduces the system's energy consumption and increases the accuracy of the controlling valves of the MEDAS. The mentioned control-accuracy increase happens due to the lower pressure difference between the inlet and outlet sides of the control valves for a given pressure setpoint, which allows a smoother movement of the actuation plate of the valves.

It should be noted that similarly to the case of the WG and the VGT vanes, the VGTv also needs a reduction in its actuation range to avoid the non-responsive working areas near the maximum and minimum saturation. In the case of the VGTv valve, the actuation range has been limited between 20% and 85% of its whole opening to improve its dynamic response.

Also, applying this compressor speed control is conditioned to achieving the pressure setpoint. Meaning that if the pressure setpoint of the MEDAS is not reached or is not stable, the demand of the temperature control to increase or decrease the compressor speed will not be fulfilled. This condition must be included since the priority of the atmosphere simulator is the pressure in the first place and then, if possible, the temperature.

e) Humidity setpoint corrections

Finally, suppose the humidity setpoint is not reached (the humidity sensor measures higher values than the setpoint). In that case, the compressor of the MTM increases its speed to increase the pressure in the cooling branch and thus condensate more water from the air at the same temperature [3]. However, this only happens if the cooling unit in the MTM is working with the entire flow (valve 5 is fully closed) since it is assumed as a better solution if the setpoint can be reached by increasing the flow passing through the cooling branch.

This correction to the compressor speed is applied conditioned to the achievement of the pressure and temperature setpoints instead of the position of actuators. The speed of the MTM mechanical compressor is increased by the action of the MEDAS humidity error if the increase of speed does not impede the fulfillment of the pressure or the temperature setpoints. If not, the increase in compressor speed demanded by the humidity setpoint will not be fulfilled. Since as explained previously, the priority of the atmosphere simulator is in the first place the pressure, then the temperature, and lastly the humidity.

f) Summary of the pressure control

As a summary of the decision-making process presented in this section, a flow diagram with the different steps is shown in Figure 4. 7.

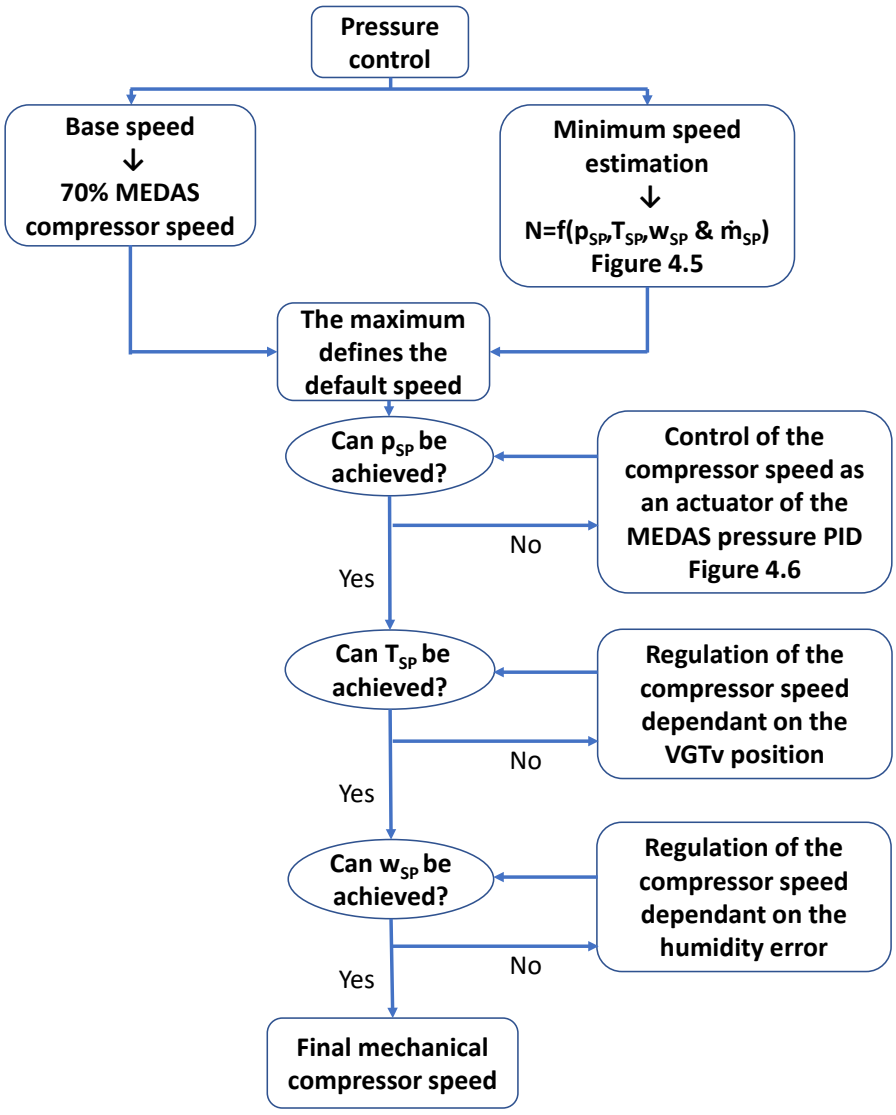

Figure 4. 7. Flow diagram of the MTM pressure control sequence

4.2.2.2 Temperature control

Following, the temperature control of the MTM responds directly to the demands of the MEDAS since its objective is to provide the airstream at a temperature from which the MEDAS can achieve its setpoint. This means that the temperature provided should be slightly higher than the MEDAS setpoint since the MEDAS can cool down the air but does not have heating capabilities.

The temperature control is also responsible for adjusting the amount of water contained in the airstream. Since to dry the air, it must be cooled down below the dew point [3]. Similar to the pressure control case, this introduces the need to define a hierarchy between the temperature and the humidity control. The temperature is defined as the priority, and when possible (after the temperature setpoint is achieved), the humidity is adjusted.

This is carried out through two PIDs: one focused on the bypass valve of the cooling branch (5 of Figure 4. 2), and the other on the electric heater (9). In the first place, the PID on the bypass valve of the cooling branch (5), known as the cooling bypass, is the one in charge of cooling down and drying the air. It is focused on controlling a temperature setpoint generated by the demands of the MEDAS on the electric heater inlet (point 'a' of Figure 4. 2). Contrarily, the electric heater oversees the heating of the air, and it controls the temperature at the far point 'c' of Figure 4. 2, located in the MEDAS.

Therefore, the temperature setpoint defined for the MTM ($T_{SP,MTM}$) presented in the following sections is only controlled by the cooling bypass. The electric heater will be working directly on the temperature setpoint of the MEDAS demanded by the user.

a) $T_{SP,MTM}$ generation

The first step is to define a default temperature setpoint ($T_{SP,MTM}$) which will be used as the reference state of the control until the MEDAS starts demanding a change in its inlet temperature to achieve the user set points. This is estimated using an experimental correlation for the turbine installed in MEDAS, defined in previous Section 4.2.2.1b), in which the expected cooling in the turbine ($\Delta T_{Turbine}$, 14 of Figure 4. 2) can be obtained depending on the expansion ratio (Equation 4. 2), and the temperature setpoint defined by the user in the MEDAS (T_{SP}). Therefore, the default value for $T_{SP,MTM}$ is obtained by Equation 4. 16.

$$\boldsymbol{T_{SP,MTM} = T_{SP} + \Delta T_{Turbine}}$$

Equation 4. 16

Heat losses correction

The temperature setpoint undergoes the first correction due to the heat losses to and from the ambient between the control point in the MTM ('a') and the MEDAS inlet ('b'). This is carried out by considering the sensors' measurements at the heater inlet ($T_{Heater,in}$, point 'a' of Figure 4. 2) and the MEDAS inlet ($T_{MEDAS,in}$, point 'b' of Figure 4. 2). The temperature setpoint is modified depending on the difference between both sensors, which can be increased or decreased depending on the direction of the heat flux. If $T_{Heater,in}$ (point 'a') is lower than $T_{MEDAS,in}$ (point 'b'), the airstream is heating up due to absorbing heat from the ambient, which will cause a decrease in the setpoint. Contrarily, when $T_{Heater,in}$ is higher than $T_{MEDAS,in}$, the heat losses will cool down

the airstream, and the setpoint will increase. This behavior of the heat losses in the MTM piping (ΔT_{MTM}) is represented by Equation 4. 17.

$$\Delta \boldsymbol{T_{MTM}} = \boldsymbol{T_{SP,MTM}} + \left(\boldsymbol{T_{Heater,in}} - \boldsymbol{T_{MEDAS,in}}\right)$$

Equation 4. 17

It should be additionally noted that the heat losses correction is activated or not depending on the electric heater (9 of Figure 4. 2) state. The heat losses correction is not applied if the heater (9) is activated. When the heater controls the temperature, it is unclear where the heat losses are located and in which direction the heat transfer happens. The heat influx between $T_{Heater,in}$ and $T_{MEDAS,in}$ is a desired actuation of the heater. Moreover, in this case, the heater actively controls the temperature setpoint in the MEDAS through a PID, which compensates for whichever heat loss between these two points.

Temperature setpoint corrections

Furthermore, $T_{SP,MTM}$ ('a' of Figure 4. 2) can be modified by the state of the VGTv valve (13 of Figure 4. 2), the actuator that manages the temperature control in the MEDAS. If the VGTv valve (13) is near saturation, the MEDAS demands that $T_{SP,MTM}$ changes to avoid a complete saturation of the VGTv. This is carried out by a simplified integral control, which increases or decreases $T_{SP,MTM}$ depending on the error of the temperature PID of the MEDAS and following Equation 4. 18. T_{SP} is the temperature setpoint of the MEDAS, T_{EI} is the temperature measurement at point 'c' of Figure 4. 2, and *C* is a constant that marks the speed at which $T_{SP,MTM}$ change, which has been defined as 0.001 for this application. The change speed is considerably slow to avoid perturbances in the system due to aggressive valve movements and maintain a smooth installation operation.

$$\boldsymbol{T_{SP,MTM}} = \boldsymbol{T_{SP,MTM}} + (\boldsymbol{T_{SP}} - \boldsymbol{T_{EI}}) * \boldsymbol{C}$$

Equation 4. 18

Humidity setpoint corrections

Lastly, there is also a correction for $T_{SP,MTM}$ due to the state of the humidity control of the MEDAS. Similar to the temperature setpoint correction, the humidity correction is carried out using a simplified integral control, which modifies $T_{SP,MTM}$ depending on the error of the humidity control of the MEDAS, following Equation 4. 19. w_{SP} is the temperature setpoint of the MEDAS, w_{EI} is the temperature measurement at point 'c,' and *C* is the constant that marks the speed at which $T_{SP,MTM}$ change. Similar to the case of the temperature, the speed coefficient *C* is defined as 0.001 for the humidity.

$$\boldsymbol{T_{SP,MTM}} = \boldsymbol{T_{SP,MTM}} + (\boldsymbol{w_{SP}} - \boldsymbol{w_{EI}}) * \boldsymbol{C}$$

Equation 4. 19

However, contrarily to the temperature case, this correction is not applied dependant on the position of the controlling actuator. Instead the correlation is demanding a lower $T_{SP,MTM}$ as long as the temperature of the MEDAS is reached ($|T_{SP} - T_{EI}| < 1$°C) and the humidity measurement is higher than the set point demanded by the user ($w_{SP} < w_{EI}$). This assures that the hierarchy sequence defined for this control is respected, since the demands due to the humidity error are only applied if the temperature can be achieved.

Summary of $T_{SP,MTM}$ generation

A summary of the decision-making process in this section is shown in Figure 4. 8 in a flow diagram with the different steps.

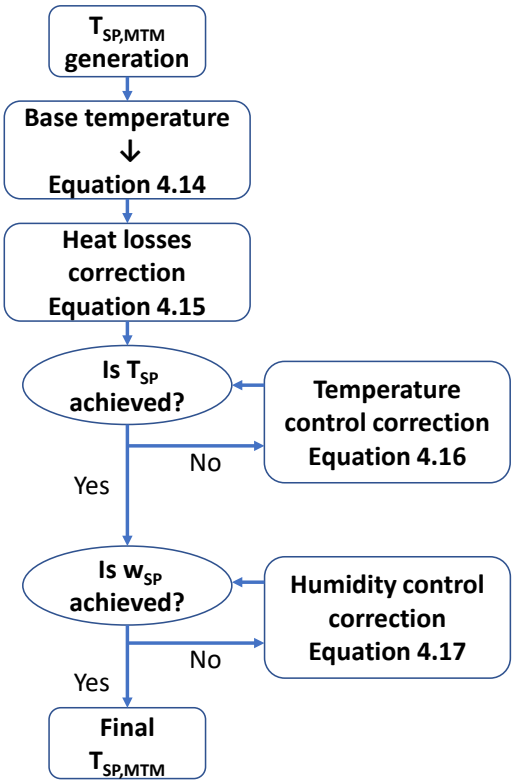

Figure 4. 8. Flow diagram of the $T_{SP,MTM}$ generation sequence

b) Heater control

Independently of the cooling bypass control of $T_{SP,MTM}$, the electric heater is controlling the temperature at the engine intake in the MEDAS (point 'c' of Figure 4. 2), in parallel with the MEDAS temperature control, utilizing a PID over the electric power supplied to the heater.

Additionally, this control has a couple of valves (11 and 10 of Figure 4. 2) working in series with the heater (9) to avoid the thermal inertia of the heater when there is a temperature setpoint change in the MEDAS. For example, the MEDAS is controlling 30ºC at the engine intake ('c'), and the user demands a setpoint of -5ºC to perform a different test on the engine. In this case, the heater is hot since it was helping the MEDAS control 30ºC. Therefore, it is faster to bypass the heater than just switching it off and cooling down all the metal to achieve the new cold setpoint.

Two valves achieve this: the MHM bypass valve and the HR valve (10 and 11 of Figure 4. 2, respectively), which are used to bypass the heater in these cases. On the one hand, the MHM bypass valve (10) is controlled in series with the heater's electric power. The valve is closed while the heater is consuming energy and only opens when the control signal of the heater is cero. On the other hand, the HR valve (11) is controlled in opposition to the MHM bypass valve (10), meaning that the HR valve is closed when the bypass is open and vice versa. This is shown in the control diagram presented in Figure 4. 9. The *x-axis* represents the temperature demand. The higher the temperature demand, the further right on the chart is the operative point. The *y-axis* represents the actuation percentage of the actuators included.

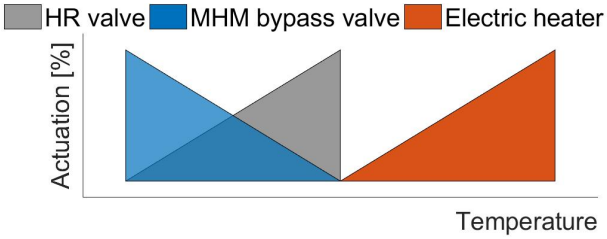

Figure 4. 9. The electric heater control sequence

It should be noted that the control defined and the location of the electric heater in the MTM layout allow the control of the temperature of the air to whichever temperature inside the MEDAS control range. This is achieved with the temperature control decoupled from the humidity since the air is heated up without adding moisture after the drying in the cooling branch.

4.2.2.3 Surge control

Finally, the objective of the surge control block is to protect the mechanical compressor of the MTM against surge risk, which can be reached depending on the demand of the MEDAS. This risk appears when the user demands cold temperature at the engine intake (point 16 of Figure 4. 2A) and low mass flow, in which the compressor of the MTM (point 2 of Figure 4. 2A) starts working with high pressure ratio to increase the cooling capabilities of the MEDAS turbine (14) but low mass flow, leading to reach surge.

In this case, the MEDAS imposes the mass flow that passes through the installation following the user setpoint. Still, the MTM compressor must provide the maximum pressure possible to reach the temperature setpoint. This leads to the MTM compressor (2) working near or inside the surge area, which is harmful and can cause damage to the component. Moreover, the pressure provided during this operation is not stable, which introduces perturbances in the pressure control of the MEDAS and does not allow to fulfill the specifications of pressure-stabilization's accuracy.

The surge prevention is achieved with a controlled valve (3 of Figure 4. 2) installed downstream of the mechanical compressor, which manages the opening and closing of a purge duct connected to the ambient (4 of Figure 4. 2) employing a PID controller. This valve is constantly monitoring the pressure ratio of the compressor while trying to achieve a maximum pressure ratio depending on the compressor's speed. Therefore, if the pressure ratio is below the setpoint, the valve closes to increase it. Contrarily, it opens when the pressure ratio is above the setpoint. In this way, when the operation points of the compressor approach the surge margin, the valve opens and lets more airflow through the compressor, displacing the operative point to the right in the compressor map, away from the surge area.

The key to this control is the definition of the maximum pressure ratio equation dependant on the compressor speed. This has been obtained through an experimental characterization. The pressure ratio was increased for a given compressor speed until instabilities in the compressor outlet pressure appeared or the formation of hot-backflows at the compressor inlet (also a clear sign that the compressor is approaching surge limit). This was done by increasing the compressor's speed from 10% to 100% in steps of 10%. The experimental campaign carried out with the MTM prototype is shown in Figure 4. 10, plotted with red markers on the compressor map. The next step is to fit the experimental points to a polynomial equation dependent on the compressor speed (red line of Figure 4. 10). This equation will provide the pressure ratio setpoint for the surge control.

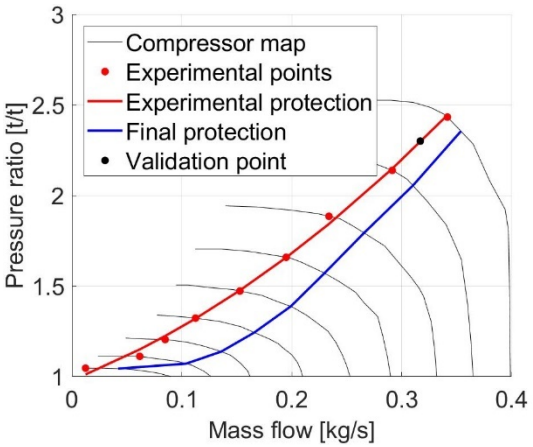

Figure 4. 10. MTM prototype surge protection curve identification

In some cases, when the compressor works in the experimental set points obtained, there is a slow increase of the temperature at the compressor intake produced by the backflows that happen when the compressor approaches surge margin. This is shown in Figure 4. 11A, in which compressor inlet temperature against time is presented for a compressor operative point with 95 krpm (black dot of Figure 4. 10). Because of this phenomenon, the final setpoint curve for the MTM prototype should be displaced to the right in the compressor map to avoid these shallow surge conditions that appeared during the validation. It should be noted that this did not happen in all the points tested during the validation, neither occur every time a given experimental point was tested. This means that the limit found is too close to surge, and small by-chance perturbances can cause the compressor to reach a dangerous stall in the compressor vanes, which causes hot backflows.

The pressure ratio setpoint equation (blue line of Figure 4. 10) is obtained by displacing the experimental polynomial fitting (red line) to the right in the compressor map until the hot-backflows at the compressor inlet disappear from all the points proposed for the identification. The result for one of the identification points is shown in Figure 4. 11B. The backflows are removed since the compressor inlet temperature does not increase, a clear improvement from the previous case shown in Figure 4. 11A. The final correlation for the compressor installed in the MTM prototype is shown in Equation 4. 20. N_{corr} is the corrected compressor speed in the percentage of the maximum speed (100 krpm).

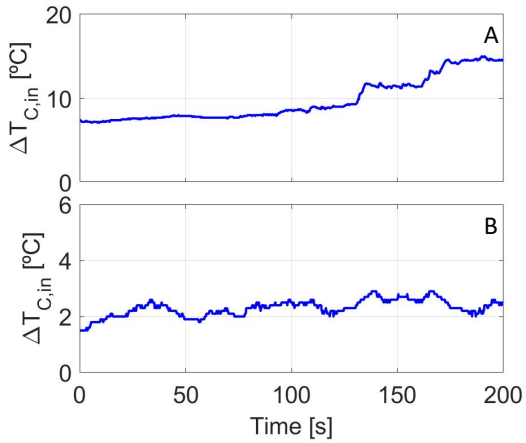

Figure 4. 11. Increase of temperature at the MTM mechanical compressor inlet while operating at 95 krpm (black dot of Figure 4. 10): (A) Experimental surge protection; (B) Final surge protection

$$\Pi_C = \mathbf{0.000195} * \boldsymbol{N_{corr}}^{\mathbf{2}} + \mathbf{0.007} * \boldsymbol{N_{corr}} + \mathbf{1.1057}$$

Equation 4. 20

Following, a methodology is proposed to obtain the surge protection curve for compressors of different sizes based on the slope of the compressor map iso-speed lines without a new experimental identification. It was observed that the setpoint identified for the pressure ratio dependant on the compressor speed was located in areas of iso-speed lines with similar slope values. Figure 4. 12A shows the corrected mass flow derivative of the compressor map iso-speed lines, represented against the corrected mass flow. Here the blue dots are the points of the final correlation shown by a blue line in Figure 4. 10, corresponding to each iso-speed line.

It can be seen how the setpoint trend reaches an asymptote when increasing the compressor speed above 40%. Therefore, if this behavior is reproduced in the derivative compressor map of another mechanical compressor unit, the setpoint curve for the surge control of the new compressor can be obtained without further testing. The expected pressure ratio limits for the surge protection curve of the standard compressor unit are shown in Figure 4. 12B, depicted by blue dots and represented on the derivative compressor map.

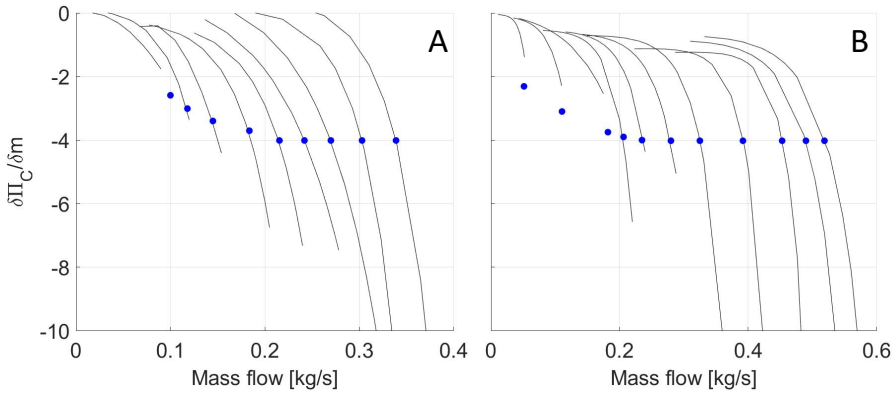

Figure 4. 12. Derivative mechanical compressor map: (A) Prototype unit (Rotrex C30/94); (B) Standard unit (Rotrex C38/92)

Lastly, the results obtained through the methodology proposed are represented in the compressor map, shown in Figure 4. 13 by a red line. However, during the experimental validation of the surge protection curve obtained, it was revealed that the pressure ratio in the compressor could be increased by reducing the margin with the surge limit without the appearance of hot-backflows. Therefore, the pressure ratio setpoint for each compressor speed was increased, obtaining the blue line shown in Figure 4. 13. This maximizes the pressure supplied by the compressor, which will increase the drying and cooling capabilities of the system. The final surge protection curve for the mechanical compressor standard unit is shown in Equation 4. 21.

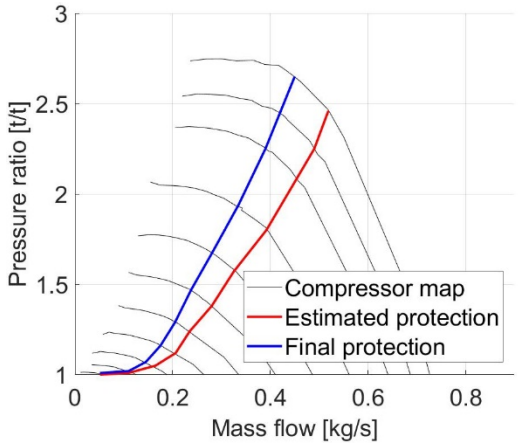

Figure 4. 13. MTM surge protection curve

$$\Pi_C = 5.127 * 10^{-7} * {N_{corr}}^3 + 1.289 * 10^{-4} * {N_{corr}}^2 - 4.799 * 10^{-4} * N_{corr} + 1$$

Equation 4. 21

Nevertheless, the methodology proposed allows a fast implementation of the surge protection in different sized compressors, which will not provide the maximum pressure possible but will allow the compressor to work without risks of reaching insufficient surge margin (hot backflows appearance risk).

It should be noted that this strategy is active and protects the compressor from a progressive approach to surge all the time the MTM is powered up. However, if a perturbance in the system appears that throws the compressor suddenly beyond surge limits, i.e., the sudden closing of a valve due to malfunctioning, this kind of control may be too slow to react. Therefore, extra security has been implemented that opens the purge valve aggressively when the compressor suddenly goes into surge (a sudden and aggressive increase of backflows).

This is carried out by monitoring the presence of backflows at the compressor inlet, generated by the compressor when it is operating into surge, with two thermocouples. The first thermocouple (2 of Figure 4. 14) is installed aligned with the compressor volute tongue (1). At an upstream distance of 44 mm (A) and penetrating ¼ of the inlet pipe diameter (D) since surge backflows travel backward, spinning around the periphery of the inlet pipe. The second thermocouple (3) is located 100 mm (B) from (2), and it measures the temperature in the center of the inlet pipe vein. This layout, shown in Figure 4. 14, allows for detecting the hot backflows that appear when the surge area of the compressor map is reached, comparing the measurement of both thermocouples [4]. In this case, the thermocouple installed near the compressor (2) is the one that changes its temperature due to the backflows, while the reference to detect this abnormal temperature increase at the compressor inlet is the one installed farther from the compressor (3). For the application described in this Ph.D. Thesis, when the difference between both exceeds 15ºC, the purge valve is opened to 50%, and if it reaches 30ºC, the installation is stopped due to excessive surge of the mechanical compressor.

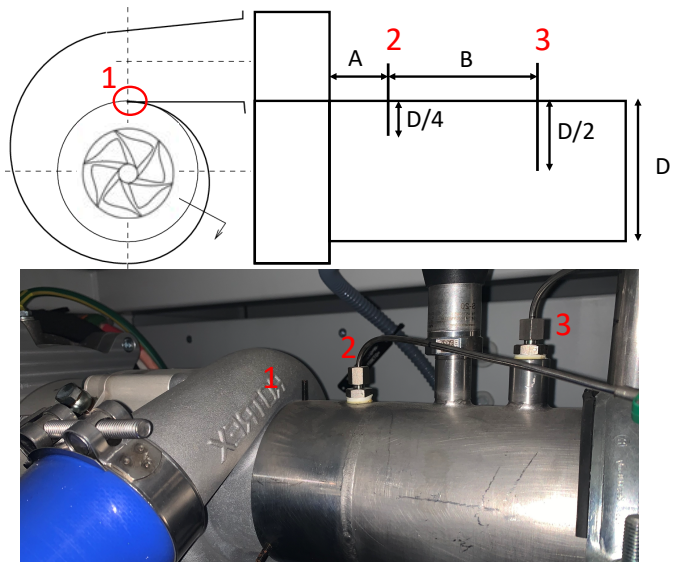

Figure 4. 14. Compressor inlet monitoring for detection of hot backflows using two thermocouples

However, if a sudden deep surge causes the backflow, the length of the backflow could increase and reach even the second thermocouple (3) [4]. In this case, the current configuration will detect that both thermocouples (2 and 3) increase their temperature together and will not activate the protection of the compressor. Therefore, an extra layer of protection has been installed to safeguard the compressor in these conditions, which monitors the reference thermocouple (3) and activates the surge protection if it increases abnormally. If the temperature rises above 60ºC, it is assumed that the backflows are reaching the reference thermocouple, and the compressor is operating in the surge, which leads to a fast opening of the purge valve to 100%. The limit of 60ºC is defined considering that the temperature in the technical area of an engine test cell should not reach 60ºC to avoid damaging the equipment installed in a test cell.

4.2.3. MTM + MEDAS Performance

Once the control strategies for the MTM actuators are implemented, a testing campaign is carried out without an engine connected to characterize the performance of the MEDAS + MTM set in both steady-state and dynamic operation. Also, the results obtained will be briefly compared against the results for a MEDAS stand-alone from previous research [1] to present the main advantages that the MTM introduces to the MEDAS performance capabilities.

4.2.3.1 Steady-state

The use of the MTM coupled with the MEDAS has a significant two-fold effect on the performance maps obtained from steady-state operative points. On the one hand, the boosting capabilities of the MTM remove the 'dead zone' of the pressure control. This is the non-controllable area of the pressure range that appears around the ambient pressure value of the test cell in which the MEDAS is installed. This is shown in Figure 4. 15, in which the mass flow performance-map of the MEDAS stand-alone is presented in Figure 4. 15A, and the same map obtained with an MTM coupled to the MEDAS in Figure 4. 15B.

In Figure 4. 15A, the 'dead zone' area is marked with a red square, in which can be seen how the minimum altitude reproduced (maximum pressure achieved) increases with the mass flow increase. This same area is marked in Figure 4. 15B, in which the 'dead zone' has disappeared, making it possible to achieve every pressure set point regardless of the mass flow demanded. It is interesting to remove the 'dead zone' when it is necessary to have high repeatability at room or close to room conditions during a testing campaign. It means being independent of barometric pressure changes due to weather changes.

In the turquoise area (from 0 meters up to 5000 meters), the 'vacuum' area is depicted, representing the simulation of altitudes above room conditions. The blue area (from 0 meters to 2000 meters) is the 'over pressure' area, representing the altitudes below room conditions, i.e., simulate sea-level conditions while installing the MEDAS in altitude. These two areas are called vacuum area and over pressure area, respectively. Room conditions are sea level in this figure since the MEDAS performance maps are built using a test cell at Valencia (Spain).

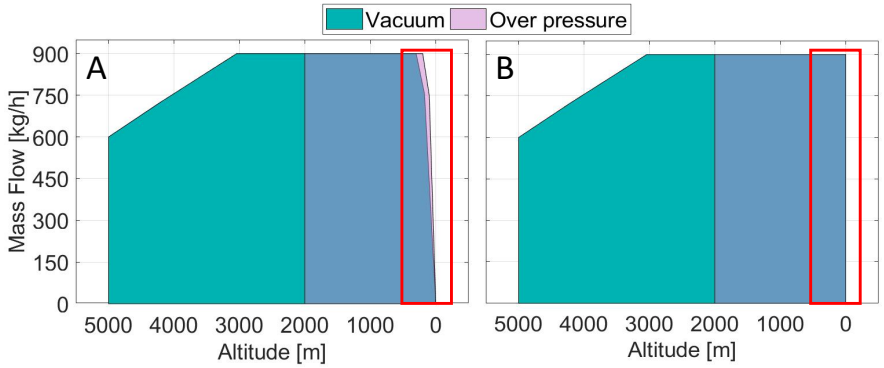

Figure 4. 15. Boosting effect of the MTM over the dead zone of the pressure control: (A) MEDAS stand-alone; (B) MEDAS coupled with MTM

On the other hand, the boosting capabilities of the MTM expand the cooling performance of the MEDAS. The MEDAS inlet pressure and temperature control allow achieving a wide temperature range, independently from the room temperature. The effects of these two actions are shown in Figure 4. 16. The

temperature performance of a MEDAS stand-alone can be seen in Figure 4. 16A and the extended performance that the coupling of the MTM provides in Figure 4. 16B. In Figure 4. 16A temperature decrease is referenced to the room temperature of the test cell in which the MEDAS is installed.

Figure 4. 16A shows how, in the case of the vacuum operation, the MEDAS stand-alone can only cool down the air as a function of the altitude simulated, which significantly limits its temperature control capabilities. Additionally, when the focus is on the engine intake temperature at overpressure mode, it is shown how there is almost no temperature control, with the temperature depending directly on the altitude simulated and the cooling water temperature of the MEDAS.

Contrarily, Figure 4. 16B shows how when the MTM is coupled, the dependence of the ambient temperature in the vacuum area and the cooling water temperature for over pressure disappear in the range between -15 ºC and +40 ºC. However, the effect of the altitude simulated is maintained when cooling down. For a given boost pressure provided by the MTM, the expansion in the turbine increases with the simulated altitude, and thus the minimum temperature achievable by the system is reduced.

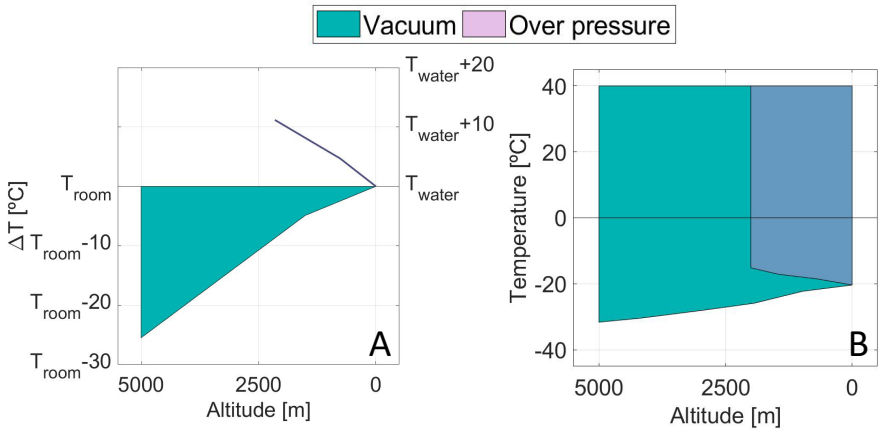

Figure 4. 16. Boosting effect of the MTM over the cooling capabilities of the MEDAS delivering 900 kg/h: (A) MEDAS stand-alone; (B) MEDAS coupled with MTM

It should be noted that the temperature results have been achieved while demanding 900 kg/h, that is, the maximum mass flow provided by the MEDAS shown in Figure 4. 15. If the required mass flow increases, the temperature control range established for the MEDAS could be reduced due to reaching the maximum power installed in the cooling and heating elements. Also, when the mass flow is higher, a higher part of the total flow bypasses the turbine (14) installed in MEDAS. This reduces the cooling capabilities of the MEDAS by

increasing the temperature of the mix between the cooled expansion in the turbine and the isothermal expansion in the WG (12).

Figure 4. 16B shows the whole temperature range, corresponding with the maximum temperature control performance achievable by the MEDAS + MTM set. However, to make independent the temperature control from the altitude demanded, the minimum temperature for the commercial units is limited by software at -15ºC, obtaining the temperature performance map shown in detail in Figure 4. 17.

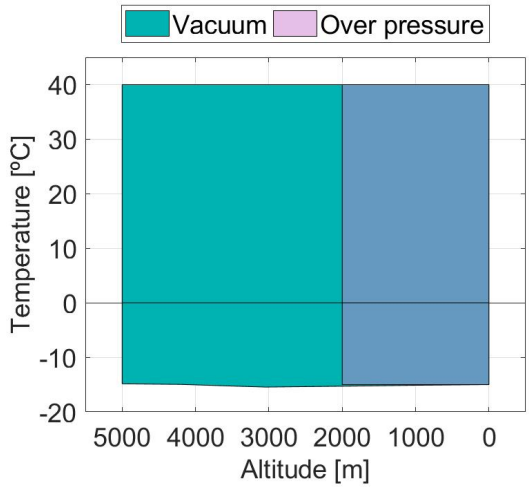

Figure 4. 17. MEDAS + MTM set temperature performance

4.2.3.2 Dynamic

Concerning the dynamic operation, the coupling of the MTM to the MEDAS removes the pressure peaks around ambient pressure shown in the dynamics of the MEDAS stand-alone presented in reference [1] while allowing to follow dynamic temperature profiles throughout the dynamic pressure test. This is a new feature since, previously, the control range temperature of the MEDAS depended on the ambient temperature and the pressure demanded by the user. At the same time, with the MTM coupled, these dependencies are removed, thus obtaining an increase in the temperature emulating capabilities. However, adding an extra set of actuators introduces some perturbances in the control of the MEDAS that slightly reduce the system's accuracy while following the pressure profile demanded.

A pressure and temperature setpoint profile has been defined to analyze the described behavior. The altitude will change from 2000 meters below sea level to 5000 meters above sea level in 30 minutes and then return to 2000 below sea level in another 30 minutes. This corresponds to a vehicle driving at 71,3 km/h

on a road with a 20% of slope (a pretty challenging test). Also, during all this up-and-down test, the temperature setpoint will be kept constant at 20ºC.

Suppose the focus is on removing the pressure peaks around the ambient pressure. In that case, the improvement is shown in Figure 4. 18. Here, the dynamic profile defined for the pressure is performed with the MEDAS stand-alone and depicted in Figure 4. 18A. The same pressure profile has been carried out with the MTM coupled to the MEDAS, shown in Figure 4. 18B.

The pressure and the setpoint demanded are shown on the *y-axis*, while the cycle time is represented on the *x-axis*. It can be seen how the perturbance in the pressure shown around seconds 750 and 3250 disappear in the case of Figure 4. 18B. The pressure peaks are marked by red circles in Figure 4. 18A. The perturbances are caused by the change in the control mode to deal with both situations, vacuum and over pressure. The MEDAS stand-alone must perform these transitions by opening and closing several valves when crossing the installation's actual altitude (room pressure), sea-level in this case, which causes delays and disturbances in following the dynamic setpoint.

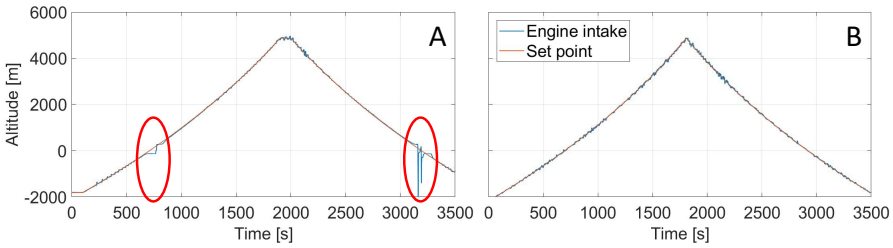

Figure 4. 18. Boosting effect of the MTM over the dynamic pressure control of MEDAS: (A) MEDAS stand-alone; (B) MEDAS coupled with MTM

Also, the dynamic capabilities to follow temperature profiles are presented in Figure 4. 19, which show a clear improvement when installing an MTM upstream of the MEDAS. In Figure 4. 19A, the MEDAS stand-alone has been trying to keep the temperature constant while performing the pressure profile shown in Figure 4. 18. It can be seen how the control range of the temperature for the MEDAS stand-alone is limited by the altitude which is being emulated. When the altitude demanded is high enough to expand the air in the turbine (between the second 800 and 2700), the temperature set point is achieved, but when the altitude emulated is close to the installation altitude or below, it is not possible to keep the temperature setpoint. Contrarily, in Figure 4. 19B, the same test is performed but with the MEDAS + MTM. In this case, the assembly can control the temperature setpoint during the dynamic test, independently of the altitude demanded.

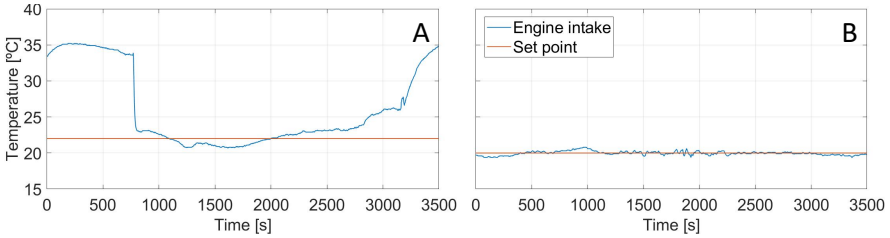

Figure 4. 19. Boosting effect of the MTM over the dynamic temperature control of MEDAS: (A) MEDAS stand-alone; (B) MEDAS coupled with MTM

Lastly, the differences in accuracy between both configurations: MEDAS stand-alone and MEDAS coupled with MTM, can be seen in Figure 4. 20. This figure presents the error between the setpoint and measurement throughout the dynamic test for both variables: altitude and temperature. It is shown how, if the perturbances due to the control mode change are not considered (around seconds 750 and 3250), the error in the altitude control increases from 100 meters (+/- 10 mbar, top chart of Figure 4. 20A) - to 150 meters (+/- 15 mbar, the top graph of Figure 4. 20B) of maximum peak error.

This is caused by the increase in the number of actuators, which generate perturbances that affect the accuracy of the control. Additionally, the increase of the MEDAS inlet pressure caused by the boosting of the MTM reduces the sensibility of the WG valve (12) actuator due to higher friction in its mechanism, which further decreases the accuracy.

In the case of the temperature, if one focuses on the time frame in which the setpoint is achieved with the MEDAS stand-alone (shown in the zoom window at the bottom-center of Figure 4. 20A), it can be seen how the temperature is not well stabilized. Also, it has a higher error than in the case with the MTM installed (bottom chart of Figure 4. 20B), which keeps the temperature error consistently below +/- 1ºC.

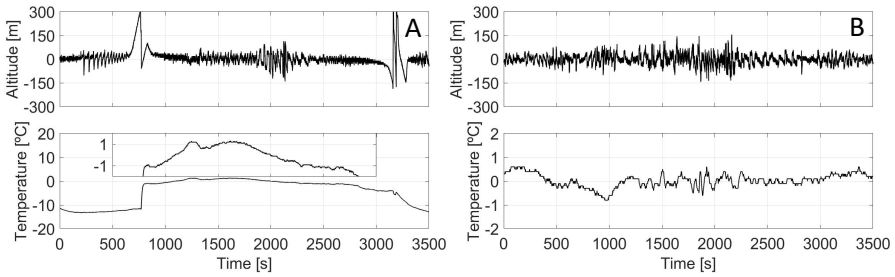

Figure 4. 20. Boosting effect of the MTM on the control accuracy during dynamic profiles of pressure and temperature: (A) MEDAS stand-alone; (B) MEDAS coupled with MTM

4.3. MHM development

With the addition of the MHM, the possibility of increasing the water content of the airstream above the room conditions is introduced. Also, the independent control of the three psychrometric variables: pressure, temperature, and humidity, is achieved for the control range defined for each one of them. The addition of the MHM allows to decouple the temperature and humidity conditioning of the airstream and avoid the restrictions found in the previous Section 4.2 for the humidity control.

4.3.1. Layout

The increase in humidity level of the airstream is carried out using a bubbling water column installed at the MTM outlet. In such a way, a percentage of the total mass flow that goes through the whole system (MTM+MHM+MEDAS) is passed through the water column to achieve the desired water content in the downstream mixture of both flows. This requires using three extra valves in the MTM to manage the flows through and around the bubbling water column and modify the control strategies defined for some already installed components in the MTM.

Figure 4. 21 shows: the scheme of the three systems (MEDAS, MTM, and MHM) coupled together (Figure 4. 21A), and an axonometric view of the MHM (Figure 4. 21B), both following the same numbered identifications for the elements. Additionally, red arrows have been included in the axonometric view to mark the flow path in the figure. The three extra valves are shown in both charts and are called: Reactor Valve (12 of Figure 4. 21A), Enhanced Valve (14 of Figure 4. 21A), and HE Valve (15 of Figure 4. 21A). Even though they are needed to control the MHM, they are physically installed within the perimeter of the MTM (Figure 4. 21A blue frame). The reason is that only the MTM has a programable logic controller (PLC); meanwhile, MHM is an entirely passive element.

Additionally, since these three valves involve an extra cost and redesign of the flow path for the equipment, two models for the MTM have been designed. On the one hand, the MTM standard (MTM ST), which will follow the component scheme shown in Figure 4. 2A, will not have these three control valves and will not be entitled to operate with and manage an MHM downstream. On the other hand, the MTM full performance (MTM FP) will include the three control valves following Figure 4. 21A and will be able to operate with or without MHM.

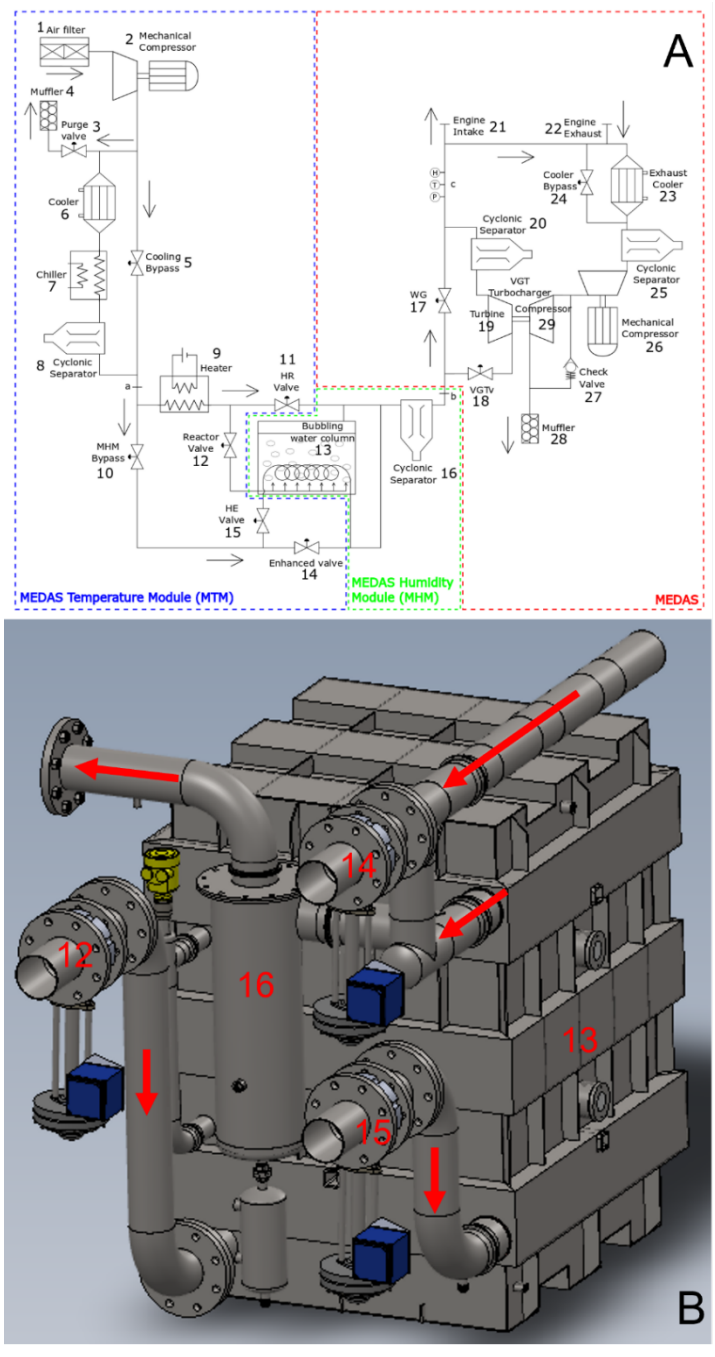

Figure 4. 21. MEDAS + MTM + MHM layout: (A) Elements' scheme; (B) MHM 3D model axonometric view

Following the air path through the complete system (Figure 4. 21A), the air enters through the air filter (1) installed in the MTM, which then goes to a mechanical compressor (2). Downstream of the compressor, there is a purging valve (3) that controls the pressure ratio of the compressor and prevents it from reaching the surge zone by opening the way to a discharge duct and thus increasing the compressor mass flow rate. Also, downstream of the mechanical compressor, the control valve (5) controls the amount of flow going through the cooling unit. The cooling components installed consist of a water-to-air cooler (6), which precools the air below 30ºC to protect the air-to-glycolic water chiller (7). After (7), the air plus water condensates generated during the cooling go to an inertial separator (8). The water condensates are separated from the airstream and extracted into the test cell drain system.

Once the air has been cooled and dried, or not depending on the demanded humidity level, it can be moisturized again to achieve the humidity setpoint. When MHM is connected, the electric heater (9) controls the water column temperature inside (13) by controlling the air temperature blown inside. Also, valve (10) manages how much airflow bypasses the bubbling water column (13) to fit the humidity level at point 'c.' In this case, valve (11) is almost closed, and valve (12) is operating in opposition with (10), helping in controlling the rate of flows going through the humid way (bubbling water-column -13-) or through the dry way (valve 10).

Concerning the temperature control at point 'b' downstream of MHM, two different states are defined attending to the humidity target. On the one hand, when the humidity target is higher than 19 g_{water}/kg_{air} (high humidity case) and on the other hand, when the demanded humidity is lower (low humidity case). If the humidity demand is lower than 19 g_{water}/kg_{air}, valve (11) regulates the temperature at point 'b,' while valve (5) stays completely closed, i.e., flow is thoroughly dried below room conditions. On the contrary, when the setpoint is higher than 19 g_{water}/kg_{air}, valve (11) is closed, and the temperature in point 'b' is regulated by the valve (5). A more detailed explanation of the temperature control strategy, when the MHM is coupled with the MTM and MEDAS, will be presented in section 4.3.3.3b) of the current chapter.

For the dry-air path, Enhanced-valve (14) bypasses a couple of air-to-water heat exchangers, placed in series each other, inside the bubbling water column (13) (see also Figure 4. 28B). HE-valve (15) is also part of the dry-air path and is placed upstream of the inlet pipe of these series-Heat-Exchangers to close and help bypass them when Enhanced-valve (14) is entirely open. Therefore, when the dry-air temperature at point 'a' is lower than the water temperature inside the bubbling water column (13), the Enhanced-valve (14) is open, and HE-valve (15) is closed. This is done to help the electric heater (9) increase the water temperature in (13), which should be kept above 70ºC, to reach the maximum humidity target for the airstream.

Contrarily, and also to help the heater (9) in managing the water temperature, valve (14) closes, and conjugated valve (15) opens when the dry-air temperature at 'a' is higher than the water temperature inside (13).

In summary, the desired relative humidity is achieved by mixing a stream of dry-air passing through the valve (10) with another of highly moist air (almost 100% relative humidity -RH-) that passes through the water inside the bubbling water column (13). If valve (14) is open, the mixture happens when dry air is colder than the moist air, possibly generating condensates. These condensates can damage the engine and turbomachinery located downstream of MHM, so a cyclonic separator (16) is installed after the mixture of both airstreams to separate the condensates. However, if the Enhanced-valve (14) is closed, dry and 100% RH airstreams are at the same temperature (water temperature inside 13) and pressure. Therefore, the mass ratio between both streams coincides with the objective relative humidity of the blended airstream.

Lastly, when the airstream exits the MHM, it enters MEDAS for the final adjustments in pressure and temperature. This is achieved without modifications in any of the functions of the components installed in MEDAS (Section 4.2.1) and despite the coupling of either the MTM or the MHM. Therefore, MEDAS is control-blind to what it has upstream. With room conditions, MTM or MTM+MHM, MEDAS control is always the same and fine-tunes the user setpoints. It is the PLC controller of the MTM which receives inputs from MEDAS and provides as output pre-conditioned airstream to MEDAS. This is achieved dynamically to follow up transient setpoints.

It should be noted that with the MHM operating as described, it is possible to achieve up to 80% actual relative humidity at altitudes like 5000 m (0.54 barA or -0,46 barG) and temperatures as high as 40ºC. High altitude (low absolute pressure), hot and humid air conditions would be physically impossible to achieve in combustion air by injecting water or steam at room conditions as traditionally done in CAHUs or other altitude simulators commonly found in the market [3]. The reason is that the specific humidity required at high altitudes and temperatures in most cases overcome 100% relative humidity at room conditions, so the excess water will condensate and never be absorbed by the airstream. This limitation will be further explained below.

4.3.2. Bubbling water column development

There are several methods to increase the water content of an airstream, such as water atomizers, steam injectors, and bubbling water columns (in chemistry disciplines, also known as bubble reactors). However, the currently being discussed application imposes restrictions that discard some of them from the list. The maximum working pressure of the atmospheric simulator was defined at 2.5 barA, which was the main criterion for not using steam injectors. The technologies used in this option restricted the maximum working pressure,

making them unsuitable for using steam injectors for this application. Also, the limitation in equipment size to keep the atmosphere simulator's compactness trend makes it impossible to use either water atomizers since they require a significant length of piping downstream of these components to assure the correct absorption of the water in the air.

Therefore, the solution proposed for humidifying the air was a bubbling water column, which has an objective to humidify an airstream that passes through it up to a water content setpoint, which will be expanded and cooled downstream to reach temperature and pressure setpoints.

In the current section, the design requirements for the installation will be explained. Afterward, the set-up parameters for the CFD code used will be shown, where the study of the effect of the mesh size and air-water interaction models is explained. Later, the designed prototype and testing methodology will be described. Lastly, the results of the parametric studies to obtain the final design of the bubbling water column are shown.

4.3.2.1 Equipment requirements

The device to be developed should generate dynamically high humidity levels corresponding to altitude conditions with high temperatures. When talking about water content in the air, the significant impact of the psychometric variables pressure and temperature on the water content in the air must be highlighted. The water content or specific humidity (g_{water}/kg_{air}) increases exponentially when the temperature increases or when the pressure decreases while keeping the relative humidity value [3].

Figure 4. 22 shows a simplified psychrometric diagram for the air without differentiating by air pressure. The greenish-blue area represents the humecting requirements in terms of water content for the equipment. These specifications have been designed given every combination of pressure, temperature, and relative humidity (RH) inside the operational range of the installation: 0.55 barA to 1.3 barA, 0 ºC to 40 ºC, and 10 % RH to 80 % RH, respectively. It should be noted that the MEDAS+MTM+MHM can control the temperature down to -15 ºC. Still, the humidity control is only active between 0 ºC and 40 ºC due to the minor differences in water content between 10 % RH and 80 % RH when the temperature goes down below 0 ºC and the limitations in drying capabilities of the MTM (minimum humidity controllable 2 g_{water}/kg_{air}).

Furthermore, the line of maximum demand for specific humidity can be seen depicted in red, representing 80 % RH at a pressure of 0.55 barA. Finally, the maximum water content the air can withstand at sea level is described in this figure by an orange line. This clearly shows how it is impossible to achieve the required humidity while emulating high altitudes by humidifying at sea-level conditions unless the air temperature is increased up to 50 ºC approximatively.

Figure 4. 22 also shows that less temperature is required to humidify up to the most demanding point if air pressure is kept close to room conditions.

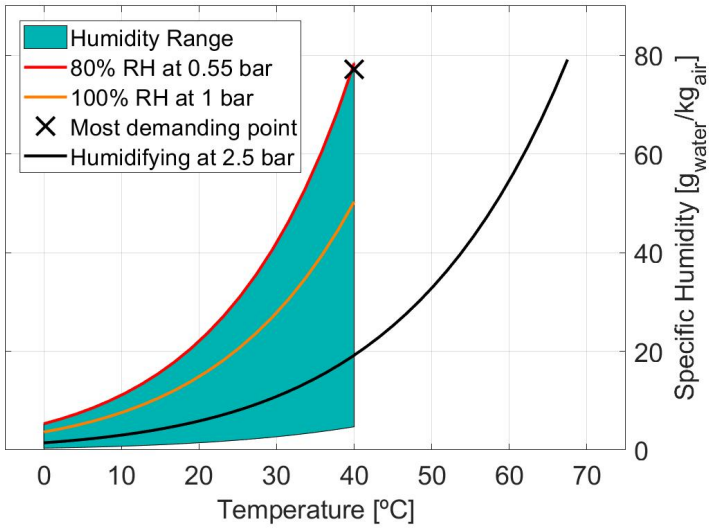

Figure 4. 22. Psychrometric conditions for the humectant process

A black line depicts the most unfavorable conditions specified for the humidifying process in Figure 4. 22, which corresponds to 2.5 barA (maximum pressure reachable by the MTM) and 100% RH. In addition, the operative point of the most demanding point in terms of water content is depicted by a black cross in Figure 4. 22 (0.55 bar, 40 ºC, and 80% RH). Suppose the focus is on this operative point, trying to reach it while working at the most unfavorable pressure conditions for the humectation (black line). To achieve the humidity target, it is necessary to get a temperature of around 68 ºC. This is shown in Figure 4. 22, in which the black line reaches the same water content level (specific humidity) as the black cross at 68ºC.

Due to the specific location of the bubbling water column (13 of Figure 4. 21) in the MTM+MHM layout, the humidifying process is carried out before the expansion and final tune of the temperature (point 'c' of Figure 4. 21). This means the air will be humidified under high pressure conditions above ambient pressure since the air is compressed in the MTM mechanical compressor (2). However, this is necessary since it will allow the temperature control range of the VGTv valve (18) to be increased to compensate for the heating up of the air during the humecting process.

According to psychometric conditions [3], the higher the pressure, the lower the amount of water the air can withstand, diluted as water vapor. Contrarily, the higher the temperature, the higher the possible water content. Therefore, to achieve the relative humidity levels while reproducing altitude conditions, it is

necessary to moisten the air either after generating the desired vacuum or before but at a much higher temperature. This is done to compensate for the air's water capacity increase when decreasing the pressure. This can be seen when comparing the evolution with the temperature of the black and red lines of Figure 4. 22, 2.5 barA, and 0.55 barA, respectively.

Lastly, some additional problems are involved in the design of the bubbling water column and the optimal water level at rest (before airflow begins to bubble through the water). On the one hand, if the water column height at rest is too high, the risk of overflowing the reactor increases since the bubbling of the air stream creates foams that grow up in the water, but without a benefit for the humidifying process [5]. On the other hand, if the water column height at rest is too low, the shorter residence time of the air inside the water reduces the water absorption capacity of the air. Similarly, when the airstream velocity increases, the risk of overflowing increases. The airstream velocity will define the final footprint of the reactor vessel while considering the maximum mass flow.

Therefore, the accurate prediction of the behavior of the air inside the water column as well as the level of the foam, as a function of the water column height at rest and the airstream velocity is indispensable to maximize the humidifying capacity of the installation while keeping controlled the stabilized height of the water column and foams.

4.3.2.2 CFD Methodology

A CFD methodology has been proposed to design the bubbling water column vessel, fulfilling the specifications presented above. With this methodology, the limits in terms of the water column height at rest and the maximum airstream velocity for an initial geometry proposed for the vessel will be obtained.

a) Solver and Models

The segregated solver of a finite volume commercial flow program is used to solve the discretized Navier–Stokes equations (StarCCM+® v.15.02.007) [6]. The coupling between the momentum and continuity equations is achieved with a predictor-corrector approach. The flow is unsteady, incompressible, and turbulent. Unsteady flow calculations (URANS) are performed using a first-order implicit formulation with an adequate time step to keep Courant–Friedrichs–Levy around 1.0 to ensure convergence and stability (time step = 0.001 sec). However, explicit formulations are not available for the Eulerian multiphase model used in this work. Therefore, the Shear-Stress Transport (SST) k−ω two-equations turbulence model has been used for turbulence. This approach is the only one suitable for the two-fluids modeling developed in this work. Table 4. 2 summarizes the main aspects of the parameters describing the CFD model.

Table 4. 2. Main CFD model parameters

Solver	**StarCCM+® v.15.02.007 [6]**
Turbulence model	k-ω-SST
Physical model	Multiphase E-E (Air + water) Multiple flow regime interaction [7]
Time discretization	Implicit; time step = 0.001 s
Transient	[0 – 20] s
Boundaries	Inlet: Velocity → V=0.1 m/s; Mass Fraction Air = 1.0 Outlet: Pressure → $p=p_{atm}$

The two-fluids model [8], [9] implemented in StarCCM+® provides a flexible framework where dispersed, stratified, or mixed two-phase flow (air + water) can be modeled by using different closure relations. For a given pair of phases, the multiphase segregated flow model considers different types of phase modeling topology.

The continuous-dispersed phase interaction [10] topology provides the means to model the interaction of a phase dispersed within another phase throughout the whole domain. Furthermore, the interface length scale is an effective mean diameter of the dispersed phase particles. Moreover, where particles are not spherical, this is absorbed as a correction factor into interphase transfer models such as bubble drag and lift force.

In addition, the multiple flow regime [7] topology is an extended definition where all types of multiphase flow, that is, dispersed (bubble, droplet, or particle) and stratified (free surface) flows, can be modeled. The solver employs a volume-fraction-based criterion to classify the flow regime into the dispersed and separated two-phase flow. In this scenario, the multiple flow regime model treats bubbly flow in the first dispersed regime, droplet flow in the second dispersed regime, and separated water–airflow in the large-scale interface regime.

b) Computational Domain

The initial computational domain simplifies the bubbling water column into a 2D water column. The system's width is 900 mm and includes a distributed grid located at 200 mm from the bottom side of the vessel, with channels of 18 mm that restrict the airflow through the grid. Figure 4. 23 represents the main aspects of the computational domain and dimensions. The bottom side of the computational domain is the constant distributed gas velocity inlet (V = 0.1 m/s). The gas phase enters the computational domain and evolves before arriving at the grid channels. The top side is open at constant pressure. Other boundaries in the computational domain are non-slip wall boundaries.

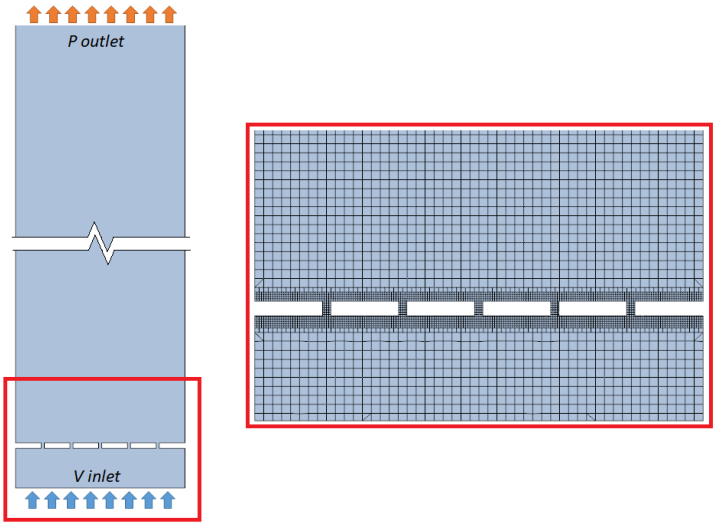

Figure 4. 23. Computational domain. Mesh and cell refinement around the grid

The mesh is performed employing a Cartesian-based grid with different embedding local refinements near the region of the grid channels where higher gradients of velocity are found. Furthermore, a mesh independence study was carried out to ensure the accuracy of the CFD calculations by changing the reference cell size from 3 mm to 25 mm (minimum embedding cell size 0.75 mm and 6.25 mm, respectively). Figure 4. 24 shows the contours of the volumetric fraction of water at t = 10 s obtained with the different meshes.

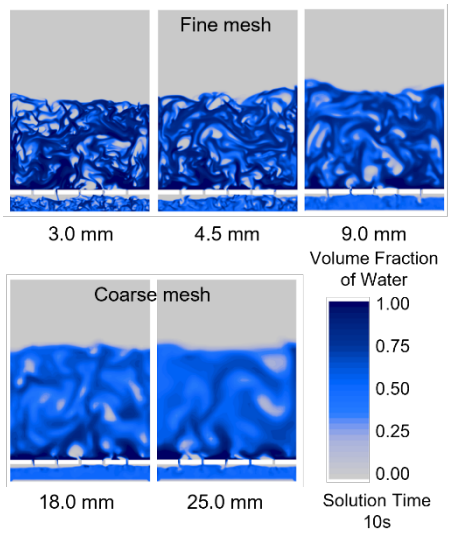

Figure 4. 24. Volume fraction of water. Mesh independence study

It can be seen how coarser meshes show less interaction between phases, and the air appears to be diffused in the water. By contrast, finer meshes detect more heterogeneous flow in the reactor, and different scales of air bubbles can be observed. Furthermore, these contours show that the water column obtained by finer meshes tends to stabilize at a lower height.

This statement is confirmed when observing the temporal variation of the water column height (Figure 4. 25A). In this Figure, $\Delta z = 0$ m means the initial water column at rest (t = 0 s.) before air injection. After 3 s, it is evident that results provided by finer meshes lead to a final lower water level $\Delta z = 0.25$ m. Nonetheless, it is observed that water level trends to decrease after 5s, with the thinnest mesh -green series-, which should not be expected since this can only happen when water mass disappears. The operation conditions and the height of the water column are adequate to avoid the water arriving at the top boundary condition. Figure 4. 25B shows the water mass imbalance in the computational domain after 20 s for every cell size mesh. The CFD solver produces a numeric mass imbalance error that increases when reducing the computational cell size. These statements are in accordance with those from other authors [11], [12]. In multiphase flows, the computational cell volumes must be greater than the volume of the liquid for the Eulerian continuum approach to provide high-quality results.

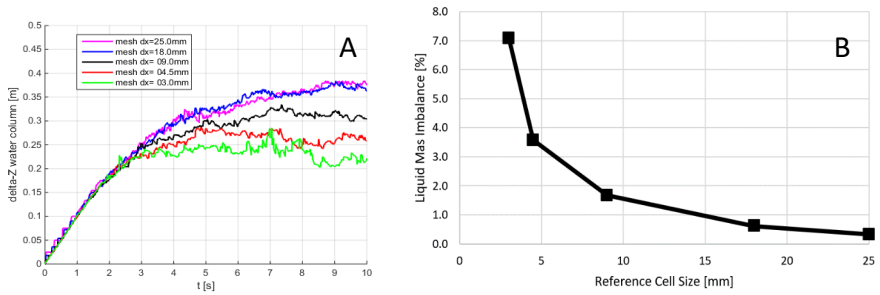

Figure 4. 25. Mesh independence study: (A) Variation of water column height; (B) Liquid mass imbalance

Therefore, an equilibrium between both features has been reached to achieve the most accurate possible solution. The cell size used in the solver mesh is 18 mm, which is considered a coarse mesh to avoid getting cells too small not to surpass 1% of mass imbalance.

c) Phase Interaction Models

Two different phase interaction models have been tested in this thesis to determine their feasibility and accuracy for this bubbling system. The reference operation condition is selected with the initial water column of 0.5 m and airstream velocity of 0.1 m/s.

Figure 4. 26 shows the volume fraction contours of water at different time steps from 0 to 20 s. Both phase interaction models (presented in Section 4.3.2.2a)) provide significantly different results after 5 s. On the one hand, the continuous phase interaction model predicts a monotonic increase in the water level compared to the stable solution observed with the multi-regime interaction model [7]. The mixing zone of the continuous phase interaction model is formed by big air bubbles and extensive zones with low water volume fraction (average volume fraction through wet volume is 0.36) that leads to a high water level for this point of operation. On the other hand, the multi-regime interaction model shows a steady solution after 10 s, with distributed liquid zones (dark blue, average volume fraction through wet volume is 0.57).

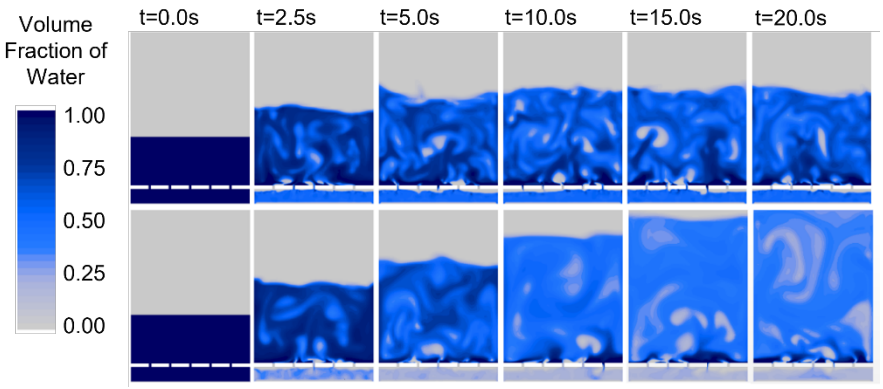

Figure 4. 26. Volume fraction of water. (Top) Multi-regime interaction model, (Bottom) continuous regime interaction model

Figure 4. 27 also shows the water column position obtained for both interaction models. The continuous interaction model (red line) predicts an increment of water level after 20 s of around $\Delta z \approx 0.85$ m. In the case of the multi-regime interaction model (blue line), Δz becomes stable ($\Delta z \approx 0.37$ m, steady column) for this reference operating condition.

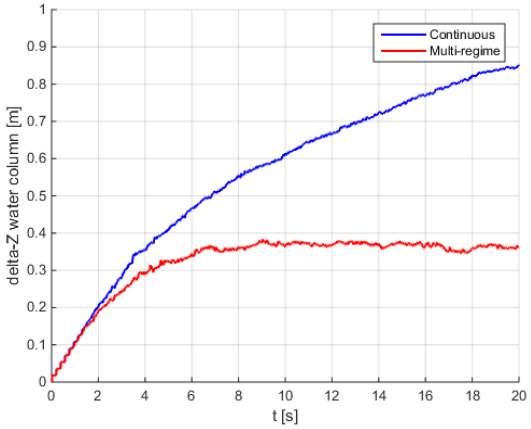

Figure 4. 27. Variation of water column height. (Blue) Multi-regime interaction model, (Red) continuous regime interaction model

4.3.2.3 Prototype development

Once the preliminary calculations run with CFD code have confirmed that the different models show discrepancies for the current application, a prototype of the bubbling water column is built and used for the experimental validation of the CFD model that must be used.

The prototype built for the testing and validation is the one that appears in Figure 4. 28. In Figure 4. 28A, the external view of the bubbling water column is depicted, in which the air inlet to the water (identified by number 1) and the air outlet (2) can be seen. Furthermore, for the validation tests, the dry air circuit through two heat exchangers (used to help heating-up the water) has been closed, as shown in numbers 3 and 4 (inlet and outlet, respectively). The two heat exchangers (6 and 10) are installed inside the water column vessel, working with dry air. They are externally finned surfaces allowing water and humid air to move around and serving (6) as airstream homogenizers and (10) as water-drops-trap before moist air leaves the bubbling water column. Nevertheless, the primary purpose of (6) and (10) is to help heat the water and humid air using the dry airstream. This is done to keep dry and moist air at the same temperature levels (the same as the water temperature) to achieve the humidity setpoint more linearly.

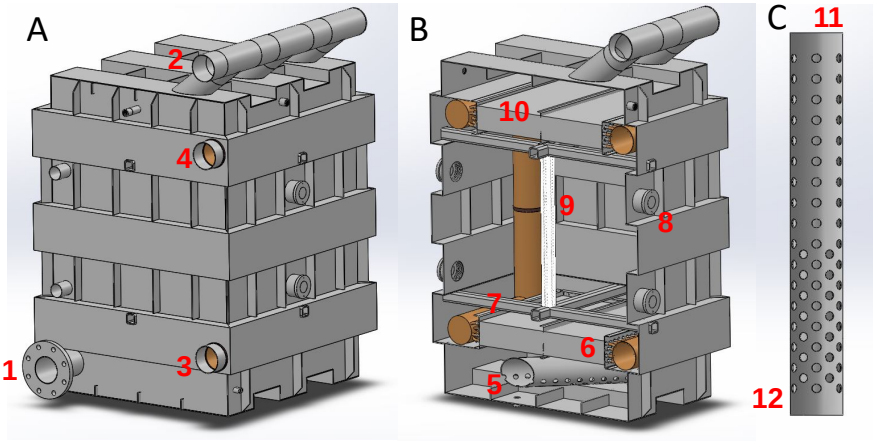

Figure 4. 28. Bubble reactor prototype description: (A) exterior; (B) cross-section; (C) holed duct. (1) air inlet, (2) air outlet, (3) heat exchanger inlet, (4) heat exchanger outlet, (5) holed duct, (6) first heat exchanger, (7) reinforcing crosses, (8) visual access, (9) measurement rule, (10) second heat exchanger, (11) beginning of the holed duct and (12) end of the holed duct

The reactor has been designed with a complex wall shape to reduce the size of the flat areas between consecutive ribs and withstand the pressure difference between the high inside pressure and the ambient pressure without using a too-thick metal wall. The bigger area inside the bubbling water column has a footprint of 0.81 m^2, while the smaller one has an area of 0.64 m^2, with a square shape.

In Figure 4. 28B, a cut cross-section of the vessel is shown, and the different internal components of the design are identified. Firstly, a hollered duct in the bottom (5) is submerged in water and through which the airstream enters the vessel. This element works as an air distributor, separating the primary airstream into several smaller streams that bubble through the water. The holes are divided into two main areas to increase the flow homogeneity along the flow distributor's length. The first half has a diameter of 18 mm and follows a grid distribution (point 11 of Figure 4. 28C) with a distance between holes of 25 mm in the axial direction and 34 mm in the tangential direction. In the second half of the duct (point 12 of Figure 4. 28C), the distribution is scattered, which allows for a higher hole density as the distance in the tangential direction decreases to 17 mm. Next, a first heat exchanger (6), which also works as a flow homogenizer, to avoid all the air following a single narrow path. Then, there is a pair of reinforcing crosses (7) to strengthen the structure and help withstand the pressure difference in the walls. Four visual access points (8) are installed in the vessel, and a measurement rule (9), with which the water level is measured during testing. A second heat exchanger (10) is installed before the air exit at the top of the reactor, serving as a droplet separator to avoid liquid water from

flowing out of the vessel. The heat exchangers (6 and 10), as already discussed, are used to heat the water using by-passed dry air at a higher temperature than the water (see Figure 4. 21).

The tests for the experimental validation of the CFD model are carried out by controlling the air mass flow that passes through the water and the initial height of the water volume. The air mass flow tested is between 0.16 kg/s to 0.25 kg/s, and the water level is kept at the 0 cm mark in the measurement rule when at rest. Furthermore, the air density at the vessel outlet is kept at a similar value for every test, with an air pressure of 2.4 barA and a temperature of 50 ºC. It should be noted that the range of mass flow selected, and the pressure and temperature conditions are the available controlling range of the atmosphere simulator in which the prototype designed was installed. Finally, the testing procedure for the developed installation is as follows:

- In the first place, before passing air through the water, the water level is adjusted to the 0 cm mark of the measurement rule.
- Then, the installation is started, and the air's mass flow, pressure, and temperature at the outlet of the bubbling water column are controlled.
- Lastly, once the three controlled variables are stabilized, the water column height is measured through the sight glasses with the help of the measurement rule.

Figure 4. 29 shows the steady-state results obtained from the model validation experiments.

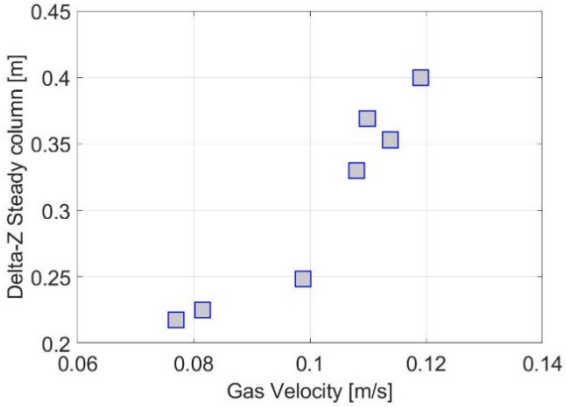

Figure 4. 29. Bubble reactor prototype experimental results

4.3.2.4 Results and Validation

To check the validity of the CFD results shown in the previous Section 4.3.2.3, in Figure 4. 30, the value obtained in the experiments is presented along with the prediction from the CFD calculations. In this figure, the continuous and

multi-regime interaction models are represented by red and blue lines, respectively, while grey squares represent the experimental results. The water level predicted by the Continuous interaction models does not correctly capture the behavior of the bubbling water column prototype in the range of operation. Both models provide equivalent results only with very low gas velocity (below 0.05 m/s).

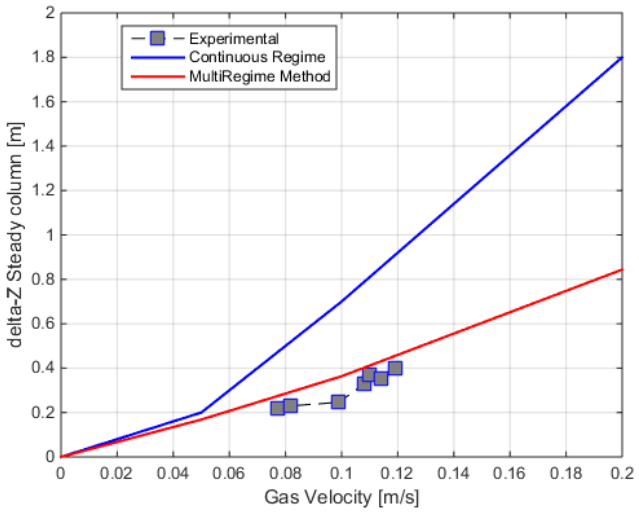

Figure 4. 30. Steady water column height. (Red) Multi-regime interaction model, (Blue) continuous regime interaction model

As the multi-regime interaction model is the one that better fits the experimental data, it is the one that has been used to further the design of the bubbling water column. Figure 4. 31 shows the results of studying the effect of the airstream velocity and the initial water column height over the increase of the water column height. In Figure 4. 31A, different airstream velocity has been calculated while keeping a given initial water column height of 0.5 m. Similarly, in Figure 4. 31B, different initial water column heights have been computed, maintaining the same air current velocity of 0.1 m/s.

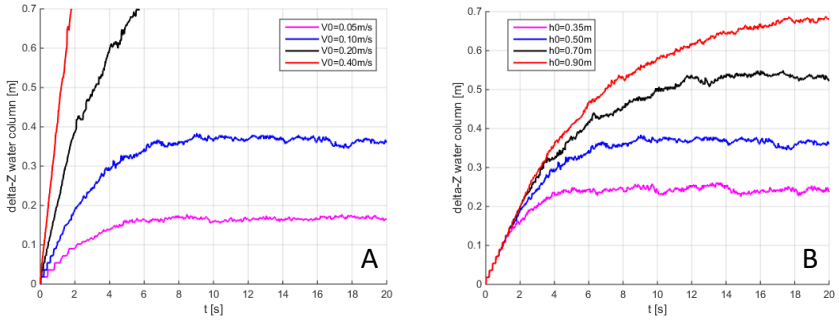

Figure 4. 31. Variation of water column height. (a) Influence of gas velocity; (b) Influence of initial column height.

Figure 4. 31A shows that the airstream velocity must be controlled as the height of the water column increases exponentially when the velocity increases. This parameter is the deciding factor for the minimum footprint area of the bubbling water column, intending to keep the airstream velocity at reasonable values when the maximum mass flow rate specified for the application passes through the vessel (0.25 kg/s).

In the case of the initial water column height, it mainly affects the residence time of the air inside the water, causing a direct effect on the final humectant capacity of the installation. Hence, it should be as high as possible, but as shown in Figure 4. 31B, it directly affects the final height of the water column, so a compromise solution must be reached.

Therefore, after the parametric studies for both the initial water height and airstream velocity are carried out, the optimal values for the design to avoid overflowing the reactor are 0.12 m/s of maximum airstream velocity and 0.5 m of initial water column height.

With these two parameters, the final geometry of the bubbling water column is obtained. The minimum footprint is calculated as the minimum area that assures that the airstream velocity at the outlet of the bubbling water column does not increase above 0.12 m/s for the design point of the installation. In the case of the study presented in this Ph.D. Thesis, the footprint obtained was 0.81 m^2 for a design point of 2.4 barA, 50 ºC, and 0.25 kg/s. Also, the vessel height was selected as 1.3 m to consider a security margin of 0.4 m over the nominal stabilized water column height of 0.9 m (initially 0.5 m with an increase of 0.4 m due to the 0.12 m/s of air velocity) to avoid overflows due to unexpected perturbances that could increase the height of the foams punctually.

Lastly, these design parameters are used on a 3D CFD model calculation of the final system to validate the design obtained, considering a wide range of operation points around the design point. In Figure 4. 32, the results of the 3D calculations are shown for a given operating point. On the one hand, Figure 4.

32A shows an operative point with lower mass flow than the design point (0.2 kg/s), in which the final water column height is kept at the optimal value of 90 cm. This means that the simplification of a 2D column represents with enough accuracy the 3D behavior, validating the pre-design with the simplified geometry. On the other hand, Figure 4. 32B shows how when increasing the mass flow way over the design (0.42 kg/s), the final water column height rises above the optimal height but does not reach overflowing conditions, thus validating the reactor height selected according to 2D previous calculations.

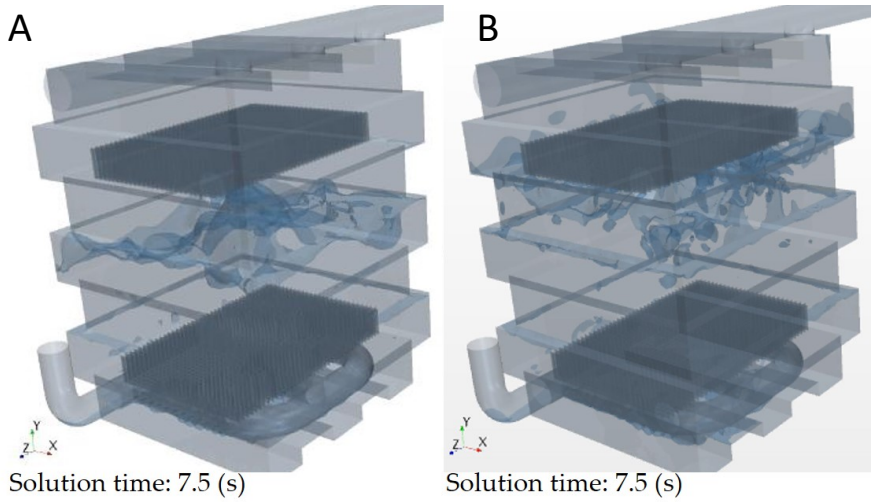

Figure 4. 32. Three-dimensional (3D) validation of the bubbling water column design. Stabilized bubbling of the operation point: (A) 0.2 kg/s; (B) 0.42 kg/s

4.3.3. Control strategies

With the addition of the MHM, the control strategies designed and presented in previous Section 4.2.2 must be modified to include the extended capabilities in terms of humidity control that the bubbling water column introduces. These modifications will be extended to the two main control blocks: pressure and temperature control, affecting all the actuators previously installed in the MTM. Also, the control strategies are developed to encompass the three new valves introduced in the layout to control the airflow through the bubbling water column (Reactor-valve (12), Enhanced-valve (14), and HE-valve (15) respectively at Figure 4. 21A inside the blue perimeter). Moreover, an extra control block will be presented: Humidity control, which will oversee the conditioning of the airflow humidity level.

It should be noted that the surge control block does not suffer any modification and stays active with or without MHM connected downstream to the MTM.

4.3.3.1 Humidity control

The humidity control block oversees controlling the humidity of the combustion air in the engine intake connection (point 'c' of Figure 4. 21). This is carried out through several control valves installed in the MTM, which regulate the amount of air that enters the water column and the temperature of the water.

Starting with the airflow regulation through the bubbling water column (13), it is carried out employing two controlled valves: the MHM bypass valve and the Reactor valve, (10) and (12) of Figure 4. 21, respectively. The MHM bypass valve (10) is actuated by a PID controller focused on controlling the humidity level at point 'c.' Additionally, the Reactor valve (12) is actuated in opposition and conjugated to the MHM bypass valve (10) to help in the regulation of the airflow through the water column (13), and make sure that when the water column should be bypassed entirely, there is no flow going through it.

It should be noted that when (12) is closed and there is a change of pressure in the MTM, an air bubble is created between the Reactor valve (12) and the water level at the water column inlet (13), which has a different pressure than the rest of the system. This causes the movement of the water body inside (13). If the pressure is higher in the air bubble than in the rest of the installation, there would be an increase in the water level. In this case, the water column inlet pipe (between 12 and 13) is dry, which does not involve further problems since it is the steady-state operation conditions of the bubbling water column (13). In contrast, if the pressure in the air bubble is lower than the system, the water will climb up through the water column inlet pipe (between 12 and 13) and will be accumulated there until the Reactor valve (12) opens again.

This means that once the water has moved and (12) opens again, the water accumulated between (12) and (13) will rush to the bubbling water column vessel (13), generating a great force that could damage the components inside and even overturn the MHM. Therefore, to avoid this risk, the Reactor valve (12) is always opened partially and never fully closed (minimum closing 5%) to allow a negligible airflow that equalizes the pressure and avoids the movement of the water body. However, the equalizer airflow is not big enough to significantly affect the main airstream that bypasses the water column temperature and humidity conditions.

Lastly, the temperature control of the water column is partially carried out using the Enhanced-valve (14 of Figure 4. 21), which allows the passing of the dry and hot flow through the heat exchangers installed inside the bubbling water column (6 and 10 of Figure 4. 28). For this control, the Enhanced-valve (14) closes the path that bypasses the heat exchangers, trying to achieve 70 ºC when the temperature at the heater (9) inlet (point 'a' of Figure 4. 21 in the MTM blue perimeter) is higher than the bubbling water column temperature.

In addition to (12), the HE-valve (15 of Figure 4. 21) located at the heat exchanger inlet is actuated in opposition to (12) to help manage the flow through the heat exchangers. This is necessary since, experimentally observed, when the Enhanced-valve (12) is fully open, around 30% of the airflow is still passing through the heat exchangers. This reduced the cooling capabilities of the MTM when the MHM was connected since a big part of the cooled air was being heated up by the water inside the bubbling water column (13).

4.3.3.2 Pressure control

Concerning the pressure control block, it only suffers slight modifications due to the installation of the MHM. The control logic presented in Section 4.2.2.1 is maintained except for an improvement in the humidity correction step. Suppose the humidity is below the setpoint and the humidity control actuator (MHM bypass valve, 10 of Figure 4. 21) is fully closed. In this case, the mechanical compressor (2) speed is lowered to reduce the pressure in the humecting phase and, according to psychrometry theory, increase the water absorption of the air inside the bubbling water column (13). Contrarily, if the humidity is above the setpoint and the MHM bypass valve (10) is fully open, the mechanical compressor (2) speed is increased to raise the pressure in the cooling branch (6, 7, and 8). This causes an increase in the condensation for a given temperature and thus increases the drying performance of the cooling system.

It should be noted that this is only carried out if the pressure and temperature setpoints are achieved to follow the hierarchy previously defined. The actualized flow diagram for the pressure control block of the MTM is presented in Figure 4. 33.

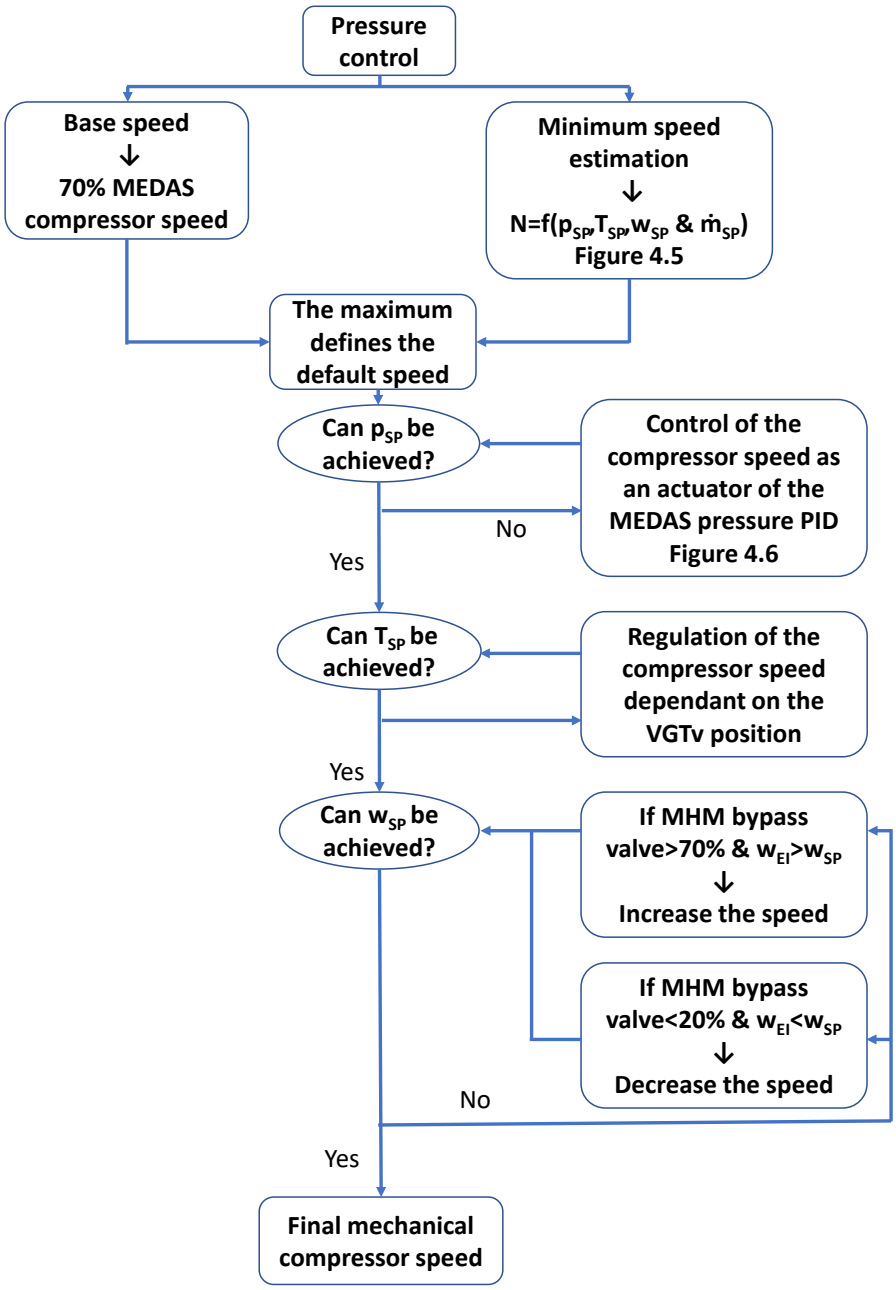

Figure 4. 33. Flow diagram of the MTM + MHM pressure control sequence

4.3.3.3 Temperature control

In the case of temperature control, the addition of the MHM generates several changes in the control strategy. In the first place, the electric heater (9) function changes from controlling the engine intake air temperature at point 'c' (engine intake in the MEDAS) to control the temperature of the heat rods. Also, the control of $T_{SP,MTM}$ (now point 'b') is divided into two cases: the demanded humidity can be considered low for the full-scale of the equipment, and another case in which there is a high humidity demand. With differences between both in the control target of the actuators involved.

a) Heater control

When the MHM is coupled to the MEDAS and the MTM, the heater (9 of Figure 4. 21) changes its target. It stops controlling the airstream temperature at point 'c' to control the bubbling water column (13) temperature. The heating of the water column is a twofold process. On the one hand, it is heated up by the hot and dry airstream passing through the heat exchangers inside the water column vessel (6 and 10 of Figure 4. 28). On the other hand, it is heated up by the hot and moist air that passes through the water. It is over this second airstream (which will be the humid stream) over which the electric heater (9) actuates.

To achieve this objective, the electric heater PID controller passes to control the heat rod temperature to 500ºC if the reactor water temperature is below 75ºC. When the water reaches 75ºC, the temperature setpoint of the heater is reduced to 200ºC to reduce the energy consumption of the system. However, if the water temperature cools down below 65ºC, the setpoint returns to 500ºC to increase the water temperature again. This hysteresis in the setpoint change is necessary to avoid consecutive changes in the setpoint and thus in the electric consumption of the heater, which could damage the component.

The manufacturer sets the maximum temperature for the heater (9) heat rods at 600ºC. Accordingly, the temperature setpoint for the heater is defined as 500ºC to have a safety margin until the material limit. Additionally, if the heat rods temperature overcomes 550ºC, the electric supply of the heater is cut off to protect the component. In this way, the electric heater (9) is protected from overheating the heat rods above the security limit value of 600ºC if suddenly the airflow through it is reduced due to any change in the setpoint demanded by the user.

b) $T_{SP,MTM}$ control

The generation of $T_{SP,MTM}$ does not change with the installation of the MHM. However, the controlling point of this setpoint in the system layout and the actuators that will control it do change. Once the MHM is installed, the control of $T_{SP,MTM}$ passes from being handled at the heater inlet (point 'a' of Figure 4. 21) to being controlled at the MHM outlet (point 'b'). In the case of the actuators that will control $T_{SP,MTM}$, it will depend on the humidity setpoint demanded by the user, which has been divided into two parts: low humidity case, when the

water content required by the user is lower than 19 g_{water}/kg_{air}; and high humidity case, when the humidity demand is higher than 19 g_{water}/kg_{air}.

This division is necessary due to the oscillations observed in the humidity control when the demanded humidity is below 19 g_{water}/kg_{air}. The high effect over the moisture of the movement of the MHM bypass valve (10) (the low sensibility of this valve) was found experimentally as the cause for these oscillations. When a small airstream passes through the bubbling water column (13) (low humidity demand conditions), the air can absorb more water due to two effects. Firstly, the lower air mass flow passing through the water column (13) causes a decrease in the airstream velocity and increases the residence time in the water. Secondly, as there is also low flow through the electric heater (9), the air temperature at the inlet of the bubbling water column (13) increases, increasing further the capability of the airstream to absorb water. Both cause a significant reduction of the MHM bypass valve (10) sensibility that keeps the measurement oscillating around the setpoint.

When demanding low humidity, this problem in the control stability can be removed by reducing the heater (9) inlet temperature conditions (point 'a'). Reducing the heater inlet temperature means that the airstream would be drier, which causes an increase in the mass flow that must pass through the bubbling water column (13) to achieve the humidity setpoint. This removes the first cause of the humidity oscillations found: low airstream velocity. Additionally, when this action is carried out, the outlet heater temperature (temperature downstream of 9) decreases as the heater inlet temperature (point 'a') is lower and the mass flow is higher, removing the effect of the second cause of the oscillations presented: high air temperature at the bubbling water column (13) inlet.

However, with the new strategy to remove the oscillations in the low humidity case, the humidity setpoint in the high humidity demand conditions cannot be reached. Hence, the definition of two working modes for the temperature is necessary when the MHM is installed. It should be noted that this change in strategy has a hysteresis also implemented: the shift from low to high humidity mode happens at 22 g_{water}/kg_{air}. Contrarily, the shift from high to low humidity happens at 19 g_{water}/kg_{air}, intending to avoid continuous mode changes, making the stabilization of the operative point impossible and risky for the installation.

The actuators involved in the temperature control mode change are the bypass valve of the cooling branch (Cooling Bypass, 5 of Figure 4. 21) and the HR-valve (11), which function will be discussed following.

In the case of low humidity, the objective is to reduce the temperature at the heater inlet (point 'a') as much as possible to reduce the temperature and humidity of the inflow of the bubbling water column (13). To achieve this objective, the cooling bypass (5) is closed completely, passing all the flow through the cooling system (6, 7, and 8) installed in the MTM, achieving the

lowest temperature and water content possible at point 'a'. In this case, the control of $T_{SP,MTM}$ is carried out using the HR-valve (11) pointing at point 'b' (MHM outlet). The HR-valve (11) opens to use the hot air that is present in the outlet of the electric heater (9) to heat the air downstream of the MHM ('b').

Contrarily, when the demanded humidity is in the high humidity range, the cooling bypass valve (5) is the actuator for the temperature control PID, which tries to achieve $T_{SP,MTM}$ at the MHM outlet (point 'b'). In contrast, the HR valve (11) stays closed to avoid hot flow bypassing the bubbling water column (13).

4.4. Atmosphere simulator performance

With the addition of the MHM, the performance of the MEDAS + MTM set presented previously in Section 4.2.3 is expanded to encompass the humidity control. This is done without modifying the mass flow and temperature control range shown in Figure 4. 15B and Figure 4. 16B, respectively.

4.4.1. Steady-state

Several steady-state points have been carried out with the atmosphere simulator set composed of the MEDAS, MTM, and MHM to characterize the humidity control in steady-state operation. The pressure, temperature, and relative humidity have been changed along the available range for these tests to obtain an accurate map of the humidity control performance. The pressure varies from 1 barA to 0.54 barA, the temperature from 0 ºC to 40 ºC, and the relative humidity from 10 % RH to 80 % RH. During these tests, the mass flow was constant at 0.25 kg/s, corresponding with the maximum flow supplied by the prototype with which the tests were carried out.

The range of humidity accomplished is shown in Figure 4. 34 by the colored blue area in a figure template like a psychrometric diagram. The specific humidity (g_{water}/kg_{air}) is presented on the *y-axis* against the temperature on the *x-axis*. Moreover, a green area is defined as the range in which the atmosphere simulator set expects to locate the ambient conditions of the installation room.

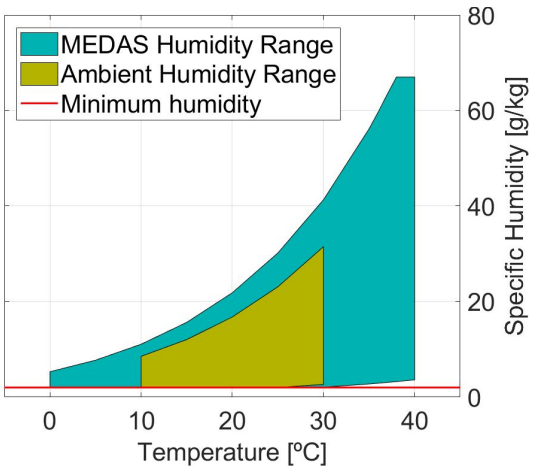

Figure 4. 34. Humidity control performance

The maximum humidity expected, corresponding to 5000 meters of altitude, 40 ºC and 80 % of RH (black cross of Figure 4. 22, corresponding to 77 g_{water}/kg_{air}), could not be achieved since the 68 ºC of temperature needed in the bubbling water column was not reached. This is due to a twofold effect: the heat losses to the ambient of the vessel walls and the amount of heat needed to evaporate the water and dissolve it in the airstream. With the prototype installation, these two reach an equilibrium with the heat influx from the water column inlet air, making it impossible to reach water temperatures higher than 63 ºC. The maximum water content achieved in these conditions was 67 g_{water}/kg_{air}. A more powerful heater (over 12 kW of the tested one -9-), more efficient insulation of the water column vessel or a more efficient heat exchange in the heater would be needed to reach the desired 68 ºC in the water.

Also, the minimum achievable humidity has been marked by a red line, which could be decreased only in two ways: higher pressure supplied by the mechanical compressor of the MTM (2 of Figure 4. 21) or lower outlet temperature provided by the chiller of the cooling branch (7); with both needing a redesign of components to be achieved. The minimum humidity achieved with this installation was 2 g_{water}/kg_{air}, which corresponds with ambient at sea level, -4.5 ºC, and 80% of RH.

4.4.2. Dynamic

To characterize the dynamic performance of the atmosphere simulator set, several tests reproducing the atmospheric conditions that could be found during a vehicle road test have been carried out. A sample of the tests carried out will be presented in the current section. These tests have been done with and without connecting an engine to the MEDAS since the bypass (between 21 and 22 at Figure 4. 21) gives the possibility of operating the MEDAS in either case.

Figure 4. 35 shows results from testing the atmosphere simulator set dynamically coupled with an engine. The engine is increasing and then decreasing its load and speed in steps. The MEDAS set reproduces the atmosphere conditions of driving from Granada to Prado Llano, at Sierra Nevada Road (from 910 meters above sea level up to 2100 meters) and then down to 1600 meters at an average velocity of 100 km/h. This road test is one commonly used by OEMs to carry out on-road tests for their vehicles under altitude and hot conditions.

Moreover, during this driving test, the emulated temperature and relative humidity at engine intake were constant at 25ºC and 80% RH. This figure is divided into four main graphs, showing pressure, temperature, relative humidity, and specific humidity results in Figure 4. 35 A, B, C, and D, respectively. Each variable has three graphs with the *x-axis* representing the time: in the upper graph, the measured variable with the setpoint demanded is presented, in the middle diagram, the error between both is shown in absolute value, and the bottom chart shows the relative error between measurement and setpoint.

The percentage errors are defined with respect to the full scale of the MEDAS for each control variable: pressure, temperature, and specific humidity, which are: 7000 m (from 2000 meters below sea level to 5000 meters above); 55 ºC (from -15 ºC to 40 ºC) and 80 g_{water}/kg_{air}, respectively. Additionally, the speed and load transients of the engine have been plotted in Figure 4. 35B and C top graphs, in black dotted and blue lines, respectively.

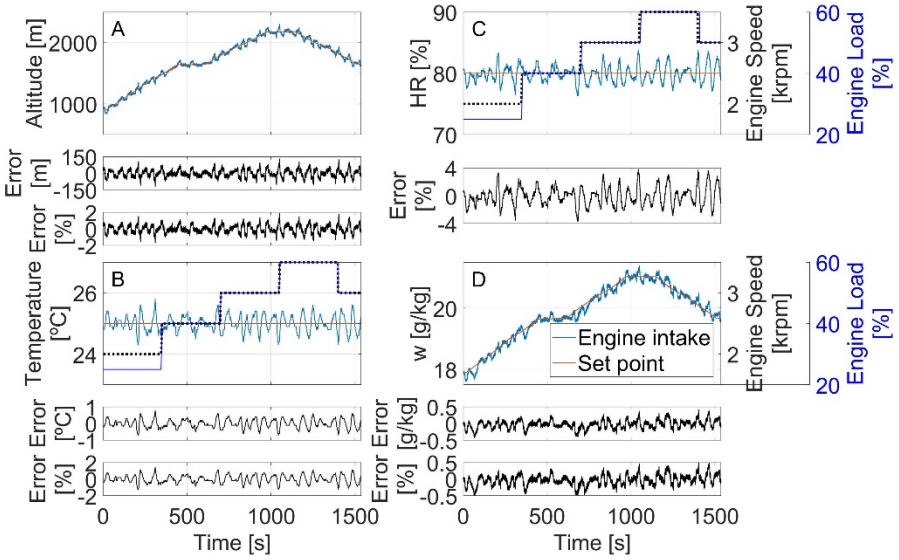

Figure 4. 35. Dynamic performance of the atmosphere simulator with an engine connected performing speed and load transients: (A) Altitude; (B) Temperature; (C) Relative humidity; (D) Specific humidity

If the focus is put on the accuracy of the controlled variables, all three variables: altitude, temperature, and specific humidity; are controlled with an average error of less than +/- 0.5 %; defined as the error of the measurement to the setpoint averaged in all the time frame of the test. The instantaneous peak errors are kept below +/- 2 % in all the cases. The relative humidity is not included during the discussion since it is a consequence of the control of the other three variables, and its error is an accumulation of them. Also, there are no apparent disturbances in any graph due to the changes in the engine operating point.

It is worth noting that the specific humidity (g_{water}/kg_{air}) shown in Figure 4. 35D is changing, even when the temperature and relative humidity are constant. This is caused by the pressure variation with altitude shown in Figure 4. 35A. Therefore, as the specific humidity is what the system controls, Figure 4. 35 shows the difficulty of controlling constant relative humidity. One must bear in mind that any change in any psychrometric variables: pressure, temperature, or relative humidity, involves a variation in specific humidity that the system must fit.

Additionally, one of the tests carried out without an engine connected is presented in Figure 4. 36, following the same graph layout as Figure 4. 35. In this case, the atmosphere simulator is performing a road test like the one shown in Figure 4. 18, which consists of a constant climb from 2000 meters below sea level up to 5000 meters above sea level in 30 min, in which the vehicle is driving at an average speed of 71.3 km/h in a road of 20% of slope. It then returns to 2000 meters below sea level in another 30 min following the same route.

The temperature and humidity also perform their independent dynamic profiles during this test. In the case of the temperature, it has been changing from 40 ºC to 0 ºC with a constant slope during the test. Contrarily, the relative humidity has been kept constant at 10 % RH. Still, as happened in the previous dynamic test, the specific humidity will change from 3.5 to 2.8 g_{water}/kg_{air} during the climb up, and it will end up at 0.5 g_{water}/kg_{air} at the end of the test.

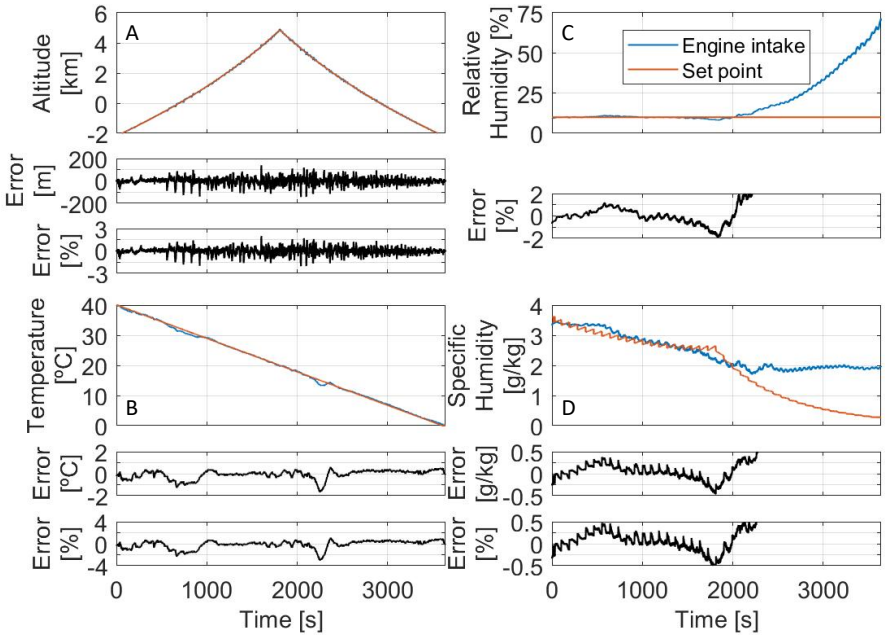

Figure 4. 36. Dynamic performance of the atmosphere simulator: (A) Altitude; (B) Temperature; (C) Relative humidity; (D) Specific humidity

Even when performing an extreme road test, it can be seen how the atmosphere simulator can keep the error in the three control variables in the same range as when following more standard road tests (Figure 4. 35). This shows how the MEDAS can adjust the three setpoints dynamically along with the whole pressure range available while keeping the error between the acceptable margin defined of 2 % of the full scale of each variable.

In the graphs showing the humidity error (Figure 4. 36C and D), after time = 2000s, the setpoint is not followed. This is due to reaching the drying limit of the system. The current installation cannot achieve a specific humidity lower than 2 g_{water}/kg_{air}. Therefore, the atmosphere simulator controls the air stream's humidity with an error of +/- 0.5 gwater/kgair during the first 2000 seconds. Still, the system limit is reached when the humidity demand goes below 2 gwater/kgair, and it is impossible to follow the setpoint.

4.5. Application of the Atmosphere Simulator on RDE+ procedures

During the development of the current Ph.D. Thesis, there was a collaborative relationship between the Institute CMT-Motores Térmicos from Universitat Politècnica de Valencia (Spain) and the engine testing and development

facilities at HORIBA MIRA in Nuneaton (England) to carry out some of the necessary steps of the development of the atmosphere simulation set and its preparation for commercial use. The central part of these works consists of using their facilities to fine-tune the installation, including developing several of the previously exposed control strategies that improve the energy consumption and control accuracy of the atmosphere simulator set. Also, the identification and definition of several necessary safety procedures presented in Chapter 3 were made using the installed units.

In the current section, some of the results obtained with the atmosphere simulator at the laboratories of HORIBA MIRA are presented. These tests tried to reproduce on-road tests performed by the HORIBA MIRA team on an engine test bench. These results have been published [13] as part of the road to engine lab testing methodology called RDE+ developed by HORIBA MIRA. The ability to reproduce atmospheric conditions offered by the atmosphere simulator is one of the main features of the proposed method.

These tests have been performed by reproducing driving cycles from different parts of Europe, such as Nuneaton in England, Innsbruck in Austria, and Avila in Spain. The reproduction of the atmospheric conditions comprises a dynamic change of the pressure, temperature, and relative humidity, following the ambient conditions in which the vehicle was performing the road test.

The results are presented in Figure 4. 37, in which the Nuneaton, Innsbruck, and Avila tests are shown in Figure 4. 37A, B, and C, respectively. Each of the three road tests shows the pressure, temperature, and relative humidity against the cycle time, with the setpoint in red and the sensor measurement in black. Moreover, the maximum available error range between the setpoint demanded and measurement has been included with the grey lines, representing 10 mbar for the pressure, 1ºC in the case of the temperature, and 10% for the relative humidity.

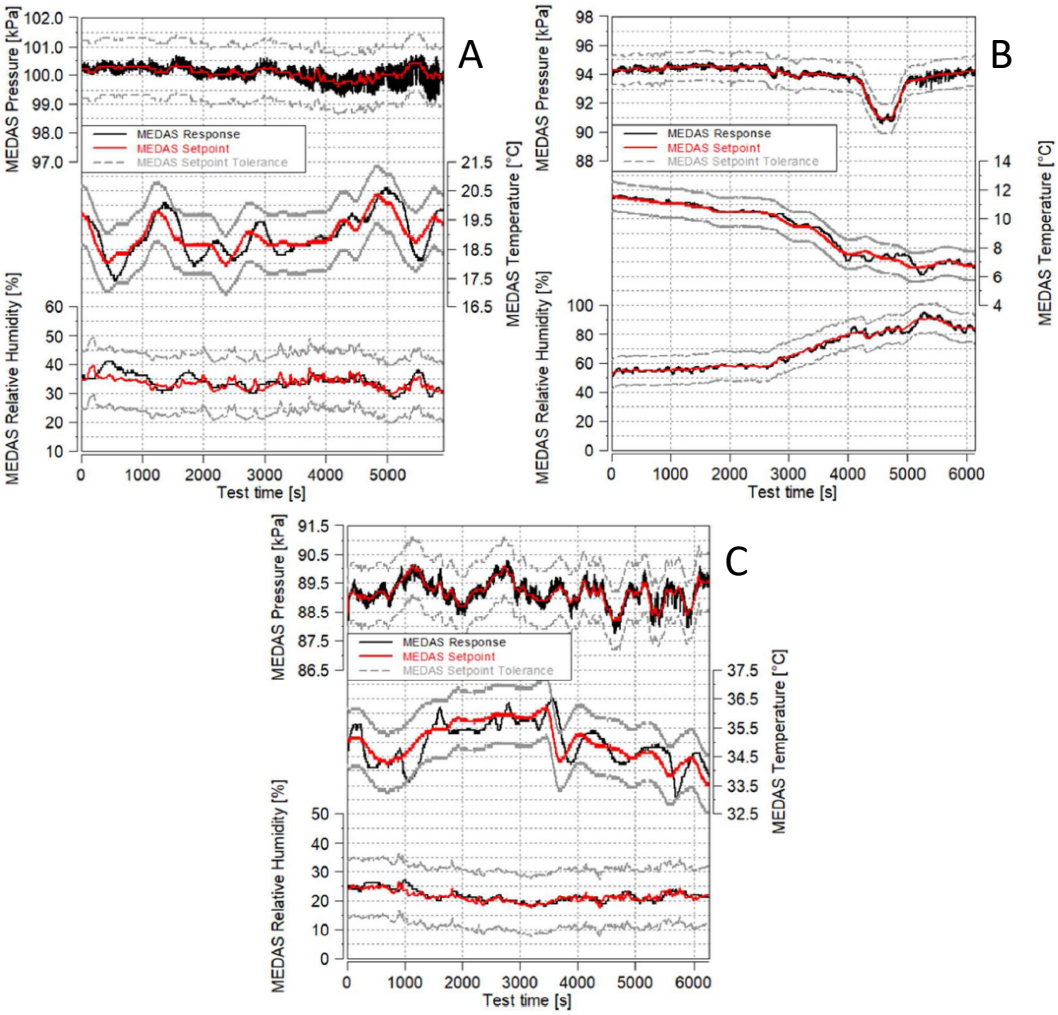

Figure 4. 37. Road tests atmospheric condition reproduction with the atmosphere simulator: (A) Nuneaton, England; (B) Innsbruck, Austria; (C) Avila, Spain. Elaborated from reference [13]

In all the tests shown in Figure 4. 37, the three control variables are within the acceptable error along with the duration of the test. This is a final validation of the atmosphere simulator developed through this Ph.D. Thesis, since Figure 4. 37 shows an accurate reproduction of the atmospheric conditions in three very different locations of the European geography, withstood by an actual vehicle during a driving test, and performed by independent laboratories and a working team that the one that carried out the development of the atmosphere simulator.

4.6. Bibliography

[1] J. Gómez, "Development of an altitude simulator and analysis of the performance and emissions of turbocharged Diesel engines at different altitudes," Ph.D. Thesis, Universitat Politècnica de València, Spain, 2018. doi: 10.4995/Thesis/10251/101284.

[2] J. M. Desantes *et al.*, "Device, method and use for conditioning intake air for testing internal combustion engines," Patent WO 2019/114935 A1, 2019

[3] F. P. Incropera and D. P. DeWitt, "Fundamentals of Heat and Mass Transfer," 4th ed. Pearson Educación, 1999.

[4] A. J. Torregrosa, A. Broatch, X. Margot, J. García-Tíscar, Y. Narvekar, and R. Cheung, "Local flow measurements in a turbocharger compressor inlet," *Experimental Thermal and Fluid Science*, vol. 88, pp. 542–553, Jul. 2017, doi: 10.1016/j.expthermflusci.2017.07.007.

[5] J. Kashdan, S. Mendez, and G. Bruneaux, "An investigation of unburnned hydrocarbon emissions in wall guided, low temperature diesel combustion," *Oil and Gas Science and Technology*, vol. 63, no. 4, pp. 433–459, 2008, doi: 10.2516/ogst:2008018.

[6] "User Guide Simcenter STAR-CCM+." Siemens Digital Industries Software, 2020. [Online]. Available: www.siemens.com/mdx

[7] T. Höhne and P. Porombka, "Modelling horizontal two-phase flows using generalized models," *Annals of Nuclear Energy*, vol. 111, pp. 311–316, Sep. 2018, doi: 10.1016/j.anucene.2017.09.018.

[8] D. Gidaspow, "Multiphase Flow and Fluidization -Continuum and Kinetic Theory Descriptions," *Academic Press, Inc.*, 1994.

[9] M. Ishii and K. Mishima, "Two-fluid model and hydrodynamic constitutive relations," *Nuclear Engineering and Design*, vol. 82, pp. 107–126, 1984, doi: 10.1016/0029-5493(84)90207-3.

[10] G. Cerne, S. Petelin, and I. Tiselj, "Coupling of the Interface Tracking and the Two-Fluid Models for the Simulation of Incompressible Two-Phase Flow," *Journal of Computational Physics*, vol. 171, no. 2, pp. 776–804, Aug. 2001, doi: 10.1006/jcph.2001.6810.

[11] E. E. Michaelides, C. T. Crowe, and J. D. Schwarzkopf, "Multiphase Flow Handbook," 2nd ed., no. 2. CRC Press, 2017.

[12] R. Sun and H. Xiao, "Diffusion-based coarse graining in hybrid continuum-discrete solvers: Theoretical formulation and a priori tests," *International Journal of Multiphase Flow*, vol. 77, pp. 142–157, Dec. 2015, doi: 10.1016/j.ijmultiphaseflow.2015.08.014.

[13] P. Roberts, A. Mason, A. Headley, L. Bates, S. Whelan, and K. Tabata, “RDE plus - A Road to Rig Development Methodology for Whole Vehicle RDE Compliance: Road to Engine Perspective,” in *SAE Technical Papers*, Sep. 2021, 2021-01-1223. doi: 10.4271/2021-01-1223.

Chapter 5
Application on a Diesel engine

5.1. Introduction

As discussed previously, the atmosphere simulator set, composed of the MEDAS coupled with an MTM and MHM, can reproduce a given set of atmospheric conditions at the intake and exhaust of a thermal engine [1]–[3]. Using these three pieces of equipment makes it possible to emulate any ambient conditions found on automotive roads on the Earth, which allows reproducing any on-road test and tuning the engine calibration in a controlled environment and repetitive way.

Moreover, the addition of the bubble reactor in the MHM considerably widens the humidity control range, way above the maximum humidity recorded on the Earth [4]. This opens the way for testing the effect of the ambient moisture on the engine and emulating the impact of injecting water into the intake without needing any modifications to the engine.

Therefore, two studies are proposed in this chapter. The first would be the impact on the engine-out pollutant emissions by increasing the humidity to levels similar to injecting water in the engine intake manifold during steady-state operation [5]–[7]. And the second is a discussion of how the three ambient conditions parameters: pressure, temperature, and humidity, within Earth's possible range, affect the performance and pollutant emissions of a turbocharged automotive diesel engine, operating at steady points and during homologation cycles.

5.2. Test bench description

The discussion is based on the results of three different engines installed in the same test cell and using the same measurement equipment in all the cases. The experimental facility in which this study was carried out consists of a reciprocating internal combustion engine coupled to an asynchronous dynamometer controlled by the AVL PUMA Open system to set torque and speed.

The engine performance and emissions were monitored during the tests. The dynamometer registered the engine torque and speed. An AVL GU21D glow-plug piezoelectric pressure transducer measured the instantaneous in-cylinder pressure. In addition, the flow properties along with the engine intake and exhaust systems were instrumented with Wika piezoresistive pressure sensors and K-type thermocouples for pressure and temperature measurement. The air and fuel mass flows were also monitored by an onboard AVL FLOWSONIC AIR mass flow sensor and an AVL 733S gravimetric balance, respectively. Finally, the engine-out pollutants emissions were measured by a Horiba MEXA ONE gas analyzer and an AVL 439 Opacimeter placed upstream of the after-

treatment system. In addition, a gas sample was also taken from the intake manifold to obtain the CO2 molar fraction and calculate the EGR rate. Table 5. 1 shows the accuracy of the instrumentation used. LP-EGR was used during the study since the HP-EGR strategy is only used during engine warm-up phases.

Table 5. 1. Test cell instrumentation accuracy

Sensor	Accuracy [% of sensor span]
Dynamometer	0.018
Encoder	0.05
AVL GU21D Glow-plug piezoelectric pressure transducer	0.3
Wika Piezoresistive pressure sensor	0.5
K-Type thermocouple	0.75
AVL FLOWSONIC AIR Mass flow meter	1
AVL 733S Gravimetric balance	0.12
Horiba MEXA ONE Gas analyser	1
AVL 439 Opacimeter	0.1

All three engines are turbocharged diesel automotive engines. Engine 1 characteristics are shown in Table 5. 2. Engine 1 was used to study the altitude effect while performing WLTC homologation cycles. Some pictures of the test bench are shown in Figure 5. 1, in which the exhaust gases analyzer was connected between the diesel oxidation catalyst (DOC) and the diesel particulate filter (DPF). In contrast, the opacimeter was connected downstream to the DPF.

Table 5. 2. Specifications of tested Engine 1

Type	HSDI Diesel Passenger Car Engine, Euro 4
Displacement	1997 cm^3
Bore	85 mm
Stroke	88 mm
Number of cylinders	4 in line
Number of valves	4 per cylinder
Turbocharger model	Variable Geometry Turbine
Compression ratio	15.5:1
Maximum power @ speed	120 kW @ 3750 rpm
Maximum torque @ speed	340 Nm @ 2000 rpm
Maximum mass flow @ speed	640 kg/h @ 4500 rpm & full load
Intake temperature control	Water Charge Air Cooler (WCAC)
EGR type	Cooled HP with an intake valve
Aftertreatment	Close-coupled DOC, underfloor DOC + DPF

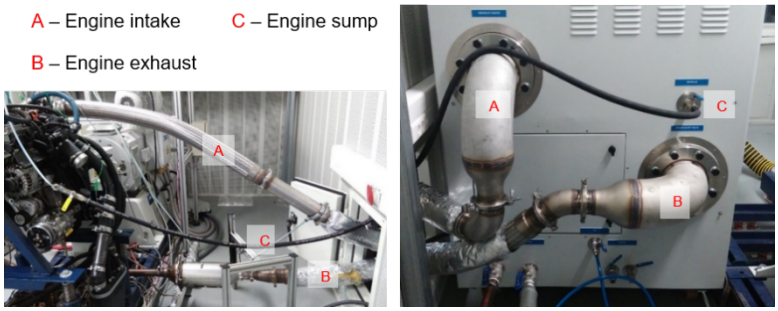

Figure 5. 1. Engine 1 (left) to MEDAS (right) connection elements

Engine 2 was used to study the effect of the water injection in the intake line during steady-state engine operation. The characteristics of these engines are depicted in Table 5. 3, in which the exhaust gases analyzer is connected upstream to the DOC and the opacimeter between the DOC and the DPF. The connection between Engine 2 and MEDAS is shown in Figure 5. 2A.

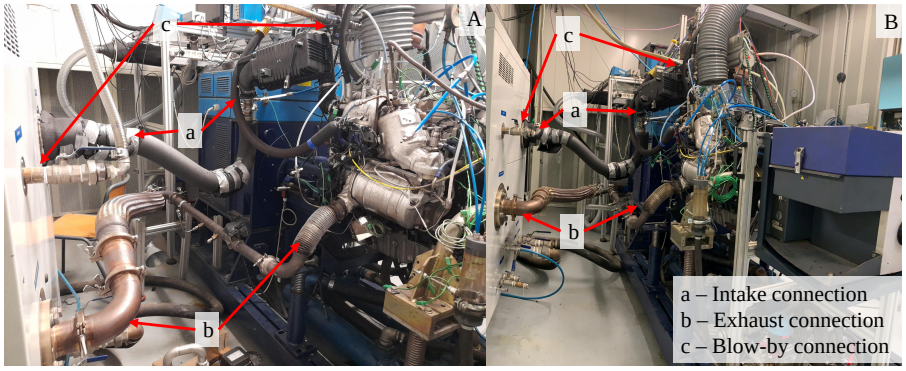

Figure 5. 2. MEDAS to engine connections. (A) Engine 2; (B) Engine 3

Table 5. 3. Specifications of tested Engine 2

Type	HSDI Diesel Passenger Car Engine, Euro 6d-Temp
Displacement	1461 cm^3
Bore	76 mm
Stroke	80.5 mm
Number of cylinders	4 in line
Number of valves	2 per cylinder
Turbocharger model	Variable Geometry Turbine
Compression ratio	15.16:1
Maximum power @ speed	84 kW @ 3750 rpm
Maximum torque @ speed	253 Nm @ 2500 rpm
Maximum mass flow @ speed	435 kg/h @ 4500 rpm & full load
Intake temperature control	WCAC
EGR type	HP and cooled LP-EGR
Aftertreatment	Closed-coupled DOC+SCRf

Engine 3 was used in both studies: to analyze the effect of injecting water in the intake line on the engine-out pollutant emissions and performance and the impact on these variables of the ambient temperature and humidity during steady-state engine operation. Its characteristics are depicted in Table 5. 4. In this case, the exhaust gases analyzer and the opacimeter were both connected upstream to the DOC. The connection of Engine 3 with the MEDAS is shown in Figure 5. 2B.

Table 5. 4. Specifications of tested Engine 3

Type	HSDI Diesel Passenger Car Engine, Euro 6
Displacement	1995 cm^3
Bore	84 mm
Stroke	90 mm
Number of cylinders	4 in line
Number of valves	4 per cylinder
Turbocharger model	Variable Geometry Turbine
Compression ratio	16.0:1
Maximum power @ speed	147 kW @ 3500 rpm
Maximum torque @ speed	400 Nm @ 1750 rpm
Maximum mass flow @ speed	630 kg/h @ 3500 rpm & full load
Intake temperature control	WCAC
EGR type	HP and cooled LP-EGR
Aftertreatment	Closed-coupled DOC+SCRf

To control the temperature at the intake manifold of Engines 2 and 3, a fluid conditioner was installed to manage the coolant provided to the water charge air cooler (WCAC). This allows decoupling the temperature at the intake manifold from the room and intake temperature, providing a more comprehensive range of operation to the engine test cell. The temperature at the intake manifold was imposed depending on the engine speed and is shown in Table 5. 5.

Table 5. 5. Intake manifold temperature

Engine speed [rpm]	Intake manifold temperature [ºC]
1500	40
2000	40
2500	45
3000	50

Moreover, the MEDAS was connected to the engine intake and exhaust, coupled with the two extension modules, the MTM and MHM. The connection of the atmosphere simulator developed (MEDAS+MTM+MHM) is the critical factor with which the study proposed could be carried out.

For the first study proposed, the WLTC cycle was carried out at four different altitudes: 0 meters, 1000 meters, 2000 meters, and 3000 meters above sea level, at a temperature of 20ºC and relative humidity of 50%.

The testing for the steady-state points was carried out under different ambient conditions. Two altitudes: 0 meters, 2000 meters above sea level; two temperatures: 30ºC and 45ºC; and three relative humidity levels: 10%, 50%, and 85%.

The steady-state engine map tested consists of four engine speeds: 1500, 2000, 2500, and 3000 rpm. And four engine loads dependent on the altitude: 5, 10, 15, and 18 bar of brake mean effective pressure (BMEP) for sea-level tests, and 4, 8, 12, and 15 bar of BMEP for the 2000 meters and 2500 meters above sea level tests. Moreover, these engine points are tested with 0, 5, and 10 % low-pressure EGR.

For the second study, the engine steady-state map tested is the same as defined previously, as the ambient conditions follow. Two altitudes: 0 meters, 2500 meters above sea level, a temperature of 45ºC, and three relative humidity levels: 10%, 40%, and 70%.

5.3. Water injection on the intake line

To study the effect of injecting water at the engine intake on a diesel engine's performance and engine-out pollutant emissions, two engines were used: Engine 2 and Engine 3, which characteristics are depicted in Table 5. 3 and Table 5. 4.

As a first approach and to confirm that profound changes of the water content in the intake airflow had a significant effect, two very different specific humidity, 10 and 60 g_{water}/kg_{air}, are tested. For an air stream to achieve the maximum water content specified at 60 g_{water}/kg_{air} for this experimental campaign, the tests must be carried out at high altitudes and temperatures. Specifically, the tests are carried out at 2500 meters above sea level and 45ºC of ambient temperature. At these ambient conditions, several engine steady-state points are measured with Engine 2, consisting of four engine speeds: 1500, 2000, 2500, and 3000 rpm; and three load levels: 5, 7, and 9 bar of BMEP. The narrow performance map proposed for this engine in altitude is forced by the high opacity levels, limiting the injection and thus load range.

In Figure 5. 3, the NOx and opacity measurements are shown. The x-axis shows the measured value with a specific humidity of 10 g_{water}/kg_{air}, and the *y* axis the measured value with a specific humidity of 60 g_{water}/kg_{air}. The different symbols correspond with the engine speeds tested, the shade of the marker color represents the load level, and the colors represent the LP-EGR rate.

From the results presented in Figure 5. 3A, the water content present in the intake airflow has a significant impact on the pollutant emission of a diesel engine. When the humidity of the combustion air increases, the NOx emissions are significantly reduced. Following the same style of representation, Figure 5. 3B shows the increase in the opacity before the DPF when the humidity in the combustion air increases.

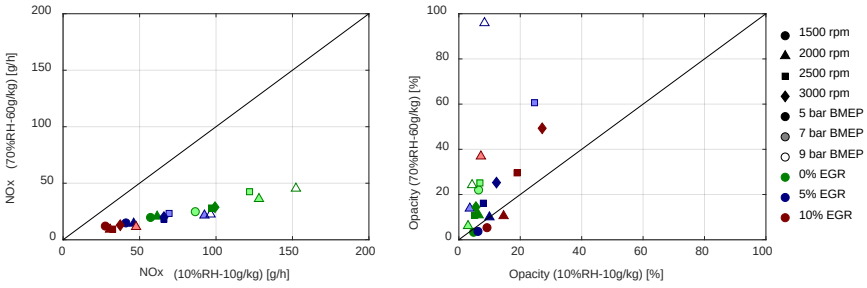

Figure 5. 3. Effect of water injection in Engine 2 pollutant emissions: NOx (left); opacity (right)

The results obtained with Engine 2 provided some exciting trends in engine-out pollutants emission. Still, due to the exaggerated increase of the opacity when increasing the water content of the combustion air, it is necessary to confirm the validity of the results with other engines to clarify if the trends found are caused by the wear and tear of this particular engine (more than 140.000 km) or are a

generalized trend in compression ignition engines. Therefore, a similar study was carried out with Engine 3, a new engine with a much lower number of working hours.

The available working area of Engine 3 is more comprehensive than Engine 2. Therefore the maximum engine load tested is increased in the study carried out with Engine 3, reaching up to 12 bar of BMEP. This study is carried out in the same conditions as the one done with Engine 2, at 2500 meters above sea level, 45 ºC, and in a humidity range from 10 to 60 g_{water}/k_{gair}. Additionally, an extra level of specific humidity (33 gwater/kgair) is included to obtain more information about the trends previously found.

Starting the discussion of the results obtained with Engine 3, it was observed how the combustion air mass flow decreases when the humidity in the air increases. Figure 5. 4 shows that the LP-EGR and the moisture are represented in the main-external *x-axis* and *y-axis*. Then for every point of these axes, the engine map measured in those conditions is described, with the engine speed in the secondary-internal *x-axis* and the engine load in the secondary-internal *y-axis*. Lastly, the black dots depict the measured points, and the color map is built by interpolating the measured data.

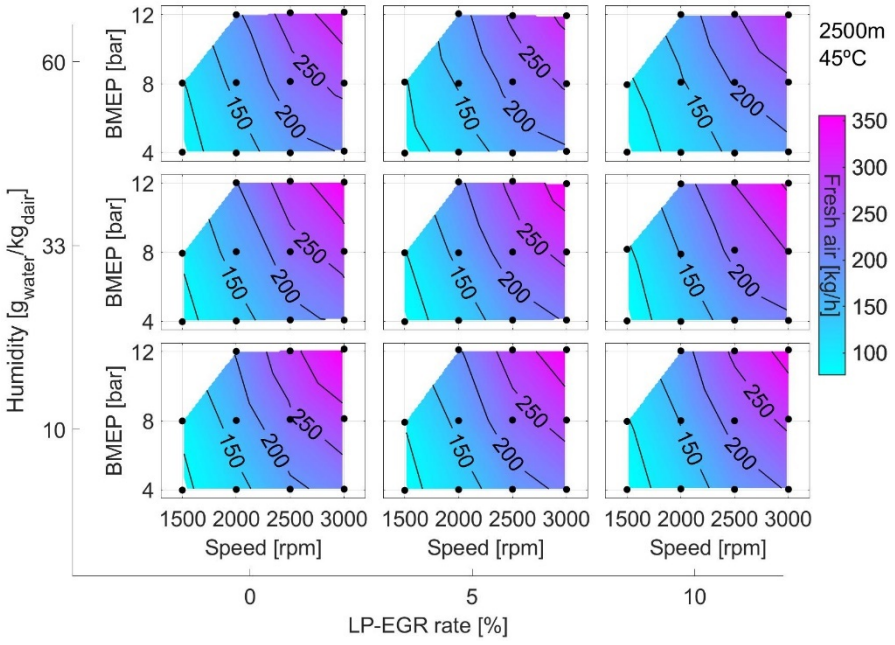

Figure 5. 4. Effect of water injection: Fresh air. Atmospheric conditions: 2500 meters above sea level, 45 ºC

The combustion air mass flow reduction can also be seen in the oxygen measured in the exhaust gases (Figure 5. 5A) and in the turbo compressor operation map (Figure 5. 5B). The compressor map moves the operation point to surge horizontally, maintaining the pressure ratio. The testing campaign designed is the cause of this behavior in the compressor operating point when the mass flow is reduced since the atmospheric and boost pressure are imposed constant for a given engine point in every humidity tested.

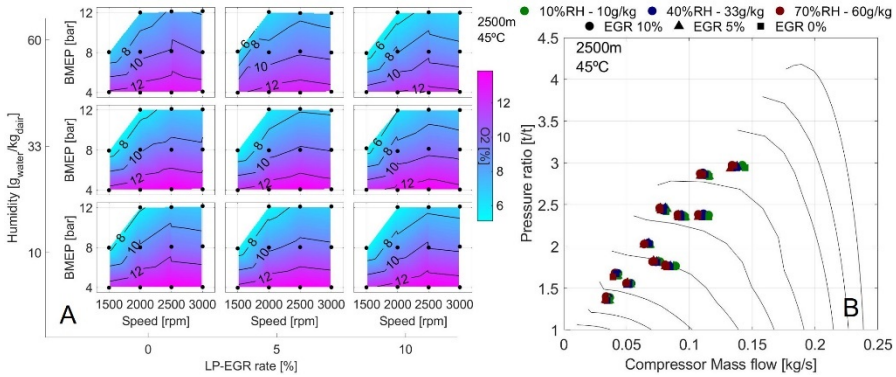

Figure 5. 5. Effect of water injection: (A) O_2 in the exhaust; (B) turbo compressor map. Atmospheric conditions: 2500 meters above sea level, 45 ºC

The displacement of the operation point of the turbo compressor to surge is due to a reduction in the volumetric engine efficiency. This is caused by the change in the composition of the air when the amount of water increases. If the ideal gases equation, Equation 5. 1, is considered, p is the gas pressure, v is the specific volume, R is the gas constant, and T is the gas temperature. For a given pressure and temperature, if the composition of the air changes, so does the specific volume.

$$\boldsymbol{p \cdot v = R \cdot T}$$

Equation 5. 1

During the tests carried out, the pressure and temperature in the intake manifold are imposed constant for the different humidity levels tested. Therefore, when the humidity in the combustion air changes, changing its composition relates directly to R and v (i.e., the specific volume of the gas). This is the leading cause of the reduction in volumetric engine efficiency. When the intake stroke happens, the air heats up due to heat transfer from the cylinder walls and expands. The specific volume is different with different humidity; therefore, the expansion magnitude changes for a given heat flux. Hence, this affects the amount of combustion air that can go inside the cylinder, thus affecting the engine's volumetric efficiency.

The variation of the gas constant for the atmospheric air (R_{air}) due to the ambient humidity has been calculated using Equation 5. 2, where R_{N2}, R_{O2}, R_{CO2}, R_{H2O}, and R_{Ar} are the gas constants for each of the main components of the air (shown in Table 5. 6), and Y_{N2}, Y_{O2}, Y_{CO2}, Y_{H2O}, and Y_{Ar} are the mass fractions of each of the main components of the air, calculated with Equation 5. 3, in which w is the specific humidity of the air in kg_{water}/kg_{air}.

$$\boldsymbol{R_{air} = R_{N_2} * Y_{N_2} + R_{O_2} * Y_{O_2} + R_{CO_2} * Y_{CO_2} + R_{H_2O} * Y_{H_2O} + R_{Ar} * Y_{Ar}}$$

Equation 5. 2

$$\boldsymbol{Y_{H_2O} = w; Y_{O_2} = 0.23163 * (1 - Y_{H_2O})};$$

$$\boldsymbol{Y_{N_2} = 0.75522 * (1 - Y_{H_2O})};$$

$$\boldsymbol{Y_{CO_2} = 0.00049 * (1 - Y_{H_2O})};$$

$$\boldsymbol{Y_{Ar} = 0.01253 * (1 - Y_{H_2O})};$$

Equation 5. 3

Table 5. 6. Gas constant for the main components of the atmospheric air

Gas constant	[J/kgK]
R_{N2}	296.84
R_{O2}	259.83
R_{CO2}	188.92
R_{H2O}	461.40
R_{Ar}	208.12

Figure 5. 6 shows the main-external axes represent the engine operation point, with engine speed on the *x-axis* and engine load on the *y-axis*. Then, for every point of the principal axes, the gas constant for the air (R_{air}) and the combustion air mass flow are represented on the *x-axis* and the *y* axis, respectively. The different colors represent the three humidity levels tested, and the symbols depict the three LP-EGR rates. Figure 5. 6 shows how the reduced mass flow decreases proportionally with the humidity increase. It can be seen how the slope increases with the engine speed, which induces us to think that the proportion between both could be constant for every engine point. Since when the combustion air mass flow increases due to the change in the engine operation point, the reduction also increases in absolute terms.

If the focus is put on the different symbols (LP-EGR rate) for a given color (humidity level, i.e., blue, which corresponds to 33 g_{water}/k_{gair}), it can be seen how when the LP-EGR rate increases (dots 10%, squares 0%) the mass flow decrease and the R_{air} increase. The humidity present in the exhaust gases due to

the combustion causes this. After mixing with the fresh air, it increases the humidity of the mix and further reduces the engine's volumetric efficiency.

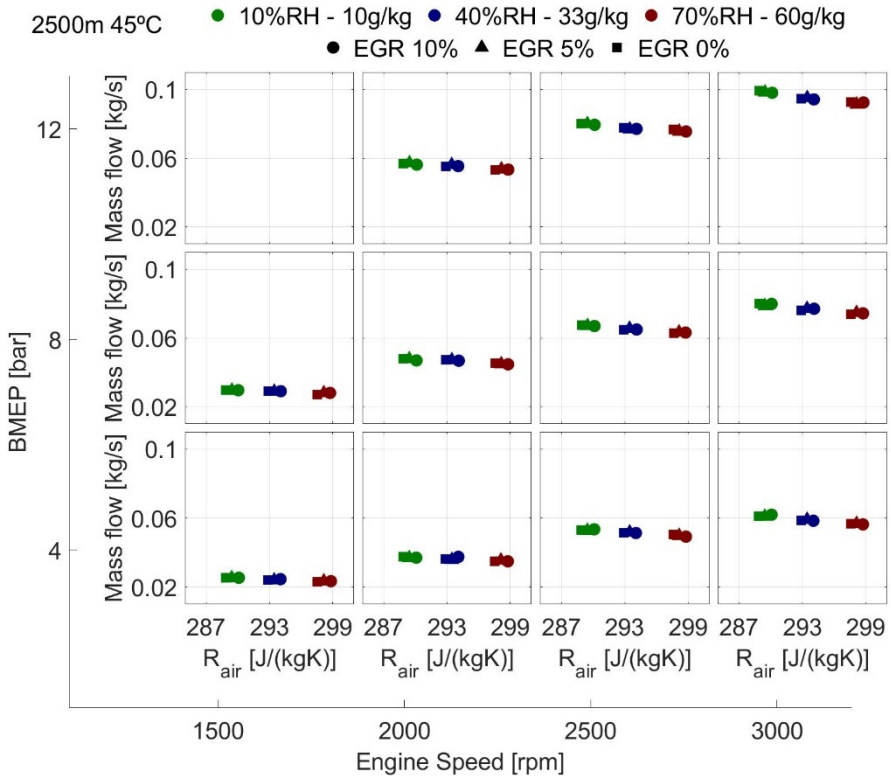

Figure 5. 6. Effect of the air composition change over the combustion air mass flow: absolute values. Atmospheric conditions: 2500 meters above sea level, 45 ºC

The mass flow reduction described previously is more apparent if the data is represented in percentages referenced to the dry case instead of total values. This is presented in Figure 5. 7, in which it can be seen how the trend of the mass flow when increasing the humidity is the same in every engine point tested. However, dispersion related to the EGR measured appears in Figure 5. 6 but is not zoomed enough to be seen. Nevertheless, the engine volumetric efficiency decreases proportionally when the combustion air composition increases the R parameter.

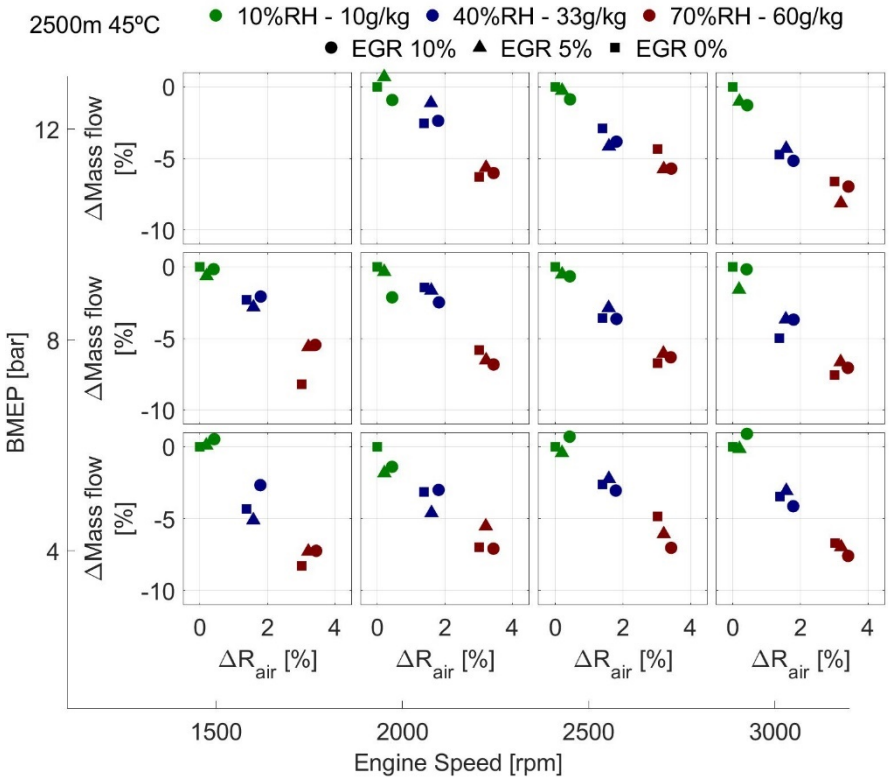

Figure 5. 7. Effect of the air composition change over the combustion air mass flow: relative values. Atmospheric conditions: 2500 meters above sea level, 45 ºC

The volumetric efficiency reduction is not the only phenomenon that affects the amount of available O_2 for combustion. As the air transport a higher amount of water, there is an effect of substitution of O_2 for water. Therefore, the O_2 available for combustion is decreased by two folds. First, the O_2 is reduced because of lower combustion air mass flow. Second, it is further reduced due to the substitution of the O_2 for water. The effect of the substitution is shown in Figure 5. 8, in which for every point of the principal axes, the change in mass flow referenced to the dry case is represented in percentage in the *x-axis* against the change in O_2, in the *y-axis*, also referenced to the dry case and in percentage.

If the focus is put on the engine point of 3000 rpm and 12 bar of BMEP (top right graph). For the high humidity case and 10% EGR (red dot), when the mass flow is reduced by 7% due to the reduction in the volumetric efficiency, the O_2 is reduced by almost 20% due to the effect of the O_2 substitution for water. This trend, higher O_2 decline than combustion air mass flow, is consistent in every engine point and for all humidity levels tested, as shown in Figure 5. 8, only varying in intensity between engine points and humidity levels.

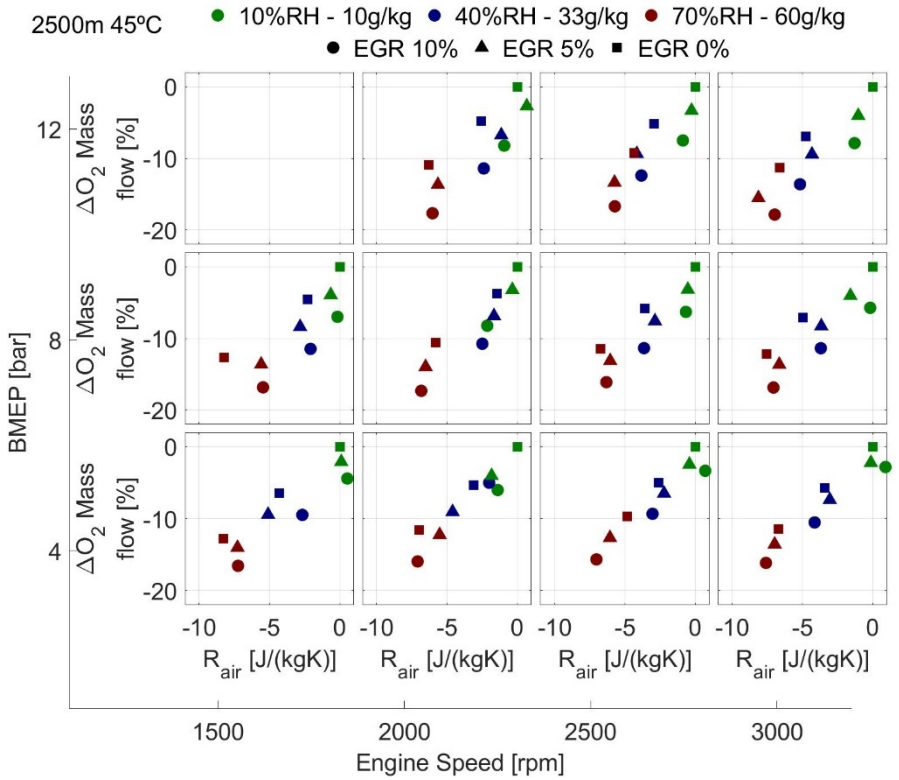

Figure 5. 8. O_2 reduction due to the substitution for water vapor. Atmospheric conditions: 2500 meters above sea level, 45 ºC

The O_2 reduction with the higher humidity, due to the volumetric efficiency reduction (lower fresh air mass flow) and the higher water content in the fresh air, was indirectly (but experimentally) shown in Figure 5. 5A in the O_2 content of the exhaust gases. It is an indirect measurement since it has been observed that fuel consumption increases with the humidity to reach a defined engine operative point. Thus, this increase in the fuel consumption added to the decrease of the O_2 intake mass flow observed in Figure 5. 6 and Figure 5. 8, leads to an enrichment of the combustion, decreasing the O_2-to-fuel ratio during the combustion, which could be the cause of the increase in Opacity found in Figure 5. 3B. The O_2-to-fuel equivalence ratio is shown in Figure 5. 9, in which can be seen how the combustions become richer with the increase in humidity and EGR. Therefore, a direct conclusion from this result is that a considerable increase in the moisture in the combustion air reduces the diesel engine efficiency due to the lower O_2-to-fuel equivalence ratio obtained.

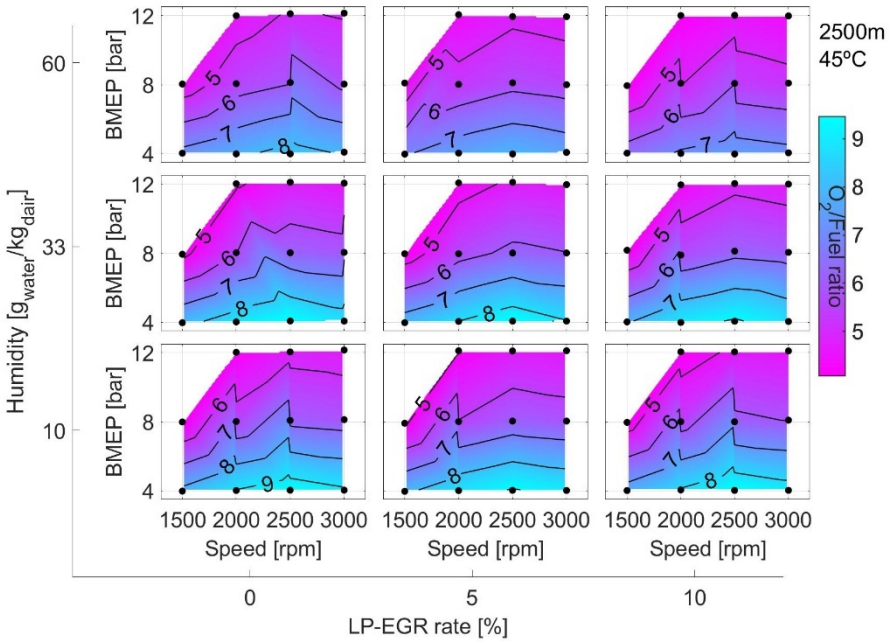

Figure 5. 9. Effect of water injection: O_2-to-fuel ratio. Atmospheric conditions: 2500 meters above sea level, 45 ºC

Concerning the pollutant emissions, the trends are like the ones obtained with Engine 2, but in smaller amplitude. Figure 5. 10 shows the NOx emissions in the same style as Figure 5. 4. This figure shows how the engine-out NOx emissions measured upstream of the DOC are reduced when the humidity increases (going up in a column of graphs). Also, this reduction is like the one obtained when the LP-EGR rate is increased (going right in a row of charts). When both effects are combined (top right graph), the NOx is significantly reduced concerning the dry case and 0% LP-EGR rate (bottom-left chart).

Considering these results, the injection of water at the intake line of a compression-ignition engine provided the same potential in NO_x control as well-established EGR strategies. Figure 5. 10 shows that it is more efficient for NOx abatement increasing humidity from 10 g_{water}/kg_{air} to 60 g_{water}/kg_{air} than EGR from 0% to 10%. It can also be concluded that combining 60 g_{water}/kg_{air} and 10% EGR can reduce emissions more than five times. Injecting water to control NO_x is especially interesting at high altitudes (like 2500 m) since the possibility of using high EGR rates at these conditions is limited by the thermomechanical limits of the turbochargers [8].

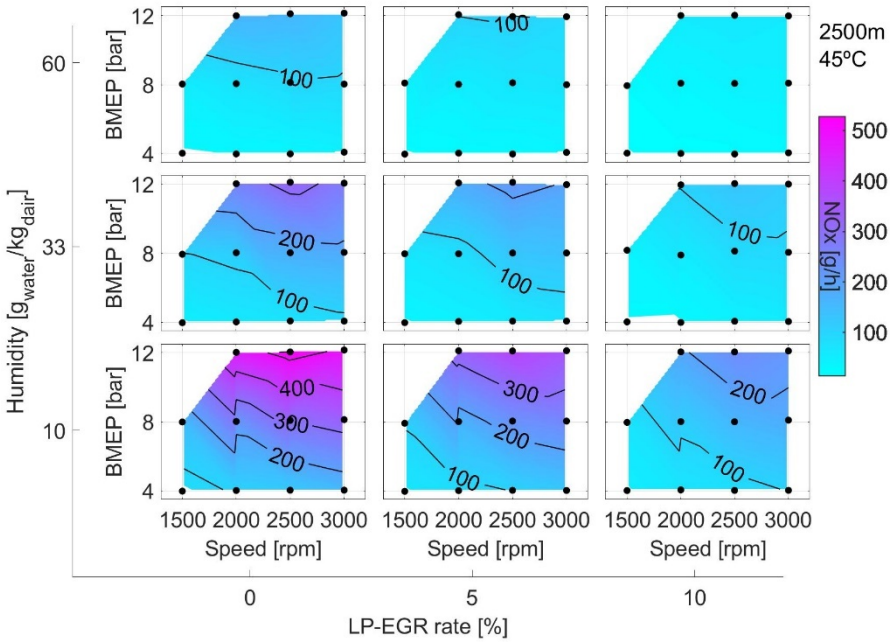

Figure 5. 10. Effect of water injection: NOx engine-out emissions. Atmospheric conditions: 2500 meters above sea level, 45 ºC

A typical way to represent the pollutant emissions of an engine is by a comparison plot of NOx-Opacity trade-off, shown in Figure 5. 11, which provides a simple way to analyze the effects of the different NOx control strategies over the combustion. This case has been used to compare the water injection strategy against the EGR. Looking at the results, it can be seen how there is no significant difference between controlling NOx with water injection or doing it with the EGR at low engine speed and load. But, at high speeds and loads, i.e., 3000 rpm and 12 bar of BMEP (top right graph), the trade-off between NOx and Opacity improves when the emission control is done by injecting water into the combustion air stream compared with more classical strategies as the EGR. For a given level of NOx production, the opacity is always lower in the water injection case.

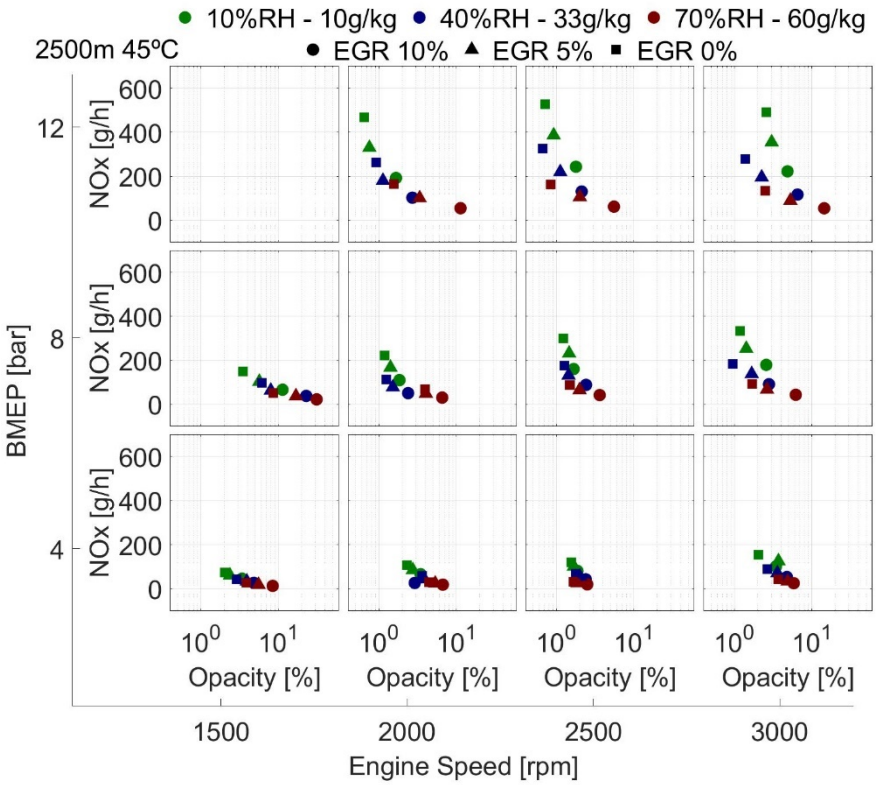

Figure 5. 11. Effect of water injection: Opacity vs. NOx trade-off. Atmospheric conditions: 2500 meters above sea level, 45 ºC

There is no apparent cause for the improvement of the trade-off when injecting water with the variables analyzed up to now. Therefore, to clarify why this is happening, a combustion analysis has been carried out through the software CALMEC for the engine point of 3000 rpm and 12 bar of BMEP. However, due to limitations in CALMEC software, the humidity levels variability is not considered in the combustion air composition, which has been proposed as future works to obtain accurate and reliable data with this tool for the application discussed. Therefore, while the results obtained are inaccurate, it is possible to identify general trends in the combustion evolution due to the humidity effect.

Starting with the NOx production, in Figure 5. 12, the maximum temperature reached by the gas inside the cylinder is presented in three graphs, one for each level of EGR tested, against the crankshaft angle on the *x-axis*. Here is shown how the reduction of the NOx emission cannot be attributed to a lower maximum temperature during the combustion due to the composition of the air as happens with the EGR. This figure shows how when the combustion air humidity increases, the maximum temperature achieved during the combustion is higher,

which could be attributed to the decrease in the O_2-to-fuel ratio shown in Figure 5. 9.

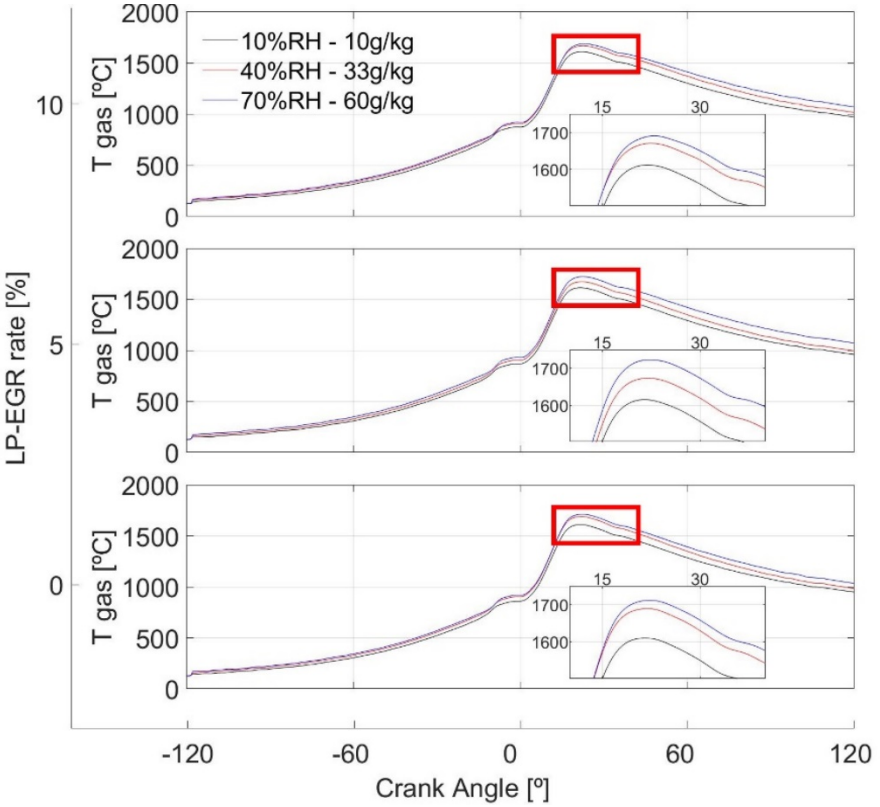

Figure 5. 12. Effect of water injection: In-cylinder temperature, humidity level arrangement

Therefore, other phenomena must be causing the engine-out NOx reduction with the increase of humidity. The lower O_2 available due to the richer combustion is the proposed cause for the NOx reduction, which reduces the oxidation rate of the nitrogen (N_2) and leads to a lower amount of NOx produced during the combustion. As discussed previously, the increase in water content of the combustion air reduces the amount of O_2 in the air due to the substitution with water vapor (Figure 5. 8). Also, it reduces the amount of combustion air that the engine is consuming (Figure 5. 6) due to a reduction in the air density but also the volumetric efficiency of the engine.

Following, the decrease of the soot produced with respect to the LP-EGR strategy can also be analyzed through the in-cylinder temperature evolution. During the combustion of the post-injection (around crank angle 40º aTDC), the soot produced during the main phase of the combustion is oxidized [9], [10].

Therefore, a higher temperature in this phase favors the higher oxidation rate and reduces the amount of soot that exits the cylinders.

On the one hand, with the focus around the crankshaft angle of 40º aTDC in Figure 5. 12, the temperature increases with higher humidity. On the other hand, if the in-cylinder temperature evolution is arranged to compare the results between EGRs and not humidity levels, as done in Figure 5. 13, it is shown that there are no significant differences in the temperature during the combustion of the post-injection for the different LP-EGR rates in any of the humidity level tested. This difference in the in-cylinder temperature behavior during the combustion end could be part of the cause for the improvement found in the NOx-Opacity trade-off (Figure 5. 11) when the NOx is controlled by increasing the humidity of the combustion air instead of using increasing the rate of EGR.

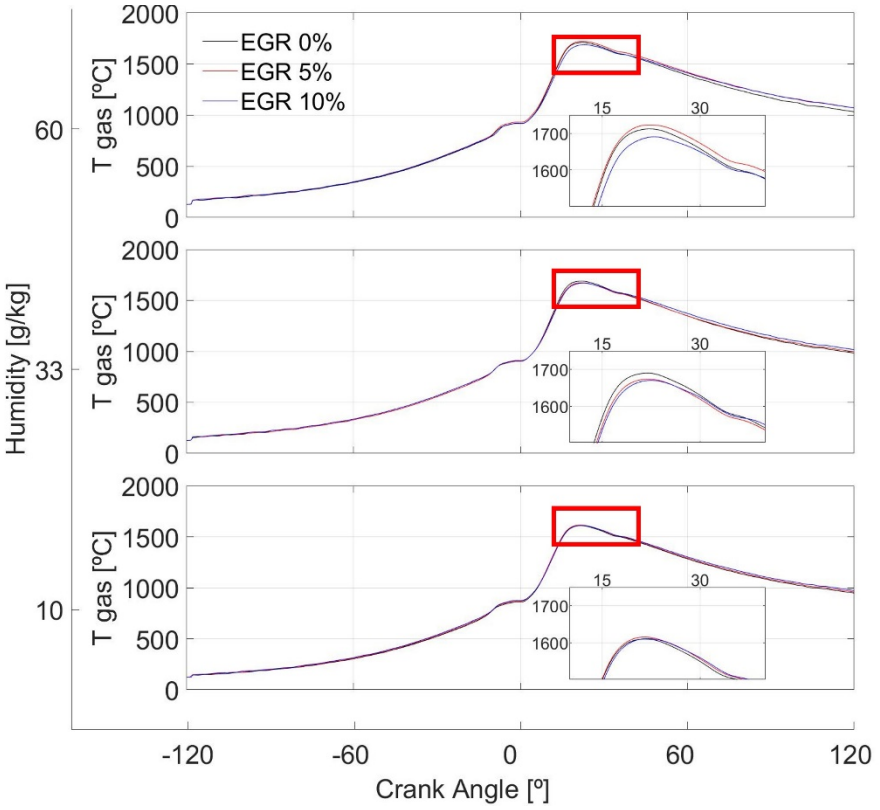

Figure 5. 13. Effect of water injection: In-cylinder temperature, EGR level arrangement

The results obtained for the rate of heat release (RoHR) through the combustion are shown in Figure 5. 14 on the *y-axis* against the crank angle on the *x-axis* and in three graphs, one for each EGR level. If the focus is put on the pre-injection phase (around crankshaft angle -10º aTDC), there is an increasing delay in the

heat release with the increase of humidity. Also, at crankshaft angle 0º aTDC, during the main phase of the combustion, the same delay is present with the rise of the humidity but much smaller than the one observed during the pre-injection. Moreover, at a crankshaft angle of 10º aTDC, during the peak of the heat release, it is shown how the maximum heat release is lower with higher humidity. These two phenomena, the combustion delay, and the lower maximum heat release peak, can be assumed as the cause of the reduction in the engine efficiency with the increase in humidity, which leads to the decrease in the O_2-to-fuel ratio shown in Figure 5. 9 that achieve any given engine operative point defined in this study.

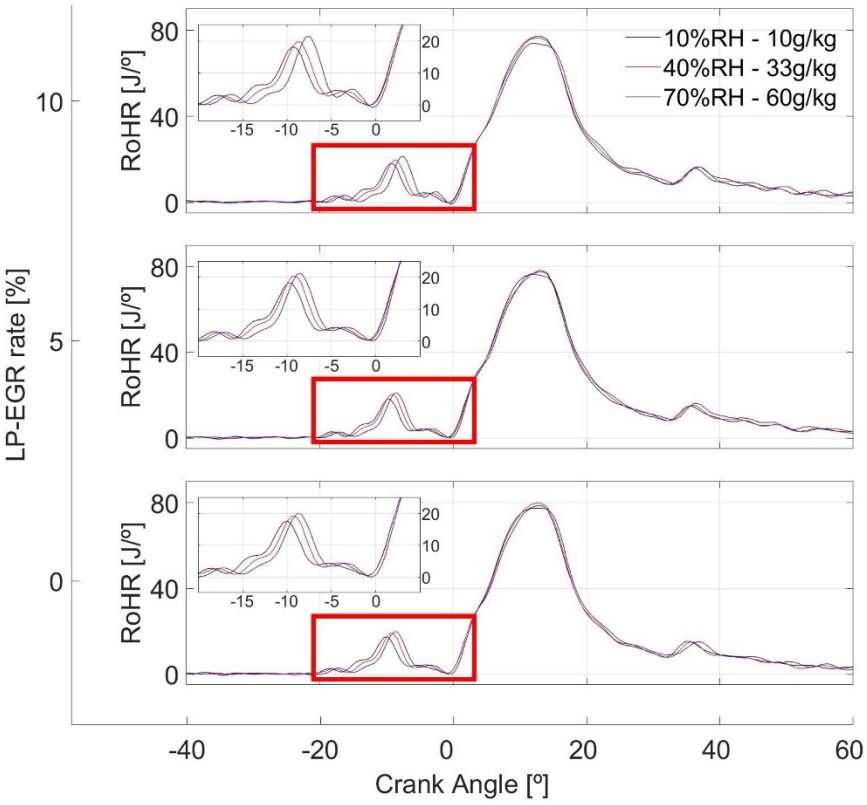

Figure 5. 14. Effect of water injection: Rate of heat release (RoHR)

Lastly, between the crankshaft angle of 30º and 40º aTDC, the post-injection happens, one of the main strategies to control soot generation. Figure 5. 14 shows how the red and blue lines (medium and high humidity) are delayed from the green line (low humidity). This is caused by the previously discussed delay at the combustion start, and the extra amount of fuel injected that could not be burned during the main phase.

Additionally, in Figure 5. 15, zoom to the RoHR evolution has been done between crankshaft angles 20º and 60º aTDC. Figure 5. 15A shows the data arranged following Figure 5. 12, while Figure 5. 15B has been arranged following Figure 5. 13. Then comparing both Figure 5. 15A and B, it can be seen how the post-injection phase of the RoHR shows more significant differences between different humidity levels for a given LP-EGR rate (Figure 5. 15A) than between different LP-EGR rates for a given humidity level (Figure 5. 15B), which could also be one of the factors contributing to the improvement of in the NOx-Opacity trade-off.

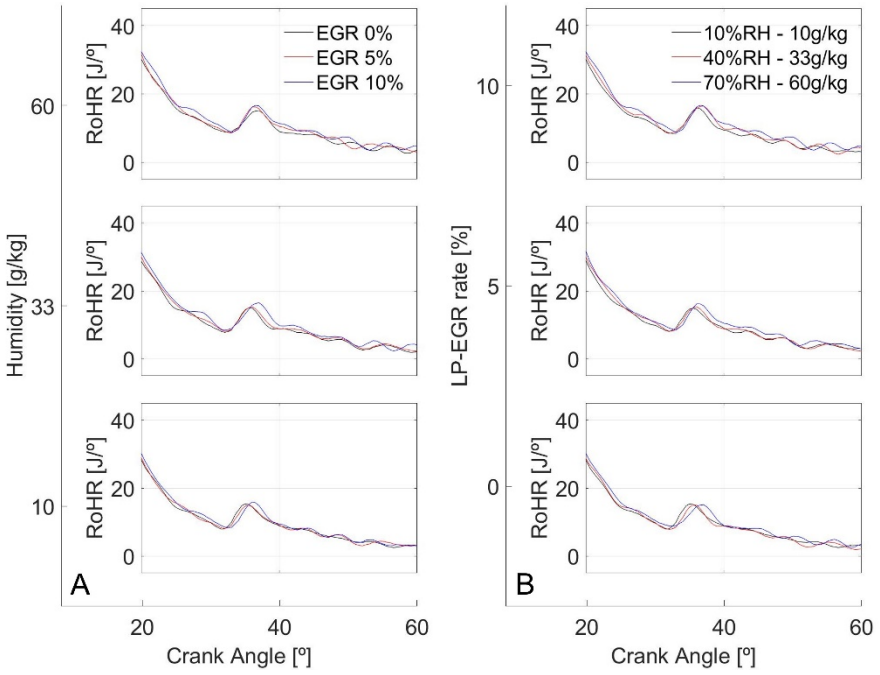

Figure 5. 15. Effect of water injection: Post-injection phase rate of heat release (DFQL)

Finishing with the combustion analysis results, the combustion delay can also be observed using the combustion parameters CA10, CA50, CA75, and CA90, which indicate the crank angle where the 10, 50, 75, and 90 % of the amount of fuel injected has been burned. In cases with 0% and 5% LP-EGR rates, the specific humidity increase from 10 g_{water}/kg_{air} to 33 g_{water}/kg_{air} shows a slight increase in the combustion speed in the initial combustion stage, but later the global trend is followed. The further increment of humidity to 60 g_{water}/kg_{air} delayed the combustion progressively from CA10 (Figure 5. 16A) to CA90 (Figure 5. 16D), ranging from 0.5º at CA10 up to 3.7º at CA90. At a 10% LP-EGR rate, the trend is generally a monotonous increase of combustion delay with the relative humidity increase (from 10 g_{water}/kg_{air} to 60 g_{water}/kg_{air}) and from 0.7º at CA10 to 3.5º at CA90.

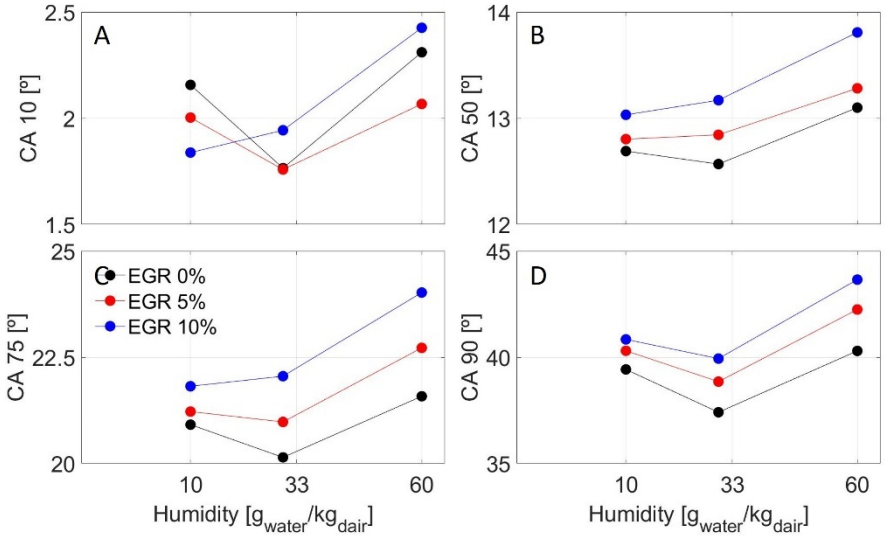

Figure 5. 16. Effect of water injection: Crank angle in which a given percentage of fuel injected is burned: (A) CA10; (B) CA50; (C) CA75; (D) CA90

Another classical way to represent the impact of a NOx control strategy over the engine is to describe the trade-off between the brake specific fuel consumption (BSFC) and the NOx emissions, as shown in Figure 5. 17. However, there are no differences in the trade-off between strategies found in this figure. Therefore, it can be concluded that there is no impact on fuel consumption between controlling the NOx emission either by injecting water in the intake line or using low-pressure EGR.

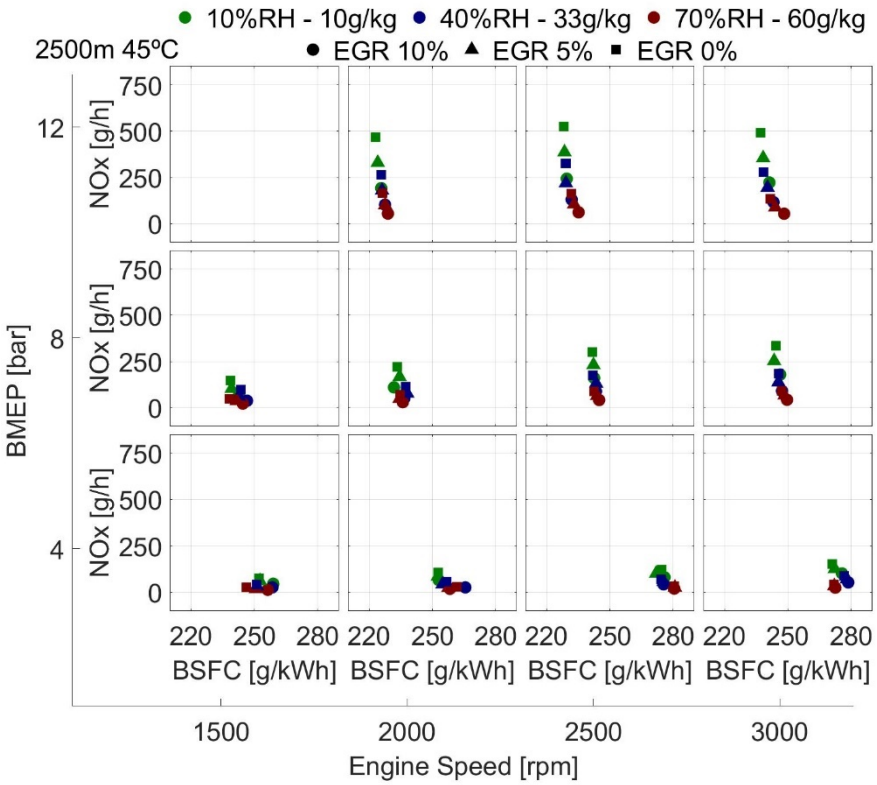

Figure 5. 17. Effect of water injection: BSFC vs. NOx trade-off. Atmospheric conditions: 2500 meters above sea level, 45 ºC

Lastly, in Figure 5. 18A and B are shown the CO and THC emissions, respectively. These two pollutants are related to the combustion quality; the better the combustion of the injected fuel, the lower these two pollutant emissions are. As shown in Figure 5. 18A and B, both emissions increase with the humidity of the combustion air, which is caused by the decreasing O_2-to-fuel ratio depicted in Figure 5. 9. With richer combustion, there is not enough oxygen available in the fuel jet to carry out complete combustions, which generates a higher amount of CO. Concerning the THC emission, the longer combustion time found in the results obtained through CALMEC (Figure 5. 16) and higher amount of fuel injected could be a possible cause of the higher THC since a higher amount of unburned fuel could be present in the cylinder when the exhaust valves opening happen.

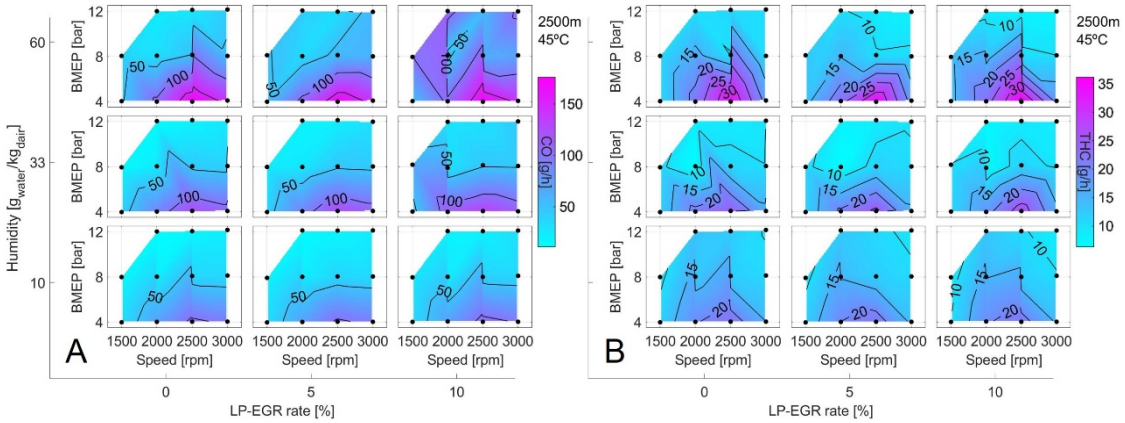

Figure 5. 18. Effect of water injection: (A) CO engine-out emissions; (B) THC engine-out emissions. Atmospheric conditions: 2500 meters above sea level, 45 ºC

5.4. Ambient conditions effect

It is known that the behavior of an automotive engine varies depending on where and in which climate the vehicle is circulating. This is caused by the different ambient conditions that the car must face, which are defined by three primary parameters: pressure, temperature, and humidity. This section will discuss the effect of each of these three parameters on a turbocharged diesel engine.

5.4.1. Effect of the pressure

The study of the effect of the ambient pressure on a diesel engine has been carried out with Engine 1 while performing worldwide harmonized light-duty cycles (WLTC) at four different altitudes: sea level (0 meters), 1000 m, 2000 m, and 3000 m above sea level.

The impact of the altitude on the engine performance during transient operation can be explained by the control of Euro 4 engines over two systems: The variable geometry turbine (VGT) of the turbocharger and the exhaust gases recirculation (EGR) valve.

The use of EGR for NOx emissions control is one of the most determining strategies in the Euro 4 engines' performance at altitude. The position of the EGR control valve is shown in Figure 5. 19, in which the EGR valve at 1000 m of altitude was closer than at sea level (Figure 5. 19A), and it completely closed over 2000 m (Figure 5. 19B). Also, the vehicle speed profile has been plotted in grey lines, referenced to the right y-axis. This strategy significantly affects the emissions formation, mainly NOx, and the engine performance. In addition, since the O_2 available through the combustion increases due to the reduction of

the EGR, the temperatures through the exhaust line increase, making it easier to reach the limit of the materials.

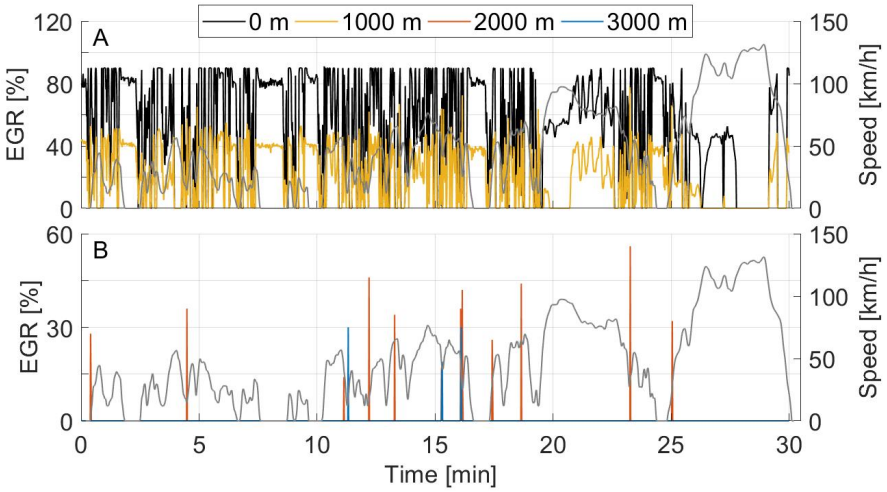

Figure 5. 19. High-pressure exhaust gases recirculation (HP-EGR) valve opening through WLTC cycle. (A) At 0 m and 1000 m; (B) at 2000 m and 3000 m

The altitude also affects the turbocharger's performance, reducing the boost pressure for a given pressure ratio provided as the intake pressure lowers, which forces the VGT control to increase the backpressure and thus the pumping losses to keep the boosting pressure at the desired value.

The differences in boost and backpressure with respect to the sea level, used as a reference, have been plotted in Figure 5. 20 for every altitude. If the focus is on the boost pressure change (Δp_2), Figure 5. 20A shows how it became negative with the altitude (p_2 at 3000 m is lower than at sea level). However, during the aggressive acceleration phases, the closed-loop control of the VGT closes the turbine stator blades, increasing the power in the turbocharger to reach similar ($\Delta p_2 = 0$) or even higher ($\Delta p_2 > 0$) boosting pressure. Similarly, in Figure 5. 20, the backpressure change (Δp_3) became negative as the altitude increased, but sudden steps to the positive region when the closed-loop worked. This way, during the high-power demand of the WLTC cycle, the setpoint of p_2 can be achieved due to the closing of the VGT stator blades. Nonetheless, the control in closed-loop significantly increased the engine pumping losses, which, if not properly calibrated, can lead to loss of performance, even with a higher boosting pressure.

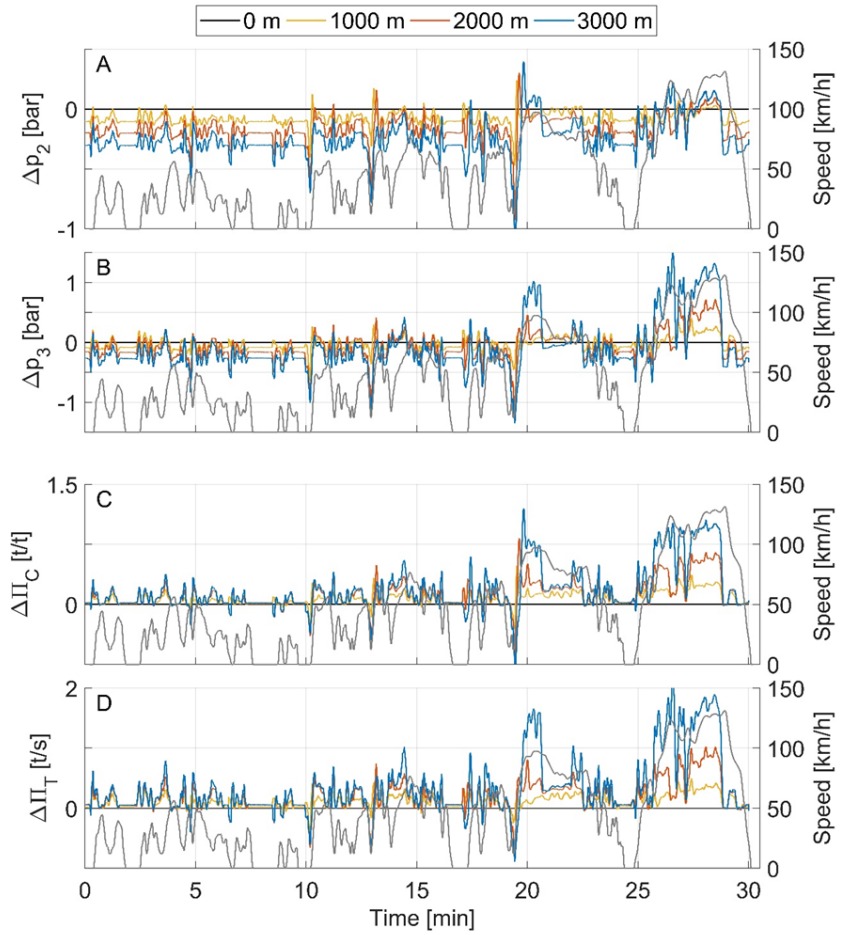

Figure 5. 20. Turbocharger behavior through WLTC cycle in altitude. Changes in: (A) boost pressure (Δp_2); (B) back pressure (Δp_3); (C) compressor compression ratio ($\Delta\Pi_C$); (D) turbine expansion ratio ($\Delta\Pi_T$) with respect to sea level.

Accordingly, in Figure 5. 20C and Figure 5. 20D, the pressure ratio for the compressor and the turbine are depicted, respectively. Generally, these two pressure ratios increase with the altitude due to the drop in ambient pressure and the closed-loop control of the VGT. The increase is beneficial in the case of the turbine pressure ratio since the rise in the altitude allows the VGT to extract more power from the exhaust gases, which partially mitigates the impact of altitude in both boost pressure and pumping losses. However, during engine and turbocharger accelerations, this effect is not enough to compensate for the much higher turbocharger speed required to provide the extra pressure ratio demanded by the compressor by the engine control. In these cases, the penalty in pumping losses due to VGT closing is more than significant due to the turbocharger

inertia, which lags the required speeds demanding the control to close the VGT aggressively.

Lastly, the compressor operation points during the WLTC cycle at the four tested altitudes have been plotted in Figure 5. 21 on the turbo compressor map. The altitude increase causes an increase in the turbo speed due to the extra power extracted in the turbine and demanded in the compressor to keep boost pressure, approaching the upper-speed limit at 3000 m over sea level. Moreover, the increase in altitude causes the compressor to approach surge limit more riskily during the engine decelerations due to a high increment of compression ratio at reduced mass flows. It is worth noting that such a risky approach to surge limit happens despite the HP-EGR being significantly reduced at 1000 m and staying completely closed at 2000 m and 3000 m, as shown in Figure 5. 19. In fact, the reduction in surge margin is one reason to close the EGR under altitude operation, to avoid a further decrease in the mass flow through the turbo compressor.

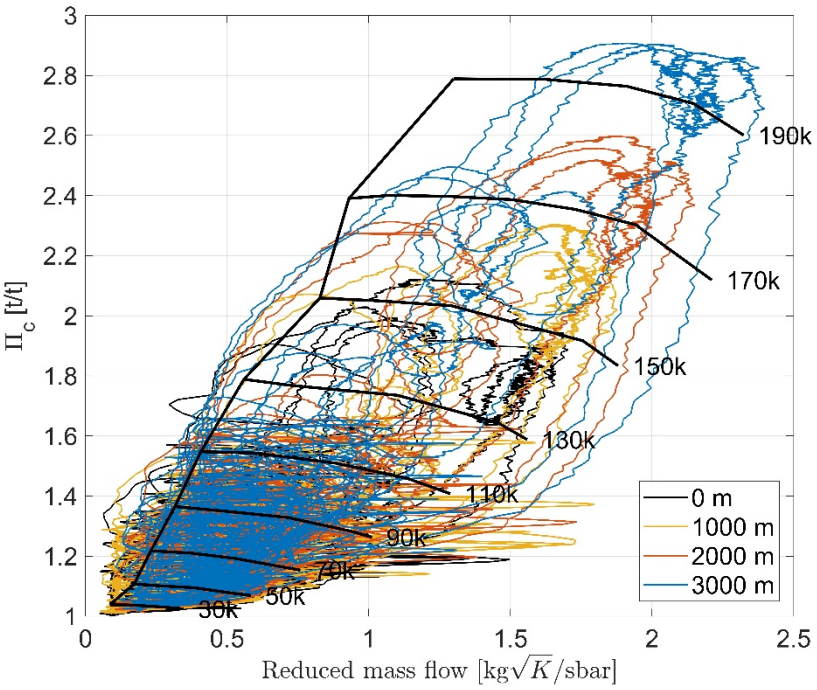

Figure 5. 21. Turbo compressor behavior in altitude: compressor map operation

Following, the deviation with respect to sea level of the accumulated air mass (kg) consumed by the engine is represented in Figure 5. 22, where it is shown that the air consumption of the engine is deeply related to the EGR valve control strategy. The first phenomenon that can be identified occurred when comparing

the sea level reference (black line) with the 1000 m test (yellow line), in which the air mass increased due to the EGR closing keeping low p2 reductions, as shown in Figure 5. 19A and Figure 5. 20A.

If the altitude is further increased to 2000 m over sea level (orange line), the effect of a lower atmosphere pressure starts to impact p2 heavily. Consequently, the intake charge density is directly affected. The air mass decreases with respect to the 1000 m test. Nevertheless, when the 2000 m test is compared against the sea level reference, it can be observed that the increase in fresh air mass due to closing the EGR is higher than the decrease caused by the lowered atmospheric pressure. Lastly, at 3000 m over sea level, the reduction of air density caused the intake of fresh air mass to decrease, even below sea level values, even though the EGR valve is completely closed.

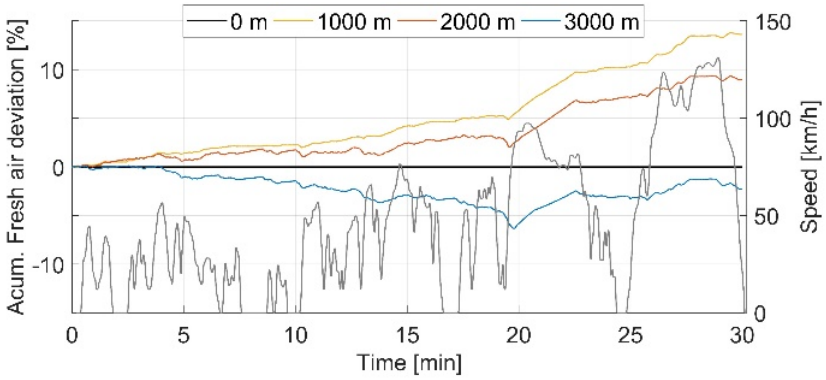

Figure 5. 22. Evolution of the accumulated fresh air deviation through a WLTC cycle at altitude, referenced to sea level data

Concerning the fuel consumption (CO_2 emissions), Figure 5. 23 shows that the fuel consumption (kg) dropped when increasing the altitude up to 2000 and 3000 m. This is, again, due to the actual calibration of the EGR valve. It reduces the amount of recirculated exhaust gases to protect the turbocharger from reaching physical limits such as surge, over speed, or compressor outlet temperature. Therefore, a lower equivalence ratio and higher cycle efficiency, due to lower intake charge temperature, are obtained during more than 25 min of the WLTC duration in 2000 and 3000 m. The absence of high-pressure EGR increases the exhaust mass flow available for the turbine, and the higher altitude increases the pressure ratio in the turbine. Both contribute to expanding the power recovered by the VGT and avoiding aggressive VGT closing during minor dynamic phases. Therefore, fuel consumption is reduced. However, the 1000 m test results do not show this 25 min phase of fuel consumption reduction since the EGR valve was opened at around 40% (Figure 5. 19).

It is worth noting that within the first 25 min, the reduction of fuel with respect to the reference was more aggressive during some engine accelerations, causing

drop peaks of fuel that increase in magnitude with the altitude. The ECU's fuel injection cuts cause this to protect the turbocharger during the aggressive accelerations of the WLTC.

In the last part of WLTC (between 25 and 30 min), during the high-velocity phase of the cycle, the fuel consumption grew dramatically at 2000 m and 3000 m. The previous reduction of brake specific fuel consumption (BSFC) was quickly lost, and, finally, more fuel was spent at 3000 m, and low decreases were seen at 2000 m. This is a consequence twofold. First, the EGR valve at sea level is already relatively or fully closed (Figure 5. 19), so no benefits from further EGR closing at altitude are obtained; and second, the strategy adopted for controlling p_2 with the VGT in a closed-loop dramatically increases pumping losses in altitude (Figure 5. 20B, D). The energy needed to overcome the turbocharger lag is responsible for the BSFC increment. The lag is caused by the highly dynamic processes involved in engine acceleration, which the turbocharger can barely follow. Therefore, high turbocharger speed accelerations are needed to keep boost pressure levels at 2000 m and 3000 m (Figure 5. 21). At these high turbo speeds, it is also easier to reach the risky operational zones of the turbocharger unit (surge or over speed).

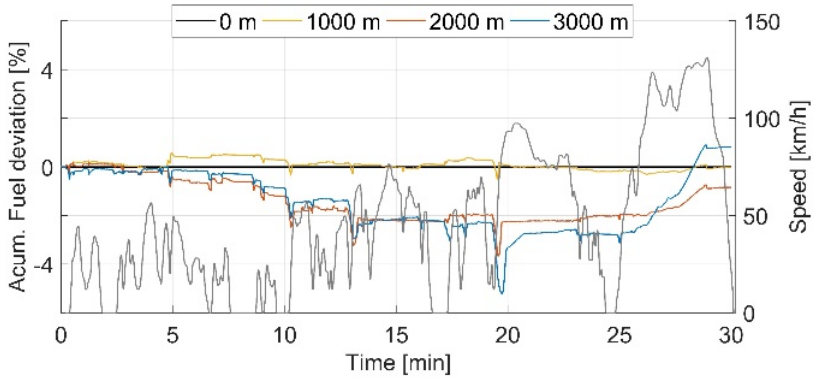

Figure 5. 23. Evolution of the accumulated fuel consumption deviation through a WLTC cycle at altitude, referenced to sea level data

Following the engine-out pollutant emissions during the cycle, the accumulated THC, NOx, CO, and Soot referenced to sea level data are presented in Figure 5. 24. Starting with THC (Figure 5. 24A), it can be seen how the generation of THC significantly increases with altitude. The decreased air density (Figure 5. 20A) increased the fuel spray penetration, causing higher jet-to-wall impingement, leading to higher unburned hydrocarbons [11], [12].

In Figure 5. 24B, it is possible to see that the generation of NOx increased with the altitude due to the high-pressure EGR closing. This is clear when looking first at the 1000 m test data, which significantly increased even there were still some EGR. Also, when comparing 2000 m and 3000 m test data with 1000 m,

the penalty in NOx emissions due to the absence of EGR had more weight than other factors. These other factors are twofold: The increase in mass flow at 2000 m and the reduction in fuel consumption at 2000 m and 3000 m. Both additional factors caused the equivalent air-to-fuel ratio to rise and lower the maximum in-cylinder temperature. But they did not lead to a reduction of NOx emitted due to the absence of EGR.

Concerning the CO emissions, Figure 5. 24C shows how the accumulated CO increased in the 1000 m test but decreased in the 2000 m and 3000 m tests. The appearance of local rich zones, which happened during the engine accelerations, was the cause of the sudden increases of the CO throughout the tests. However, the CO emissions were reduced at 2000 m and 3000 m during the middle part of the WLTC (and a couple of accelerations at 1000 m) due to the reduction of fuel consumption and the consequent decrease of the equivalence ratio. Especially during the pedal release phases and further accelerations, which are in the absence of EGR, the amount of oxygen available was increased (mainly at 2000 m), the combustion temperature was raised, and the amount of carbon involved in the combustion was reduced referenced to the sea level test. Thus, the total CO emitted was reduced. Also, in Figure 5. 24A, local reductions in the THC emitted at 2000 m and 3000 m tests, at about 10, 13, and 20 min, can be observed, which supports the previous analysis.

Lastly, Figure 5. 24D represents the increase of soot generation with the altitude, mainly attributed to fuel jet impingement in the combustion chamber walls and fuel cracking due to the higher in-cylinder temperatures and lower available O_2. Fuel impingement was also claimed in the case of THC, which follows the same path of increment as soot mass.

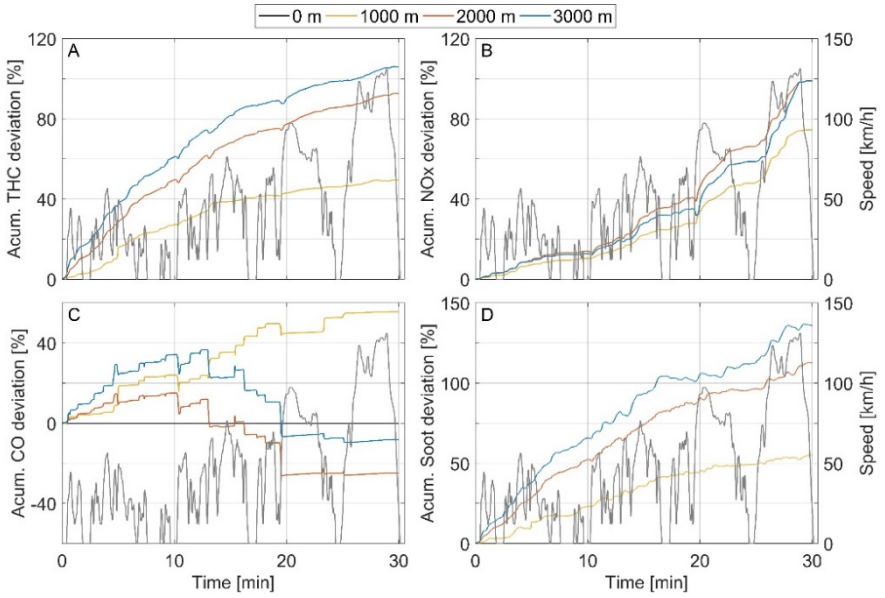

Figure 5. 24. Evolution of the accumulated pollutant emissions deviation through a WLTC cycle at altitude, referenced to sea level data. (A) THC; (B) NOx; (C) CO; (D) Soot

5.4.2. Effect of the temperature

For the study of the ambient temperature effect over a diesel engine, the engine used is Engine 3, previously detailed in Section 5.2. The current research is carried out at an ambient temperature of 30ºC and 45ºC, while the pressure and the relative humidity were kept constant at 1.013 bar and 10%, respectively.

In Figure 5. 25, the operation point of the compressor can be seen represented in the compressor map, in which the colors represent the two ambient temperatures tested, blue for 30ºC and red for 45ºC. It is shown that the increase in the temperature reduces the pressure ratio of the turbo compressor for the three levels of EGR tested. Also, at high engine speed and load, the operative point of the compressor is moved towards the choke. The increase in compressor inlet temperature increases the power demand, which has to be supplied by the turbine, by either closing the blades and increasing the turbine inlet pressure or with a higher turbine inlet temperature due to less efficient combustion and higher fuel-to-air equivalence ratio.

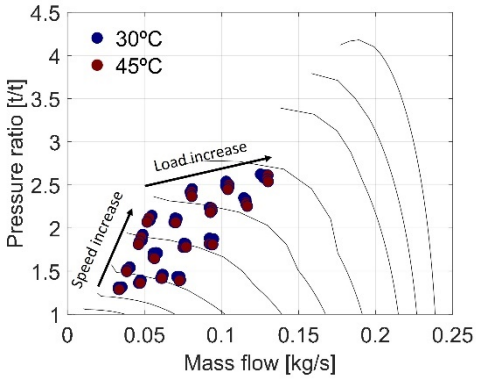

Figure 5. 25. Effect of ambient temperature: Turbo compressor operation map

Figure 5. 26 shows inlet turbine pressure (p_3) and temperature (T_3) in Figure 5. 26A and B, respectively. The values measured for the ambient temperatures of 30ºC and 45ºC are represented in the *x-axis* and *y-axis*, respectively. The colors represent the engine speeds and the symbols the load levels. Also, the LP-EGR rate is shown by the shade of the color in the markers. It can be seen how there is no change in p_3, but T_3 has a consistent increase for all the points when the ambient temperature increases to 45ºC. Thus, the turbine's increase in power is caused by the rise in the fuel-to-air equivalence ratio instead of using the turbine blades to increase p_3 and the expansion ratio in the turbine.

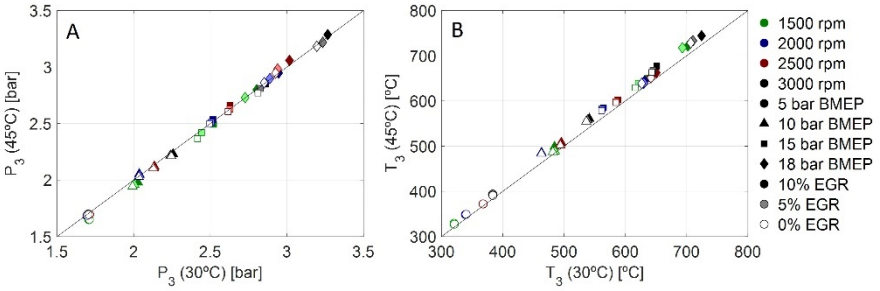

Figure 5. 26. Effect of ambient temperature: (A) Turbine inlet pressure (p_3); (B) Turbine inlet temperature (T_3)

Concerning the fresh air consumed by the engine presented in Figure 5. 27A, there is a slight reduction in the mass flow measured by the engine control unit (ECU) when the ambient temperature is increased. This increases the fuel-to-air equivalence ratio lowers the engine's efficiency, and causes the increase in fuel consumption shown in Figure 5. 27B, further increasing the fuel-to-air ratio as shown in Figure 5. 27C.

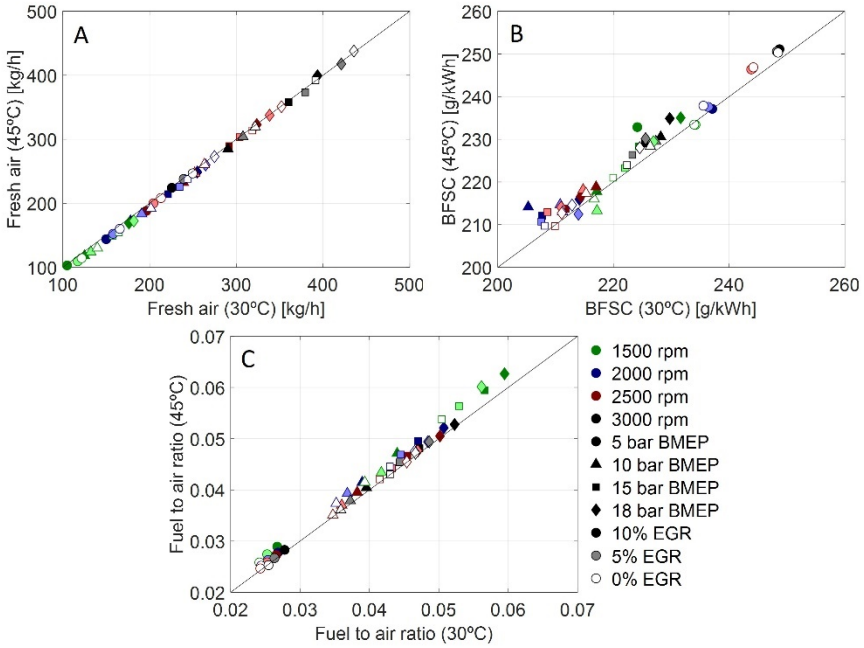

Figure 5. 27. Effect of ambient temperature: (A) Fresh air; (B) Break specific fuel consumption (BSFC); (C) Fuel-to-air equivalence ratio

The increase in the fuel-to-air equivalence ratio significantly affects the different pollutants emitted by the engine. Figure 5. 28 shows the primary pollutants generated by a diesel engine, represented following the same graph layout as Figure 5. 27.

Figure 5. 28A is shown how the engine-out NOx emissions decrease with the increase of the ambient temperature. The decrease in NOx production is the result of richer combustion. The lack of available oxygen causes a reduction in NOx production even with a higher combustion temperature. The higher equivalence fuel-to-air ratio also increases the opacity, represented in Figure 5. 28B, in which can be seen how the particulate generation increases significantly at high load when the ambient temperature is increased.

The engine-out CO emissions are shown in Figure 5. 28C and D. Figure 5. 28C shows the total of the engine points measured, while Figure 5. 28D shows a zoom of the low CO emission area. The CO production shows the same behavior as the opacity. The richer combustion and lack of available oxygen impede the complete combustion of the injected fuel, making the CO increase, with a higher impact at higher engine loads. Lastly, Figure 5. 28E shows the total unburned hydrocarbons (THC) emitted, which do not present any trend that could be related to the ambient temperature change.

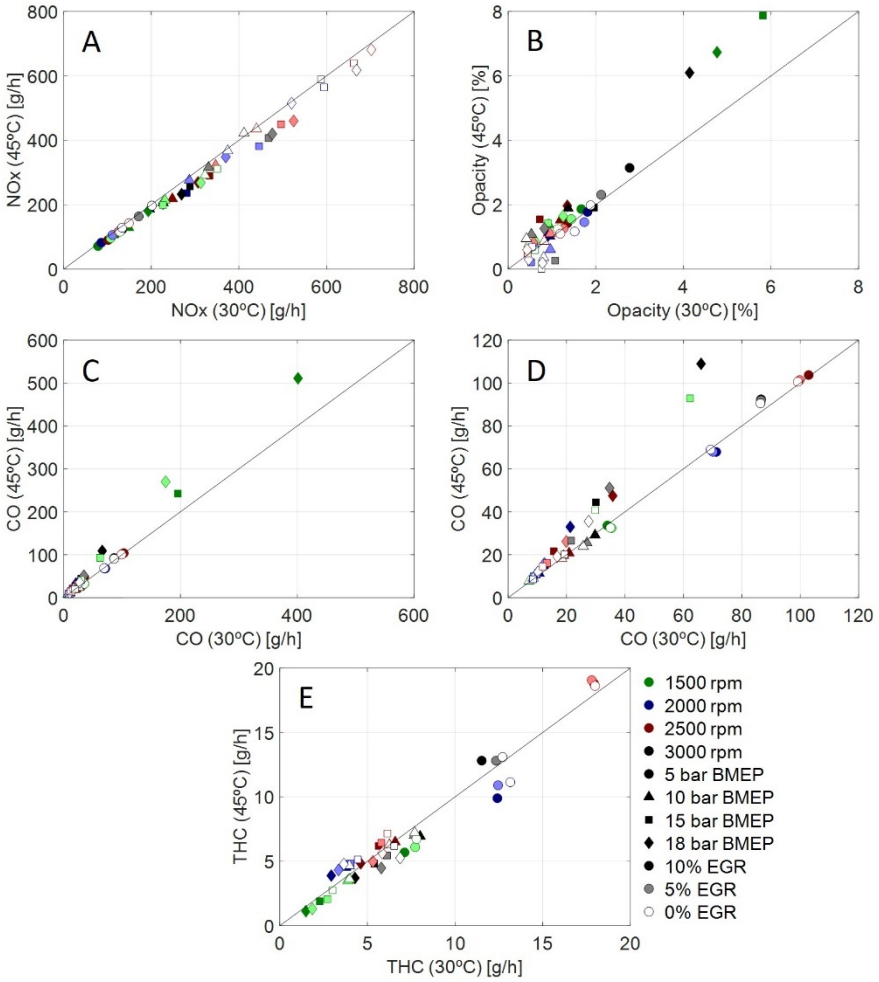

Figure 5. 28. Effect of ambient temperature: (A) NOx; (B) opacity; (C) CO; (D) zoom on the low CO production area; (E) THC

5.4.3. Effect of the humidity

After studying the effect of injecting water in the intake line and seeing the significant results of reducing the volumetric efficiency, NOx, and soot production, the next question is if there is also an effect when the humidity in the intake lane changes between realistic atmospheric values. The previous water injection study considers injecting an amount of water impossible to find in the Earth's atmosphere. Therefore, a new testing campaign was defined to see if there is also an effect on the engine performance when the humidity range is narrower and more like ambient humidity values.

This section will discuss the changes in the performance and engine-out pollutant emissions of a diesel engine when the ambient humidity varies between 4 and 30 g_{water}/kg_{air}. The engine used for the ambient humidity effect study was Engine 3, with the ambient temperature and pressure kept at 30ºC and 0.797 bar (2000 meters above sea level), respectively.

Following the results obtained, as shown in Figure 5. 29A, the combustion air mass flow is reduced when the humidity increases, as observed in section 5.3. Also, if the focus is put in the central column (5% of EGR), it can be seen how the engine map is reduced when the humidity is increased. This is due to the increase of the opacity when the humidity increases (Figure 5. 29B), making it much easier to reach the smoke limits of the engine. When the smoke limit is reached, the engine limits the fuel injection, not allowing it to get the load level demanded (in this case, 15 bar of BMEP). In Figure 5. 29B, it can be seen how the graph corresponding to 5 % of EGR with 13 g_{water}/kg_{air} has an opacity higher than 25 % at 1500 rpm and 15 bar of BMEP, engine point which is not possible to reach when the ambient humidity is increased to 23 g_{water}/kg_{air} due to the engine limiting the fuel injection because of the opacity increase above the maximum limits.

This effect was not previously observed due to a narrower engine load range. In the current discussion, the engine load range was wider to confirm the possible engine map reduction due to the ambient humidity.

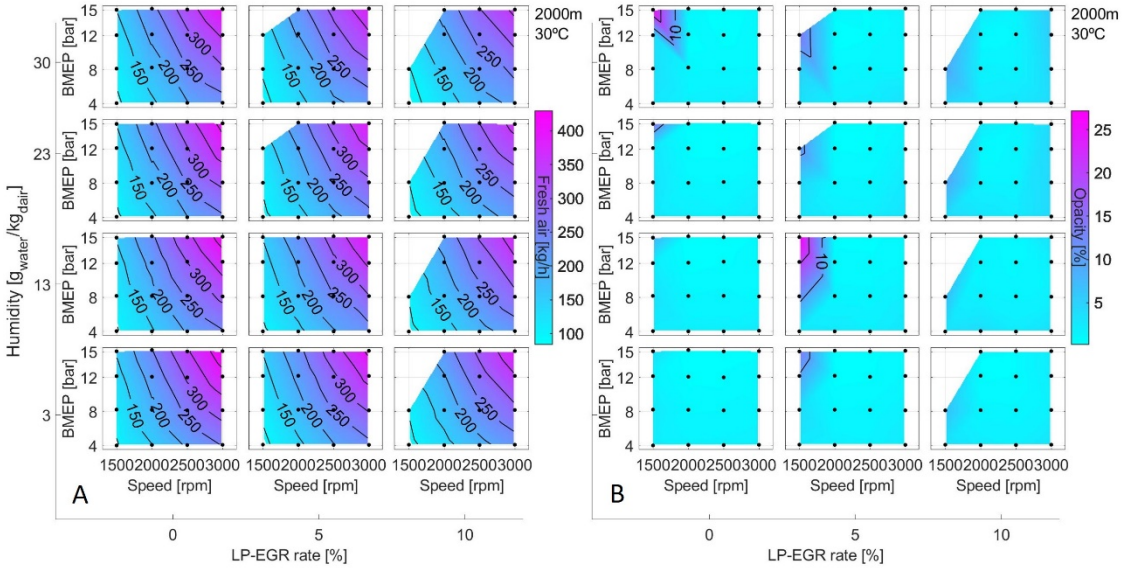

Figure 5. 29. Effect of ambient humidity: (A) Fresh air; (B) opacity. Atmospheric conditions: 2000 meters above sea level, 30 ºC

Concerning the engine-out NOx emissions, Figure 5. 30 shows how the NOx is reduced significantly, at around half than the dry case (top row compared with the bottom row in Figure 5. 30). This could be useful to consider during the calibration of the LP-EGR control. If a humidity sensor is included in the engine and used for its LP-EGR calibration, it is possible to achieve the objective in NOx emission with a lower LP-EGR rate. As explained in section 5.3, this is beneficial in soot production since reducing NOx by employing water content in the combustion air provides a better NOx-opacity trade-off (Figure 5. 11).

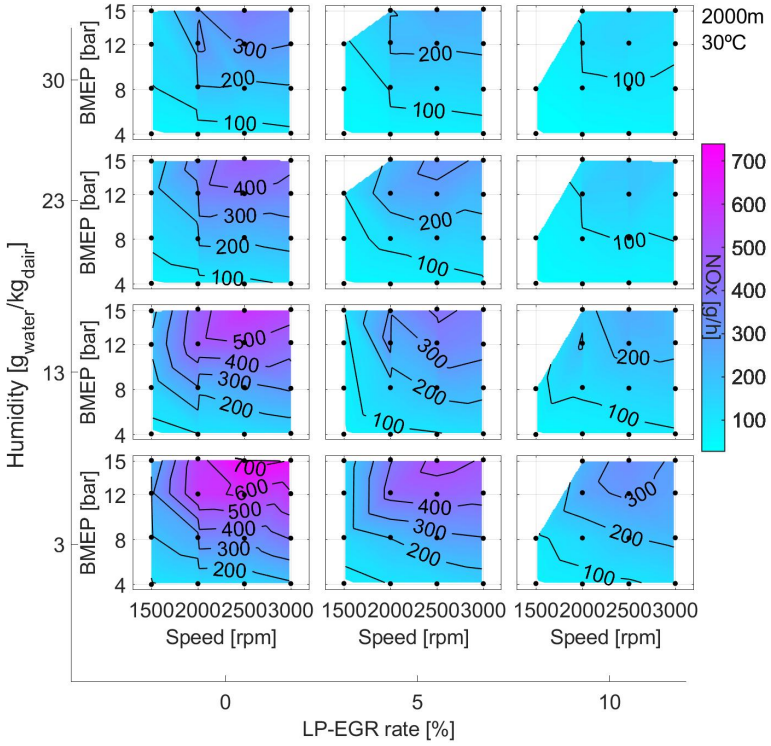

Figure 5. 30. Effect of ambient humidity: NOx emissions. Atmospheric conditions: 2000 meters above sea level, 30 ºC

Some Diesel engines have installed ambient sensors, such as ECM-baroCAN [13], which allows monitoring the ambient humidity. However, any of the three engines tested in this Ph.D. Thesis had any correction with the ambient moisture implemented in the calibration.

Lastly, the results for the rest of the primary emissions are plotted in Figure 5. 31, in which some general trends can be seen. The CO_2 emitted is represented in Figure 5. 31A, which does not present any significant difference when the humidity change. This shows that a change in humidity between Earth's

atmospheric levels does not affect the fuel consumption of the engine significantly, similarly to what is observed in the section 5.3 results that show how the NOx-BSFC trade-off was not affected.

The THC emissions are plotted in Figure 5. 31B, which shows how the THC decreases slightly when the humidity increase. This is coherent with the results obtained in section 5.3 shown in Figure 5. 18B, in which the THC engine-out emissions decrease slightly when moving from the bottom row to the medium row and then increase sharply in the top row. Thus, following the results obtained, raising the humidity level in the combustion air reduces the THC. Still, there is an inflection point in the combustion air water content between 33 and 60 g_{water}/k_{gair}, after which the THC starts to increase sharply.

Concerning the CO and soot emissions, these two are depicted in Figure 5. 31C and D, respectively. Both the CO and the opacity show similar trends, in which the emission increase with the ambient humidity. This is caused by the higher content of inert gas (water vapor) in the combustion air, leading to lower oxygen available and an incomplete combustion process that generates a higher quantity of these two pollutants.

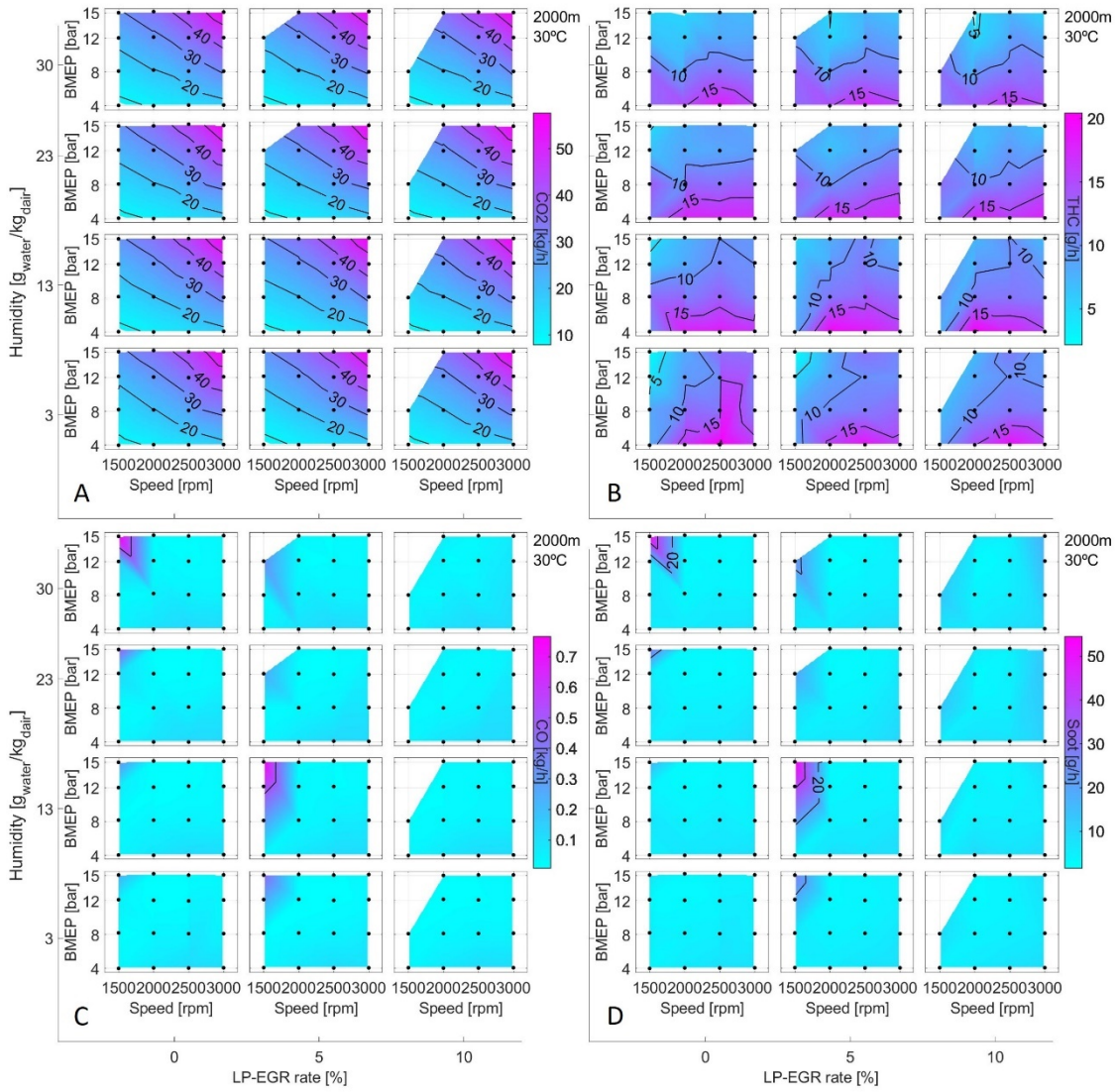

Figure 5. 31. Effect of ambient humidity: (A) CO_2; (B) THC; (C) CO; (D) Soot. Atmospheric conditions: 2000 meters above sea level, 30 ºC

5.5. Bibliography

[1] J. R. Serrano, P. Piqueras, E. J. Sanchis, and B. Diesel, "Analysis of the driving altitude and ambient temperature impact on the conversion efficiency of oxidation catalysts," *Applied Sciences (Switzerland)*, vol. 11, no. 3, pp. 1–21, Feb. 2021, doi: 10.3390/app11031283.

[2] J. R. Serrano, A. Gil, P. Quintero, R. Tabet, and J. Gómez, "Design of a bubble reactor for altitude simulators used to humidify a combustion air stream by means of CFD multi-phase models," *Applied Sciences (Switzerland)*, vol. 11, no. 1, pp. 1–15, Jan. 2021, doi: 10.3390/app11010295.

[3] A. Broatch, V. Bermúdez, J. R. Serrano, R. Tabet, J. Gómez, and S. Bender, "Analysis of passenger car turbocharged diesel engines performance when tested at altitude and of the altitude simulator device used," *Journal of Engineering for Gas Turbines and Power*, vol. 141, no. 8, Aug. 2019, doi: 10.1115/1.4043395.

[4] J. Kuttippurath *et al.*, "Observed rainfall changes in the past century (1901–2019) over the wettest place on Earth," *Environmental Research Letters*, vol. 16, no. 2, Jan. 2021, doi: 10.1088/1748-9326/abcf78.

[5] A. A. Iyer, "Experimental study on the effect of water injection in an internal combustion engine," *IOSR Journal of Mechanical and Civil Engineering*, vol. 17, no. 10, pp. 58–64, Mar. 2017, doi: 10.9790/1684-17010055864.

[6] M. Kettner, S. Dechent, M. Hofmann, E. Huber, H. Arruga, and R. Mamat, "Investigating the influence of water injection on the emissions of a diesel engine," *Journal of Mechanical Engineering and Sciences*, vol. 10, no. 1, pp. 1863–1881, Jun. 2016, doi: 10.15282/jmes.10.1.2016.11.0179.

[7] X. Ma, F. Zhang, K. Han, Z. Zhu, and Y. Liu, "Effects of intake manifold water injection on combustion and emissions of diesel engine," *Energy Procedia*, vol. 61, pp. 777–781, 2014, doi: 10.1016/j.egypro.2014.11.963.

[8] V. Bermúdez, J. R. Serrano, P. Piqueras, and B. Diesel, "Fuel consumption and aftertreatment thermal management synergy in compression ignition engines at variable altitude and ambient temperature," *International Journal of Engine Research*, 2021, doi: 10.1177/14680874211035015.

[9] C. W. Lautenberger, J. L. de Ris, N. A. Dembsey, J. R. Barnett, and H. R. Baum, "A simplified model for soot formation and oxidation in CFD simulation of non-premixed hydrocarbon flames," *Fire Safety Journal*, vol. 40, no. 2, pp. 141–176, Mar. 2005, doi: 10.1016/j.firesaf.2004.10.002.

[10] C. Fach, N. Rödel, J. Schorr, C. Krüger, A. Dreizler, and B. Böhm, "Multi-parameter imaging of in-cylinder processes during transient engine operation for the investigation of soot formation," *International Journal of Engine Research*, 2021, doi: 10.1177/14680874211019976.

[11] H. Hiroyasu, M. Arai, and M. Tabata, “Empirical Equations for the Sauter Mean Diameter of a Diesel Spray,” *SAE Transactions*, vol. 98, pp. 868–77, Jan. 1989, Accessed: Dec. 27, 2021. [Online]. Available: http://www.jstor.org/stable/44580992.

[12] K. D. Kihm, D. P. Terracina, Payne S. E., and J. A. Caton, “Synchronised droplet size measurements for coal-water slurry sprays generated from a high-pressure diesel injection system,” 1993. Accessed: Dec. 27, 2021. [Online]. Available: http://minsfet.utk.edu/publications/1994_Synchronized%20Droplet%20Size.pdf

[13] Labcell LTD, “ECM - baroCAN. Ambient, intake air, and cabin air module.” [Online]. Available: www.labcell.com

Chapter 6
Conclusions and future works

6.1. Main conclusions

The main conclusions found during the development of the current Ph.D. Thesis will be presented below. Starting with the final performance obtained for the atmosphere simulator and the lessons learned from developing the customized components. Afterward, several conclusions were obtained from the 1D models developed during the Ph.D. works. Finally, conclusions were found about the effect of the different ambient conditions on the performance and pollutant emissions of compression ignition turbocharged Diesel engines.

6.1.1. Atmosphere simulator performance

The maximum mass flow of the atmosphere simulator has been increased, achieving 1500 kg/h instead of the previous 1200 kg/h while maintaining the footprint size of the installation and the electrical power consumption. This has been carried out by improving the exhaust line of the MEDAS to reduce the pressure drop in this area and increasing the pressure at the mechanical compressor inlet, which displaces the operative point of the compressor away from the choke area and increases the actual mass flow that is passing through the compressor. Also, the turbocharger compressor connection in series downstream of the Rotrex e-charger has helped increase MEDAS efficiency and mass flow, but only at the medium to high altitude range.

Regarding the temperature performance, the temperature control range has been improved along with the entire altitude range of the altitude simulator (from -2000 meters below sea level to 5000 meters above). This has been achieved without extra energy consumption by re-designing the VGT blades control (by CAN-protocol) and the WG-valve pressure-control strategy since now WG-valve never opens until VGT-blades (VGT-can) is fully open. But the critical aspect of increasing the control range of the turbine has been using the pre-conditioned air provided by the MTM to the MEDAS in terms of pressure and temperature. Thanks to the MTM is possible to achieve from -15 ºC to 40 ºC independently from the simulated pressure and ambient conditions. Even though the minimum preconditioned temperature downstream MTM is 3ºC.

Moreover, the objective of achieving a humidity control range that allows reproducing any ambient conditions found in a vehicle road has been completed since the maximum specific humidity level (g_{water}/kg_{air}) recorded in the Earth's atmosphere is 30 g_{water}/kg_{air} [1], much lower than the maximum humidity achieved by the atmosphere simulator assembly developed (67 g_{water}/kg_{air}). Also, the drying capability has been increased thanks to MTM, down to 2 $g_{water}/kg_{air.}$

Following, the objective of reducing the power consumption of the assembly has been reached thanks to the several improvements carried out over the atmosphere simulator with this target. Firstly, installing the turbocharger

compressor in series with the mechanical compressor allows the reduction in mechanical compressor consumed power since the power extracted in the turbine while cooling the air is used to reduce the pressure ratio in the mechanical compressor. Secondly, the mass flow control range has been expanded, reducing the minimum mass flow achievable by the MEDAS, which allows fitting the mass flow conditioned by the MEDAS much better to the engine size, reducing the mass flow bypassed and thus wasted when testing small ICEs. Finally, the control strategies developed for the MTM reduce the power consumption of the mechanical compressor by fitting the boosting pressure provided to the MEDAS to the minimum that the MEDAS needs to achieve the user-demanded set points.

Lastly, concerning the accuracy of the pressure, temperature, and humidity control, it has been able to control the three variables with an average error of +/- 0.5 % and a peak error of +/- 2 % for the full scale of each variable. This has been achieved in both MEDAS operative modes: either maintaining stable atmospheric conditions, as could be driving a vehicle in a given altitude plateau -without any change in barometric pressure, temperature, or humidity-, or performing dynamic changes of the atmospheric conditions, i.e., while climbing a mountain or when suddenly starts to rain.

6.1.2. 1D modeling

Several conclusions have been obtained from the modeling of the MEDAS presented in Section 3.3.4, mainly concerning the components modeling and the correlations for the pressure drop developed.

6.1.2.1 Components

In the case of the modeling of the components, the conclusions obtained are focused on two of them: the turbocharger VGT and the mechanical compressor, which is shown the usefulness of the radial turbomachinery map extrapolation capabilities of the 1D modeling software VEMOD.

Concerning the turbocharger turbine modeling, it has been found that the code implemented in VEMOD cannot directly extrapolate the results from a complete VGT actuated by displacing the stator backplate instead of rotating the stator blades. However, employing the methodology proposed in this Ph.D. Thesis, which consists of simplifying the different VGT positions to a fixed geometry turbine, it is possible to achieve accurate results for the extrapolation of the VGT complete map. To avoid this issue, a modification of the extrapolation code must be carried out to generalize the VGT extrapolation methods instead of a specialized one for rotating stator blades.

Contrarily, in the case of mechanical compressor modeling, it has been proved that the extrapolation tool of VEMOD provides an accurate extrapolation of the

choke area for a centrifugal compressor map from a few experimental points. This has been validated experimentally after the extrapolation was performed.

These two cases validate using the VEMOD extrapolation tool to obtain a complete map for radial turbomachinery without performing an extensive experimental campaign.

6.1.2.2 Pressure-drop correlations

An original procedure has been proposed to obtain the correlations for the drop of pressure in the piping geometries that connect the different elements installed in MEDAS. It consists of CFD simulations of individual components within the operative flow range and developing low order empirical models based on Re numbers upstream and downstream of the element. The procedure also provided several conclusions about the strengths and limitations of this proposed procedure.

From the results obtained during the experimental validation, it can be concluded that the pressure drop correlations obtained through CFD calculations are accurate in the case of simple geometries in which the flow has low velocity, i.e., the MEDAS inlet or the engine intake connection and dilution pipe.

However, when the complexity of the geometry and the flow velocity increases, as happens in the geometries located at the inlet and outlet of the mechanical compressors, the CFD predictions overestimate the pressure drop. Therefore, it is necessary to fit the correlations with experimental measurements in these cases. It has been concluded that this is caused by the simplifications introduced in the CFD to insulate the flow elements in the code to reduce the calculation time to a reasonable time frame, which makes it impossible to predict all the interactions of the correct flow behavior in these cases.

6.1.3. Effect of the ambient conditions on a diesel engine

6.1.3.1 Altitude

The altitude effects on the turbocharged Diesel engine's performance cover mainly two aspects: the engine performance limitation, to avoid damage or even early failure of some components, and the engine pollutants emission.

Firstly, for the engine performance limitation, it has been concluded that the performance of the turbocharged diesel engine is limited for protecting mainly the turbo compressor, which is more prone to reaching risky working zones, approaching temperature, surge, and over speed limits when increasing altitude. For these reasons, the EGR has been avoided as a generalized strategy. But this fact contributes to stress on the turbine itself, whose inlet temperature limit is more easily reached at high altitudes. Additionally, the closed-loop strategy to control p_2 (compressor outlet pressure) with the VGT increases the backpressure

of the cylinders significantly, leading to excessive pumping work and causing a reduction in engine performance.

Finally, the pollutant emissions are heavily affected by the altitude at which the diesel engine is working. The EGR valve closing, the exhaust backpressure increase, the air mass flow reduction, and the in-cylinder pressure reduction led to an increase in NOx, THC, and Soot. However, the CO decreases due to the sharp decrease in fuel consumption to protect the turbocharger, lowering the fuel-to-air ratio and improving the combustion process.

6.1.3.2 Temperature

Concerning the conclusions found about the ambient temperature effect on the performance of a diesel engine, they are focused on the turbo compressor operation. Since all the turbocharged engines studied has a water charge air cooling (WCAC) system that controls the temperature downstream of the compressor, making entirely independent the cylinder intake and exhaust temperature from the ambient temperature.

The increase in ambient temperature increases the compressor's power demand, which must be compensated by increasing the power produced in the turbine. In the studied engines, it has been found that the increase in the turbine's power output happens by increasing the turbine inlet temperature. At the same time, the pressure remains constant, which is caused by the higher fuel-to-air ratio. It has been found that when the ambient temperature increases, the combustion air flow the ECU measures decrease, leading to a higher fuel-to-air ratio since the fuel consumption does not change to keep the engine load point. Therefore, it can be concluded that the increase in ambient temperature leads to a reduction in engine efficiency.

The increase in the fuel-to-air ratio also affects pollutant emissions. The NOx emissions decrease since the lower amount of O_2 reduces the generation rate of NOx, even with a higher temperature caused by the richer combustion. Concerning the CO and Soot emissions, both follow the same trend, in which the production of these two pollutant increase due to the lack of O_2 caused by the higher fuel-to-air ratio. Finally, for the THC, there were no changes observed when increasing the ambient temperature.

6.1.3.3 Humidity

Lastly, several conclusions have been found related to the effect of ambient humidity on diesel engine performance and pollutant emissions.

In the first place, for the engine performance, the increase of the combustion air water content causes a reduction in the engine efficiency since it has been found that the rise in humidity delays the beginning of both the pilot and main combustion and reduces the maximum heat release during the main combustion.

In turn, this causes an increase in the fuel consumption to achieve a given engine load point to the dry case.

Moreover, the increase in ambient humidity affects the amount of O_2 available during combustion in three different ways. Firstly, the rise in moisture involves a decrease in the density of the combustion air, which reduces the mass flow flowing into the cylinders. Secondly, the composition of the combustion air changes when increasing the humidity, reducing the amount of dry air (mainly N_2 and O_2) by replacing it with water vapor. Finally, the increase in humidity reduces the engine's volumetric efficiency, reducing the combustion air mass flow. The latter happens due to the change in composition, which is related directly to the specific volume of the mixture. This causes a higher expansion rate inside the cylinder for a given heat flux during the intake stroke, which is the leading cause of the engine's volumetric efficiency reduction.

Therefore, it has been found that combustion air humidity affects all the primary engine-out pollutant emissions of a diesel engine. CO increases when the humidity increases due to the increase in the fuel-to-O_2 ratio and the decrease in engine efficiency. Also, the THC rises due to the rise in the fuel injected and the delay in the combustion, leaving higher levels of unburned hydrocarbons at the late combustion phases.

The NOx decreases significantly when the combustion air humidity increases, having a higher potential for NOx control than more common strategies like the EGR. The decrease of NOx has been concluded to be caused by the reduction of O_2 available during the combustion due to the higher fuel-to-air ratio and the substitution of O_2 by water vapor instead of a drop in the maximum in-cylinder temperature.

Moreover, it has been found that the control of NOx using the combustion air humidity provides a better result in soot production than controlling them by employing EGR. This is caused by the increase in available fuel at the end of the combustion due to the combustion delay and the increase in injected fuel, which increases the temperature during the post-injection phase and favors the oxidation of the soot, reducing the opacity at the cylinder outlet.

6.1.4. Components development

Several conclusions have been obtained from designing and developing the unique components installed in the atmosphere simulator, i.e., the axial cyclonic separators, the exhaust gases heat exchangers, the piping geometry connecting the elements, and the bubble water column used for moistening the air stream.

6.1.4.1 Cyclonic separator

During the design of the axial cyclonic water droplet separator carried out through CFD calculations, several design rules that improve the pressure drop of this component have been obtained.

Firstly, a complete NACA profile causes an unnecessary increase in the flow velocity, leading to a rise in the pressure drop. The sharp end of the NACA profile dramatically increases the speed of the rotating flow, which can be avoided if the NACA profile is truncated and the pointed end removed.

Secondly, a smooth area increment in the diffuser increases the effective flow section, significantly reducing the flow take-off from the walls. This allows the reduction of turbulence and flow velocity, which ends up in a reduction of the pressure drop.

Lastly, rounding the edge of the inlet section of the diffuser improves the flow inlet into the diffuser, further reducing the flow take-off from the diffuser walls and thus the pressure drop.

Thus, the final solution for the cyclonic separator presented in Section 3.3.3.2 consists of a variable section cyclone with an inlet section of 314 mm and an outlet section of 180 mm, with a truncated NACA profile, and a diffuser made of two cones and with a rounded inlet section.

6.1.4.2 Exhaust cooler

The development of the new exhaust gasses coolers also brought to light some crucial conclusions relative to the design process of this kind of heat exchanger.

In the first place, the design methodology proposed, composed of a 0D model adjusted using CFD calculations, has been proved helpful for the fast design of tubes and shell exhaust gas heat exchangers since it provided accurate results during the experimental validation of the final solution obtained.

Following, it has been found that to improve the heat transfer of the tube and shell heat exchanger, the design effort should be put into improving the gas side instead of the waterside of the heat exchanger. This is based on the temperature of the tube walls, which was found equal to the cooling water temperature in all the operative points calculated through CFD, meaning that the heat transfer on the waterside has reached a maximum and cannot be increased. Therefore, to improve the heat transfer of the heat exchanger and thus its efficiency, the effort must be focused on increasing the heat transfer between the exhaust gases and the tube walls.

Finally, the design limit of this type of exhaust cooler has been found. The objectives proposed at the beginning of the design process: equipment compactness, low-pressure drop, and high heat transfer for the tubes and shell exhaust cooler, were impossible to achieve simultaneously. It has been found that the actions that must be taken to achieve one objective oppose the fulfillment of the others. As an example, assuming that the size of the component is fixed (compactness achieved), if the low-pressure drop target is achieved, then the heat transfer target will not be reached, and vice versa. This behavior makes

impossible the achievement of all three objectives proposed for this component, which forces to reach a compromise between the three in the final design.

Therefore, the final solution adopted for the application described in Section 3.3.3.1 consists of a tube and shell heat exchanger, being the gas side inside the tubes and waterside in the shell, with a length of 0.826 m, a shell diameter of 324 mm, and an inlet tube diameter of 10 mm in the case of the Medium Duty MEDAS (MEDAS MD) and a length of 1.028 m, a shell diameter of 324 mm, and an inlet tube diameter of 11 mm for the Heavy Duty MEDAS (MEDAS HD).

6.1.4.3 Bubbling water column

Some conclusions concerning the calculation utilizing a CFD code on a bubbling case came to light.

It has been shown how the continuous-phase-interaction model always overestimates the increase in height that the water can reach inside the column when an airflow stream, at any velocity, bubbles through it. Therefore, this model type leads to an oversized solution of the water column obtained. Nevertheless, this phase interaction model can be used to obtain a valid geometry for bubbling water columns that avoids problems of overflowing, as shown in Section 4.3.2. However, it must be noted that it is not possible to design the optimal geometry for the application studied with this model.

By contrast, the multi-regime-interaction model can accurately predict the air bubbling behavior and the water level inside the water column for the range of air velocities tested. Therefore, it can be concluded that this is the phase interaction model that should be used to design equipment for the application described in the current Ph.D. Thesis.

It should be noted that the cell size around the phase interaction is crucial for achieving a correct solution. If the cell size is too small, there would be increased errors in the calculations, i.e., a higher ratio of mass imbalance. If it is too big, both phases will fade, reducing the resolution and accuracy of the CFD calculation. Therefore, for applications like those depicted in this Ph.D. Thesis, the cell size for the interphase calculation should be around 18 mm to achieve an accurate result.

Lastly, to optimize the design, it is necessary to fit the footprint to the mass flow range used in the application to keep the air velocity through the water-column controlled. Also, a compromise should be reached on the initial water-column height considering the maximum target for water content in the air current and the maximum total height available for the equipment. In the case of the application described in this Ph.D. Thesis, an initial water-column height of 0.5 m, a footprint of 0.81 m^2, and an equipment height of 1.3 m have been adopted as a final design.

6.2. Conclusions on the broader research context

Thanks to this Ph.D. Thesis, several design methodologies and components have been developed to obtain an atmosphere simulator capable of accurately reproducing most of the environmental conditions that a vehicle may encounter while driving on the road and affect the performance and pollutant emissions of an ICE. Additionally, the atmosphere simulator's altitude simulating capabilities have been validated against the results of an altimetric chamber.

With the atmospheric simulator developed, the important effect that the atmospheric conditions (pressure, temperature, and humidity) have on the performance and emission of pollutants of a compression ignition ICE has been demonstrated. Also, it has been shown that thanks to using the developed equipment, it is possible to study the effect of water injection in the intake line of an ICE without modifying any component or the engine layout.

A real-time monitoring and diagnosis system has been developed and incorporated into the atmosphere simulator to control the state of the tractor oil used in the mechanical compressors installed. Moreover, an original pressure management system has been designed and included in the oil tank to minimize the oil leaks in the turbocharger to the primary air circuit.

During the development of this Ph.D. Thesis, a series of methodologies related to the design of components have been developed. In the first place, a method based on CFD calculations and validated experimentally has been developed to design a bubbling water column used in the humidification process of a pressurized air current. Secondly, a method based on mixing 0D models, CFD calculations, and experimental results has been developed to design a shell and tube heat exchanger, allowing us to find the design limits of this heat exchanger type. Lastly, several design rules have been obtained purely through CFD calculations to design an axial particle/droplet separator based on standard manufacturing parts and minimizing the 3D printed pieces.

Lastly, a 1D model of the altitude simulator has been developed through which the behavior of the system can be predicted based on boundary conditions, such as the installation altitude of the equipment, the operating point of the coupled engine, or the ambient temperature of the test cell.

This model includes several models obtained through original modeling methodologies, such as the pressure drop correlations obtained through CFD calculations and experimentally validated. This method correlates the inlet and outlet Reynolds number with the pressure drop of a given flow path in a given piping geometry. Another would be the variable geometry turbine extrapolation model, which allows a specific extrapolation model designed for rotating blades VGT to model any VGT independently of the actuation mechanism.

6.3. Future works

Several improvement works could be carried out but were left out of the current Ph.D. Thesis, since they could not be completed during the period assigned to the Ph.D. studies. These works are related to the atmosphere simulator's control loop redesign, 1D modeling of the atmosphere simulator, and the detailed analysis of the effect of the combustion air humidity on a diesel combustion process.

6.3.1. Atmosphere simulator

6.3.1.1 Control redesign

The control software of the atmosphere simulator has been optimized to achieve the different set points demanded by the user through PIDs and simplified integral controllers that actuate over the control valves and mechanical compressors installed. However, an adaptive predictive control based on experimental models could be developed to perform the actuation of the control elements, which will allow for the faster and more accurate achievement of the user set points [2], [3].

To develop this kind of control, an extensive experimental characterization to identify the effect that each actuator has over the sensors installed, to build an accurate system model that would allow predicting in which position each actuator must be placed to achieve the set points.

Additionally, an adaptive feature could be included that would allow adjusting the model of the actuator programmed to consider the minor discrepancies that could appear concerning the initial characterization due to wear and tear of the components or the manufacturing tolerances.

6.3.1.2 1D Modelling

For the atmosphere simulator 1D modeling, the development of a complete VEMOD model of the whole atmosphere simulator is pendant, which will allow the estimation of the operative conditions and design limitations depending on the supplies and boundary conditions. This would be an exciting tool to develop since it would be helpful for future improvements and redesigns of the installation or the development of new sizes of the current layout that would allow higher mass flow provided, as shown in Section 3.3.4 of this Ph.D. Thesis.

6.3.2. Effect of the humidity on a diesel combustion process

Following, the last of the future works proposed is to fully understand why the increase in the combustion air humidity causes the changes in performance and pollutant emissions in a diesel engine shown in Section 5.3. To achieve this objective, it would be necessary to start an experimental featuring of diesel combustion in a single-cylinder engine with different levels of water content in

the combustion air. Trying to identify the fundamental processes in which the combustion air humidity affects the combustion and replicate the results found in multi-cylinder engines presented in the current Ph.D. Thesis.

Therefore, it is proposed to use the atmosphere simulator developed to further study the effect of the combustion air humidity in a simpler single-cylinder engine to reach a definitive conclusion for the results obtained with the multi-cylinder engine.

6.4. Bibliography

[1] J. Kuttippurath *et al.*, "Observed rainfall changes in the past century (1901–2019) over the wettest place on Earth," *Environmental Research Letters*, vol. 16, no. 2, Jan. 2021, doi: 10.1088/1748-9326/abcf78.

[2] K. Ogata and J. G. Aranda Pérez, "Sistemas de control en tiempo discreto," 2ª Ed. Prentice Hall Hispanoamericana, 1996.

[3] K. Ogata and M. Á. Martínez, "Ingeniería de control moderna." 3ª Ed. Prentice Hall Hispanoamericana, 1998.

Chapter 7
Global Bibliography

C. E. Agu, L. A. Tokheim, M. Eikeland, and B. M. E. Moldestad, "Improved models for predicting bubble velocity, bubble frequency and bed expansion in a bubbling fluidized bed," *Chemical Engineering Research and Design*, vol. 141, pp. 361–371, Jan. 2019, doi: 10.1016/j.cherd.2018.11.002.

H. An, P. Cui, L. Fang, W. Wang, D. Zhao, and W. Yuan, "Study on the Performance of Heat and Mass Transfer of Cross Flow Dehumidifier in an Industrial Plant," in *Procedia Engineering*, 2017, vol. 205, pp. 1515–1522. doi: 10.1016/j.proeng.2017.10.381.

Armstrong International Inc., "Conditioned steam humidifiers," 2020. Accessed: Jan. 19, 2022. [Online]. Available: https://haarla.fi/wp-content/uploads/2021/06/Conditioned-Steam-Humidifiers-598-20171101.pdf

F. J. Arnau, J. Martín, P. Piqueras, and Á. Auñón, "Effect of the exhaust thermal insulation on the engine efficiency and the exhaust temperature under transient conditions," *International Journal of Engine Research*, vol. 22, no. 9, pp. 2869–2883, Sep. 2021, doi: 10.1177/1468087420961206.

C. J. Bartholomew *et al.*, "The effect of moderate levels of simulated altitude on sustained cognitive performance," *International Journal of Aviation Psychology*, vol. 9, no. 4, pp. 351–359, 1999, doi: 10.1207/s15327108ijap0904_3.

A. Baylar and F. Ozkan, "Applications of venturi principle to water aeration systems," Environmental Fluid Mechanics, vol. 6, no. 4, pp. 341–357, Aug. 2006, doi: 10.1007/s10652-005-5664-9.

Beckhoff Automation GmbH, "Beckhoff EL33xx-00x0," Jul. 2021. Accessed: Dec. 22, 2021. [Online]. Available: https://download.beckhoff.com/download/document/io/ethercat-terminals/el33xxen.pdf

B. Bendz, M. Rostrup, K. Sevre, T. 0 Andersen, and P. M. Sandset, "Association between acutehypobaric hypoxia and activation ofcoagulation in human beings," *The Lancet*, vol. 356, 2000, doi: 10.1016/S0140-6736(00)03165-2.

V. Bermúdez, J. M. Lujan, B. Pla, and W. G. Linares, "Effects of low pressure exhaust gas recirculation on regulated and unregulated gaseous emissions during NEDC in a light-duty diesel engine," *Energy*, vol. 36, no. 9, pp. 5655–5665, 2011, doi: 10.1016/j.energy.2011.06.061.

V. Bermúdez, J. v. Pastor, J. J. López, and D. Campos, "Experimental correlations for transient soot measurement in diesel exhaust aerosol with light extinction, electrical mobility and diffusion charger sensor techniques," *Measurement Science and Technology*, vol. 25, no. 6, Apr. 2014, doi: 10.1088/0957-0233/25/6/065204.

V. Bermúdez, J. R. Serrano, P. Piqueras, J. Gómez, and S. Bender, "Using an altitude simulation machine to analyze performance and emissions of a turbocharged Diesel engine operating on plateaus at high altitude," *THIESEL Conference*, 2016.

V. Bermúdez, J. R. Serrano, P. Piqueras, J. Gómez, and S. Bender, "Analysis of the role of altitude on diesel engine performance and emissions using an atmosphere simulator," *International Journal of Engine Research*, vol. 18, no. 1–2, pp. 105–117, Feb. 2017, doi: 10.1177/1468087416679569.

V. Bermúdez, J. R. Serrano, P. Piqueras, and B. Diesel, "Fuel consumption and aftertreatment thermal management synergy in compression ignition engines at variable altitude and ambient temperature," *International Journal of Engine Research*, 2021, vol. 1, no. 13, doi: 10.1177/14680874211035015.

V. Betageri and R. Mahesh, "Effects of the Real Driving Conditions on the NOx Emission of a Medium Duty Diesel Commercial Vehicle," in *SAE Technical Papers*, Jan. 2017, 2017-26-0124. doi: 10.4271/2017-26-0124.

J. Bird and W. Grabe, "Humidity effects on gas turbine performance," *ASME 1991 International Gas Turbine and Aeroengine Congress and Exposition*, vol. 2, 1991, doi: 10.1115/91-GT-329.

A. Broatch, J. R. Serrano, A. Abbad, R. Tabet, S. Bender, and J. Gómez, "Emissions and performance correlations of a turbocharged diesel engine when operating on plateaus at high altitude inside an altitude chamber or connected to an altitude simulator," *EAEC Conference*, 2017.

A. Broatch, V. Bermúdez, J. Ramón Serrano, R. Tabet-Aleixandre, J. Gómez, and S. Bender, "Analysis of passenger car turbocharged diesel engines performance when tested at altitude and of the altitude simulator device used," *ASME ICEF Conference*, 2018, ICEF2018-9549.

A. Broatch, V. Bermúdez, J. R. Serrano, R. Tabet, J. Gómez, and S. Bender, "Analysis of passenger car turbocharged diesel engines performance when tested at altitude and of the altitude simulator device used," *Journal of Engineering for Gas Turbines and Power*, vol. 141, no. 8, Aug. 2019, doi: 10.1115/1.4043395.

R. L. Brugler, “Air handling unit,” Patent 270483, 1952.

G. Cerne, S. Petelin, and I. Tiselj, “Coupling of the Interface Tracking and the Two-Fluid Models for the Simulation of Incompressible Two-Phase Flow,” *Journal of Computational Physics*, vol. 171, no. 2, pp. 776–804, Aug. 2001, doi: 10.1006/jcph.2001.6810.

C. A. Chaffin and T. L. Ullman, “Effects of Increased Altitude on Heavy-Duty Diesel Engine Emissions,” in *SAE Technical*, 1994, no. 412, pp. 776–5760. doi: 10.4271/940669.

D. Chen and H. Peng, “A thermodynamic model of membrane humidifiers for PEM fuel cell humidification control,” *Journal of Dynamic Systems, Measurement and Control, Transactions of the ASME*, vol. 127, no. 3, pp. 424–432, Sep. 2005, doi: 10.1115/1.1978910.

S. Chen, C. Liu, Z. Wu, and Q. Yu, “Effects of co-current airflow on water atomization in a curved diffuser,” *Energy Exploration and Exploitation*, vol. 39, no. 2, pp. 657–668, Mar. 2021, doi: 10.1177/0144598720905699.

J. J. Cottrell, “Altitude exposures during aircraft flight. Flying higher,” *Chest*, vol. 93, no. 1, pp. 81–84, 1988, doi: 10.1378/chest.93.1.81.

G. de Nicolao, R. Scattolini, and C. Siviero, “Modelling the volumetric efficiency of ic engines: parametric, non-parametric and neural techniques,” *Control Engine Practice*, vol. 4, no. 10, pp. 1405–1415, 1996, doi: 10.1016/0967-0661(96)00150-5.

J. W. Dennis, “Turbocharged Diesel Engine Performance at Altitude,” *SAE Transactions*, vol. 80, no. 4, pp. 2670–2689, Sep. 1971, Accessed: Dec. 28, 2021. [Online]. Available: https://www.jstor.org/stable/44650353

J. M. Desantes, J. Galindo, F. Payri, P. Piqueras, and J. R. Serrano, “Device for conditioning the atmosphere in tests of alternative internal combustion engines, method and use of said device,” Patent WO 2016/116642 A1, 2016

J. M. Desantes *et al.*, “Device, method and use for conditioning intake air for testing internal combustion engines,” Patent WO 2019/114935 A1, 2019

“Design of compressor air inlet protection for electrical ECS,” 2014. [Online]. Available: https://cordis.europa.eu/project/id/323414

H. Erlach and J. Simperl, “Method for supplying an internal combustion engine with conditioned combustion gas, device for carrying out said method, method for determining the quantities of pollutants in the exhaust gases of an internal combustion engine, and device for carrying out said method,” Patent US 7302834 B2, 2007

European Commission Regulation, “COMMISSION REGULATION (EU) 2017/1347 of 13 July 2017 correcting Directive 2007/46/EC of the European Parliament

and of the Council on type-approval of motor vehicles with respect to emissions from light passenger and commercial vehicles (Euro 5 and Euro 6) and on access to vehicle repair and maintenance information, amending Directive 2007/46/EC of the European Parliament and of the Council," no. L 192/1. Official Journal of the European Union, Jul. 13, 2017.

European Council, "COUNCIL DIRECTIVE of 26 June 1991 amending Directive 70/220/EEC on the approximation of the laws of the Member States relating to measures to be taken against air pollution by emissions from motor vehicles," no. L 242/1. Official Journal of the European Communities, Jun. 26, 1991.

European Parliament and Council, "DIRECTIVE 94/12/CE FROM EUROPEAN PARLIAMENT AND COUNCIL of 23 March 1994 relating to measures to be taken against air pollution by emissions from motor vehicles and by which the Directive 70/220/CEE is modified," no. L 100/42. Official Journal of European Communities, Mar. 23, 1994.

European Parliament and Council, "DIRECTIVE 98/69/CE FROM EUROPEAN PARLIAMENT AND COUNCIL of 13 October 1998 relating to measures to be taken against air pollution by emissions from motor vehicles and by which the Directive 70/220/CEE is modified," no. L 350/1. Official Journal of the European Union, Oct. 13, 1998.

European Parliament and Council, "REGULATION (CE) No715/2007 OF THE EUROPEAN PARLIAMENT AND OF THE COUNCIL of 20 June 2007 on the type of homologation of motor vehicles regarding emissions from passenger cars and light commercial vehicles (Euro 5 and Euro 6) and on access to information related to the repair and maintenance of vehicles," no. L 171/1. Official Journal of the European Union, Jun. 29, 2007.

J. Galindo, J. R. Serrano, P. Piqueras, and J. Gómez, "Description and Performance Analysis of a Flow Test Rig to Simulate Altitude Pressure Variation for Internal Combustion Engines Testing," *SAE International Journal of Engines*, vol. 7, no. 4, pp. 1686–1696, Oct. 2014, doi: 10.4271/2014-01-2582.

D. G. Gardner, V. A. Zaccardi, P. A. Jalbert, and M. D. Bryant, "Reducing the Cost of Aircraft Engine Emission Measurements," *Proc. Int. Instrum. Symp.*, vol. 49, pp. 57–66, 2003.

M. Ghazikhani, M. Ebrahim Feyz, O. Mahian, and A. Sabazadeh, "Effects of altitude on the soot emission and fuel consumption of a light-duty diesel engine," *Transport*, vol. 28, no. 2, pp. 130–139, Jun. 2013, doi: 10.3846/16484142.2013.798743.

D. Gidaspow, "Multiphase Flow and Fluidization -Continuum and Kinetic Theory Descriptions," *Academic Press, Inc.*, 1994.

J. Gómez, "Development of an altitude simulator and analysis of the performance and emissions of turbocharged Diesel engines at different altitudes," Ph.D. Thesis, Universitat Politècnica de València, Spain, 2018. doi: 10.4995/Thesis/10251/101284.

E. Gorritxategi, "Online Wear Pattern Diagnostics in Rotating Machines Advanced Monitoring Technologies," Sep. 2018. Accessed: Dec. 22, 2021. [Online]. Available: https://www.mrotalk.eu/wp-content/uploads/2018/09/Atten2_Oil-sensors-for-industry.pdf

C. He *et al.*, "Emission characteristics of a heavy-duty diesel engine at simulated high altitudes," *Science of the Total Environment*, vol. 409, no. 17, pp. 3138–3143, Aug. 2011, doi: 10.1016/j.scitotenv.2011.01.029.

D. Heuwetter, W. Glewen, C. Meyer, D. Foster, M. Andrie, and R. Krieger, "Effects of low pressure EGR on transient air system performance and emissions for low temperature diesel combustion," *SAE International*, 2011, 2011-24-0062. doi: 10.4271/2011-24-0062.

H. Hiroyasu, M. Arai, and M. Tabata, "Empirical Equations for the Sauter Mean Diameter of a Diesel Spray," *SAE Transactions*, vol. 98, pp. 868–77, Jan. 1989, Accessed: Dec. 27, 2021. [Online]. Available: http://www.jstor.org/stable/44580992.

T. Höhne and P. Porombka, "Modelling horizontal two-phase flows using generalized models," *Annals of Nuclear Energy*, vol. 111, pp. 311–316, Sep. 2018, doi: 10.1016/j.anucene.2017.09.018.

D. T. Hountalas, G. C. Mavropoulos, T. C. Zannis, and S. D. Mamalis, "Use of water emulsion and intake water injection as NOx reduction techniques for heavy duty Diesel engines," *SAE Technical Paper*, 2006, 2006-01-1414, doi: 10.4271/2006-01-1414.

M. F. Hsieh and J. Wang, "Development and experimental studies of a control-oriented SCR model for a two-catalyst urea-SCR system," *Control Engineering Practice*, vol. 19, no. 4, pp. 409–422, Feb. 2011, doi: 10.1016/j.conengprac.2011.01.004.

D. M. Human, T. L. Ullman, and T. M. Baines, "Simulation of High Altitude Effects on Heavy-Duty Diesel Emissions," *SAE International*, 1990, 900883.

F. P. Incropera and D. P. DeWitt, "Fundamentals of Heat and Mass Transfer," 4th ed. Pearson Educación, 1999.

M. Ishii and K. Mishima, "Two-fluid model and hydrodynamic constitutive relations," *Nuclear Engineering and Design*, vol. 82, pp. 107–126, 1984, doi: 10.1016/0029-5493(84)90207-3.

"ISO 12103-1 Arizona Test Dust Contaminants," 2015. Accessed: Dec. 22, 2021. [Online]. Available: https://www.fiatec.com/upload/meine_bilder/dust-pdf/ISO_12103-1_Arizona_Test_Dust_A2_A4_2015.pdf

A. A. Iyer, "Experimental Study on the Effect of Water Injection in an Internal Combustion Engine," *IOSR Journal of Mechanical and Civil Engineering*, vol. 17, no. 10, pp. 58–64, Mar. 2017, doi: 10.9790/1684-17010055864.

Y. Karagöz, L. Yüksek, T. Sandalci, and A. S. Dalkiliç, "An experimental investigation on the performance characteristics of a hydroxygen enriched gasoline engine with water injection," *International Journal of Hydrogen Energy*, vol. 40, no. 1, pp. 692–702, Jan. 2015, doi: 10.1016/j.ijhydene.2014.11.013.

J. Kashdan, S. Mendez, and G. Bruneaux, "An investigation of unburnned hydrocarbon emissions in wall guided, low temperature diesel combustion," *Oil and Gas Science and Technology*, vol. 63, no. 4, pp. 433–459, 2008, doi: 10.2516/ogst:2008018.

B. Kegl and S. Pehan, "Reduction of Diesel Engine Emissions by Water Injection," in *SAE Transactions Section 3: Journal of engines*, 2001, vol. 110, pp. 2040–2047. [Online]. Available: https://about.jstor.org/terms

M. Kettner *et al.*, "Investigating the influence of water injection on the emissions of a diesel engine," *Journal of Mechanical Engineering and Sciences*, vol. 10, no. 1, pp. 1863–1881, Jun. 2016, doi: 10.15282/jmes.10.1.2016.11.0179.

K. D. Kihm, D. P. Terracina, Payne S. E., and J. A. Caton, "Synchronised droplet size measurements for coal-water slurry sprays generated from a high-pressure diesel injection system," 1993. Accessed: Dec. 27, 2021. [Online]. Available: http://minsfet.utk.edu/publications/1994_Synchronized%20Droplet%20Size.pdf

J. Ko, D. Jin, W. Jang, C. L. Myung, S. Kwon, and S. Park, "Comparative investigation of NOx emission characteristics from a Euro 6-compliant diesel passenger car over the NEDC and WLTC at various ambient temperatures," *Applied Energy*, vol. 187, pp. 652–662, Feb. 2017, doi: 10.1016/j.apenergy.2016.11.105.

J. Kuttippurath *et al.*, "Observed rainfall changes in the past century (1901–2019) over the wettest place on Earth," *Environmental Research Letters*, vol. 16, no. 2, Jan. 2021, doi: 10.1088/1748-9326/abcf78.

Labcell LTD, "ECM - baroCAN. Ambient, intake air, and cabin air module." [Online]. Available: www.labcell.com

M. Lapuerta, O. Armas, J. R. Agudelo, and A. F. Agudelo, "Estudio del efecto de la altitud sobre el proceso de combustión de motores diesel. Study of altitude effect on diesel engine combustion process."

M. Lapuerta, O. Armas, J. R. Agudelo, and C. A. Sánchez, "Study of the Altitude Effect on Internal Combustion Engine Operation. Part 1: Performance," *Información Tecnológica*, vol. 17, no. 5, pp. 21–30, Nov. 2006, doi: 10.4067/S0718-07642006000500005.

C. W. Lautenberger, J. L. de Ris, N. A. Dembsey, J. R. Barnett, and H. R. Baum, "A simplified model for soot formation and oxidation in CFD simulation of non-premixed hydrocarbon flames," *Fire Safety Journal*, vol. 40, no. 2, pp. 141–176, Mar. 2005, doi: 10.1016/j.firesaf.2004.10.002.

L. Leckelt, R. Vetsch, and B. Boudreau, "U-shaped air treatment arrangement in an air handling unit," Patent WO 2018/035217 A1, 2018

A. Li, Z. Zheng, and Y. Song, "A Simulation Study of Water Injection Position and Pressure on the Knock, Combustion, and Emissions of a Direct Injection Gasoline Engine," *ACS Omega*, vol. 6, no. 28, pp. 18033–18053, Jul. 2021, doi: 10.1021/acsomega.1c01792.

Z. Liu and J. Liu, "Effect of Altitude on the Performance and Combustion Characteristics of Direct Injection Compression Ignition Engines," *International Journal of Engine Research*, 2021, Accessed: Dec. 27, 2021. [Online]. Available: http://mc.manuscriptcentral.com

J. M. Luján, C. Guardiola, B. Pla, and P. Bares, "Estimation of trapped mass by in-cylinder pressure resonance in HCCI engines," *Mechanical Systems and Signal Processing*, vol. 66–67, pp. 862–874, 2016, doi: 10.1016/j.ymssp.2015.05.016.

X. Ma, F. Zhang, K. Han, Z. Zhu, and Y. Liu, "Effects of intake manifold water injection on combustion and emissions of diesel engine," in *Energy Procedia*, 2014, vol. 61, pp. 777–781. doi: 10.1016/j.egypro.2014.11.963.

Mahle Powertrain, "MAHLE Powertrain takes delivery of altitude and climatic equipment for new RDE test facility," *Mahle Powertrain press release*. 2017. Accessed: Mar. 21, 2022. [Online]. Available: https://www.mahle-powertrain.com/en/news-and-press/press-releases/-mahle-powertrain-takes-delivery-of-altitude-and-climatic-equipment-for-new-rde-test-facility-58305

A. Maiboom, X. Tauzia, S. Rahman Shah, and J.-F. Hétet, "Experimental Study of an LP EGR System on an Automotive Diesel Engine, compared to HP EGR with respect to PM and NOx Emissions and Specific Fuel Consumption," *Source: SAE International Journal of Engines*, vol. 2, no. 2, pp. 597–610, 2010, doi: 10.2307/26275447.

J. Martin, F. Arnau, P. Piqueras, and A. Auñon, "Development of an Integrated Virtual Engine Model to Simulate New Standard Testing Cycles," in *SAE Technical Papers*, 2018, 2018-01-1413. doi: 10.4271/2018-01-1413.

E. E. Michaelides, C. T. Crowe, and J. D. Schwarzkopf, "Multiphase Flow Handbook," 2nd ed., no. 2. CRC Press, 2017.

A. Moratal, "Experimental analysis of thermal management influence on performance and emissions in diesel engines at low ambient temperature," Ph.D. Thesis, Universitat Politècnica de València, 2018.

B. Nitu, I. Singh, L. Zhong, K. Badreshany, N. A. Henein, and W. Bryzik, "Effect of EGR on Autoignition, Combustion, Regulated Emissions and Aldehydes in DI Diesel Engines.," *SAE Transactions*, vol. 111, pp. 2028–2042, 2002, Accessed: Dec. 28, 2021. [Online]. Available: http://www.jstor.org/stable/44743219

K. Ogata and J. G. Aranda Pérez, "Sistemas de control en tiempo discreto." 2ª Ed. Prentice Hall Hispanoamericana, 1996.

K. Ogata and M. Á. Martínez, "Ingeniería de control moderna." 3ª Ed. Prentice Hall Hispanoamericana, 1998.

G. Osculati *et al.*, "Effects of hypobaric hypoxia exposure at high altitude on left ventricular twist in healthy subjects: Data from HIGHCARE study on Mount Everest," *European Heart Journal Cardiovascular Imaging*, vol. 17, no. 6, pp. 635–643, Jun. 2016, doi: 10.1093/ehjci/jev166.

Y. Park and C. Bae, "Experimental study on the effects of high/low pressure EGR proportion in a passenger car diesel engine," *Applied Energy*, vol. 133, pp. 308–316, Nov. 2014, doi: 10.1016/j.apenergy.2014.08.003.

F. Payri, J. Galindo, H. Climent, and C. Guardiola, "Measurement of the oil consumption of an automotive turbocharger," *Experimental Techniques*, vol. 29, pp. 25–27, 2005, doi: 10.1111/j.1747-1567.2005.tb00236.x.

H. Peng, Y. Cui, L. Shi, and K. Deng, "Effects of exhaust gas recirculation (EGR) on combustion and emissions during cold start of direct injection (DI) diesel engine," *Energy*, vol. 33, no. 3, pp. 471–479, 2008, doi: 10.1016/j.energy.2007.10.014.

B. Pla, J. de la Morena, P. Bares, and I. Jiménez, "Cycle-to-cycle combustion variability modelling in spark ignited engines for control purposes," *International Journal of Engine Research*, vol. 21, no. 8, pp. 1398–1411, Oct. 2020, doi: 10.1177/1468087419885754.

A. S. Ramadhas and H. Xu, "Influence of Coolant Temperature on Cold Start Performance of Diesel Passenger Car in Cold Environment," in *SAE Technical Papers*, Feb. 2016, 2016-28-0142. doi: 10.4271/2016-28-0142.

A. Ramos, "Emisiones contaminantes diésel en condiciones transitorias de motores y vehículos empleando combustibles alternativos," Ph.D, Thesis, Universidad De Castilla-La Mancha, Spain, 2016.

A. Ramos, J. Muñoz, F. Andrés, and O. Armas, "NOx emissions from diesel light duty vehicle tested under NEDC and real-word driving conditions," *Transportation Research Part D: Transport and Environment*, vol. 63, pp. 37–48, Aug. 2018, doi: 10.1016/j.trd.2018.04.018.

M. R. Rampure, A. A. Kulkarni, and V. v. Ranade, "Hydrodynamics of bubble column reactors at high gas velocity: Experiments and computational fluid dynamics

CFD simulations," in *Industrial and Engineering Chemistry Research*, Dec. 2007, vol. 46, no. 25, pp. 8431–8447. doi: 10.1021/ie070079h.

S. Reifarth, "EGR-Systems for Diesel Engines," Licentiate Thesis, Royal Institute of Technology, Stockholm, 2010.

J. H. Roberts, W. R. Beyerly, M. W. Mason, J. R. Glazier, and R. H. Wiley, "PW4084 Engine testing in altitude & sea level test facilities," *SAE Technical Papers*, 1994, 942140. doi: 10.4271/942140.

P. Roberts, A. Mason, A. Headley, L. Bates, S. Whelan, and K. Tabata, "RDE plus - A Road to Rig Development Methodology for Whole Vehicle RDE Compliance: Road to Engine Perspective," in *SAE Technical Papers*, Sep. 2021, 2021-01-1223. doi: 10.4271/2021-01-1223.

M. Rüdisüli, T. J. Schildhauer, S. M. A. Biollaz, and J. R. van Ommen, "Scale-up of bubbling fluidized bed reactors - A review," *Powder Technology*, vol. 217. pp. 21–38, Feb. 2012. doi: 10.1016/j.powtec.2011.10.004.

S. Savic, G. Mitsis, C. Haertel, S. Khaidarov, and P. Pfeiffer, "Spray interaction and droplet coalescence in turbulent air-flow. An experimental study with application to gas turbine high fogging," 2002. [Online]. Available: https://www.researchgate.net/publication/268056048

J. R. Serrano, B. Tormos, K. L. Gargar, and F. Bouffaud, "Study of the effects on turbocharger performance generated by the presence of foreign objects at the compressor intake," *Experimental Techniques*, vol. 37, no. 2, pp. 30–40, Mar. 2013, doi: 10.1111/j.1747-1567.2011.00795.x.

J. R. Serrano, P. Piqueras, E. Angiolini, C. Meano, and J. de La Morena, "On Cooler and Mixing Condensation Phenomena in the Long-Route Exhaust Gas Recirculation Line," in *SAE Technical Papers*, Sep. 2015, 2015-24-2521. doi: 10.4271/2015-24-2521.

J. R. Serrano, R. Navarro, L. M. García-Cuevas, and L. B. Inhestern, "Turbocharger turbine rotor tip leakage loss and mass flow model valid up to extreme off-design conditions with high blade to jet speed ratio," *Energy*, vol. 147, pp. 1299–1310, Mar. 2018, doi: 10.1016/j.energy.2018.01.083.

J. R. Serrano, P. Piqueras, A. Abbad, R. Tabet, S. Bender, and J. Gómez, "Impact on reduction of pollutant emissions from passenger cars when replacing euro 4 with euro 6d diesel engines considering the altitude influence," *Energies*, vol. 12, no. 7, 2019, doi: 10.3390/en12071278.

J. R. Serrano, F. J. Arnau, L. M. García-Cuevas, and V. Samala, "A robust adiabatic model for a quasi-steady prediction of far-off non-measured performance in vaneless twin-entry or dual-volute radial turbines," *Applied Sciences (Switzerland)*, vol. 10, no. 6, Mar. 2020, doi: 10.3390/app10061955.

J. R. Serrano, F. J. Arnau, J. Martín, and Á. Auñón, "Development of a variable valve actuation control to improve diesel oxidation catalyst efficiency and emissions in a light duty diesel engine," *Energies*, vol. 13, no. 17, Sep. 2020, doi: 10.3390/en13174561.

J. R. Serrano, A. Gil, P. Quintero, R. Tabet, and J. Gómez, "Design of a bubble reactor for altitude simulators used to humidify a combustion air stream by means of CFD multi-phase models," *Applied Sciences (Switzerland)*, vol. 11, no. 1, pp. 1–15, Jan. 2021, doi: 10.3390/app11010295.

R. K. Shah, E. C. Subbarao, and R. A. Mashelkar, "Heat transfer equipment design." Hemisphere Publishing Corp., 1988. doi: 10.1080/07373938908916636.

S. Sm and Srinivas M, "Improvement of Fuel Efficiency in a Petrol Engine by using Water Injection," 2017. [Online]. Available: www.tsijournals.com

J. C. Smith, P. J. Maloney, and M. Osterhout, "Altitude simulator for dynamometer testing," Patent US 6561014 B1, 2003

K. A. Subramanian, "A comparison of water-diesel emulsion and timed injection of water into the intake manifold of a diesel engine for simultaneous control of NO and smoke emissions," *Energy Conversion and Management*, vol. 52, no. 2, pp. 849–857, Feb. 2011, doi: 10.1016/j.enconman.2010.08.010.

R. Sun and H. Xiao, "Diffusion-based coarse graining in hybrid continuum-discrete solvers: Theoretical formulation and a priori tests," *International Journal of Multiphase Flow*, vol. 77, pp. 142–157, Dec. 2015, doi: 10.1016/j.ijmultiphaseflow.2015.08.014.

M. Szedlmayer and C. B. M. Kweon, "Effect of Altitude Conditions on Combustion and Performance of a Multi-Cylinder Turbocharged Direct-Injection Diesel Engine," in *SAE Technical Papers*, Apr. 2016, 2016-01-0742. doi: 10.4271/2016-01-0742.

X. Tauzia, A. Maiboom, and S. R. Shah, "Experimental study of inlet manifold water injection on combustion and emissions of an automotive direct injection Diesel engine," *Energy*, vol. 35, no. 9, pp. 3628–3639, 2010, doi: 10.1016/j.energy.2010.05.007.

D. Testa, "Apparatus and method for altimetric conditioning of internal combustion engines," Patent EP 2295950 B1, 2013

"The delineation of European mountain areas," 2000. Accessed: Apr. 01, 2019. [Online]. Available: https://ec.europa.eu/regional_policy/sources/docgener/studies/pdf/montagne/mount4.pdf

W. D. Toff *et al.*, "Effect of Hypobaric Hypoxia, Simulating Conditions During Long-Haul Air Travel, on Coagulation, Fibrinolysis, Platelet Function, and

Endothelial Activation," *Journal of the American Medical Association*, vol. 295, no. 19, pp. 2251–2261, 2006, doi: 10.1001/jama.295.19.2251.

A. J. Torregrosa, A. Broatch, X. Margot, J. García-Tíscar, Y. Narvekar, and R. Cheung, "Local flow measurements in a turbocharger compressor inlet," *Experimental Thermal and Fluid Science*, vol. 88, pp. 542–553, Jul. 2017, doi: 10.1016/j.expthermflusci.2017.07.007.

"User Guide Simcenter STAR-CCM+." Siemens Digital Industries Software, 2020. [Online]. Available: www.siemens.com/mdx

R. van Helen, R. Verbeek, F. Willenms, and R. van der Welle, "Optimization of Urea SCR DeNOx Systems for HD Diesel Engines," *SAE Technical Paper*, 2004-01-0154.

"Vehicles in use Europe 2017," 2017. Accessed: Apr. 01, 2019. [Online]. Available: https://www.acea.be/statistics/article/Report-Vehicles-in-Use

X. Wang, Y. Ge, L. Yu, and X. Feng, "Effects of altitude on the thermal efficiency of a heavy-duty diesel engine," *Energy*, vol. 59, pp. 543–548, Sep. 2013, doi: 10.1016/j.energy.2013.06.050.

X. Wang *et al.*, "On-vehicle emission measurement of a light-duty diesel van at various speeds at high altitude," *Atmospheric Environment*, vol. 81, pp. 263–269, Dec. 2013, doi: 10.1016/j.atmosenv.2013.09.015.

M. Weilenmann, P. Soltic, C. Saxer, A. M. Forss, and N. Heeb, "Regulated and nonregulated diesel and gasoline cold start emissions at different temperatures," in *Atmospheric Environment*, 2005, vol. 39, no. 13, pp. 2433–2441. doi: 10.1016/j.atmosenv.2004.03.081.

M. Yang, Y. Gu, K. Deng, Z. Yang, and Y. Zhang, "Analysis on altitude adaptability of turbocharging systems for a heavy-duty diesel engine," *Applied Thermal Engineering*, vol. 128, pp. 1196–1207, 2018, doi: 10.1016/j.applthermaleng.2017.09.065.

L. Yu *et al.*, "Experimental investigation of the impact of biodiesel on the combustion and emission characteristics of a heavy duty diesel engine at various altitudes," *Fuel*, vol. 115, pp. 220–226, 2014, doi: 10.1016/j.fuel.2013.06.056.

Y. Zama, W. Ochiai, T. Furuhata, and M. Arai, "Experimental study on spray angle and velocity distribution of diesel spray under high ambient pressure conditions," *Atomization and Sprays*, vol. 21, no. 12, pp. 989–1007, 2011.

Y. Zeldóvich, "Oxidation of Nitrogen in Combustion and Explosions," *Acta Pysichochimica*, vol. 21, pp. 557–628, 1946, doi: 10.1515/9781400862979.404.

A. Zukauskas and J. Ziugzda, "Heat transfer of a cylinder in crossflow." 1985. Accessed: Dec. 22, 2021. [Online]. Available: https://ui.adsabs.harvard.edu/abs/1985wdch.book.....Z